

1 The Pennsylvania State University
2 The Graduate School
3 Eberly College of Science

4 **DEVELOPMENT OF SCALABLE APPROACHES TO NEUTRINO MASS**
5 **MEASUREMENT WITH THE PROJECT 8 EXPERIMENT**

6 A Thesis in
7 The Physics Department
8 by
9 Andrew Douglas Ziegler

10 © 2023 Andrew Douglas Ziegler

11 Submitted in Partial Fulfillment
12 of the Requirements
13 for the Degree of

14 Doctor of Philosophy

15 December 2023

¹⁶ The thesis of Andrew Douglas Ziegler was reviewed and approved* by the following:

Luiz de Viveiros Souza
Assistant Professor of Physics
Thesis Advisor
Chair of Committee

Carmen Carmona
Assistant Professor of Physics

¹⁷ Doug Cowan
Professor of Physics and Astrophysics

Xingjie Ni
Associate Professor of Electrical Engineering

¹⁸ Stephanie Wissel
Associate Professor of Physics

¹⁹ *Signatures are on file in the Graduate School.

²⁰ Abstract

21 Neutrinos are fundamental particles in the standard model and play an important role
22 in the current understanding of the universe, however, the masses of the neutrinos, one
23 of the most fundamental parameters for any particles, is currently unknown. This fact
24 represents a gaping hole in our current knowledge of the universe that may provide
25 clues to the energy scale of possible physics beyond the standard model. This thesis
26 summarizes research and development as a member of the Project 8 collaboration towards
27 an experiment to measure the neutrino mass to a sensitivity below $50 \text{ meV}/c^2$, which
28 is an order of magnitude below the most sensitive direct measurements of the neutrino
29 mass to date. Project 8 will perform this measurement using Cyclotron Radiation
30 Emission Spectroscopy (CRES) to measure the beta-decay endpoint spectrum of atomic
31 tritium. I present an analysis of the signal reconstruction performance of an antenna
32 array system designed to perform large-scale CRES measurements. Next, I discuss an
33 approach to calibrating an antenna array CRES experiment using a unique probe antenna
34 designed to mimic radiation from CRES events. Finally, I present design studies for a
35 resonant cavity that could be used to perform a CRES experiment with atomic tritium
36 at multi-cubic-meter scales.

Table of Contents

38	List of Figures	viii
39	List of Tables	xxvi
40	Chapter 1	
41	Introduction	1
42	1.1 Summary	1
43	1.2 Outline	4
44	Chapter 2	
45	Neutrinos and Neutrino Masses	6
46	2.1 Introduction	6
47	2.2 Neutrinos and Beta-decay	6
48	2.3 Neutrino Oscillations	7
49	2.4 Neutrino Masses in the Standard Model	10
50	2.5 Neutrino Absolute Mass Scale	13
51	2.5.1 Limits from Cosmology	13
52	2.5.2 Limits from Neutrinoless Double Beta-decay Searches	15
53	2.5.3 Limits from Beta-decay	16
54	Chapter 3	
55	Direct Measurement of the Neutrino Mass with Project 8	21
56	3.1 Introduction	21
57	3.2 Cyclotron Radiation Emission Spectroscopy and Project 8	22
58	3.2.1 Cyclotron Radiation Emission Spectroscopy — CRES	22
59	3.2.2 The Project 8 Collaboration	26
60	3.2.3 The Project 8 Phased Development Plan	30
61	3.3 Phase II: First Tritium Beta Decay Spectrum and Neutrino Mass Mea- surement with CRES	33
62	3.3.1 The Phase II CRES Apparatus	34
63	3.3.2 CRES Track and Event Reconstruction	38
64	3.3.3 Results from Phase II	42
65	3.4 Phase III R&D: Antenna Array CRES	46
66	3.4.1 The Basic Approach	46

68	3.4.2 The FSCD: Free-space CRES Demonstrator	48
69	3.5 Pilot-scale Experiments	53
70	3.5.1 Choice of Frequency	53
71	3.5.2 Pilot-scale Experiment Concepts	56
72	3.6 Phase IV	58

73 **Chapter 4**

74 **Signal Reconstruction Techniques for Antenna Array CRES and the**

75 **FSCD**

76	4.1 Introduction	60
77	4.2 FSCD Simulations	61
78	4.2.1 Kassiopeia	62
79	4.2.2 Locust	66
80	4.2.3 CRESana	70
81	4.3 Signal Detection and Reconstruction Techniques for Antenna Array CRES	71
82	4.3.1 Digital Beamforming	75
83	4.3.2 Matched Filtering	85
84	4.3.3 Machine Learning	97
85	4.4 Analysis of Signal Detection Algorithms for the Antenna Array Demonstrator	102
86	4.4.1 Introduction	103
87	4.4.2 Signal Detection with Antenna Array CRES	106
88	4.4.2.1 Antenna Array and DAQ System	106
89	4.4.2.2 Real-time Signal Detection	108
90	4.4.3 Signal Detection Algorithms	112
91	4.4.3.1 Power Threshold	112
92	4.4.3.2 Matched Filtering	114
93	4.4.3.3 Machine Learning	118
94	4.4.4 Methods	120
95	4.4.4.1 Data Generation	120
96	4.4.4.2 Template Number and Match Estimation	121
97	4.4.4.3 CNN Training and Data Augmentation	122
98	4.4.5 Results and Discussion	123
99	4.4.5.1 Trigger Classification Performance	123
100	4.4.5.2 Computational Cost and Hardware Requirements	125
101	4.4.6 Conclusion	127

102 **Chapter 5**

103 **Antenna and Antenna Measurement System Development for the**

104 **Project 8 Experiment**

105	5.1 Introduction	129
106	5.2 Antenna Measurements for CRES experiments	130
107	5.2.1 Antenna Parameters	130
108	5.2.1.1 Radiation Patterns	130
109	5.2.1.2 Directivity and Gain	131

110	5.2.1.3	Far-field and Near-field	132
111	5.2.1.4	Polarization	133
112	5.2.1.5	Antenna Factor and Effective Aperture	134
113	5.2.2	Antenna Measurement Fundamentals	136
114	5.2.2.1	Friis Transmission Equation	136
115	5.2.2.2	S-Parameters and Network Analyzers	137
116	5.2.2.3	Antenna Array Commissioning and Calibration Measurements	138
117	5.2.3	The Penn State Antenna Measurement System	140
118	5.3	Development of a Synthetic Cyclotron Antenna (SYNCA) for Antenna Array Calibration	143
119	5.3.1	Introduction	143
120	5.3.2	Cyclotron Radiation Phenomenology	146
121	5.3.3	SYNCA Simulations and Design	152
122	5.3.4	Characterization of the SYNCA	156
123	5.3.5	Beamforming Measurements with the SYNCA	160
124	5.3.6	Conclusions	163
125	5.4	FSCD Antenna Array Measurements with the SYNCA	164
126	5.4.1	Introduction	164
127	5.4.2	Measurement Setups	165
128	5.4.2.1	FSCD Array Setup	165
129	5.4.2.2	Synthetic Array Setup	167
130	5.4.3	Simulations, Analysis, and Results	168
131	5.4.3.1	Simulations	169
132	5.4.3.2	Phase Analysis	169
133	5.4.3.3	Magnitude Analysis	174
134	5.4.3.4	Beamforming Characterization	175
135	5.4.4	Conclusions	180

138	Chapter 6		
139	Development of Resonant Cavities for Large Volume CRES Measurements		181
140	6.1	Introduction	181
141	6.2	Cylindrical Resonant Cavities	182
142	6.2.1	General Field Solutions	182
143	6.2.2	TE and TM Modes	183
144	6.2.3	Resonant Frequencies of a Cylindrical Cavity	185
145	6.2.4	Cavity Q-factors	187
146	6.3	The Cavity Approach to CRES	191
147	6.3.1	A Sketch of a Molecular Tritium Cavity CRES Experiment	191
148	6.3.2	Magnetic Field, Cavity Geometry, and Resonant Modes	193
149	6.3.3	Trade-offs Between the Antenna and Cavity Approaches	196
150	6.4	Single-mode Resonant Cavity Design and Simulations	198
151	6.4.1	Open Cylindrical Cavities with Coaxial Terminations	198

153	6.4.2 Mode Filtering	201
154	6.4.3 Simulations of Open, Mode-filtered Cavities	203
155	6.5 Single-mode Resonant Cavity Measurements	206
156	6.5.1 Cavities and Setup	206
157	6.5.2 Results and Discussion	209
158	Chapter 7	
159	Conclusion and Future Prospects	212
160	Bibliography	214

¹⁶¹ List of Figures

¹⁶² 2.1	A diagram of two different neutrino mass ordering scenarios. In the inverted hierarchy (inverted mass ordering) the lightest neutrino mass is m_3 , whereas, in the normal hierarchy (normal mass ordering) m_1 is the lightest neutrino. What cannot be measured by neutrino oscillations is the neutrino absolute mass scale, which is essentially the mass of the lightest neutrino mass eigenstate.	8
¹⁶⁸ 2.2	The masses of the neutrinos as a function of the lightest neutrino mass in both the normal (a) and inverted (b) mass ordering regimes.	10
¹⁷⁰ 2.3	The neutrino mass observable measured by cosmology as a function of the lightest neutrino mass eigenstate.	14
¹⁷² 2.4	Feynman diagrams for double beta-decay (a) and $0\nu\beta\beta$ (b).	15
¹⁷³ 2.5	The discovery probabilities for the future generation of $0\nu\beta\beta$ experiments as a function of $m_{\beta\beta}$ and m_{least} . Figure from [1].	16
¹⁷⁵ 2.6	A Feynman diagram of beta decay	17
¹⁷⁶ 2.7	A figure from Fermi's 1934 paper on a theory of beta-decay depicting the kinetic energy spectrum of the emitted electron. The effect of the neutrino mass, written as μ , is to distort the shape of the spectrum near the endpoint from the zero-mass spectrum.	17
¹⁸⁰ 2.8	The tritium beta-decay spectrum. The affect of a massive neutrino on the spectrum is to change it's shape near the endpoint by an amount proportional to the size of the neutrino mass. This suggests that a sufficiently high-statistic and high-resolution measurement of the spectrum endpoint would be able to measure the neutrino mass.	19

185	3.1	A cartoon illustration of the CRES technique. An electron is contained in a magnetic trap so that it's cyclotron radiation can be detected by an array of antennas. Detecting the cyclotron radiation allows us to measure its cyclotron frequency and determine its kinetic energy.	23
186			
187			
188			
189	3.2	An illustration of an electron in a bathtub magnetic trap generated by two well-separated coils.	24
190			
191	3.3	A plot of the main components of an electron's trajectory in a cylindrically symmetric trap.	26
192			
193	3.4	A plot of the final state distributions of atomic and molecular tritium. The final state distribution provides the primary contribution to the width of the molecular spectrum whereas thermal doppler broadening is responsible for the width of the atomic spectrum.	27
194			
195			
196			
197	3.5	Neutrino mass exclusion plot including limits from cosmological measure- ments and the KATRIN experiment. Allowed ranges for neutrino masses under the normal and inverted hierarchies are shown as the blue and orange lines respectively. The black dashed line shows Project 8's goal neutrino mass sensitivity for the Phase IV experiment.	30
198			
199			
200			
201			
202	3.6	Sensitivity calculations for a cavity based CRES experiment that demon- strate the neutrino mass measurement goals of the Project 8 collaboration throughout the phased development plan. The blue curves indicate molec- ular tritium sources and the red curves indicate atomic tritium sources. In the current plan Phase III contains two tritium experiments. The first is the Low-frequency Apparatus (LFA) which is a molecular tritium experiment and the second is the atomic tritium pilot-scale experiment that ends Phase III. The sensitivity of these experiments is primarily a function of statistics, however, there is a critical density beyond which CRES electrons do not have enough time to radiate between collisions for a high-resolution frequency measurement leading to worse sensitivity. . .	31
203			
204			
205			
206			
207			
208			
209			
210			
211			
212			
213	3.7	The Phase II CRES apparatus used to perform the first measurement of the tritium beta-decay spectrum using CRES.	34
214			
215	3.8	Diagram of the CRES cell portion of the Phase II apparatus.	36
216			
217	3.9	RF system diagram for the Phase II apparatus.	37
218			
217	3.10	The time-frequency spectrogram of a tritium CRES event in the Phase II apparatus.	39
218			

219	3.11 The sparse spectrogram obtained by placing a power cut on the raw 220 spectrogram shown in Figure 3.10.	41
221	3.12 Fits to the measured 17.8-keV ^{83m}Kr conversion line using the deep and 222 shallow trap configurations.	43
223	3.13 Measurements of the 17.8-keV ^{83m}Kr line using the deep trap configuration 224 for different values of the magnetic field from the field shifting solenoid. .	44
225	3.14 The measured tritium spectrum from Phase II with Bayesian and frequen- 226 tist fits.	45
227	3.15 A cartoon illustration of the basics of the antenna array CREES technique.	47
228	3.16 An image of the MRI magnet installed in the Project 8 laboratory at the 229 University of Washington, Seattle.	49
230	3.17 (a) A model of the FSCD antenna array, magnetic trap, and tritium 231 containment vessel design.(b) A more detailed model of a prototype 232 design for the 5-slot waveguide antenna design.	50
233	3.18 (a) A plot of the decay rate for the two-body dipolar spin exchange 234 interaction for cc and dd state. (b) A plot of the decay rate of the dipolar 235 spin exchange interaction for d+d states as a function of magnetic field 236 magnitude. Lowering the magnetic field is key for reducing the losses 237 from this interaction.	55
238	3.19 A conceptual sketch of a large-volume antenna array based CREES experi- 239 ment to measure the neutrino mass.	56
240	3.20 A conceptual sketch of a pilot-scale cavity CREES experiment with an 241 atomic tritium beamline.	57

242	3.21 An illustration of a possible arrangement of ten pilot-scale cavity experiments for Phase IV. The experiments are arranged in a circle with an approximate diameter of 50 meters. Each atomic beamline connected to the bottom of each cavity is approximately 10 m in length. The cavities themselves are designed to operate at 325 MHz and are approximately 11 m tall. The circular arrangement of cavities has some advantages when it comes to cancellation of fringe fields from neighboring magnets, which is important due to the small magnetic field magnitudes consistent with these CRES frequencies. The advantage of ten independent atomic sources and cavities is that there is no single point of failure for the experiment. If an experiment goes down for repairs the other nine may continue running. Figure courtesy of Michael Huehn at UW-Seattle.	59
254	4.1 The geometry and parameters of the coils used to simulate the FSCD magnetic trap in Kassiopeia. Some axial profiles of the magnetic trap at different radial positions are show to demonstrate the shape of the magnetic field and trap depth as a function of position. Calulation of the magnetic field profiles was graciously done by René Reimann.	63
259	4.2 A map of the average ∇B -drift frequency for electrons trapped in the prototype FSCD trap shown in Figure 4.1. Negative drift frequencies indicate electrons that are drifting opposite to the standard direction, which means that they are close to escaping the magnetic trap.	65
263	4.3 The receiver chain used by Locust when simulating CRES events in the FSCD.	68
265	4.4 A high-level diagram depicting the process of CRES event reconstruction. The first step consists of identifying the presence of a signal in the data. This step is necessary to avoid the danger of performing a reconstruction of a false event, which would constitute a background contribution to the tritium spectrum measured by CRES.	72
270	4.5 An illustration of two PDFs associated a binary hypothesis test. The decision threshold is represented by the vertical line that partitions both distributions. The orange and red areas correspond to the true negative and false positive probabilities and the blue and green areas correspond to the false negative and true positive probabilities respectively. To decided between the two hypotheses we perform the likelihood ratio test specified by the Neyman-Pearson theorem. This approach achieves the highest true positive probability for a given false positive probability.	74

278	4.6 An example ROC curve formed by computing the P_{FP} and the P_{TP} for 279 a given likelihood ratio test. As the decision threshold is increased P_{FP} 280 decreases at the expense of a lower P_{TP} . The black dashed line indicates 281 the lower bound ROC curve obtained by randomly deciding between \mathcal{H}_0 282 and \mathcal{H}_1	75
283	4.7 An illustration of the constructive interference condition which is the 284 operating principle of digital beamforming using a uniform linear array 285 as an example.	76
286	4.8 System level diagram of the laboratory setup used for beamforming 287 demonstrations at Penn State. For more information on this system see 288 Chapter 5. Signals near 26 GHz are fed to a dipole antenna using an 289 arbitrary waveform generator (AWG) and vector network analyzer (VNA), 290 which drive a mixer. The dipole radiation is collected by an array of 291 antennas connected to the digitizer data acquisition (DAQ) system. . . .	78
292	4.9 Photographs of the beamforming demonstration setup. In (a) I show a 293 top-down view of the dipole antenna and the array of eight horn antennas. 294 Manual repositioning of the horn antennas allows one to synthesize a full- 295 circular antenna array. The dipole antenna is mounted on a camera tripod 296 mount that allows for manual position tuning. (b) is a close up image of 297 the dipole, which is manufactured from two segments of semi-rigid coaxial 298 cable. (c) is another image of the dipole and array.	79
299	4.10 An example of digital beamforming reconstruction of a dipole antenna 300 using a synthetic array of horn antennas. The beamforming image on 301 the right is constructed by computing the time-averaged power of the 302 summed signals for a two-dimensional grid of beamforming positions. In 303 the image one can see a clear maximum that corresponds to the position 304 of the dipole antenna. On the left I show the frequency spectrum of the 305 time-series at the maximum power pixel. White gaussian noise is added 306 to the signal to mimic a more realistic signal-to-noise-ratio. The signal 307 emitted by the dipole is clearly visible as the high power peak in the 308 frequency spectrum.	79
309	4.11 Beamforming images visualizing the reconstruction of an electron without 310 (a) and with (b) the cyclotron phase correction. The images were generated 311 using data from Locust simulations. The cyclotron phase refers to a phase 312 offset equal to the relative azimuthal position of an antenna in the array. 313 This phase offset is caused by the circular electron orbit and must be 314 corrected for during reconstruction.	81

315	4.12 Beamforming images visualizing the reconstruction of an electron located 316 off the central axis of the FSCD trap. In (a) we performing beamforming 317 without the ∇B -drift correction, and in (b) we include the ∇B -drift 318 correction.	82
319	4.13 A plot of a typical frequency spectrum obtained by applying a Fourier 320 transform to the time-series obtained from beamforming. The frequency 321 spectra are plotted without noise on top of an example of a typical noise 322 spectrum to visualize a realistic signal-to-noise ratio. In the example we 323 see that without beamforming it would not be possible to detect anything 324 since the signal amplitudes would be reduced by a factor of sixty relative 325 to the noise. Additionally, we see that the ∇B -drift correction is needed 326 to detect this electron since it comes from a simulation of an electron with 327 a significant off-axis position.	83
328	4.14 A plot of the total signal power received by the FSCD array from trapped 329 electrons with different radial positions and pitch angles generated using 330 Locust simulations. The lines on the plot indicate a 10 dB detection 331 threshold above the mean value of the noise in the frequency spectrum. 332 With static beamforming electrons with radial positions larger than about 333 two centimeters are undetectable due to the change in the electron's 334 position over time causing losses from beamforming phase mismatch. This 335 is corrected by including ∇B -drift frequencies in the beamforming phases. 336 Both beamforming techniques fail to detect electrons below $\approx 88.0^\circ$, since 337 these signal are composed of several relatively weak sidebands that are 338 comparable to the noise.	84
339	4.15 Example of a convolution of a CRES signal template with a segment of 340 noisy data. A simulated CRES signal was simulated using Locust and 341 normalized to create a matched filter template. When this template is 342 convolved with noisy data the contains the matching signal the con- 343 volution output increases dramatically compared to data with only noise. 344 The decreasing convolution output as the time offset of the convolution 345 increases is caused by zero-padding of the data and template.	87

346	4.16 An example two-dimensional parameter distribution of a matched filter 347 template bank and random test signals. θ refers to the pitch angle of the 348 electron and E is the kinetic energy. The template bank forms a regular 349 grid of in pitch angle and energy, whereas, the test signals are uniformly 350 distributed in pitch angle and follow the tritium beta-decay kinetic energy 351 distribution. This is why there are fewer test signals at higher energies. 352 The need for high match across the full parameter space prevents one from 353 reducing the density of templates in this low activity region. A zoomed in 354 version of the template bank illustrates the relative density of templates 355 and signals needed for match $> 90\%$	89
356	4.17 The matched filter scores of a dense grid of templates in pitch angle energy 357 space. Dense template grids allow one to estimate the kinetic energy of 358 the electron by identifying the best matching template. The uncertainty 359 on this value is proportional to the space of templates that also match 360 the test signal well. In the worst case matched filter templates can be 361 completely degenerate where templates with different parameters match 362 a signal with equal likelihood.	90
363	4.18 The mean match of the dense template grid shown in Figure 4.17 for 364 different numbers of templates. Grids of different sizes were obtained by 365 decimating a dense grid of templates and the average match for each grid 366 was computed using the same set of randomly distributed test signals. 367 Plotting the mean match against the size of the grid allows one to visualize 368 the exponential relationship between match and template bank size. The 369 noise in each curve is caused by sampling effects from the decimation 370 algorithm. In general, longer templates are harder to than shorter templates.	91
371	4.19 Matched filter template bank ROC curves as a function of mean match. 372 One can see that for low match a matched filter is on average worse than 373 the more straight forward beamforming detection approach.	91
374	4.20 Boundaries of detectable electrons in pitch angle kinetic energy space 375 for a series of different signal detection algorithms. A detectable signal 376 is defined as a signal that is above a consistent decision with at least 377 50% probability. This non-rigorous treatment of detection probability is 378 primarily useful for the visualization the relative increases in detection 379 performance provided by the different algorithms. The static beamforming 380 (Static-BF) algorithm is the digital beamforming algorithm introduced 381 above without the ∇B -drift correction. The DNN algorithm refers to a 382 convolutional neural network classifier trained to detect CRES signals 383 (see Section 4.3.3).	93

384	4.21 Two example illustrations of the correlation between kinetic energy and pitch angle imparted by the shape of the FSCD magnetic trap. The correlations manifest themselves as degeneracies in the matched filter score where multiple matched filter templates have the same matched filter for a particular signal. These degeneracies are a sign that the magnetic trap must be redesigned in order to break the correlation between pitch angle and kinetic energy.	97
391	4.22 A visualization of the correlation between energy and pitch angle in the FSCD magnetic trap. The image is formed by computing the match of the best template from a grid consisting of pitch angles from 84 to 90 degrees in steps of 0.05 degrees, kinetic energies from 17574 to 18574 eV, located at 2 cm from the central axis, and simulated for a length of three FSCD time-slices. The signals used to compute the best matching template consisted of a grid from 84 to 90 degrees in steps of 0.05 degrees, kinetic energies from 18550 to 18575 eV in steps of 0.25 eV, located 2 cm from the central axis, and simulated for three FSCD time-slices. The colored regions of the plot show how well signals with lower energy can match those of higher energy for the FSCD magnetic trap, which is proportional to the achievable energy resolution of the FSCD design.	98
403	4.23 A representation of a matched filter template bank as a convolutional neural network. The network has a single layer composed of the templates, which act as convolutional filters. The activation of the neural network is an absolute value followed by a max operator.	100
407	4.24 A graphical depiction of CRES signal detection using a CNN. A noisy seg- ment of data is converted to a frequency series using digital beamforming and a FFT. The complex-valued frequency series is input into a trained CNN model that classifies the data as signal or noise using a decision threshold on the CNN output.	102
412	4.25 The detection efficiency and false alarm rate (false positive rate) as a function of the decision threshold for different values of the noise temperature. The model is trained to output a value close to one for data that contains a signal and outputs a value near zero when the data contains only noise. One sees that a lower decision threshold will have a high detection efficiency at the cost of a high rate of false alarms.	103
418	4.26 ROC curves for a CNN model classifying CRES signals. One can see that the area under the curve, which is a figure of merit that describes the performance of the classifier, is roughly linearly dependent with the noise temperature.	103

422	4.27 An illustration of the conceptual design for an antenna array CRES	
423	tritium beta-decay spectrum measurement. The antenna array geometry	
424	consists of a 20 cm interior diameter with 60 independent antenna channels	
425	arranged evenly around the circumference. The nominal antenna design	
426	is sensitive to radiation in the frequency range of 25-26 GHz, which	
427	corresponds to the cyclotron frequency of electrons emitted near the	
428	tritium beta-spectrum endpoint in a 1 T magnetic field. The array is	
429	located at the center of the magnetic trap produced by a set of current-	
430	carrying coils. The nominal magnetic trap design is capable of trapping	
431	electrons up to 5 cm away from the central axis of the array and traps	
432	electrons within an approximately 6 cm long axial region centered on the	
433	antenna array.	105
434	4.28 A high-level diagram of the DAQ system architecture envisioned for the	
435	FSCD.	107
436	4.29 A block diagram illustration of the real-time triggering algorithm proposed	
437	for antenna array CRES reconstruction.	108
438	4.30 An illustration of the digital beamforming procedure. The blue lines	
439	indicate the various distances from the beamforming position to the	
440	antenna. In the situation depicted the actual position of the electron	
441	matches the beamforming position, so we should expect constructive	
442	interference when the phase shifted signals are summed. To prevent the	
443	electron's ∇B -motion from moving the electron off of the beamforming	
444	position, the beamforming phase include a time-dependence to follow the	
445	trajectory of the electron in the magnetic trap.	109
446	4.31 Frequency spectra of simulated CRES signals post-beamforming. The	
447	signal of a 90° electron consists of a single frequency component that is	
448	easy to detect with a power threshold on the frequency spectrum. This	
449	power threshold is still effective for signals with relatively large pitch	
450	angles such as 89.0° and 88.75°, which are composed of a main carrier	
451	and a few small sidebands. Signals with smaller pitch angles, below about	
452	88.5°, tend to be dominated by sidebands such that no single frequency	
453	component can be reliably distinguished from the noise with a power	
454	threshold.	110

455	4.32 PDFs of the power threshold test statistic for CRES signals with various pitch angles as well as the PDF for the noise-only signal case. The average PDF computed for pitch angles ranging from 85.5 to 88.5° is also shown. As the pitch angle is decreased the signal PDF converges towards the noise PDF which indicates that the power threshold trigger is unable to distinguish between small pitch angle signals and noise.	113
461	4.33 Plots of the estimated PDFs for the matched filter template bank test statistic for CRES signals with various pitch angles as well as the estimated PDF for the noise only signal case. We assume an estimated number of templates of 10^5 and perfect match between signal and template i.e. $\Gamma_{\text{best}} = 1$. The mean PDF includes signals ranging from 85.5 – 88.5° in pitch angle. There is a much larger distinction between the signal PDFs at small pitch angle compared to the power threshold indicating a higher detection efficiency for these signals.	117
469	4.34 The mean match of the matched filter template bank to a test set of randomly parameterized signals as a function of the number or density of templates. The parameter space includes pitch angles from 85.5 – 88.5° and energies from 18575 – 18580 eV.	121
473	4.35 Histograms of the trained CNN model output from the test dataset. The blue histogram shows the model outputs for signal data. The oddly shaped peak near the end is the result of the softmax function mapping the long tail of the raw output distribution to the range [0, 1].	123
477	4.36 ROC curves describing the detection efficiency or true positive rates for the three signal classification algorithms examined in this paper.	124
479	5.1 An example radiation pattern generated using HFSS simulations. The color and radial distance of the surface from the origin indicate the relative magnitude of radiation power emitted by the antenna in that direction. The primary goal of most antenna measurements is typically to measure the antenna pattern, which is used to derive many useful antenna performance parameters.	130

485	5.2 An illustration of the three field regions important for the analysis of 486 an antenna system. Very close to the antenna the electric fields are 487 primarily reactive so there is no radiation. If a receiving antenna were 488 placed in this region most of the energy would be reflected back to the 489 transmitter. Outside of the reactive near-field is the radiative near field. 490 At these distances the antenna does radiate, but the radiation pattern is 491 not well-defined since it changes based on the distance of the receiving 492 antenna. It is only in the far-field region where the radiation pattern 493 becomes constant as a function of distance, which is where the majority 494 of antenna engineering is assumed to take place. The antenna arrays 495 developed by Project 8 for CRES measurements operate in the radiative 496 near-field due to the importance of limiting power loss from free-space 497 propagation, which complicates the design of the antenna system.	132
498	5.3 An illustration of the Friis measurement technique commonly used for 499 antenna characterization measurements.	136
500	5.4 Illustration of a two-port S-parameter measurement setup. S-parameters 501 characterize how incoming waves of voltage or power scatter off of the RF 502 device under test. This allows you to measure important properties of the 503 device. In particular, we can use this framework to model a two antenna 504 radiation pattern measurement, which we can then automate using a VNA.	138
505	5.5 Two measurement approaches to characterizing an antenna array for CRES 506 measurements. The full-array approach (a) requires a complete antenna 507 array with all the associated hardware. The synthetic array approach 508 (b) utilizes a single antenna and a set of rotation/translation stages to 509 reposition the transmitter or the receiving antenna to synthesize the signals 510 that would be received by the full-array. This approach reduces the cost 511 and complexity of array measurements. A down-side of the synthetic 512 array approach is that multi-channel effects such as reflections cannot 513 be measured. Utilizing both the full-array and the synthetic array is a 514 powerful way to quantify the impact of errors from the multi-channel array.	139
515	5.6 Illustration of the antenna measurement system developed for the Project 516 8 Collaboration. The reference and test antennas can be connected to 517 different data acquisition configurations depending on the measurement 518 goals. The reference antenna is typically a standard horn antenna and 519 the test antenna is mounted on a set of translation stages for positioning. 520 Automated translation stages allow for relatively painless data-taking enabling 521 synthetic antenna array measurements using only a single receiving 522 antenna. Anechoic form designed to mitigate RF reflections surrounds 523 the setup.	140

524	5.7	Diagrams of two measurement system configurations. Configuration (a) utilizes a VNA and is more suited to antenna characterization. Configuration (b) utilizes an AWG and VNA as a signal generation system and digitizer to collect measurement data, which is more suited to simulating CRES measurements. The transmission chain utilizes a quadrature hybrid and a pair of baluns to drive the cross-dipole variant test antenna developed for synthetic CRES measurements.	141
531	5.8	A sketch of an antenna array large-volume CRES experiment. Electrons from β -decays are confined in a magnetic field using a set of trap coils. The cyclotron radiation produced by the motion of the trapped electrons can be detected by a surrounding antenna array to determine the electron energies. Measuring the energies of many electrons produces a β -decay spectrum.	144
537	5.9	A schematic of the antenna array test stand. The circular antenna array has a radius of 10 cm with 60 independent channels (limited number shown for clarity). The test stand includes an arbitrary waveform generator (AWG), local oscillator (LO), and data acquisition (DAQ) hardware. Finally, a specialized Synthetic Cyclotron Antenna (SYNCA) is used to inject signals to test the antenna array.	145
543	5.10	An electron (red dot) performing cyclotron motion in the x-y plane. The resulting cyclotron radiation is observed by an antenna located at the field point of interest.	146
546	5.11	A plot of the numeric solution to Equation 5.31. The time-domain representation of the signal (a) is composed of a zero frequency term and a series of harmonics separated by the main cyclotron frequency as shown in the plot of the frequency spectrum (b). We can see that the relative amplitude of the harmonics beyond $k = 7$ are smaller than the main carrier by a factor of about 10^{-5} and are completely negligible.	149
552	5.12	The amplitude maxima of the cyclotron radiation form an Archimedean spiral as the radiation propagates outward from the cyclotron orbit center (a). A circular antenna array located at a fixed radius from the orbit center will receive electric fields with equal magnitude in each of its channels, but the phase of the electric field incident on each array channel will be linearly out of phase from its neighbor antennas by an amount equal to the angular separation of the two channels (b).	151

559	5.13 An idealized crossed-dipole antenna consists of two electric dipole antennas oriented perpendicular to each other and is fed with four signals with a quadrature phase relationship. An example antenna feed circuit is shown which is composed of a chained combination of a quadrature hybrid-coupler (Quad) and two baluns.	152
560		
561		
562		
563		
564	5.14 A model of the PCB crossed-dipole antenna with dimensions. The design has an inside diameter of 2.16 mm for the central circular trace, which is 0.13 mm wide. The dipole arms each have a width of 1.27 mm and protrude beyond the circular trace by 1.40 mm, which gives an overall width of 4.96 mm for the length of the antenna PCB trace from end-to-end. The overall size of the antenna is 20.0 mm the majority of which is the PCB dielectric material. This design was observed in simulation to maintain the field characteristics of the idealized crossed-dipole while being simpler to fabricate due to the increased size of the antenna.	153
565		
566		
567		
568		
569		
570		
571		
572		
573	5.15 A comparison of the electric field magnitudes, normalized by the maximum value of the electric field in each simulation, plotted on a 10 cm square to visualize the Archimedean spirals formed by the electron (a), the crossed-dipole antenna (b), and a PCB crossed-dipole antenna (c). The matching patterns indicate that the electric fields have similar phase characteristics. These images were generated using Locust simulations for the electron and ANSYS HFSS for both antennas.	154
574		
575		
576		
577		
578		
579		
580	5.16 A comparison of the normalized electric field magnitudes for the ideal crossed-dipole, PCB crossed-dipole, and a simulated electron as a function of the polar angle (θ). (a) Shows the total electric field, (b) shows the ϕ -polarized electric field component, and (c) shows the θ -polarized electric field component. These images were generated using Locust simulations for the electron and ANSYS HFSS for both antennas.	155
581		
582		
583		
584		
585		
586	5.17 A comparison of the normalized electric field magnitudes for the crossed-dipole, PCB crossed-dipole, and a simulated electron as a function of the azimuthal angle (ϕ) evaluated at $\theta = 90^\circ$. This image was generated using Locust simulations for the electron and ANSYS HFSS for both antennas.	156
587		
588		
589		

590	5.18 (a) A cartoon schematic which highlights the routing of the semi-rigid 591 coax transmission lines. (b) A photograph of a SYNCA constructed 592 using the modified crossed-dipole PCB antenna design. Visible in the 593 photograph of the SYNCA are four blobs of solder which are an artifact 594 of the SYNCA's hand-soldered construction. These solder blobs are the 595 most significant deviation from the SYNCA design shown in Figure 5.14 596 and are responsible for a significant fraction of the irregularities seen in 597 the antenna pattern.	157
598	5.19 A schematic of the VNA characterization measurements (a). This setup 599 allows for antenna gain and phase measurements across a full 360° of 600 azimuthal angles using a motorized rotation stage and control of the radial 601 position of the SYNCA using a translation stage. A photo of the setup in 602 the lab is shown in (b).	158
603	5.20 Linear interpolations of the measured electric field magnitude (a) and 604 phase (b). The data was acquired using a VNA at 120 points spaced 605 by 3 degrees from 0 to 357 degrees of azimuthal angle. The different 606 color lines indicate the vertical offset of the horn antenna relative to the 607 SYNCA PCB and the dashed line shows the expected shape from electron 608 simulations. No significant difference in the antenna pattern is observed 609 for the measured vertical offsets.	159
610	5.21 (a) A depiction of the relative phase differences for signals received by a 611 circular antenna array from an isotropic source. The phases correspond to 612 a unique spatial position. (b) A schematic of the setup used to perform 613 digital beamforming.	160
614	5.22 Digital beamforming maps generated using a simulated 60 channel array 615 and electron simulated using the Locust package. (a) and (b) show the 616 beamforming maps for simulated electrons without the cyclotron spiral 617 phases and with the cyclotron spiral phases respectively. (c) and (d) 618 show the beamforming maps produced from SYNCA measurements. We 619 observe good agreement between simulated electrons and the SYNCA 620 measurements.	161

621	5.23 A plot of the SYNCA's reconstructed position using the synthesized horn-	
622	antenna array and digital beamforming. (a) Shows the reconstructed	
623	position of the SYNCA compared with the target position indicated by	
624	the positioning system readout. (b) Shows the reconstruction error, which	
625	is the difference between the target and reconstructed positions. The error	
626	bars in (b) are the uncertainty in the mean position of the 2D Gaussian	
627	used to fit the digital beamforming reconstruction peak obtained from	
628	the fit covariance matrix. The mean fit position uncertainty of 0.02 mm	
629	is an order of magnitude smaller than the typical reconstruction error of	
630	0.3 mm obtained by calculating the standard deviation of the difference	
631	between the reconstructed and target position.	163
632	5.24 A diagram of the array measurement system used to test the prototype	
633	FSCD antenna array. A VNA is used as the primary measurement tool,	
634	which is connected to the array through a series of switches. The other port	
635	of the VNA connects to the SYNCA through the quad-balun chain used	
636	to provide the SYNCA feed signals. During measurements the SYNCA	
637	is positioned inside the center of the antenna array and translated to	
638	different radial and axial positions using a 3-axis manual translation stage	
639	setup.	165
640	5.25 Photos of the prototype FSCD antenna (a), the FSCD array and SYNCA	
641	(b), and the translation stages and coordinate system used to position the	
642	SYNCA (c).	166
643	5.26 A photo of the FSCD antenna and the SYNCA in the synthetic array	
644	measurement setup at Penn State.	168
645	5.27 The unwrapped phases of signals received by the FSCD antenna array	
646	from an electron with a 90° pitch angle located in the plane of the antenna	
647	array. The data points indicated the phases extracted from simulation	
648	and the dashed lines show the model predictions.	170
649	5.28 Plots of the measured unwrapped phases from the FSCD array (a) and the	
650	synthetic array (b) compared to the model predictions for a series of radial	
651	positions. The different phases of the sinusoidal phase oscillations in the	
652	two plots reflects differences in the coordinate systems of the measurements.	171
653	5.29 The phase errors between the measurement and model for the synthetic	
654	array (blue) and the FSCD array (orange) for a series of radial positions.	
655	The label JUGAAD refers to an alternative name for the FSCD array	
656	setup. As the SYNCA is translated off-axis phase errors with progressively	
657	higher oscillation frequency enter into the measurements.	172

658	5.30 Two dimensional plots of the phase errors for the synthetic array (a)		
659	and the FSCD (JUGAAD) array (b). In both plots we observe evidence		
660	of a similar diffraction pattern with bilateral symmetry, but the FSCD		
661	array measurments have an additional phase error contribution from the		
662	different antennas and paths through the switch network.	173	
663	5.31 The amplitude of the signals from CRESana for the FSCD array from a		
664	90° electron. As the electron is moved from $R = 0$ the signals begin to		
665	have unequal amplitudes depending on the distance from the electron to		
666	the antenna.	175	
667	5.32 The normalized magnitudes of the S21 parameters measured in the FSCD		
668	(orange) and synthetic array (blue) setups. The dominant observed		
669	behavior as a function of radius is the increase in the number of magnitude		
670	peaks, which was noted in the phase error curves. There does not appear		
671	to be a strong change in the relative amplitude of a group of antennas as		
672	predicted by CRESana.	176	
673	5.33	177	
674	5.34 Beamforming images from the synthetic array (a) and FSCD array (b)		
675	setups with the SYNCA positioned 15 mm off the central axis. In both		
676	images we see a clear maxima that corresponds to the true SYNCA		
677	position. However, in the FSCD array there is an additional faint peak		
678	located at the opposite position of the beamforming maximum. This		
679	additional peak is the mirror of the true peak and is the result of reflections		
680	between antennas in the FSCD array.	178	
681	5.35 A comparison of the maximum signal amplitude obtained by beamforming		
682	to the signal amplitude obtained with an ideal summation as a function		
683	of the radial position of the SYNCA. The amplitudes for the synthetic		
684	array are shown in (a) and the FSCD array are shown in (b). In both		
685	setups we observe that the signal amplitudes obtained from beamforming		
686	are smaller than the signal amplitude that could be attained with the		
687	ideal summation without phase mismatch.	179	
688	5.36 The ratio of the beamforming signal amplitude to the ideal signal ampli-		
689	tude for the FSCD and synthetic arrays. We see that the FSCD array has		
690	a larger power loss from phase error compare to the synthetic array which		
691	indicates that calibration errors associated with the multiple channels as		
692	well as reflections are impacting the signal reconstruction.	179	
693	6.1 Geometry of a cylindrical waveguide with radius b	182	

694	6.2 The geometry of a cylindrical cavity with length L and radius b	185
695	6.3 Relation of mode frequency to cavity length for a cylindrical cavity with 696 a radius of 18.32 cm.	186
697	6.4 A series RLC circuit.	187
698	6.5 Illustration of the behavior of the input impedance of the series RLC 699 circuit as a function of the driving frequency. The BW is proportion to 700 the width of the resonance, which is inversely proportional to Q.	189
701	6.6 A series RLC circuit coupled to an external circuit with input impedance 702 R_L	190
703	6.7 A cartoon depiction of a cavity CRES experiment. A metallic cavity filled 704 with tritium gas is inserted into a uniform background magnetic field 705 to perform CRES measurements. Electrons from beta-decays inside the 706 cavity can be trapped and used to excite a resonant mode(s). By coupling 707 to the cavity mode with a suitable probe one can measure the cyclotron 708 frequency of the electron and perform CRES.	191
709	6.8 Examples of the resonant mode frequencies of a cylindrical cavity. This 710 cavity has a radius of 18.32 cm and a length to diameter ratio of 4.55. . . .	195
711	6.9 An image of an open cavity with coaxial terminations used for dielectric 712 constant measurements. Figure from [2].	199
713	6.10 The simplified geometry of an open cavity with coaxial terminations. 714 Figure from [3].	200
715	6.11 Electric field regions for the open cavity boundary value problem. Figure 716 from [3].	200
717	6.12 Two mode filtering concepts to break the degeneracy of TE_{01} and TM_{11} 718 modes. The resistive approach uses dielectric materials to impede currents 719 that travel vertically along the cavity while leaving azimuthal currents 720 unperturbed. An alternative approach is to impede the currents using 721 grooves cut into the cavity wall, which achieve the same effect with an 722 inductive impedance.	203

723	6.13 Four cavity design variations. (a) is a standard sealed cylindrical cavity, 724 (b) is an open cavity with smooth walls, (c) is an open cavity with resistive 725 walls, and (d) is an open cavity with grooved walls. The main cavity and 726 coaxial terminator parameter are identical for all four cavities.	204
727	6.14 The frequencies and Q-factors of the resonant modes identified by HFSS 728 for the cavity variations shown in Figure 6.13. The fully-sealed cavity with 729 smooth walls has several high-Q modes near the TE_{011} resonance. Introdu- 730 cing the open-termination preserves the Q-factors of the $TE_{01\ell}$ modes 731 and suppresses the Q-factors of the modes whose boundary conditions do 732 not match the cylindrical partition. Both the resistive and grooved wall 733 perturbations shift the resonant frequencies of the TM modes away from 734 the TE_{011} mode. By properly tuning the geometry of the grooves or the 735 resistive spacers several MHz of frequency separation can be achieved.	205
736	6.15 A cartoon depicting the design of the open-ended cavity prototype designed 737 to operate at approximately 6 GHz. The main cavity wall was composed of 738 a single copper pipe. A mode-filtered version of this cavity was constructed 739 by	207
740	6.16 Images depicting the measurement of the filtered and non-filtered open 741 cavities using the VNA. The coupling loop in the figure is shown in the 742 TE orientation.	208
743	6.17 HFSS simulation results for a the as-built cavity with the coaxial termi- 744 nators removed. The TE_{011}/TM_{111} frequency is approximately 5.78 GHz.	209
745	6.18 Measurements of the filtered and non-filtered prototype cavities acquired 746 with the VNA.	210

List of Tables

748 4.1	A summary of the CNN model layers and parameters. The output of each 749 1D-Convolution and Fully Connected layer is passed through a LeakyReLU 750 activation function and re-normalized using batch normalization before 751 being passed to the next layer in the model. The output of the final Fully 752 Connected layer in the model is left without activation so that the model 753 outputs can be directly passed to the Binary Cross-entropy loss function 754 used during training.	119
755 6.1	A table of the values of p'_{nm}	184
756 6.2	A table of the values of p_{nm}	185
757 6.3	A table of cavity design parameters used for HFSS simulations.	204
758 6.4	A table of parameters describing the cavity prototypes. Certain values 759 such as the cavity length and the distance between dielectric spacers are 760 approximate due to variation in the machining of the copper. In particular, 761 the filtered cavity was constructed from conducting copper segments that 762 varied in size from 1.50" to 1.85".	207

⁷⁶³ **Chapter 1** |
⁷⁶⁴ **Introduction**

⁷⁶⁵ **1.1 Summary**

⁷⁶⁶ Neutrinos are one of the fundamental particles that comprise the standard model of
⁷⁶⁷ particle physics and account for a significant fraction of the matter in the universe.
⁷⁶⁸ Neutrinos are the most abundant fermions in the universe, but due to their weak
⁷⁶⁹ interactions neutrinos seldom interact with other particles. Regardless, neutrinos play a
⁷⁷⁰ unique role in the evolution of the early-universe, therefore, a detailed understanding
⁷⁷¹ of the properties of the neutrino is important to understanding the cosmology of the
⁷⁷² universe as well as understanding the universe at the fundamental particle physics scale.

⁷⁷³ Unlike other fermions it was unclear that neutrinos had nonzero mass until neutrino
⁷⁷⁴ flavor oscillations were definitively observed in the late 90's and early 00's. Flavor
⁷⁷⁵ oscillations require that neutrinos experience time so that when acted upon by the
⁷⁷⁶ time-evolution operator the initial neutrino state can evolve to a new flavor state. This
⁷⁷⁷ implies that the neutrino flavor states are really a superposition of at least three separate
⁷⁷⁸ neutrino states with well-defined masses. Measurements of neutrino oscillations that have
⁷⁷⁹ taken place over the past couple of decades have measured the differences between
⁷⁸⁰ neutrino mass eigenstates with increasing precision. However, oscillation measurements
⁷⁸¹ cannot tell us the mass scale of the neutrinos, which is required in order to measure the
⁷⁸² absolute neutrino masses.

⁷⁸³ The neutrino mass scale remains an unknown quantity in the standard model of
⁷⁸⁴ particle physics. The value of the neutrino mass influences the evolution of the early
⁷⁸⁵ universe and is likely relevant to the energy-scale of new physics responsible for the factor
⁷⁸⁶ of 10^{-6} difference between the neutrino and electron masses. A model-independent way
⁷⁸⁷ to measure the neutrino mass is to measure the tritium beta-decay spectrum near its
⁷⁸⁸ endpoint. Energy conservation requires that the neutrino mass carry away some kinetic
⁷⁸⁹ energy from the beta-decay electron in the form of its mass, which causes a distortion in

790 the shape of the tritium beta-decay spectrum near the endpoint. The isotope tritium has
791 many advantages for this measurement, and has been used by the KATRIN collaboration
792 to perform the most sensitive direct neutrino mass measurement to date.

793 KATRIN represents the state-of-the-art experiment in the current generation of
794 neutrino mass direct measurement experiments and has a final projected sensitivity to
795 neutrino masses $m_\nu < 200$ meV. This sensitivity does not fully exhaust the allowed
796 parameter space of neutrino masses under the normal and inverted neutrino mass
797 ordering scenarios, which motivates the development of a next generation of neutrino
798 mass measurement experiments.

799 The Project 8 collaboration is developing a next-generation neutrino mass direct
800 measurement experiment designed to be sensitive to $m_\nu < 40$ meV. This sensitivity
801 is sufficient to exhaust the range of neutrino masses allowed under the inverted mass
802 ordering regime. Project 8 intends to achieve its sensitivity goal utilizing two technologies
803 that are novel to the space of direct neutrino mass measurement — atomic tritium and
804 cyclotron radiation emission spectroscopy (CRES). Atomic tritium is required in order to
805 avoid systematic broadening the tritium beta-decay spectrum caused by the final state
806 of the ${}^3\text{He}^+ \text{-T}$ molecule, and the CRES technique enables a differential measurement of
807 the tritium spectrum that is background-free and able to be directly integrated with the
808 atomic tritium source.

809 The Project 8 collaboration is currently engaged in a research and development
810 program intended to simultaneously develop the atomic tritium and CRES technologies
811 so that they can be combined in a next-generation experiment. This past year (2022)
812 Project 8 has used the CRES technique to measure the molecular tritium beta-decay
813 spectrum and place an upper limit on the neutrino mass: $m_\beta \leq 152$ eV. This measurement,
814 while not competitive scientifically, represents the first proof-of-principle that the CRES
815 technique can be used to measure the neutrino mass.

816 The future goals of the Project 8 collaboration are to develop the technologies
817 and techniques necessary to scale-up the volumes in which CRES measurements can
818 be performed. Project 8's first neutrino mass measurement with CRES utilized a
819 measurement volume on the cubic-centimeter scale, however, sensitivity calculations
820 estimate that an experiment sensitive to neutrino masses of 40 meV will require several
821 tens of cubic-meters of experiment volume filled with atomic tritium. Developing a new
822 approach to performing CRES measurements that can be successfully scaled to these
823 volumes is a necessary step towards Project 8's neutrino mass measurement goal, and is
824 the primary topic of my dissertation research.

825 A parallel development is the technology necessary to produce, cool, trap, and
826 recirculate a supply of atomic tritium that is compatible with CRES measurements. The
827 atomic tritium system is equally important as the large-volume CRES measurement
828 technology, but it will not be the focus of this dissertation since I did not contribute
829 significantly to this effort.

830 The Project 8 collaboration has identified two scalable approaches to neutrino mass
831 measurement using the CRES technique. One approach is to use an array of antennas
832 that surrounds a volume of trapped atomic tritium that can perform CRES measurements
833 by collection the cyclotron radiation emitted by beta-decay electrons into free-space. The
834 other approach uses a resonant cavity filled with atomic tritium to perform CRES by
835 measuring the excitation of resonant cavity modes caused by the motion of electrons
836 trapped inside the cavity volume.

837 The cavity and antenna approaches to CRES have been studied in detail over the past
838 five years, and, while both approaches offer a physically viable path towards a 40 meV
839 neutrino mass measurement the collaboration has elected to pursue the cavity approach
840 for the foreseeable future. The major advantage of the cavity approach is a significant
841 reduction in the cost and complexity of the experiment design and data analysis, which
842 provides a less risky path towards Project 8’s scientific goals.

843 In this dissertation I summarize my most impactful contributions to the research and
844 development of antenna array and cavity CRES. In short these contributions are

- 845 • the development and analysis of signal reconstruction algorithms for antenna array
846 CRES, which provided key inputs to sensitivity analyses of antenna array CRES
847 experiments,
- 848 • the development of a specialized antenna designed to synthesize fake CRES radia-
849 tion, which enabled bench-top testing and validation of the antenna array CRES
850 technique,
- 851 • the development of an open-cavity design for CRES measurement whose mode
852 structure can be tuned using perturbations that modify the impedance of the cavity
853 walls. The development of this cavity concept was one of many developments that
854 eventually lead to the adoption of cavities as the CRES technology of choice for
855 the future of Project 8.

856 1.2 Outline

857 The outline of this dissertation is as follows. In Chapter 2 I provide an introduction to
858 the basic physics of neutrinos and beta-decay, which provides context for a discussion of
859 various methods to measure the neutrino absolute mass scale.

860 Chapter 3 is an overview of the CRES technique and the Project 8 collaboration.
861 I highlight the Project 8 Phase II experiment, which was the first measurement of
862 the tritium beta-decay spectrum with CRES, and I discuss the planned research and
863 development for an antenna array CRES experiment in Phase III of the Project 8
864 collaboration’s experiment plan. I end Chapter 3 with a discussion of the pilot-scale and
865 Phase IV experiments, that will combine a scalable CRES measurement technology with
866 atomic tritium and measure the neutrino mass with 40 meV sensitivity.

867 Chapter 4 discusses the first of the contributions mentioned above, which is the
868 development of signal reconstruction techniques for antenna array CRES and an antenna
869 array demonstrator experiment called the FSCD. I discuss the important tools that Project
870 8 uses to simulate antenna array CRES before introducing three signal reconstruction
871 algorithms that can be used to detect CRES signals using the array. I end Chapter 4
872 with a paper that summarizes a detailed analysis and comparison of the signal detection
873 performance of each algorithm.

874 Chapter 5 describes my contributions to the development of antennas and an antenna
875 measurement system for Project 8, which is the second major contribution of this
876 dissertation. I begin with a general overview of basic principle of antennas and antenna
877 measurements, before including a paper that describes the development of unique antenna
878 designed to mimic the cyclotron radiation emitted by electrons in free-space when trapped
879 in a magnetic field. I call this antenna the synthetic cyclotron radiation antenna (SYNCA)
880 and its main purpose is to serve a fake electron for laboratory validation measurements
881 of Project 8’s antenna array CRES simulations. Chapter 5 ends with an overview
882 of laboratory measurements of a prototype antenna array that were compared with
883 simulations to provide upper bounds on reconstruction errors caused by imperfections in
884 real-life measurements.

885 Chapter 6 discusses the cavity approach to CRES, which was adopted as the preferred
886 CRES technology for Phase IV late into my dissertation work. The chapter stars by
887 discussing resonant cavities in general before introducing the operating principles of the
888 cavity approach to CRES. I end the chapter by discussing a study of and open-cavity
889 design that could be used for CRES measurements and integrated with atomic tritium

890 and an electron gun calibration source for the pilot-scale and Phase IV experiments.

891 Finally, in Chapter 7 I conclude by briefly discussing the future directions of the
892 Project 8 collaboration as we continue towards a direct measurement of the neutrino
893 mass.

894 **Chapter 2 |**

895 **Neutrinos and Neutrino Masses**

896 **2.1 Introduction**

897 In this chapter I provide a cursory overview of background information relevant to
898 neutrinos and neutrino mass measurements.

899 In Section 2.2 I provide some background information on the history of neutrinos and
900 beta-decay. In Section 2.3 I describe the discover of neutrino oscillations, which proved
901 unambiguously that neutrinos have non-zero masses. In Section 2.4 I discuss the current
902 state of the theoretical understanding of neutrino masses in the standard model. Lastly,
903 in Section 2.5 I discuss methods for measuring the absolute scale of the neutrino mass.

904 **2.2 Neutrinos and Beta-decay**

905 Late in the 19th century the phenomena of radioactivity was first observed in experiments
906 performed by Henri Becquerel with uranium, and further studied using thorium and
907 radium by Marie and Pierre Curie [4,5]. Early work in radioactivity classified different
908 forms of radiation based on it's ability to penetrate different materials. Rutherford was
909 the first to separate radioactive emissions into two types, alpha and beta radiation [6].
910 Alpha rays can be easily stopped by a piece of paper or thin foil of metal, whereas beta
911 radiation could penetrate metals several millimeters thick. Later a third form of radiation
912 was identified by Villard [7], which was still more penetrating, and was eventually termed
913 gamma radiation by Rutherford.

914 When these forms of radioactivity were first discovered it was unclear what physically
915 constituted an alpha, beta, or gamma particle. Experiments with radioactivity in
916 magnetic fields was eventually able to identify the charge composition of different forms
917 of radiation. In particular, experiments by Becquerel identified that beta radiation had

918 an identical charge-to-mass ratio to the electron discovered by Thompson in his work on
919 cathode rays [8]. This was strongly suggestive that beta particles were indeed electrons.

920 Further studies of beta radiation lead to the discovery that radioactivity resulted in
921 the transmutation of elements [9] caused by the decay of a heavier nucleus to a lighter
922 species. One feature of beta radiation, which we now properly call beta-decay, that
923 was different from alpha-decays and gamma radiation is that the electrons produced by
924 beta-decay have a continuous spectrum of kinetic energies, whereas, alpha and gamma
925 particles are emitted with discrete energies. This feature of beta-decay was first observed
926 by Chadwick in 1914 [10], and was extremely puzzling at the time since the continuous
927 spectrum apparently violates energy conservation [11].

928 Famously, in 1930 Pauli proposed the existence of a new neutral particle, which he
929 termed the "neutron", that was also produced during beta-decay in order to resolve the
930 missing energy problem posed by the beta-decay spectrum [12]. Because this particle
931 carried no charge, it was hypothesized at the time that it had simply not been observed
932 in any experiments up to that time. This "neutron", which was initially estimated to
933 have a mass no larger than that of an electron, was eventually renamed the "neutrino" by
934 Fermi [13] after the discovery of the neutron by Chadwick in 1932 [14]. Later, in 1933,
935 Fermi developed a quantum mechanical theory for beta-decay in which both an electron
936 and neutrino are produced by the decay of a neutron to a proton inside the radioactive
937 nucleus [15].

938 Little more than a speculation when first introduced, indirect evidence for the existence
939 of neutrinos was obtained in 1938 by the simultaneous observation of the electron and
940 recoiling nucleus in cloud chambers by Crane and Halpern [16]. However, it wasn't
941 until the Cowan-Reines experiment [17] in 1956 that direct evidence for the existence of
942 neutrinos was observed by detecting the inverse beta-decays caused by neutrinos from a
943 nuclear reactor interacting with protons contained in water molecules. The difficulty in
944 detecting neutrinos is caused by their weak interactions with other particles. Further,
945 experiments revealed that different types of neutrinos existed based on the nature of the
946 leptons produced in neutrino charged-current interactions [18], but the existence of a
947 neutrino mass remained an open question that would take more than 40 year to resolve.

948 **2.3 Neutrino Oscillations**

949 The first hint of neutrino flavor transitions or neutrino oscillations was indicated by
950 the solar neutrino problem, which referred to discrepancies between the predicted flux

of ν_e from the standard solar model and measurements of the solar neutrino flux such as the famous experiment at the Homestake mine by Ray Davis Jr. and collaborators in the 1960's [19]. Essentially, fewer electron-type neutrinos than expected were being observed from the sun. Finally, in the early 2000's the SNO experiment was able to resolve the solar neutrino problem by identifying neutrino oscillations as the cause of the observed deficit [20]. Furthermore, measurements of the atmospheric flux of neutrinos by the Super-Kamiokande experiment and others revealed that fewer muon-type neutrinos survived passage through the earth than expected providing strong evidence for neutrino oscillations for both flavors [21].

The origin of neutrino oscillations is that the weak eigenstates are distinct from the mass eigenstates [22]. The neutrino mass eigenstates represent physical particles in the sense that they are solutions to the free-particle Hamiltonian, whereas, the neutrino weak eigenstates correspond to the neutrino states that interact via the weak charged-current interaction. The neutrino weak eigenstates are a linear superposition of the neutrino mass eigenstates

$$\nu_\ell = \sum_i U_{\ell i} \nu_i, \quad (2.1)$$

where $\ell = e, \mu, \tau$ and $i = 1, 2, 3$. The matrix elements $U_{\ell i}$ are the elements of the Pontecorvo-Maki-Nakagawa-Sakata (PMNS) matrix that describes the mixing between the neutrino flavor and mass states.

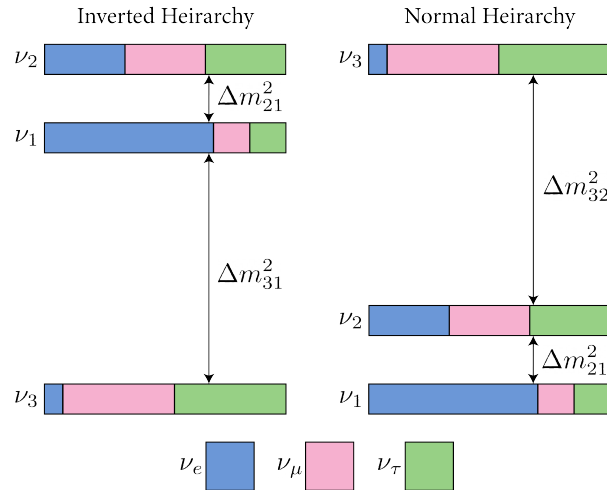


Figure 2.1. A diagram of two different neutrino mass ordering scenarios. In the inverted hierarchy (inverted mass ordering) the lightest neutrino mass is m_3 , whereas, in the normal hierarchy (normal mass ordering) m_1 is the lightest neutrino. What cannot be measured by neutrino oscillations is the neutrino absolute mass scale, which is essentially the mass of the lightest neutrino mass eigenstate.

969 One standard parameterization of the PMNS matrix is

$$\begin{aligned}
U_{PMNS} &= \begin{bmatrix} U_{e1} & U_{e2} & U_{e3} \\ U_{\mu 1} & U_{\mu 2} & U_{\mu 3} \\ U_{\tau 1} & U_{\tau 2} & U_{\tau 3} \end{bmatrix} \\
&= \begin{bmatrix} 1 & 0 & 0 \\ 0 & c_{23} & s_{23} \\ 0 & -s_{23} & c_{23} \end{bmatrix} \begin{bmatrix} c_{13} & 0 & s_{13}e^{-i\delta} \\ 0 & 1 & 0 \\ -s_{13}e^{i\delta} & 0 & c_{13} \end{bmatrix} \begin{bmatrix} c_{12} & s_{12} & 0 \\ -s_{12} & c_{12} & 0 \\ 0 & 0 & 1 \end{bmatrix} \\
&\quad \times \begin{bmatrix} e^{i\alpha_1/2} & 0 & 0 \\ 0 & e^{i\alpha_2/2} & 0 \\ 0 & 0 & 1 \end{bmatrix}, \tag{2.2}
\end{aligned}$$

970 where $c_{ij} = \cos \theta_{ij}$ and $s_{ij} = \sin \theta_{ij}$. The parameters α_1 and α_2 are only included in the
971 PNMS matrix if neutrinos are Majorana particles, something which represents a current
972 area of research in neutrino physics. The phase δ quantifies the degree of CP-violation
973 in the neutrino sector. Including the Majorana phases the PMNS matrix contains six
974 independent parameters. In addition, neutrino oscillation probabilities depend on the
975 squared mass differences between neutrino mass eigenstates

$$\Delta m_{ij}^2 = m_i^2 - m_j^2, \tag{2.3}$$

976 where $ij = 12, 32, 31$ respectively. Because $\Delta m_{32}^2 = \Delta m_{31}^2 - \Delta m_{21}^2$, this adds an additional
977 two parameters that must be constrained by neutrino oscillations.

978 A giant experimental effort over the past couple of decades has greatly contained the
979 majority of parameters in the PMNS matrix, many to relative uncertainties of only a
980 few percent. However, some parameters still remain relatively unconstrained, which is
981 the origin of the current uncertainty in the ordering of the neutrino masses (see Figure
982 2.1). The neutrino masses can be organized by their relative mass. The current neutrino
983 oscillation data can confirm that $m_2 > m_1$, however, the sign of Δm_{32}^2 is still unknown.
984 This leads to two scenarios where neutrino masses follow the ordering $m_3 > m_2 > m_1$,
985 which is called the normal mass ordering (NMO), or alternatively neutrino masses may
986 be ordered $m_2 > m_1 > m_3$, which is called the inverted mass ordering (IMO). Next-
987 generation neutrino oscillation experiments such as JUNO [23], Hyper-Kamiokande [24],
988 and DUNE [25] are poised to resolve this ambiguity in the coming years.

989 Neutrino oscillation probabilities are only sensitive to the neutrino masses via the
990 squared mass differences. Therefore, oscillation probabilities are unaffected by the

absolute scale of the neutrino mass. However, oscillations can be used to obtain a lower bound on the neutrino masses by setting the mass of the lightest neutrino mass state to zero. This results in different lower limits depending on the ordering of the neutrino mass states. Current best-fit values [26] with 1σ -uncertainties for the squared mass differences are

$$\Delta m_{21}^2 = (7.42^{+0.21}_{-0.20}) \times 10^{-5} \text{ eV}^2, \quad (2.4)$$

$$\Delta m_{31}^2 = (2.5176^{+0.026}_{-0.028}) \times 10^{-3} \text{ eV}^2 \text{ (NMO)}, \quad (2.5)$$

for the normal mass ordering, and in the case of the inverted ordering we have

$$\Delta m_{32}^2 = (-2.498^{+0.028}_{-0.028}) \times 10^{-3} \text{ eV}^2 \text{ (IMO).} \quad (2.6)$$

By letting the lightest neutrino mass in each ordering scenario (m_{least}) take on a range of values one can visualize the relative masses of the neutrinos as a function of m_{least} (see Figure 2.2).

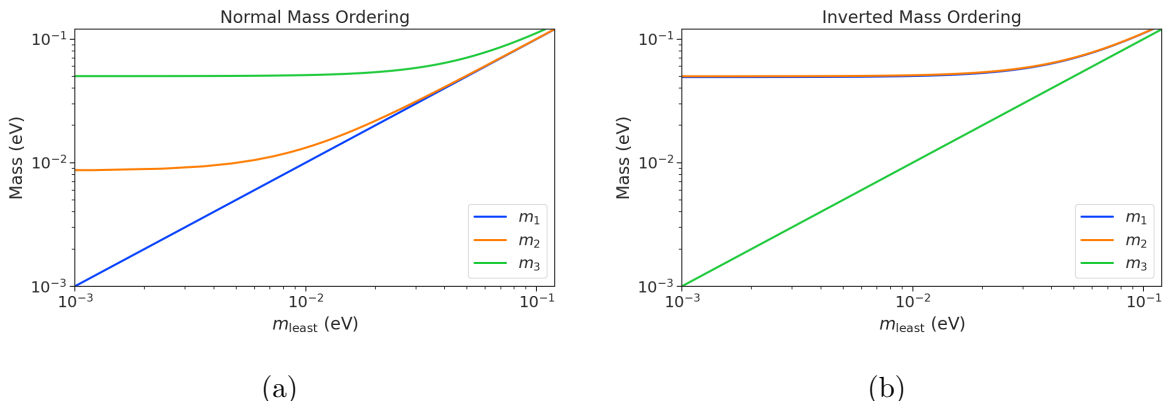


Figure 2.2. The masses of the neutrinos as a function of the lightest neutrino mass in both the normal (a) and inverted (b) mass ordering regimes.

2.4 Neutrino Masses in the Standard Model

In this section, I briefly summarize the current theoretical understanding of neutrino masses in the standard model [27–29]. Neutrinos are spin 1/2 particles, which are described using the Dirac equation.

$$(i\hbar\gamma^\mu\partial_\mu - mc)\psi(x) = 0, \quad (2.7)$$

1004 where the field that describes the particle is denoted as $\psi(x)$. In the standard model
 1005 fermions acquire mass through the Yukawa interaction, which add to the standard model
 1006 Lagrangian terms of the form

$$\mathcal{L}_{\text{Yukawa}} = -Y_{ij}^\ell \bar{L}_{Li} \phi E_{Rj} + \text{h.c.}, \quad (2.8)$$

1007 where Y_{ij}^ℓ is an element of the 3×3 Yukawa coupling matrix for leptons, L_{Li} is the
 1008 left-handed lepton doublet for generation i , ϕ is the Higgs doublet, and E_{Rj} is the
 1009 right-handed lepton field for generation j . Neutrinos are represented only as left-handed
 1010 neutrinos and right-handed antineutrinos in the standard model, which is consistent
 1011 with experimental observations. Since there are no right-handed neutrino singlet fields,
 1012 there are no Yukawa interaction terms, thus neutrinos in the standard model are strictly
 1013 massless. Therefore, non-zero neutrino mass is evidence for physics beyond the standard
 1014 model.

1015 For the charged leptons, the Yukawa interaction leads to masses of the form

$$m_{ij}^\ell = Y_{ij}^\ell \frac{v}{\sqrt{2}}, \quad (2.9)$$

1016 where v is the Higgs vacuum expectation value. The observation of massive neutrinos
 1017 motivates the extension of the standard model to explain the origin of neutrino masses,
 1018 which can be approached in different ways, but all approaches add additional degrees of
 1019 freedom to the standard model. One approach is to introduce to the standard model a
 1020 right-handed neutrino field that allows one to include Yukawa terms of the form

$$\mathcal{L}_{\nu \text{Yukawa}} = -Y_{ij}^\ell \bar{L}_{Li} \phi \nu_{Rj} + \text{h.c.} \quad (2.10)$$

1021 where ν_{Rj} is the right-handed neutrino singlet. Because experimental evidence strongly
 1022 predicts only three active neutrinos, these additional neutrinos are sterile and do not in-
 1023 teract via the strong, weak, or electromagnetic interactions. After spontaneous symmetry
 1024 breaking, the Yukawa interaction leads to mass terms given by

$$\mathcal{L}_D = -M_{Di} \bar{\nu}_{Ri} \nu_{Lj} + \text{h.c.}, \quad (2.11)$$

1025 which is called a Dirac mass term. One of the issues with constructing neutrino masses
 1026 in this way is that the required Yukawa couplings are at least a factor of 10^6 smaller than
 1027 that of an electron, which begs the question: why are the Yukawa couplings so small for

1028 the neutrinos?

1029 An alternative approach is to allow the neutrinos to have a Majorana mass, which is
1030 possible because neutrinos are electrically neutral particles. The Majorana mass terms
1031 for the neutrino have the form

$$\mathcal{L}_M = -\frac{1}{2}(M_{Rij}\bar{\nu}_{Ri}\nu_{Rj}^c M_{Lij}\bar{\nu}_{Li}\nu_{Lj}^c) + \text{h.c.}, \quad (2.12)$$

1032 where M_{Rij} and M_{Lij} are right-handed and left-handed Majorana mass matrices. A
1033 consequence of neutrinos being Majorana particles is lepton number violation, which
1034 predicts the occurrence of neutrino-less double beta-decay at a rate proportional to the
1035 neutrino mass.

1036 In the most general case neutrinos have both Dirac and Majorana mass terms, which
1037 allows one to generate neutrino masses with Yukawa couplings similar to the rest of
1038 the standard model. Considering just one generation of neutrinos for illustration, the
1039 combined Lagrangian can be written as

$$\mathcal{L}_{D+M} = -m_D\bar{\nu}_R\nu_L - \frac{1}{2}(m_L\bar{\nu}_L\nu_L^c + m_R\bar{\nu}_R\nu_R^c) + \text{h.c.}, \quad (2.13)$$

1040 or equivalently,

$$\mathcal{L}_{D+M} = -\frac{1}{2} \begin{bmatrix} \bar{\nu}_L & \bar{\nu}_R^c \end{bmatrix} \begin{bmatrix} m_L & m_D \\ m_D & m_R \end{bmatrix} \begin{bmatrix} \nu_L^c \\ \nu_R \end{bmatrix} + \text{h.c..} \quad (2.14)$$

1041 An example mass generation mechanism with this approach is the Type-I see-saw
1042 mechanism [30], in which we take $m_L = 0$ and $m_R \gg m_D$. By diagonalizing Equation
1043 2.14 one obtains the mass eigenvalues that represent the physical masses of the neutrinos.
1044 The light neutrino mass eigenstate, which represents the observed neutrino mass, has a
1045 mass given by

$$m_1 \approx \frac{m_D^2}{m_R}, \quad (2.15)$$

1046 and the heavy neutrino mass eigenstate, which represents the unobserved sterile neutrino,
1047 has a mass

$$m_2 \approx m_R. \quad (2.16)$$

1048 For m_D similar to the other quark or lepton masses, one obtains physical neutrino masses
1049 consistent with observations from sterile neutrino masses of $m_R \approx O(10^{15})$ GeV. This
1050 mass scale is well beyond the capabilities of modern particle accelerators.

1051 2.5 Neutrino Absolute Mass Scale

1052 The neutrino absolute mass scale or simply "neutrino mass" cannot be probed with
1053 neutrino oscillations, since oscillation probabilities are determined by the squared mass
1054 differences between neutrino mass eigenstates, therefore, alternative techniques are needed
1055 to perform an effective measurement of the neutrino mass.

1056 2.5.1 Limits from Cosmology

1057 The Λ CDM model summarizes our current cosmological understanding of our universe [31].
1058 Λ CDM predicts that the universe originated from a single expansion event colloquially
1059 called the "Big Bang". During the Big Bang, the universe originated as a hot spacetime
1060 singularity, which abruptly experienced rapid expansion in a process known as inflation.
1061 After expansion the inflationary field eventually decayed into a population of quarks,
1062 gluons, leptons, and photons, which were kept in thermal equilibrium by the high-
1063 temperatures of the early universe.

1064 As the universe continued to expand its density and temperature decreased until
1065 the formation of neutral atoms, primarily hydrogen, was possible. At which point the
1066 population of photons produced during the Big Bang thermally decoupled. A direct
1067 prediction of the Λ CDM model is that this population of photons should still be present,
1068 but with a significantly reduced temperature due to the expansion of the universe. This
1069 is consistent with the observation of the CMB (cosmic microwave background), which is
1070 a population of microwave radiation with a blackbody temperature of 2.7 K. The CMB
1071 is extremely uniform in all directions with slight anisotropies that can be analyzed to
1072 study the evolution of the early universe. A series of experiments have measured the
1073 CMB with increasing levels of precision, which has lead to a significant increase in our
1074 current understanding of cosmology.

1075 In addition to the CMB, inflation predicts the existence of a $C\nu B$ (cosmic neutrino
1076 background) [32], which are the remnant neutrinos produced during the Big Bang. Since
1077 neutrinos only interact via the weak force, they decouple from the hot Big Bang plasma
1078 at an earlier time than the CMB radiation. The temperature at which the $C\nu B$ decouples
1079 depends on the neutrino rest mass. Neutrinos play a unique role in the Λ CDM model,
1080 due to the fact that neutrinos act as radiation early in the universe but as matter in the
1081 late universe. This leads to specific signatures that impact the expected anisotropies
1082 of the CMB as well as the distribution of matter in the universe [33]. By combining
1083 measurements of the CMB with measurements of the large-scale structure (LSS) of the

universe one can constrain the neutrino mass scale by fitting these datasets with the Λ CDM model. This analysis results in some of the most stringent constraints on the neutrino mass. Recent analyses [31] have been able to constrain the neutrino mass scale to

$$\Sigma_{m_\nu} \equiv \sum_i m_i < 0.11 \text{ eV}, \quad (2.17)$$

where m_i are the neutrino mass eigenstates.

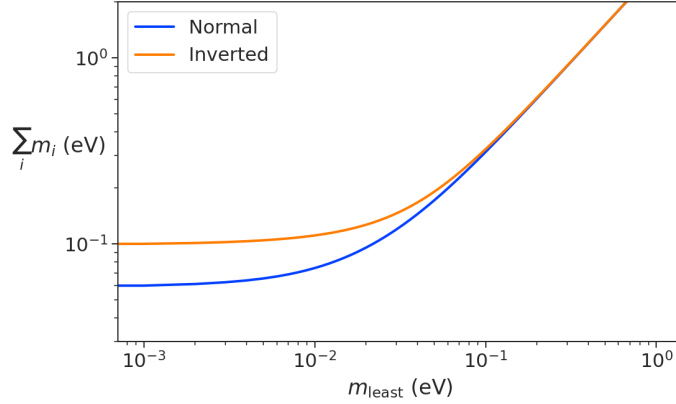


Figure 2.3. The neutrino mass observable measured by cosmology as a function of the lightest neutrino mass eigenstate.

The observable Σ_{m_ν} constrains the neutrino mass by setting the mass of the lightest neutrino mass eigenstate (m_{least}). In the normal mass ordering Σ_{m_ν} can be rewritten in the form

$$\Sigma_{m_\nu} = m_{\text{least}} + \sqrt{\Delta m_{21}^2 + m_{\text{least}}^2} + \sqrt{\Delta m_{32}^2 + m_{\text{least}}^2}, \quad (2.18)$$

where it is clear that a measurement of Σ_{m_ν} effectively sets the neutrino mass scale through m_{least} . The analogous formula for the inverted mass ordering is

$$\Sigma_{m_\nu} = m_{\text{least}} + \sqrt{-\Delta m_{32}^2 + m_{\text{least}}^2} + \sqrt{-\Delta m_{31}^2 + m_{\text{least}}^2}. \quad (2.19)$$

In figure 2.3 we plot the observable Σ_{m_ν} as a function of m_{least} .

Upcoming experiments [34] are planned to refine measurements of the CMB, LSS, and other cosmological observables. With this additional data it is possible that in the near future cosmological measurements will be able to positively constrain the neutrino absolute mass scale. However, the strength of these limits strictly depend on the accuracy of the Λ CDM model, which highlights the need for direct experimental measurements of the neutrino mass to confirm the predictions of cosmology and to fix the neutrino mass

1101 parameter in future cosmological analyses.

1102 2.5.2 Limits from Neutrinoless Double Beta-decay Searches

1103 If neutrinos are Majorana fermions, then the neutrino is equivalent to its own antiparticle
1104 and lepton conservation is not an exact law of nature [35]. Limits on the rate of
1105 neutrinoless double beta-decay ($0\nu\beta\beta$), are some of the most powerful current tests of
1106 lepton number conservation [31]. If $0\nu\beta\beta$ were observed it would direct evidence that
1107 neutrinos are Majorana fermions, and provide a method for measuring the neutrino mass
1108 scale.

1109 Standard double beta-decay occurs when two neutrons contained in the nucleus
1110 spontaneously decay into two protons, which results in the production of two electrons
and two neutrinos (see Figure 2.4). However, during $0\nu\beta\beta$ the two neutrinos self-annihilate

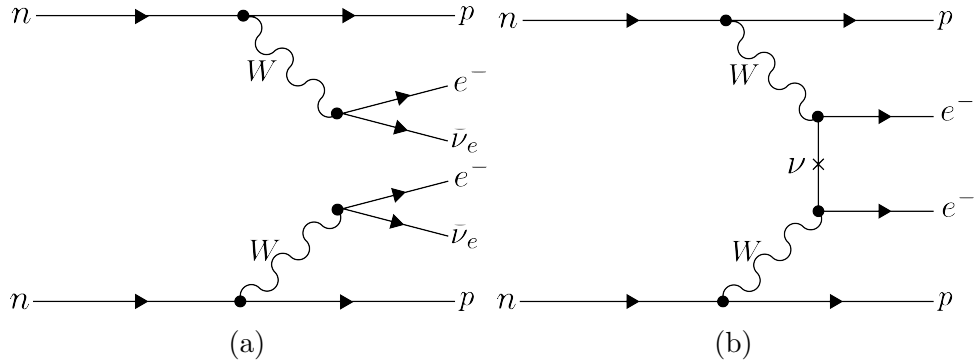


Figure 2.4. Feynman diagrams for double beta-decay (a) and $0\nu\beta\beta$ (b).

1111

1112 producing only two electrons, which violates lepton number by two.

1113 Assuming that the exchange of two Majorana neutrinos is the dominant channel for
1114 $0\nu\beta\beta$, then a measurement of the $0\nu\beta\beta$ half-life for a particular isotope can be used to
1115 set the neutrino absolute mass scale [36]. The half-life is written in terms of the effective
1116 neutrino mass for $0\nu\beta\beta$ ($m_{\beta\beta}$) using the equation

$$T_{1/2}^{0\nu} = \frac{1}{G|\mathcal{M}|^2 m_{\beta\beta}^2}, \quad (2.20)$$

1117 where G is the phase-space factor for the decay and \mathcal{M} is the relevant nuclear matrix
1118 element. $m_{\beta\beta}$ is given by an incoherent sum of the neutrino mass eigenstates weighted

1119 by the PMNS mixing matrix parameters,

$$m_{\beta\beta} = \left| \sum_i U_{ei}^2 m_i \right|. \quad (2.21)$$

1120 The information provided from $0\nu\beta\beta$ on the neutrino mass scale can be visualized by
 1121 expressing the value of $m_{\beta\beta}$ in terms of m_{least} and two relative Majorana phases [1]. The
 1122 allowed regions for $m_{\beta\beta}$ as a function of m_{least} are shown in Figure 2.5 as the regions
 1123 bounded by the black curves overlayed with the discovery probabilities of future $0\nu\beta\beta$
 decay experiments based on current neutrino data.

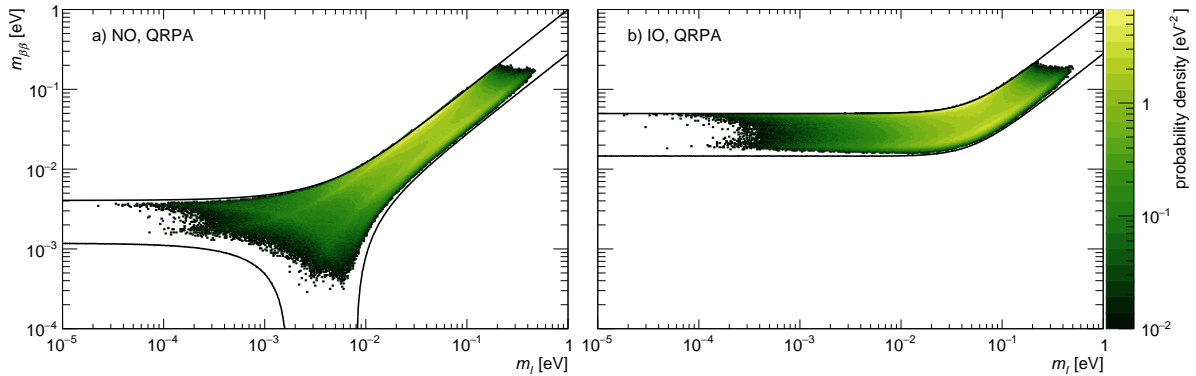


Figure 2.5. The discovery probabilities for the future generation of $0\nu\beta\beta$ experiments as a function of $m_{\beta\beta}$ and m_{least} . Figure from [1].

1124
 1125 Because of the possibility of cancellation due to the unknown Majorana phases
 1126 included in the sum specified by Equation 2.21, the information gained is necessarily
 1127 imperfect. Additionally, theoretical uncertainties in the calculation of the nuclear matrix
 1128 elements complicates the calculation of $m_{\beta\beta}$ from a measurement of $0\nu\beta\beta$ half-life. Similar
 1129 to cosmology, there is a high degree of complementarity between direct measurements
 1130 of the neutrino mass and $0\nu\beta\beta$. In particular, a measurement of m_{least} to less than
 1131 than 0.1 eV sensitivity provides significant information for $0\nu\beta\beta$ searches based of the
 1132 discovery probabilities of Figure 2.5.

1133 2.5.3 Limits from Beta-decay

1134 Certain processes involving neutrinos, in particular beta-decay (see Figure 2.6), have
 1135 initial states with well-defined total energies and final states that can be measured with
 1136 high accuracy and precision. Beta-decay involves the decay of an unstable isotope where
 1137 a neutron spontaneously converts to a proton and emits and electron and anti-neutrino

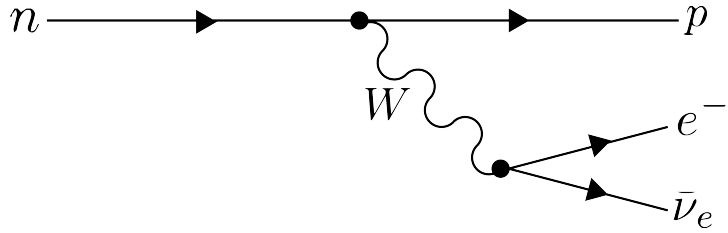


Figure 2.6. A Feynman diagram of beta decay

1138 ("neutrino" for brevity) to conserve charge and lepton number [4]. Therefore, by applying
 1139 the principles of energy and momentum conservation, a measurement of the kinematics
 1140 of the final state can be used to constrain the neutrino mass [37].

1141 Using beta-decay to measure the neutrino mass can be tied back to Fermi's original
 1934 theory of nuclear beta-decay [15] (see Figure 2.7). Because the constraints on the

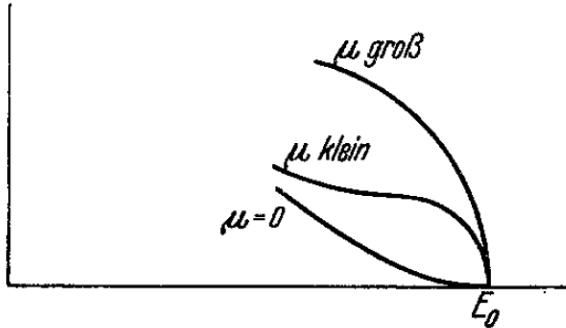


Figure 2.7. A figure from Fermi's 1934 paper on a theory of beta-decay depicting the kinetic energy spectrum of the emitted electron. The effect of the neutrino mass, written as μ , is to distort the shape of the spectrum near the endpoint from the zero-mass spectrum.

1142 neutrino mass from beta-decay depend only on the final state measurement capabilities
 1143 and the principles of energy and momentum conservation, neutrino mass measurements
 1144 with beta-decay are sometimes called direct measurements. A direct measurement like
 1145 beta-decay contrasts with other neutrino mass measurements approaches that are model-
 1146 dependent such as cosmology and $0\nu\beta\beta$, which provide complementary ways to study
 1147 the physics of massive neutrinos.
 1148

1149 The isotope of choice for direct neutrino mass measurements with beta-decay has
 1150 been tritium (3H_2) for many decades, because it conveniently fulfills many experimental
 1151 requirements. Of upmost importance is a decay with a low Q-value, which is the available
 1152 kinetic energy based on the mass difference between the initial and final states. The
 1153 effect of a massive neutrino on the shape of the spectrum is magnified for low Q-values

1154 and tritium decays have an unusually low Q-value of 18.6 keV.

1155 Additionally, tritium beta-decay is a super-allowed decay, which results in a relatively
1156 short half-life of 12.3 years. Therefore, it is relatively easy to obtain a high-activity
1157 using a small source mass. High-activity is desirable because of the low-activity near
1158 the tritium spectrum endpoint. For tritium beta-decays only a factor of 3×10^{-13} of
1159 the decays occur in the last 1 eV of the spectrum. Isotopes with Q-values lower than
1160 tritium are known [37], but this is outweighed by exceedingly long half-lives leading to
1161 unobtainable source masses.

1162 The measurement involves quantifying the effect of the neutrino's mass on shape of
1163 the electron's kinetic energy spectrum near the endpoint. The shape of the kinetic energy
1164 spectrum (see Figure 2.8) is given by

$$\frac{d\Gamma}{dE} = \frac{G_F^2 |V_{ud}|^2}{2\pi^3} (G_V^2 + 3G_A^2) F(Z, \beta) \beta (E + m_e)^2 (E_0 - E) \\ \times \sum_{i=1,2,3} |U_{ei}|^2 [(E_0 - E)^2 - m_i^2]^{1/2} \Theta(E_0 - E - m_i), \quad (2.22)$$

1165 where G_F is the Fermi coupling constant, V_{ud} is an element of the CKM matrix, E is
1166 the kinetic energy of the electron, β is the velocity of the electron divided by the speed
1167 of light, E_0 is the endpoint energy assuming zero neutrino mass, $F(Z, \beta)$ is the Fermi
1168 function, and $\Theta(E_0 - E - m_i)$ is the Heaviside function, which enforces energy conservation.
1169 One can see that the decay spectrum is actually a combination of three spectra with
1170 different endpoints based on the actual values of the neutrino mass eigenstates, m_i . This
1171 results in "kinks" in the spectrum shape due to the overlapping spectra, but such an
1172 effect would likely be impossible to resolve given the finite energy resolution of a real
1173 experiment and low statistics.

1174 The neutrino mass scale variable measured by beta-decay is given by

$$m_\beta^2 = \sum_i |U_{ei}|^2 m_i^2, \quad (2.23)$$

1175 where m_β is the electron-weighted neutrino mass or simply "neutrino mass" for brevity.
1176 m_β corresponds to a particular weighted sum of the neutrino masses, which is distinct
1177 from effective neutrino masses such as $m_{\beta\beta}$ [37]. Assuming unitarity, the neutrino mass
1178 can be expressed in terms of the PMNS matrix elements, squared mass differences, and
1179 the lightest neutrino mass eigenstate. For the normal mass ordering the equation is

$$m_\beta^2 = m_{\text{least}}^2 + |U_{e2}|^2 \Delta m_{21}^2 + |U_{e3}|^2 \Delta m_{31}^2, \quad (2.24)$$

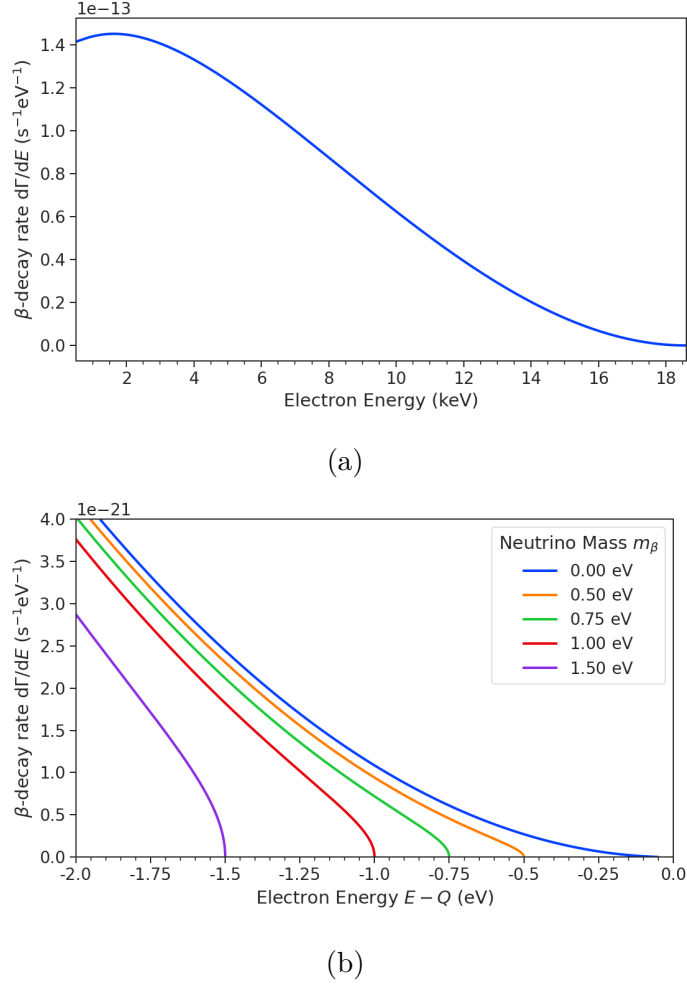


Figure 2.8. The tritium beta-decay spectrum. The affect of a massive neutrino on the spectrum is to change it's shape near the endpoint by an amount proportional to the size of the neutrino mass. This suggests that a sufficiently high-statistic and high-resolution measurement of the spectrum endpoint would be able to measure the neutrino mass.

and for the inverted ordering the equation is

$$m_\beta^2 = m_{\text{least}}^2 + |U_{e1}|^2(-\Delta m_{32}^2 - \Delta m_{21}^2) + |U_{e2}|^2(-\Delta m_{32}^2). \quad (2.25)$$

Therefore, a measurement of the neutrino mass in combination with neutrino mixing parameters is effectively a measurement of m_{least} .

Since the neutrino mass is small (< 1 eV), it's effect on the spectrum is limited to the endpoint region. The affect of a non-zero neutrino mass on the endpoint spectrum is plotted for the reader in Figure 2.8. Resolving the small changes in the spectrum shape requires an experimental technique with high statistics, excellent energy resolution, and

₁₁₈₇ low background activity.

1188 **Chapter 3 |**

1189 **Direct Measurement of the Neutrino Mass**

1190 **with Project 8**

1191 **3.1 Introduction**

1192 A promising technique for direct measurements of the neutrino mass beyond the projected
1193 limit of the ongoing KATRIN experiment [38] is tritium beta-decay spectroscopy with an
1194 atomic tritium source [39]. Atomic tritium, combined with a large-volume, high-resolution
1195 energy measurement technique, is capable of measuring the neutrino mass with sensitivity
1196 below the 50 meV limit allowed by neutrino oscillations.

1197 Cyclotron Radiation Emission Spectroscopy or CRES is a high-resolution energy
1198 measurement technique compatible with atomic tritium production and storage that can
1199 enable the next-generation of neutrino mass direct measurement experiments [40]. The
1200 Project 8 collaboration is currently engaged in a program of research and development
1201 (R&D) aimed at developing the technology necessary for a 40 meV sensitivity measurement
1202 of the neutrino mass using CRES and atomic tritium [41].

1203 In Section 3.2 I provide an introduction to the basics of the CRES technique as well as
1204 the goals of the Project 8 experiment. Additionally, I sketch out the phased experiment
1205 development plan being implemented by Project 8 to build towards a next-generation
1206 neutrino mass experiment.

1207 In Section 3.3 I give a brief overview of Phase II of the Project 8 experiment [42, 43],
1208 which completed early in 2023. Although the bulk of the work presented in this thesis is
1209 relevant to designs of future Project 8 experiments, a description of the work in Phase II
1210 provides useful context for the rest of the work.

1211 In Section 3.4 I introduce a CRES measurement concept based on antenna arrays [44],
1212 which could be the basis for the ultimate Project 8 neutrino mass experiment. A
1213 significant portion of the R&D efforts of Project 8 in Phase III were directed towards

1214 simulating and modeling this experimental concept in order to understand the achievable
1215 sensitivity to the neutrino mass.

1216 Lastly, in Section 3.5 I introduce conceptual designs of pilot-scale experiments and
1217 Phase IV that combine atomic CRES with a large-volume CRES detection technique.
1218 This includes a design concept for an antenna array based experiment, but also a design
1219 for a resonant cavity based experiment. Resonant cavities are discussed in more depth in
1220 Chapter 6 and have become the default choice for the Phase IV experiment.

1221 **3.2 Cyclotron Radiation Emission Spectroscopy and Project** 1222 **8**

1223 **3.2.1 Cyclotron Radiation Emission Spectroscopy — CRES**

1224 Time and frequency are two of the most precisely measured quantities in physics. It is
1225 often advantageous to convert measurements of other physical quantities like mass or
1226 length into frequency measurements due to the digital nature of frequency measurements
1227 that make them immune to many sources of noise. Atomic clocks, which operate by
1228 measuring the frequencies of various atomic transitions, have been used to measure
1229 time with astounding relative uncertainties of 10^{-18} seconds [45]. The extreme precision
1230 possible with frequency measurements is often summarized using the a quote from the
1231 Physicist Arthur Schawlow who said advise his students to "Never measure anything but
1232 frequency!" [46].

1233 Neutrino mass measurements using tritium beta-decay require us to measure pertur-
1234 bations of the 18600 eV tritium endpoint to a precision as low as 0.1 eV, therefore, a
1235 spectroscopic technique with extremely high resolution is required for this measurement.
1236 The intuitive explanation for why frequency measurements are capable of such high reso-
1237 lutions is that they are essentially counting measurements, which average the number of
1238 oscillations of a physical system over time. By observing a rapidly oscillating system over
1239 a sufficient length of time one can obtain essentially arbitrary precision on a frequency
1240 limited only by the time available for measurement and the SNR of the system.

1241 What is required is that one translate the kinetic energy of the electron into a frequency,
1242 and a straightforward way to accomplish this is to place a gaseous supply of tritium into
1243 a magnetic field. When an atom decays the resulting electron will immediately begin
1244 to orbit around a magnetic field line at the cyclotron frequency, which is proportional
1245 to its kinetic energy (see Figure 3.1). The acceleration caused by the orbit leads to the

1246 emission of cyclotron radiation that can be detected using an array of antennas or a
 1247 different RF sensor such as a resonant cavity. The frequency of the radiation gives the
 1248 electron's kinetic energy, which is used to build the beta-decay spectrum and measure
 1249 the neutrino mass. The name for this measurement technique is Cyclotron Radiation
 1250 Emission Spectroscopy or CRES [40].

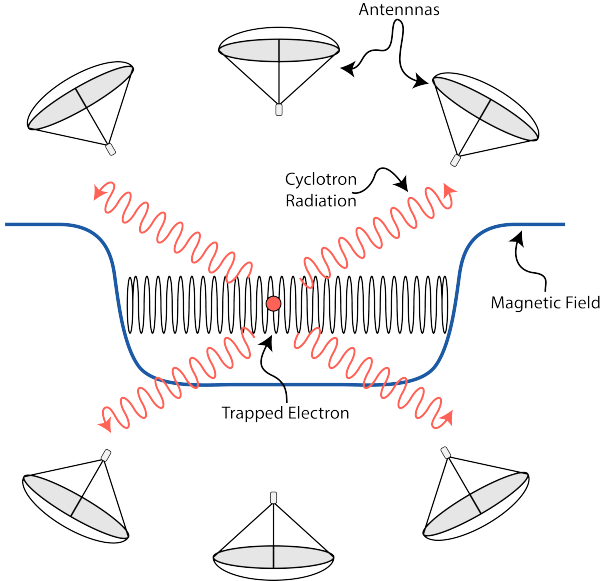


Figure 3.1. A cartoon illustration of the CRES technique. An electron is contained in a magnetic trap so that its cyclotron radiation can be detected by an array of antennas. Detecting the cyclotron radiation allows us to measure its cyclotron frequency and determine its kinetic energy.

1251 For non-relativistic particles the cyclotron frequency is simply a function of the
 1252 charge-to-mass ratio of the particle, however, from the relativistic form of the cyclotron
 1253 frequency

$$f_c = \frac{qB}{2\pi m_e \gamma} = \frac{1}{2\pi} \frac{qB}{m_e + E_{\text{kin}}/c^2}, \quad (3.1)$$

1254 one can see that the kinetic energy (E_{kin}) of the electron is directly proportional to the
 1255 inverse of the cyclotron frequency (f_c). Electrons with kinetic energies of 18.6 keV are in
 1256 the weakly relativistic regime with $\beta = \frac{v}{c} = 0.263$ and $\gamma = 1.036$.

1257 The required frequency resolution needed for neutrino mass measurement can be
 1258 obtained by differentiating Equation 3.1,

$$\frac{df_c}{dE_{\text{kin}}} = \frac{1}{2\pi} \frac{-qBc^2}{(m_e c^2 + E_{\text{kin}})^2}, \quad (3.2)$$

1259 from which we can obtain the relationship between fractional differences in energy and

1260 frequency,

$$\frac{df_c}{f_c} = \frac{1 - \gamma}{\gamma} \frac{dE_{\text{kin}}}{E_{\text{kin}}}. \quad (3.3)$$

1261 Therefore, an energy precision of 1 eV for an 18.6 keV electron requires a frequency
1262 precision of approximately 2 ppm.

1263 The minimum observation time required to achieve this resolution can be estimated
1264 using the uncertainty principle as formulated by Gabor [47]. Electrons from tritium
1265 beta-decay experience random collisions with the background gas particles, which limits
1266 the uninterrupted radiation lifetime. The time between collision events, referred to
1267 as track length in the context of CRES measurements, is an exponentially distributed
1268 variable. Differences in the track lengths of a population of mono-energetic electrons leads
1269 to uncertainty or broadening in the distribution of measured frequencies proportional to
1270 the mean track length, τ_λ . The resulting frequency distribution has a Lorentzian profile,
1271 whose width is given by the Gabor limit,

$$\tau_\lambda \Delta f_c = \frac{1}{2\pi} \implies \Delta f_c = \frac{1}{2\pi\tau_\lambda}. \quad (3.4)$$

1272 The cyclotron frequency for a 18.6-keV electron in a 1 T field is approximately
1273 27 GHz, from which one can estimate the minimum observation time for 2 ppm frequency
1274 resolution at approximately 3 μ sec. The Gabor limit is not the true lower bound on the
1275 frequency resolution for a CRES signal, since it is based on the details of the Fourier
1276 representation of a time-series with a fixed length. If one takes the approach of fitting
1277 the CRES signal in the time-domain, then one finds that the limit on frequency precision
1278 is given by the Cramér-Rao lower bound (CRLB) [48], which depends on the track length
1279 and SNR. The CRLB allows for better precision on the cyclotron frequency, however,
1280 the Gabor limit provides an intuitive limit with the correct order of magnitude.

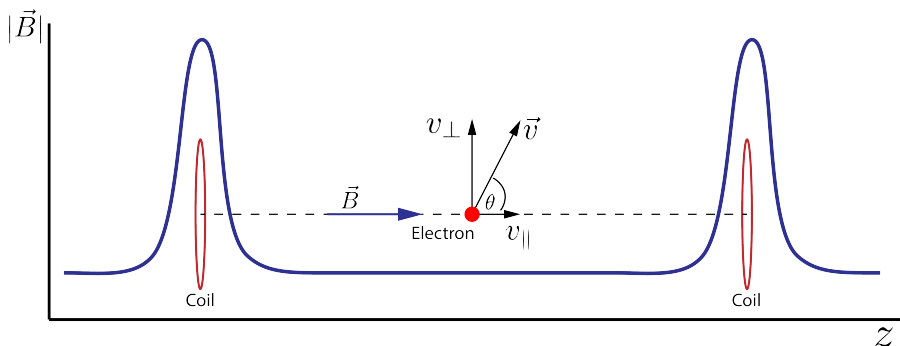


Figure 3.2. An illustration of an electron in a bathtub magnetic trap generated by two well-separated coils.

Ensuring that an electron remains under observation long enough so that it's frequency can be precisely measured requires a magnetic trap. A magnetic trap is a local minimum in a background magnetic field generated an appropriate configuration of electromagnetic coils. Since magnetic fields can do no work, there is no danger of the magnetic trap affecting the kinetic energy electron after it is emitted from the beta-decay. One common approach to creating a magnetic trap is the "bathtub" trap configuration, which in it's simplest form consists of two high magnetic field pinch coils aligned on a central axis that are well separated (see Figure 3.2). This configuration produces a trap with a flat uniform bottom and relatively steep walls, which is ideal for CRES measurements.

Electrons produced in the trap oscillate back and forth between the trap walls at a frequency that depends upon the pitch angle, unless they are produced with pitch angles too small to be contained in the trap. Pitch angle is defined as the angle between the component of the electron's velocity perpendicular to the magnetic field and the component parallel to the magnetic field,

$$\tan \theta = \frac{v_{\perp}}{v_{\parallel}}. \quad (3.5)$$

The axial motion of the electron leads to variation in the cyclotron frequency due to the changing value of the magnetic fields. This leads to frequency modulation that generate sidebands in the cyclotron radiation spectrum. Resolving these sideband frequency components is necessary for a complete reconstruction of the CRES signal in the experiment.

Electrons trapped in a cylindrically symmetric trap have three primary components of motion (see Figure 3.3). The dominant component, typically with the highest frequency, is the electron's cyclotron orbit, which encodes information on the electron's kinetic energy. Axial motion from the electron's pitch angle leads to frequency modulation but also a shift in the average magnetic field experienced by an electron. This leads to a correlation between the kinetic energy of the electron and the pitch angle depending on the particular shape of the magnetic trap, which can negatively impact energy resolution. To reduce this correlation one must engineer the trap to have a flat bottom with very steep wall both of which are more easily achieved with a small aspect ratio bathtub trap. Radial gradients in the trap leads to a third component of motion called grad-B drift [49]. The equation for the drift velocity is

$$\mathbf{v}_{\nabla B} = \frac{m_e v_{\perp}^2}{2qB} \frac{\mathbf{B} \times \nabla B}{B^2}. \quad (3.6)$$

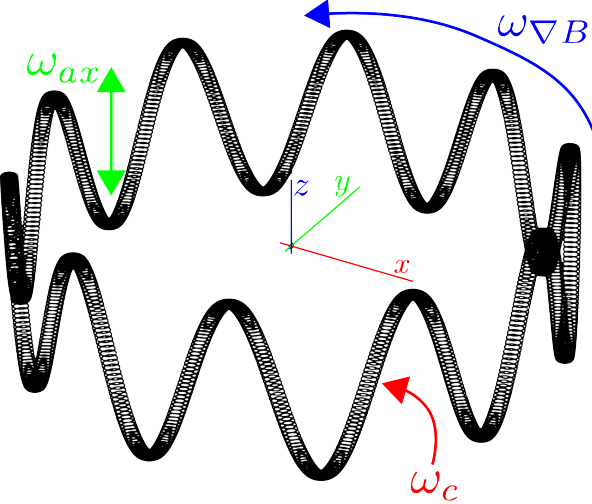


Figure 3.3. A plot of the main components of an electron's trajectory in a cylindrically symmetric trap.

1311 These additional components of motion all influence the shape of the CRES signal so
 1312 modeling their effects is critical to proper measurement of the kinetic energy.

1313 The total power of the radiation emitted by an electron in a free-space environment
 1314 is given by the Larmor equation [50]

$$P(\gamma, \theta_p) = \frac{1}{4\pi\epsilon_0} \frac{2}{3} \frac{q^2 \omega_c^2}{c} (\gamma^2 - 1) \sin^2 \theta_p, \quad (3.7)$$

1315 where ω_c is the cyclotron frequency multiplied by 2π and θ_p is the pitch angle to distinguish
 1316 it from the spherical angle coordinate. A single electron with a 90° pitch angle and
 1317 18.6 keV of kinetic energy in a 1 T magnetic field emits a total radiation power of 1.2 fW,
 1318 which is quite small compared with typical RF systems, furthermore, one is typically
 1319 only able to receive a fraction of this total power with an antenna or other detection
 1320 system. Therefore, RF systems in CRES experiments must be operated at cryogenic
 1321 temperatures to limit the noise power such that adequate SNR can be achieved for signal
 1322 detection and reconstruction. Alternatively, longer tracks enable detection of weaker
 1323 signals due to the increase in the total signal energy available for the detection algorithm.

1324 3.2.2 The Project 8 Collaboration

1325 The Project 8 collaboration¹ is a group of institutions in the United States and Germany
 1326 aiming to measure the neutrino mass by developing a novel spectrometer technology

¹<https://www.project8.org/>

1327 based on CRES. In the ultimate Project 8 experiment the CRES technique will be used
1328 to measure the beta-decay spectrum using a large source of atomic tritium sufficient to
1329 achieve the required statistics in the last $O(10)$ eV of the decay spectrum. Project 8 is
1330 targeting a neutrino mass sensitivity below 50 meV [51], which exhausts the range of
1331 possible neutrino masses under the inverted hierarchy and is a factor of four less than
1332 sensitivity projections for the ongoing KATRIN experiment.

1333 Project 8's proposed experiment requires the development of two novel technologies:
1334 the production and trapping of a source of atomic tritium on cubic-meter scales and
1335 technology to enable CRES measurements of individual electrons in the same volume.

1336 Atomic Tritium

1337 Previous measurements of the tritium beta-decay spectrum for neutrino mass measure-
1338 ments have relied on sources of molecular tritium for their measurements [38, 52, 53] due
1339 to the technical challenges associated with the production and storage of atomic tritium.

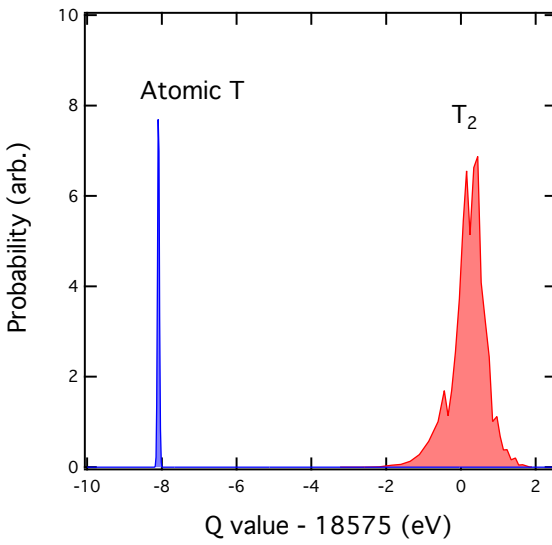


Figure 3.4. A plot of the final state distributions of atomic and molecular tritium. The final state distribution provides the primary contribution to the width of the molecular spectrum whereas thermal doppler broadening is responsible for the width of the atomic spectrum.

1340 One must supply sufficient energy to the tritium molecules to break the molecular
1341 bond and create atomic tritium. Common approaches to this include the use of hot
1342 coaxial filament atom crackers as well as plasma atom sources. Both involve heating the
1343 tritium atoms to temperatures of > 2500 K, which must then be cooled to temperatures
1344 on the order of a few mK so that the tritium atoms can be trapped. Cooling the atoms

1345 requires the construction of a large tritium infrastructure and cooling system that can
1346 supply a source of cold atoms to the trap.

1347 Once cold tritium atoms are produced they cannot make contact with any surfaces
1348 to avoid recombination of the atoms to molecules. Therefore, a magnetic trap is required
1349 to store the atoms for a sufficient length of time that they have a chance to decay before
1350 escaping the trap. Trapping the atoms requires the construction of a large and complex
1351 magnet system that must be cooled to cryogenic temperatures.

1352 The significant experimental complexity caused by atomic tritium makes a molecular
1353 source the obvious choice from practical considerations. However, the drawback of
1354 molecular tritium for neutrino mass measurement is the irreducible broadening in the
1355 electron's kinetic energy due to the final state spectrum of molecular tritium (see Figure
1356 3.4). The broadening of the final state spectra has a RMS amplitude of 436 meV [54, 55]
1357 caused by variation in the final vibrational state of the daughter molecule. For atomic
1358 tritium the primary sources of broadening in the final state spectrum are magnetic
1359 hyperfine splittings (magnitude of $O(10^{-5})$ eV) and thermal Doppler broadening caused
1360 by the motion of the trapped atom. For atomic tritium at a temperature of 1 mK thermal
1361 broadening is the dominant contribution, providing about 1 meV RMS of broadening to
1362 the electron's kinetic energy.

1363 The larger energy broadening with molecular tritium leads to an irreducible statistical
1364 uncertainty that limits the achievable sensitivity to approximately 100 meV at 90%
1365 confidence. For previous direct measurements of the neutrino mass this uncertainty is an
1366 insignificant contribution to the overall uncertainty budget, however, for experiments
1367 like Project 8 atomic tritium is a key component to the success of the experiment.

1368 CRES for Neutrino Mass Measurement

1369 Several features of the CRES technique make it an attractive choice for a next generation
1370 neutrino mass measurement experiment. For example, with a CRES experiment the
1371 volume of the source gas can be the same as the volume of the CRES spectrometer.
1372 This is due to the fact that CRES is a remote-sensing technique that can observe the
1373 energy of the electron without altering its trajectory or directly interacting with the
1374 electron. Given that tritium gas is transparent to cyclotron radiation the kinetic energies
1375 of electrons can be measured with an appropriate sensing technology, such as a cavity or
1376 antenna array, located directly outside the atom trapping volume.

1377 The current state-of-the-art tritium beta-decay spectroscopy experiment, KATRIN,
1378 utilizes the magnetic adiabatic collimation with an electrostatic filter (MAC-E filter)

technique to measure the beta-decay spectrum of molecular tritium. In this approach, a source of molecular tritium is located outside the spectrometer. When a beta-decay occurs the electron must exit the tritium source and travel through the MAC-E filter before it can be detected on the other side of the filter using a charge sensor. The measurement statistics of the MAC-E filter are limited by the transverse areas of the tritium source and the filter due to the need to travel through the experiment without scattering. This scaling is less favorable than the volumetric scaling of CRES due to the ability to co-locate source and detector.

Another promising aspect of the CRES technique is the inherently high precision of frequency based measurements. The endpoint of the molecular tritium beta-decay spectrum is approximately 18.6 keV, which dwarfs the neutrino mass scale of $< 1 \text{ eV}/c^2$ by at least a factor of 10^5 . Measuring the effect of such a small mass on a high energy electron requires excellent energy resolution. Since frequency measurements are essentially counting measurements they are intrinsically quite accurate due to the ability to measure the cyclotron frequency by effectively averaging over millions of cyclotron orbits. Using off-the-shelf RF components its is possible to achieve part-per-million accuracy on the kinetic energy with the CRES technique.

CRES is also nearly immune to typical sources of backgrounds that plague other experiments. Since CRES operates via non-destructive measurements of the electron's cyclotron frequency potential sources of background electrons are effectively filtered out by limiting the frequency bandwidth of the measurement. The fiducial volume of the experiment is free from any surfaces that could introduce stray electrons and electrons from sources outside the fiducial volume can be prevented from entering the experiment.

Neutrino Mass Sensitivity Goals

Project 8's ultimate goal is to combine CRES with atomic tritium to measure the neutrino mass with 40 meV sensitivity at the 90% confidence level (see Figure 3.5). This sensitivity is sufficient to fully exhaust the range of allowable neutrino masses under the inverted neutrino mass ordering regime and is approximately an order of magnitude less than the projected final sensitivity of the KATRIN experiment. Excluding the full neutrino mass parameter space would require a sensitivity an order of magnitude lower than what is proposed by Project 8, which would require an experiment whose size and complexity are currently well beyond proposals for the next-generation of neutrino mass direct measurement experiments.

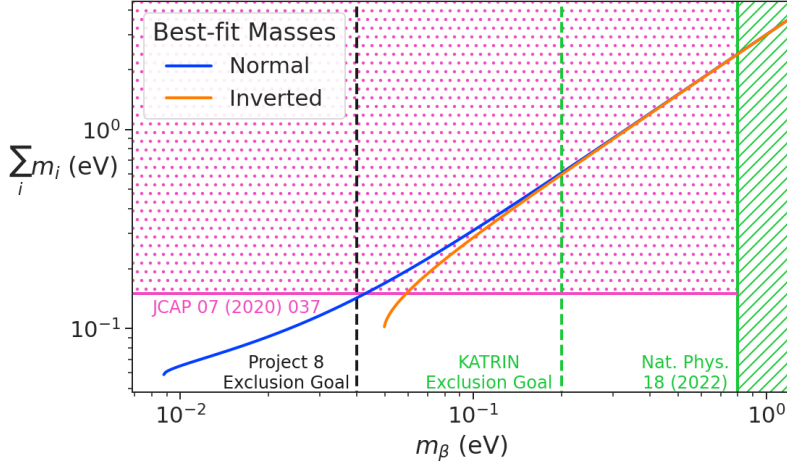


Figure 3.5. Neutrino mass exclusion plot including limits from cosmological measurements and the KATRIN experiment. Allowed ranges for neutrino masses under the normal and inverted hierarchies are shown as the blue and orange lines respectively. The black dashed line shows Project 8’s goal neutrino mass sensitivity for the Phase IV experiment.

1412 3.2.3 The Project 8 Phased Development Plan

1413 Reaching 40 meV sensitivity requires the simultaneous development and eventually
 1414 combination of CRES and atomic tritium. These technologies require a significant up-
 1415 front research and development (R&D) investment to build-out the required capabilities
 1416 for a 40 meV CRES experiment. Therefore, Project 8 is following a phased experiment
 1417 plan in which incremental progress can be made towards the ultimate goal of a 40 meV
 1418 neutrino mass measurement with CRES.

1419 Phase I and II: Proof of Principle and First Tritium Measurements

1420 The earlier phases of the Project 8 experiment, Phase I and II, were focused on demon-
 1421 stration and development of the CRES technique itself as well as a proof-of-principle
 1422 measurement of the neutrino mass using the CRES technique.

1423 In Phase I, Project 8 performed a proof-of-principle measurement of the ^{83m}Kr
 1424 spectrum using CRES, which marked the first ever energy spectrum measurement with
 1425 CRES. The experiment included all of the main components expected for the full-scale
 1426 version of the experiment. An electron source consisting of a gas of ^{83m}Kr was supplied
 1427 to a waveguide gas cell constructed out of a segment of WR-42 waveguide and sealed
 1428 with Kapton windows at the top and bottom. A magnetic trapping region was created
 1429 in the waveguide cell using a single electromagnetic coil wrapped around the waveguide

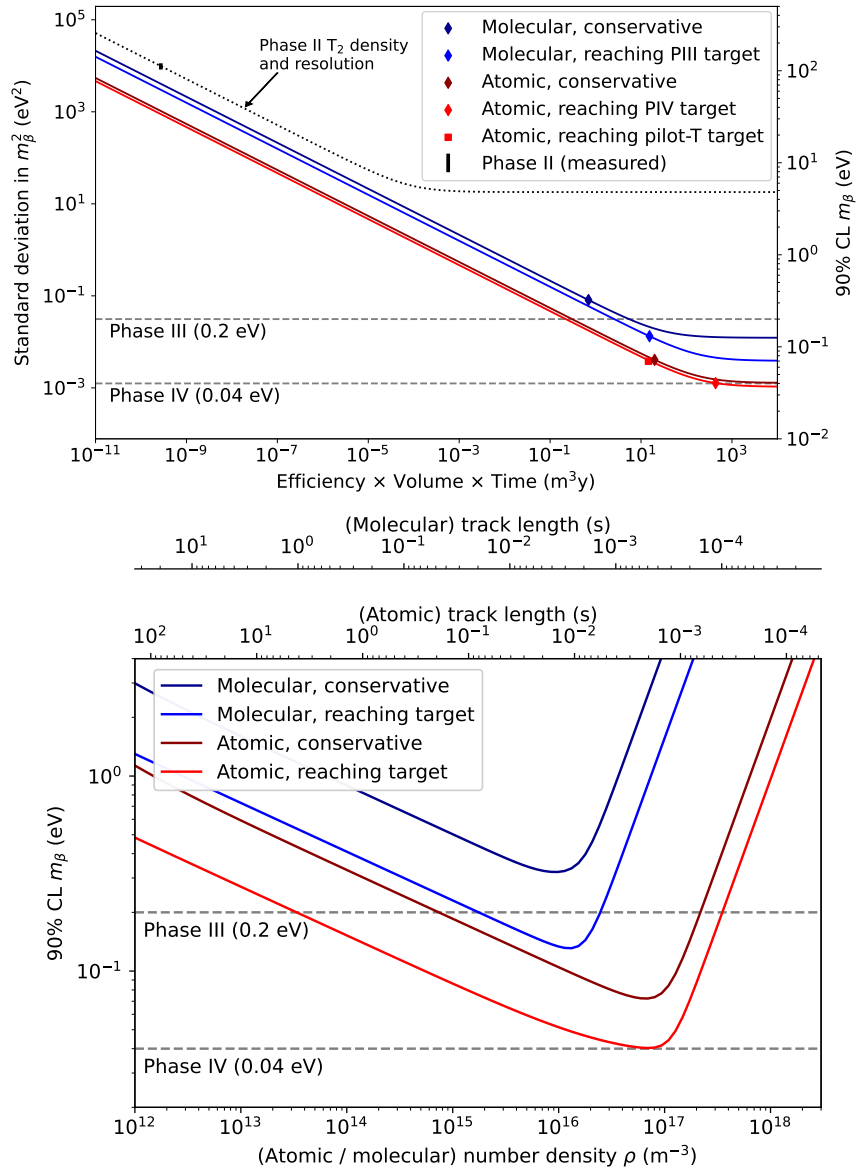


Figure 3.6. Sensitivity calculations for a cavity based CRES experiment that demonstrate the neutrino mass measurement goals of the Project 8 collaboration throughout the phased development plan. The blue curves indicate molecular tritium sources and the red curves indicate atomic tritium sources. In the current plan Phase III contains two tritium experiments. The first is the Low-frequency Apparatus (LFA) which is a molecular tritium experiment and the second is the atomic tritium pilot-scale experiment that ends Phase III. The sensitivity of these experiments is primarily a function of statistics, however, there is a critical density beyond which CRES electrons do not have enough time to radiate between collisions for a high-resolution frequency measurement leading to worse sensitivity.

1430 which provided a trapping volume on the order of a few cubic-millimeters. Detection of
1431 the cyclotron radiation was performed by connecting the waveguide cell to an additional
1432 segment of waveguide that transmitted the radiation to a cryogenic amplifier.

1433 Success in Phase I was achieved with the 2014 publication of the measured ^{83m}Kr
1434 conversion spectrum [56], which contains a mono-energetic 17.8-keV as well as several
1435 other conversion lines at higher energies. Publication of this result marked the official
1436 end of Phase I and the start of Phase II in which Project 8 shifted its focus to the
1437 demonstration of the first tritium beta-decay spectrum using CRES. Phase II successfully
1438 concluded in 2023 with the submission of the papers demonstrating the first tritium
1439 beta-decay spectrum endpoint and neutrino mass measurement using CRES. For more
1440 information on Phase II please see Section 3.3.

1441 **Phase III: Research and Development and a Pilot-scale Experiment**

1442 After Phase II Project 8 has shifted focus to R&D towards the construction of an
1443 experiment that demonstrates all the technologies required for a 40 meV measurement of
1444 the neutrino mass. The goal for this pilot-scale experiment is to successfully retire all
1445 technological and engineering risks associated with the Phase IV experiment, while being
1446 a scientifically interesting experiment in its own right that has sensitivity to neutrino
1447 masses on par with KATRIN’s final projected sensitivity.

1448 Phase III R&D is divided into two equally important efforts — atomic tritium
1449 and CRES detection techniques. Atomic tritium development in Phase III includes
1450 the development of all aspects of the tritium system. This includes the production of
1451 tritium atoms, atomic cooling and recirculation systems, purity and isotope concentration
1452 monitoring, and atom trapping. Currently, Project 8 is operating small scale demonstrator
1453 systems developing atom crackers to show that atom production at the estimated rates
1454 needed for Phase IV is achievable. Future efforts will continue the current developments
1455 on atom production and expand to include demonstrations of atomic cooling with an
1456 evaporative beam line as well as atom trapping using Halbach magnet arrays.

1457 The need for new CRES detection techniques is driven by the drastic increase in scale
1458 from Phase II to the Phase IV and the pilot-scale experiments. The physical volume
1459 used for CRES in Phase II was on the order of a few cubic-centimeters, and achieving
1460 Project 8’s sensitivity target of 40 meV requires an experiment volume on the multi-cubic
1461 meter scale. Therefore, the waveguide gas cell CRES detection technique used in Phase
1462 II is not a feasible option for the future of Project 8 due to it’s inability to scale to the
1463 required size.

1464 Two alternative CRES detection techniques have been proposed for the pilot-scale
1465 experiment — antenna arrays and resonant cavities (see Section 3.4 and Chapter 6).
1466 Both approaches have relative advantages and disadvantages, however, the improved
1467 understanding of the antenna array and cavity approaches to CRES in the recent years
1468 has led to cavities being the preferred technology for the pilot-scale experiment and
1469 Phase IV due to the estimated reduced cost and complexity of this approach. Since a
1470 large degree of the work presented in this thesis is focused on the development of the
1471 antenna array CRES technique as well as the design of demonstrator experiments, we
1472 described the proposed R&D plan for antenna array CRES in Phase III in Section 3.4.

1473 Cavity CRES R&D in Phase III consists of a series of demonstrator experiments
1474 intended to demonstrate cavity CRES at a variety of scales and magnetic fields using
1475 electrons from ^{83m}Kr , an electron gun, and potentially molecular tritium sources. The
1476 near-term cavity effort in Project 8 is the cavity CRES apparatus (CCA), which is a
1477 small-scale cavity experiment operating near 26 GHz, that will perform the first CRES
1478 measurements using a small cavity. This experiment will pave the way towards larger
1479 scale cavity experiments in preparation for the eventual pilot-scale tritium experiment.

1480 The pilot-scale experiment is the first experiment, which will combine atomic tritium
1481 and large-volume CRES detection in the same experiment. It will directly demonstrate
1482 all the technologies required for Phase IV such that no technical risks remain for scaling
1483 the experiment to required scale. A robust approach to scaling the pilot-scale experiment
1484 is to simply build multiple copies of it for the Phase IV experiment.

1485 **Phase IV: Project 8’s Ultimate Neutrino Mass Experiment**

1486 The design of Phase IV should be a direct extension of the pilot-scale CRES experiment
1487 that marks the official end of Phase III (see Section 3.5). The Phase IV experiment
1488 represents the final experiment in the Project 8 neutrino mass measurement experiment
1489 plan and will have sensitivity to neutrino masses of 40 meV.

1490 **3.3 Phase II: First Tritium Beta Decay Spectrum and** 1491 **Neutrino Mass Measurement with CRES**

1492 In Phase II Project 8 demonstrated the first ever measurement of the tritium beta-decay
1493 spectrum endpoint using the CRES technique, which lead to the first neutrino mass
1494 measurement by the Project 8 collaboration. This milestone was made possible by many

improvements in the CRES technique and in the understanding of CRES systematics, which takes an important first step towards larger scale measurements of the tritium beta-decay spectrum with CRES. In this section, I briefly describe some important elements of the Phase II experiment, with the goal of contextualizing the research and development efforts for Phases III and IV of Project 8. For more complete descriptions of the work that lead to Project 8's Phase II results please refer to the relevant publications by the collaboration [42, 43].

3.3.1 The Phase II CRES Apparatus

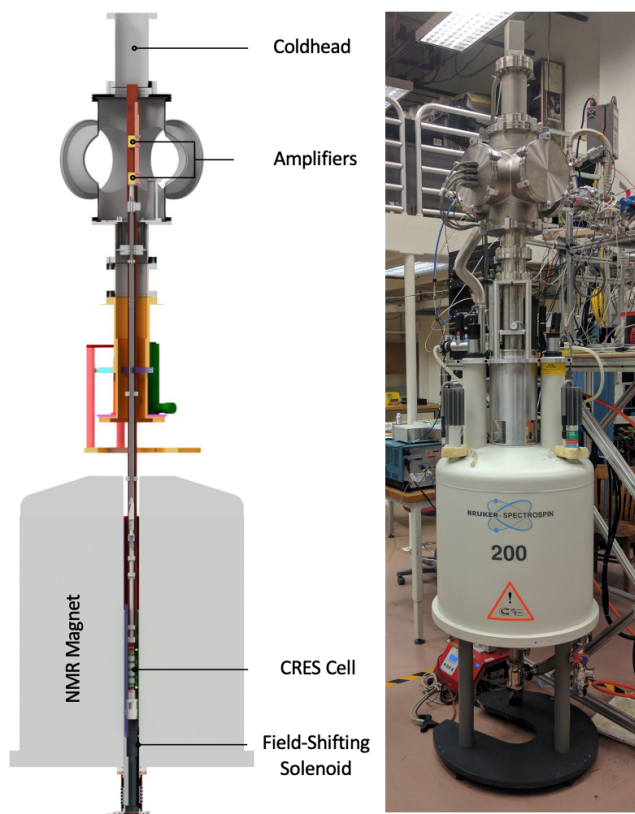


Figure 3.7. The Phase II CRES apparatus used to perform the first measurement of the tritium beta-decay spectrum using CRES.

Magnet and Cryogenics

The magnetic field for the the Phase II experiment is provided by a nuclear magnetic resonance (NMR) spectroscopy magnet with a central bore diameter of 52 mm (see Figure

1506 3.7). The magnet produces a background magnetic field with an average value of 0.959 T
1507 and a 10 ppm variation across the bore diameter achieved using several shim coils built
1508 into the magnet. Using an external NMR field probe the variation of the magnetic field
1509 along the vertical axis of the magnet bore was measured to obtain an accurate model of
1510 the magnetic field so that the CRES cell could be positioned for optimal magnetic field
1511 uniformity.

1512 An external solenoid magnet was installed inside the magnet bore to provide the
1513 ability to shift the magnitude of the background magnetic field by values on the order of
1514 a few mT. The solenoid has inside diameter of 46 mm and a length of 350 mm, which
1515 terminates in a vacuum flange that allows it to be inserted into the NMR magnet bore
1516 from the bottom. By shifting the value of the magnetic field by a few mT, the cyclotron
1517 frequencies of electrons produced by the 17.8 keV ^{83m}Kr internal-conversion line [57]
1518 can be shifted over a range of frequencies on the order of 100 MHz. This allows one to
1519 study the frequency dependent behavior of multiple CRES systematics such as detection
1520 efficiency that directly affect the measured shape of the tritium spectrum.

1521 The inside of the magnet bore diameter was pumped down to a vacuum of less than
1522 10 μtorr using a turbomolecular pump, which allows for cryogenic cooling of the CRES
1523 cell and RF system. Cooling power was supplied to the Phase II apparatus using a
1524 cryopump with its coldhead mounted above the primary magnet and CRES cell. This
1525 arrangement allowed for sufficient cooling power to be delivered to the amplifiers to cool
1526 them to a temperature of \approx 40 K, while keeping the amplifiers far enough from the
1527 magnet so as not to be damaged by the large field strength. Thermal contact between
1528 the coldhead, amplifiers, RF system, and CRES cell is achieved using a copper bar that
1529 runs the full length of the apparatus. To prevent freeze-out of ^{83m}Kr on the walls of the
1530 CRES cell a separate heater was installed to keep the CRES cell near a temperature of
1531 85 K during the operation of the experiment.

1532 **CRES Cell**

1533 Located in the most uniform region of the magnetic field is the CRES cell, which is the
1534 region of the apparatus where radioactive decays of ^{83m}Kr and T_2 emit electrons that can
1535 be trapped and measured using CRES (see Figure 3.8). The CRES cell is manufactured
1536 from a segment of cylindrical waveguide designed to operate at K-band frequencies
1537 near 26 GHz. The diameter of the waveguide determines which resonant modes of the
1538 waveguide will couple to the electron and transmit its radiation to the amplifiers. For
1539 Phase II a waveguide diameter of 1 cm was selected, which allows electrons to couple to

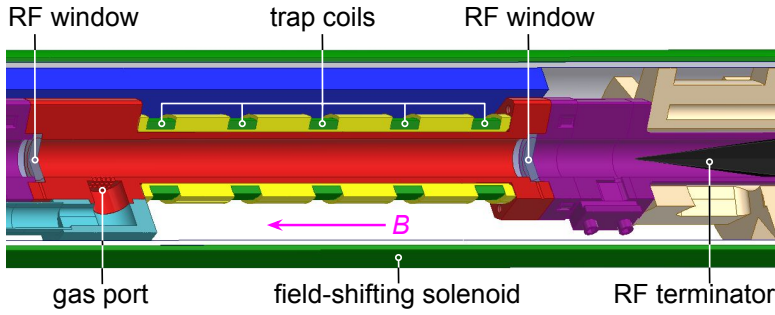


Figure 3.8. Diagram of the CRES cell portion of the Phase II apparatus.

1540 the TE₁₁ and TM₀₁ cylindrical waveguide modes. To reduce complexity in modeling and
 1541 analyzing the CRES data, it is ideal to select a diameter that prevents electrons from
 1542 coupling to higher-order waveguide modes beyond the fundamental TE and TM modes.

1543 Around the exterior of the cylindrical waveguide are several magnetic coils used to
 1544 produce magnetic traps inside the CRES cell volume. Without a magnetic trap electrons
 1545 produced from decays inside the CRES cell quickly impact the cell wall, which prevents
 1546 a measurement of their cyclotron frequency using CRES. Each coil along the length of
 1547 the waveguide produces a separate trap that is approximately harmonic in shape. By
 1548 independently controlling the currents provided to each coil the traps can be configured
 1549 to have equal values of the magnetic field at the trap bottom despite a non-uniform field
 1550 from the NMR magnet.

1551 Two primary magnetic trap configurations were used during the Phase II experiment.
 1552 The first was a shallow trap configuration used primarily for its high energy resolution to
 1553 study systematics using ^{83m}Kr decays, and the second was a deeper trap that could trap a
 1554 higher percentage of pitch angles. The trade-off with this trap is that the higher trapping
 1555 efficiency comes at the cost of lower energy resolution due to the greater variation in pitch
 1556 angle. The deep trap was the trap used to measure the tritium beta-decay spectrum in
 1557 Phase II.

1558 The source gases were delivered into the CRES cell through a gas port located near the
 1559 top end of the cylindrical waveguide. To prevent the gases from escaping the cell, vacuum
 1560 tight RF transparent windows are needed to contain the tritium and krypton source
 1561 gas across a 1 atm pressure differential, while still transmitting the cyclotron radiation
 1562 without distortion. The crystalline material, CaF₂, which has a thermal expansion
 1563 coefficient similar to that of copper, was used for this purpose in the CRES cell. Two
 1564 windows, each 2.4 mm thick, were used to seal off the ends of the CRES cell. The
 1565 thickness of 2.4 mm corresponds to half of a cyclotron wavelength when one accounts for

1566 the permittivity of CaF_2 .

1567 **RF System**

1568 The RF system in the Phase II apparatus transferred the cyclotron radiation from the
1569 CRES cell to the receiver chain. The receiver chain performs the down-conversion and
1570 digitization required to obtain signals that can be analyzed to determine the cyclotron
frequencies of electrons in the CRES cell (see Figure 3.9).

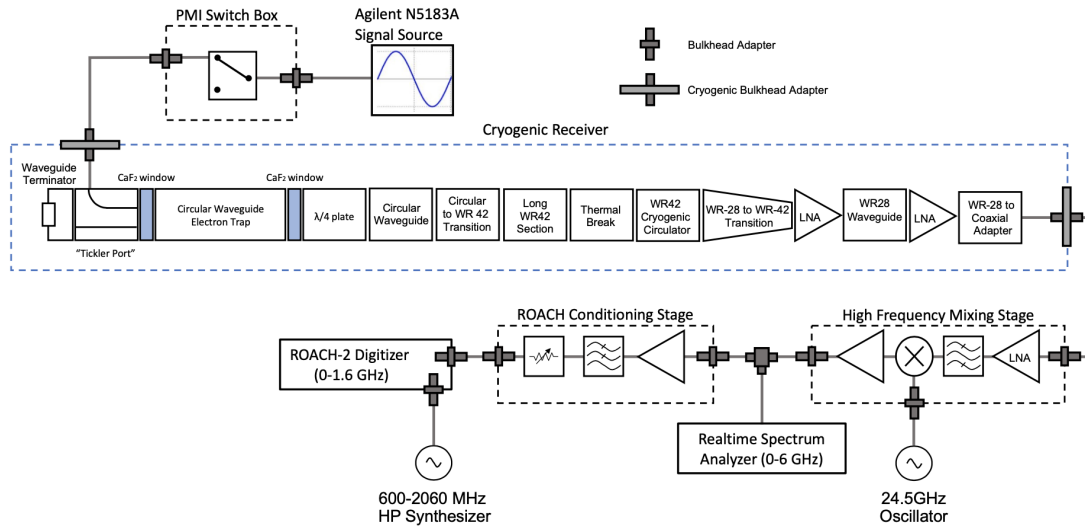


Figure 3.9. RF system diagram for the Phase II apparatus.

1571
1572 Below the CRES cell, at the bottom of the Phase II apparatus, is a tickler port and
1573 waveguide terminator. The tickler port is used to inject signals into the CRES cell and
1574 RF system for testing and calibration purposes. The waveguide terminator is designed to
1575 absorb cyclotron radiation emitted by electrons that transmits out of the bottom of the
1576 CRES cell. This lowers the total power received from electrons in the CRES cell, since all
1577 the energy radiated downwards is absorbed into the terminator. Earlier iterations of the
1578 Phase II apparatus used an RF short in this location that reflected this power up towards
1579 the amplifiers, however, interference between the upward traveling and reflected radiation
1580 led to a disappearance in the signal carrier that made reconstruction impossible.

1581 Radiation traveling upward passes through the CaF_2 window passes through a $\lambda/4$
1582 plate, which transforms the circularly polarized cyclotron radiation into linear polarization.
1583 The linearly polarized fields next travel through a segment of circular waveguide that
1584 transitions into a long segment of WR-42 waveguide that carries the fields out of the
1585 high magnetic field region. A thermal break segment is included, which consists of a a

1586 segment of gold-plated stainless steel WR-42 waveguide, to help thermally isolate the
1587 relatively warm CRES cell from the colder amplifiers. The radiation then passes through
1588 a cryogenic circular, which prevents signals reflected from the amplifiers from interfering
1589 with the CRES cell before a WR-42 to WR-28 transition connects the waveguide to the
1590 first of the cryogenic amplifiers. The radiation passes through two cryogenic amplifiers
1591 before being coupled to a coaxial termination at the top of the Phase II apparatus.

1592 The coaxial cable transfers the cyclotron radiation signals to a high-frequency mixing
1593 stage that performs an analog frequency down-conversion using a 24.5 GHz LO. Two forms
1594 of digitization can be used at this stage to readout the CRES data. One is a real-time
1595 spectrum analyzer that digitizes the CRES signal data in time-domain and computes the
1596 frequency spectrum in real-time, which allows for direct visualization of CRES signal
1597 spectrograms as the experiment is running. The real-time spectrum analyzer is most
1598 useful for taking small amount of streamed data for debugging and analysis of the system.
1599 The other method, which was used to collect the majority of the CRES data in Phase II,
1600 is a ROACH-2 FPGA and digitizer system. The ROACH system consists of a fast ADC
1601 that samples the CRES signal data at 3.2 GSps. Internal digital down-conversion stages
1602 implemented in the FPGA perform a mixing operation that reduces the bandwidth of the
1603 CRES signals to 100 MHz. The FPGA implements a 8192 sample FFT and packetizes
1604 time and frequency domain records in parallel. The packetized data is then transferred
1605 from the ROACH to be analyzed by the data-processing pipeline.

1606 **3.3.2 CRES Track and Event Reconstruction**

1607 **Time-Frequency Spectrogram**

1608 The online data-processing is intended to identify interesting data that could contain
1609 CRES signals using a software real-time triggering algorithm. Interesting segments of
1610 data identified by this algorithm are collected into files that are transferred to a server for
1611 offline processing and analysis. The data files contain a continuous series of time-domain
1612 samples, broken into a set of records, which are 4096 samples long. The time-series is
1613 made up of 8-bit IQ samples acquired at 100 MHz.

1614 Each time-series record is accompanied by an associated frequency spectrum consisting
1615 of 4096 frequency bins approximately 24.4 kHz wide, which is represented as a power
1616 spectral density. The individual frequency spectra can be organized temporally to create
1617 a time-frequency spectrogram that represents the evolution of the cyclotron frequency
1618 spectrum over the course of the CRES event (see Figure 3.10). The time-frequency

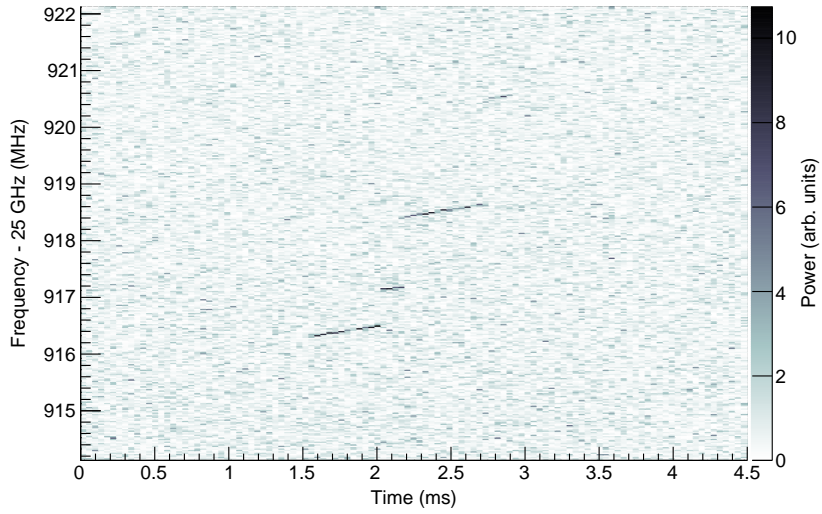


Figure 3.10. The time-frequency spectrogram of a tritium CRES event in the Phase II apparatus.

1619 spectrogram is represented as a two-dimensional image where the color of each pixel is
 1620 proportional to the power spectral density. Each vertical slice of pixels in the image
 1621 represents a frequency spectrum, therefore, each horizontal bin represents the data
 1622 obtained over a duration of $4096 \times 0.01 \text{ MHz}^{-1} = 40.96 \mu\text{sec}$.

1623 CRES Event Data Features

1624 Phenomenologically, a CRES signal appears as a sinusoidal signal whose frequency slow
 1625 increases ("chirps") over time. Axial motion of the electron in the trap leads to the
 1626 formation of frequency sidebands that surround the more powerful carrier frequency, due
 1627 to Doppler modulation of the electron's frequency as it bounces between the walls of the
 1628 magnetic trap. The critical piece of information that must be extracted from the track
 1629 and event reconstruction procedure is the carrier frequency, since it is this frequency
 1630 that gives the cyclotron frequency and thus the kinetic energy. While axial motion from
 1631 non- 90° pitch angles does change the average magnetic field experienced by an electron
 1632 and, therefore, changes the cyclotron frequency. Because of low-SNR sidebands were
 1633 unable to be observed in Phase II, so a correction for the effect of the pitch angle on the
 1634 cyclotron frequency was not possible.

1635 In the time-frequency spectrogram representation the chirping carrier frequency
 1636 appears as a linear track of high-power frequency bins (see Figure 3.10). The vertical
 1637 slope of the tracks is caused by the emission of energy from the electron in the form of

1638 cyclotron radiation, therefore, the size of the slope parameter is directly proportional
1639 to the Larmour power. The continuous track is periodically interrupted by random
1640 jumps to higher frequency and lower energy caused by random inelastic collisions with
1641 background gas molecules. The length of a track is an exponentially distributed variable
1642 whose mean value is inversely proportional to the gas density. The size of the frequency
1643 discontinuities is directly proportional to the energies of the rotational and vibrational
1644 states of background gas molecules.

1645 A CRES event refers to the collection of tracks produced by a trapped electron until
1646 it inevitably scatters into a pitch angle that can no longer be trapped. The goal of track
1647 and event reconstruction is to first identify the set of tracks present in a time-frequency
1648 spectrogram that represents a segment of data acquired in the Phase II apparatus. These
1649 tracks must then be clustered into events from which we can determine the first track
1650 produced by the electron and thus estimate it's starting cyclotron frequency and kinetic
1651 energy.

1652 **Track Reconstruction**

1653 The first step in CRES event reconstruction is the identification of tracks in the time-
1654 frequency spectrogram, which is essentially an image processing task. Track finding
1655 starts by normalizing the power spectral density based on the average noise power.
1656 Next a power threshold is applied to the normalized spectrogram where only bins that
1657 have a signal-to-noise ratio greater than five are selected to build tracks. In this case
1658 signal-to-noise ratio is defined as the ratio between the normalized, unitless power of a
1659 bin divided by the average normalized power across the full frequency spectrum.

1660 The sparse spectrogram produced by this power cut consists only of a sparse collection
1661 of high-power frequency bins that could be part of a CRES signal track (see Figure
1662 3.11). In this form is it much easier to identify tracks "by eye", however, for the Phase II
1663 analysis Project 8 developed its own custom-made track finding algorithm, called the
1664 sequential track finder (STF).

1665 The STF algorithm processes the sparse spectrogram in sequential fashion, processing
1666 each time-slice one-by-one until the end of the spectrogram is reached. Tracks are found
1667 by searching for points in the sparse spectrogram that appear to fall on a straight line.
1668 Multiple configurable parameters are built into the STF algorithm that allow the user to
1669 tune the criteria for adding a point to an existing track or creating a new track. These
1670 include parameters such as maximum time and frequency differences between subsequent
1671 points in a track as well as minimum SNR values for the start and endpoints of the track.

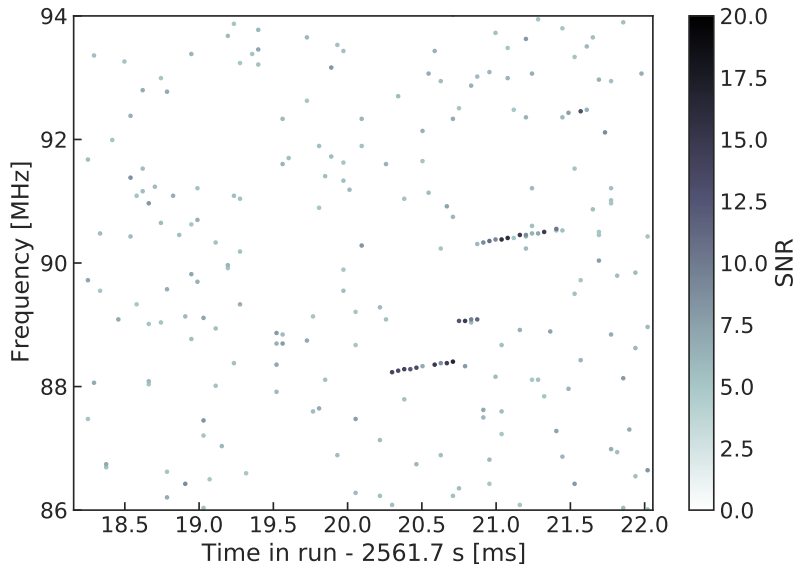


Figure 3.11. The sparse spectrogram obtained by placing a power cut on the raw spectrogram shown in Figure 3.10.

1672 Additionally, tracks are required to have a minimum length and slope to be considered
 1673 potential CRES tracks rather than random noise fluctuations.

1674 The resulting output of the STF is a collection of track objects that consist of the track
 1675 point objects and their properties. The final step is to calculate track-level properties
 1676 and apply cuts to reject false tracks found by the STF. This involves the fitting of a
 1677 line to the collection of track points as well as the total and average power of the track
 1678 obtained by computing the sum and mean of the points powers. The starting frequency
 1679 of the track is determined by calculating the time coordinate that intersects with the
 1680 linear fit. A cut is performed to remove all tracks that do not have a specified average
 1681 power over their duration, which helps to remove the majority of noise fluctuations that
 1682 have passed all previous cuts up to this point.

1683 Event Reconstruction

1684 After track reconstruction comes event reconstruction where the identified tracks are
 1685 grouped into events that correspond to the trajectory of a single electron in the trap. This
 1686 procedure attempts to match tracks head to tail by checking if the start and end times
 1687 of a pair of tracks falls within a certain tolerance. This tolerance is a configurable
 1688 parameter that can be tuned to an optimal value using Monte Carlo simulations of events
 1689 in the Phase II apparatus.

1690 After the event building procedure has completed there remains a small likelihood
1691 that false tracks have made it through to the event reconstruction stage. Typically, cuts
1692 at the track level are able to remove 95% of the false tracks identified by the STF, which
1693 leads to a significant number of false tracks at the event building stage. However, the
1694 additional event-level information makes it possible to reject events that contain these
1695 false tracks with a high degree of confidence.

1696 Two event level features are associated with events caused by real electrons — the
1697 duration of the first track as well as the number of tracks in the event. Real electrons
1698 tend to have event structures with longer first tracks and a higher number of total tracks.
1699 Based on the values of these two criteria, a minimum threshold on the average power in
1700 the first track was configured to reject false events. The average power in the first track
1701 was chosen due to the critical nature of the starting frequency of the first track in an
1702 event to the krypton and tritium spectrum analyses.

1703 **3.3.3 Results from Phase II**

1704 The main result from Phase II was the measurement of the tritium beta-decay spectrum
1705 using CRES, which lead to the first neutrino mass limit with CRES. However, Phase
1706 II also included a significant ^{83m}Kr measurement campaign to understand important
1707 systematics relevant to the tritium spectrum measurement, but also to understanding the
1708 fundamentals of the CRES technique itself. This required high-resolution measurements
1709 of the ^{83m}Kr internal-conversion spectrum [57], which is an interesting science result in
1710 its own right.

1711 The results from Phase II represents a significant effort from the entire Project 8
1712 collaboration over several years. Because the focus of my contributions to Project 8 is
1713 directed towards the research and development efforts for the Phase III experiments, the
1714 goal in this section is not to provide a detailed description of the analyses that lead to
1715 the Phase II results. Rather, I will provide brief descriptions of a few plots representative
1716 of the main results from Phase II.

1717 **Measurements with Krypton**

1718 Measurements with krypton were a key calibration tool for Phase II of the experiment and
1719 will continue to be useful in Phase III. In the context of Project 8 krypton measurements
1720 refers to CRES measurements of the internal-conversion spectrum of the metastable state
1721 of krypton-83, ^{83m}Kr , produced by electron capture decays of ^{83}Rb . A supply of ^{83}Rb

1722 was built into the Phase II apparatus gas system that supplied the CRES cell with ^{83m}Kr
1723 via emanation.

1724 The ^{83m}Kr internal-conversion spectrum consists of several lines based on the orbital
1725 of the electron ejected during the decay. The conversion lines useful to Project 8 are
1726 those that emit electrons with kinetic energies that fall inside the detectable frequency
1727 bandwidth of the Phase II apparatus. These are the K; L2 and L3; M2 and M3; and N2
1728 and N3 lines with kinetic energies of 17.8 keV, \approx 30.4 keV, \approx 31.9 keV, and \approx 32.1 keV,
1729 respectively. The different energies of the lines allow a onw to test the linearity of the
1730 relationship between kinetic energy and frequency across the range of frequencies covered
1731 by the continuous tritium spectrum.

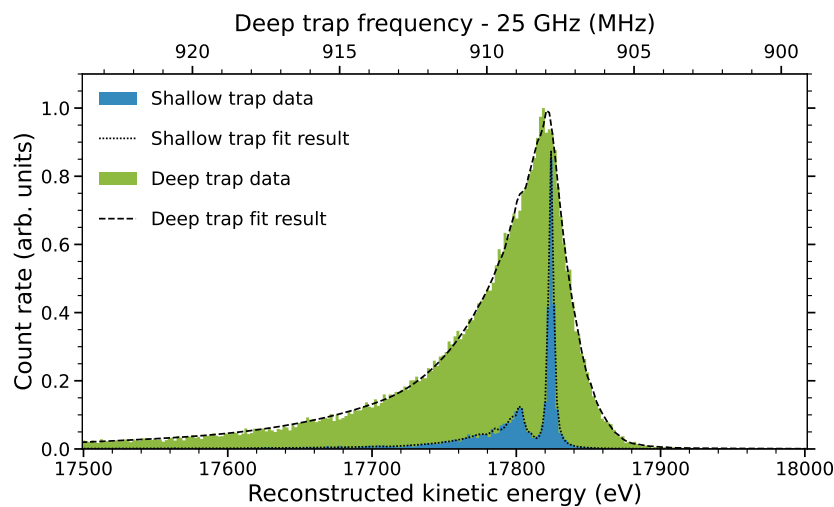


Figure 3.12. Fits to the measured 17.8-keV ^{83m}Kr conversion line using the deep and shallow trap configurations.

1732 Numerous detector related effects relevant to the tritium analysis can be characterized
1733 by measuring the shape of the krypton spectrum. Specific examples include variations
1734 in the magnetic field as a function of the radial position of the electron, variation in
1735 the magnetic field caused by the trap shape, variation in the average magnetic field for
1736 electrons with different pitch angles, and the effect of missing tracks due to scattering.
1737 These spectrum shape measurements focused on the 17.8-keV krypton line and utilized
1738 different trap geometries based on the particular goal of the dataset (see Figure 3.12).

1739 Krypton measurements with a shallow trap allow for high energy resolution, since
1740 variation in frequency due to pitch angle differences is sharply reduced in the shallow
1741 trap configuration. With this trap the main 17.8-keV peak of the conversion spectrum is
1742 clearly visible along with additional satellite peaks at lower energy, which correspond to

1743 the shakeup/shakeoff spectrum of the decay. The high accuracy of the fit demonstrates a
 1744 high degree of understanding of the CRES systematics.

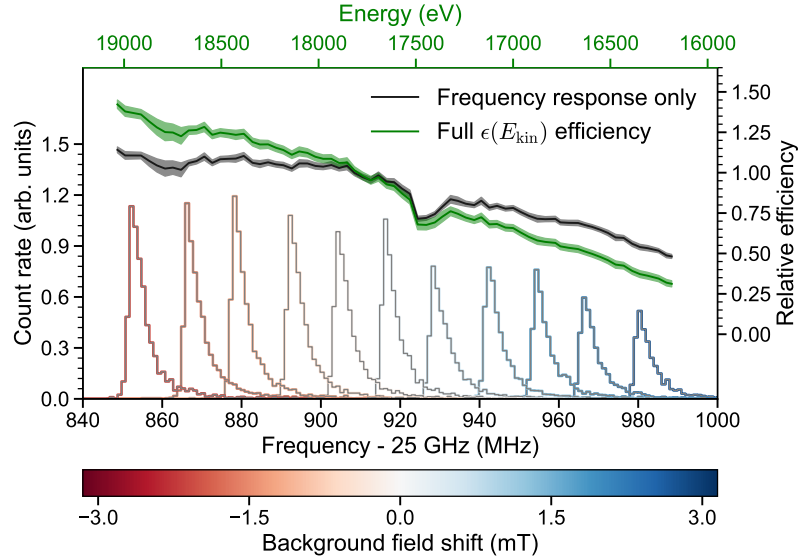


Figure 3.13. Measurements of the 17.8-keV ^{83m}Kr line using the deep trap configuration for different values of the magnetic field from the field shifting solenoid.

1745 The broadening of the krypton spectrum seen for the deeper track is due to the large
 1746 range of electron pitch angles that can be trapped. Furthermore, with a deeper trap
 1747 there is a larger parameter space of electron that could be produced with pitch angles
 1748 that are trappable but not visible in the time-frequency spectrogram. These electrons
 1749 live in the trap and can scatter multiple times before randomly scattering to a visible
 1750 pitch angle. This leads to one or more missing tracks earlier in the event, which leads to
 1751 a misreconstruction of the true starting frequency. By measuring the krypton spectrum
 1752 shape in the same trap used to detect tritium events, the effect this has on the spectrum
 1753 shape can be characterized to mitigate its impact on the tritium measurements.

1754 Changes in the Krypton spectrum shape as a function of CRES frequency were
 1755 used to study the detection efficiency of the Phase II apparatus. Variations in the
 1756 detection efficiency as a function of frequency directly influences the measured shape of
 1757 the continuous tritium spectrum, which can lead to errors in the neutrino mass estimate
 1758 if not modeled appropriately. Using the field shifting solenoid the cyclotron frequency
 1759 of the krypton 17.83 keV line was shifted across the full frequency range of the tritium
 1760 spectrum data (see Figure 3.13). Variations in the deep trap krypton spectrum shape
 1761 can be used to infer the detection efficiency as a function of frequency and correct for

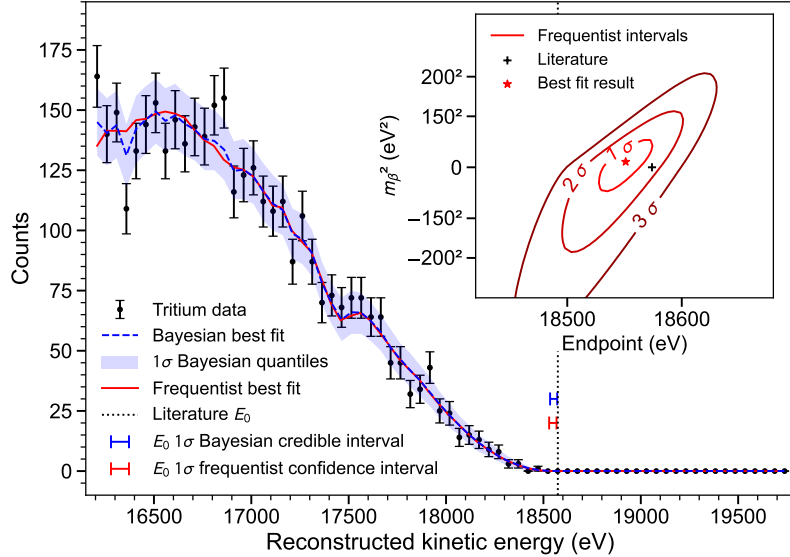


Figure 3.14. The measured tritium spectrum from Phase II with Bayesian and frequentist fits.

1762 this affect in the tritium measurements.

1763 Tritium Spectrum and Neutrino Mass Results

1764 The tritium measurement campaign resulted in the collection of 82 days of detector
 1765 live time during which 3770 total tritium events were detected. The track and event
 1766 reconstruction analysis extracted the starting frequencies of these tritium events, which
 1767 were used to build a frequency spectrum of tritium beta-decays. The resulting frequency
 1768 spectrum was then converted to an energy spectrum using the information gleaned from
 1769 the krypton measurement campaign to obtain the tritium beta-decay spectrum (see
 1770 Figure 3.14).

1771 CRES is inherently a very low background technique with the dominant source of
 1772 noise being random RF fluctuations. Monte Carlo simulations backed validated using
 1773 measurements of the RF noise background were used to set track and event cuts to
 1774 guarantee that zero false events would occur over the duration of the experiment with
 1775 90% confidence. Notably, the measured spectrum has zero events beyond the tritium
 1776 spectrum endpoint, which allows us to constrain the background rate in the Phase II
 1777 apparatus to less than 3×10^{-10} counts/ev/s. Achieving a low background is critical for
 1778 future neutrino mass experiments that seek to measure the neutrino mass with less than
 1779 100 meV sensitivity.

1780 Bayesian and frequentist based fits to the measured tritium spectrum, incorporating

1781 information gained about CRES systematics from the krypton measurements, were
1782 performed to extract upper limits on the tritium beta-decay spectrum endpoint as well as
1783 the neutrino mass. The estimated spectrum endpoints are 18553^{+18}_{-19} eV for the Bayesian
1784 analysis and 18548^{+19}_{-19} eV for the frequentist analysis. The quoted uncertainties are
1785 $1-\sigma$, and both results are within $2-\sigma$ of the literature endpoint value of 15574 eV. The
1786 estimated neutrino mass for both results is consistent with $m_\beta^2 = 0$. The 90% confidence
1787 upper limits for the Bayesian analysis is $m_\beta < 155$ eV/c² and $m_\beta < 152$ eV/c for the
1788 frequentist analysis.

1789 Though the neutrino mass results from Phase II are not competitive with KATRIN
1790 the experiment was a promising first step towards the development of more precise
1791 neutrino mass measurements using CRES. The low-background and high-resolution
1792 achievable with krypton measurements are promising features of the technique that were
1793 demonstrated with the Phase II apparatus. As new technologies are developed to enable
1794 CRES measurements in larger volume, many of the lessons learned from Phase II will
1795 continue to influence the operation and design of future experiments.

1796 **3.4 Phase III R&D: Antenna Array CRES**

1797 The goal of Phase III in the Project 8 experimental program is to develop the technologies
1798 and expertise required to build an experiment that uses CRES to measure the neutrino
1799 mass with a target sensitivity of 40 meV. One of the key technologies is a method for
1800 performing high resolution CRES measurements in a large volume, which allows one to
1801 observe a sufficient quantity of tritium to measure the low-activity endpoint region of
1802 the tritium spectrum.

1803 **3.4.1 The Basic Approach**

1804 One possible approach, suggested in the original CRES publication [40], is to use many
1805 antennas to surround a volume of tritium gas in a magnetic field (see Figure 3.15). When
1806 a decay occurs the electron will begin to emit cyclotron radiation that can be collected
1807 by the array and used to perform CRES. Each antenna in the array collects only a small
1808 fraction of the electron's signal power, which is less than 1 fW for a 18.6 keV kinetic
1809 energy electron in a 1 T magnetic field. Scaling to large volumes with the antenna
1810 array approach is accomplished by increasing the number of antennas in the array, which
1811 increases the volume under observation proportionally, so that a sufficient population of

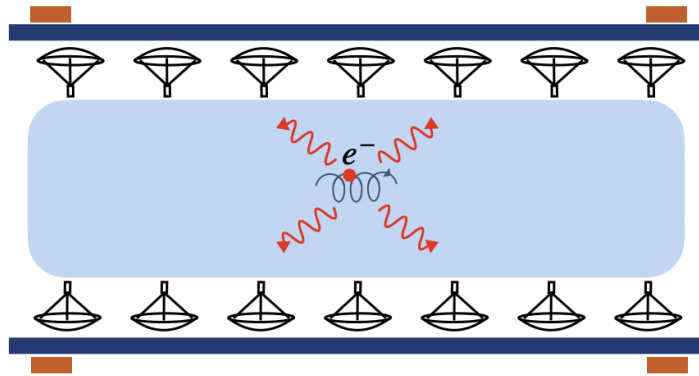


Figure 3.15. A cartoon illustration of the basics of the antenna array CRES technique.

1812 tritium atoms can be observed to measure the tritium spectrum endpoint shape.

1813 Several features of the antenna array approach make it an attractive candidate technol-
 1814 ogy for a large volume experiment. One example is the accurate position reconstruc-
 1815 tion made possible by the multichannel nature of the array. Using techniques like digital
 1816 beamforming it is possible to estimate the radial and azimuthal positions of the electron
 1817 in the magnetic trap with a precision significantly less than the size of the cyclotron
 1818 wavelength. This capability allows one to perform event-by-event estimations of the
 1819 magnetic field experienced by an electron, which is crucial to achieving high energy
 1820 resolution with the CRES technique.

1821 The easy availability of position information with the antennas array approach
 1822 is potentially a unique advantage that provides significant flexibility in the magnetic
 1823 field uniformity requirements compared to other proposed approaches to large volume
 1824 CRES (see Chapter 6). Spatial discrimination using digital beamforming leads to pileup
 1825 reduction, which helps to reduce the potential of background events caused by missing
 1826 tracks or by incorrectly clustering a group of tracks into an event. Limits on the
 1827 background rate for a neutrino mass measurement with 40 meV sensitivity are stringent
 1828 and the total activity of the tritium source for such an experiment is gigantic relative to
 1829 the activity near the endpoint. Thus, pileup discrimination could be an important tool
 1830 for a large scale CRES experiment.

1831 Another beneficial quality of the antenna array approach is that the volume of the
 1832 experiment can be scaled independent of frequency by simply adding more antennas to
 1833 the array (see Figure 3.19). Resonant cavities, the proposed alternative large volume
 1834 CRES technology, are ideally operated in magnetic fields that cause electrons to move
 1835 with cyclotron frequencies near the fundamental cavity resonance, to avoid complex
 1836 coupling of the electron to many cavity modes simultaneously. This leads to a coupling

1837 between the cavity volume and the magnetic field magnitude, which forces one to lower
1838 the magnetic field in order to increase the experiment scale. Whereas, for antenna arrays,
1839 in principle there is no physical limitation on the size of the antenna array that can be
1840 used at a particular magnetic field. However, the nature of scaling an antenna array
1841 based experiment leads to rapidly increasing cost and complexity due to the large number
1842 of antennas, amplifiers, and data streams that require substantial computer processing
1843 power to effectively analyze.

1844 **3.4.2 The FSCD: Free-space CRES Demonstrator**

1845 The complexity of the antenna array CRES technique requires the construction of a
1846 small scale demonstration experiment to develop an understanding of technique itself and
1847 relevant systematics. Without a demonstrator experiment it is not possible to sufficiently
1848 retire the technical risks associated with the full-scale experiment. Therefore, Phase
1849 III of the Project 8 experimental program is primarily focused on the development and
1850 operation of demonstrator experiments to inform the design of the Phase IV experiment.

1851 The demonstrator experiment developed for antenna array CRES in Phase III is called
1852 the Free-space CRES Demonstrator or FSCD. The FSCD is intended as a demonstration
1853 of antenna array CRES, but is also a capable neutrino mass measurement experiment
1854 in its own right, with a target neutrino mass sensitivity of a few eV using a molecular
1855 tritium source.

1856 **Magnetic Field**

1857 The background magnetic field for the FSCD is provided by a hospital-grade MRI magnet
1858 (see Figure 3.16). The magnet produces a magnetic field of approximately 0.958 T, which
1859 corresponds to a tritium spectrum endpoint frequency of approximately 25.86 GHz. The
1860 magnet is installed in the Project 8 laboratory located at the University of Washington,
1861 Seattle, and is shimmed to produce a uniform magnetic field with variations on the
1862 ppm-level. Measurements of the magnetic field non-uniformities are performed using a
1863 NMR probe and rotational gantry to capture measurements of the magnetic field around
1864 an elliptical surface in the center of the MRI magnet. During the operation of the FSCD
1865 an array of Hall or NMR magnetometers would be used to periodically measure the
1866 magnetic field to monitor its time stability.

1867 Inside the field of the MRI magnet additional electromagnets would be installed that
1868 provide the capability to shift the value of the background magnetic field and produce



Figure 3.16. An image of the MRI magnet installed in the Project 8 laboratory at the University of Washington, Seattle.

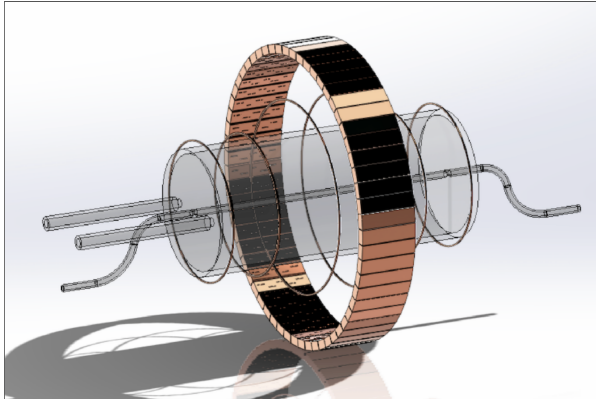
1869 a magnetic trap. Shifting the background magnetic field by a few μ T lets one control
 1870 the cyclotron frequencies of electrons with a fixed kinetic energy, which is key to an
 1871 effective calibration of the FSCD. The preferred calibration method for the FSCD is
 1872 a mono-energetic electron gun that can inject electrons into the magnetic trap with a
 1873 known kinetic energy. In combination with the field shifting magnet, one can vary the
 1874 cyclotron frequencies of the electrons to measure the response of the antenna array as a
 1875 function of the radiation frequency and electron position. This procedure characterizes
 1876 the response of the antenna array and provides further information on magnetic field
 1877 uniformity, which is important to achieving good energy resolution.

1878 The design of the magnetic trap is absolutely critical to the success of a CRES
 1879 experiment. The ideal shape is the perfect magnetic box, which has a flat bottom and
 1880 step function walls. Any variation in the average magnetic field experienced by an
 1881 electron leads to changes in the cyclotron frequency that can make determining the true
 1882 starting kinetic energy more difficult. This includes changes in the magnetic field caused
 1883 by the walls of the magnetic trap as well as radial magnetic field variations.

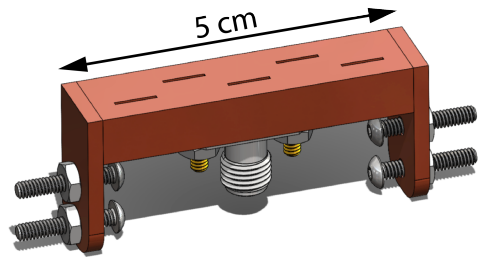
1884 The ideal box trap is completely uniform and has infinitely steep walls that cause
 1885 no change in the electron's cyclotron frequency as it is reflected from the trap wall,
 1886 however, such a trap cannot be made from any combination of magnetic coils since it
 1887 violates Maxwell's equations. One of the goals of magnetic trap design is to identify the
 1888 configuration of coils that produces a trap that approximates the perfect box trap as
 1889 closely as possible.

1890 **Antenna Array**

1891 The canonical antenna array design for CRES is a uniform cylindrical array of antennas
1892 that surrounds the magnetic trap volume. Since the FSCD is a demonstrator experiment,
1893 the antenna array design is the simplest form of the uniform cylindrical array, which is a
single circular ring of antennas with a diameter of 20 cm (see Figure 3.17). Along this



(a)



(b)

Figure 3.17. (a) A model of the FSCD antenna array, magnetic trap, and tritium containment vessel design.(b) A more detailed model of a prototype design for the 5-slot waveguide antenna design.

1894
1895 circle are sixty slotted waveguide antennas that fully populate the available space around
1896 the array circumference. In order to maximize the power collected from each electron
1897 it is optimal to cover as large a fraction of the solid angle around the magnetic trap as
1898 possible.

1899 The distance between antennas around the circumference of the array is proportional
1900 to the wavelength of the cyclotron radiation. Therefore, maximizing the solid angle
1901 coverage of the array, while minimizing channel count to keep the hardware and data
1902 acquisition costs manageable, biases one towards smaller array diameters. Antenna
1903 near-field effects limit the minimum diameter of the array for a given antenna design
1904 since the radiation from electrons that are too close to the array cannot be detected
1905 due to destructive interference caused by path-length differences from the electron to
1906 different points on the antenna surface.

1907 Slotted waveguide antennas are used in the FSCD antenna array due to their high
1908 efficiency and low loss, which comes from the lack of dielectric materials in the antenna
1909 structure. Coupling to the waveguide can be performed with a coaxial cable connected
1910 at the center or on either end of the waveguide. One of the drawbacks of waveguide

1911 antennas is the large amount of space required to fit them inside the limited MRI magnet
1912 volume. Alternative antenna designs, constructed from microstrip printed circuit boards
1913 require significantly less space at the cost of slightly higher energy loss in the antenna
1914 structure.

1915 The FSCD antenna design is a 5 cm long segment of WR-34 waveguide with 5 vertical
1916 slots cut into the side. The distance between slots along the length of the waveguide is
1917 a half wavelength for optimal power combination between the individual antenna slots.
1918 Each slot is offset from the center of the antenna face a small distance in order to most
1919 effectively couple the slot to waveguide modes inside the antenna.

1920 The passive power combination achieved by placing 5 slots in a single waveguide is a
1921 compromise intended to reduce the cost and complexity of the antenna array system.
1922 Each additional channel in the array requires it's own cryogenic amplifier and also increase
1923 the required computer power to process the raw data collected by digitizing each channel.
1924 Passive summation, achieved by combining antennas into arrays axially, reduces the array
1925 channel count at the cost of losses from imperfect passive combination. Imperfect passive
1926 combination is caused by effects such as re-radiation of energy from and destructive
1927 interference between slots in the waveguide antenna.

1928 Interference and re-radiation eventually limit the achievable the axial extent of passive
1929 power combination. The 5-slot designed developed for the FSCD is optimized to minimize
1930 the impact of these losses while achieving the maximum amount of axial coverage with a
1931 single ring of antennas. Scaling beyond the volume covered by a single ring of antennas is
1932 achieved by stacking additional rings of antennas together to cover a larger trap volume
1933 for a higher statistics measurement of the tritium spectrum endpoint region. A likely
1934 scenario for the FSCD experiment involves a staged experiment approach, where first
1935 a series of measurements is performed using only a single ring of antennas followed by
1936 experiments that add additional rings to the FSCD. The goal would be to first understand
1937 the principles of antenna array CRES using the simplest possible experiment, before
1938 attempting to scale the technique by expanding the antenna array size.

1939 **Tritium Source**

1940 While the primary purpose of the FSCD is as a technology demonstrator, it is unlikely
1941 for the collaboration to gain the required confidence in the antenna array CRES tech-
1942 nique to perform neutrino mass measurements at the 40 meV sensitivity level without
1943 an intermediate scale measurement of the neutrino mass using antenna array CRES.
1944 Therefore, the FSCD has an additional scientific goal of measuring the neutrino mass

1945 with a rough sensitivity goal of a few eV. This level of precision is achievable using a
1946 source of molecular tritium with a volume of approximately 1 L at a density comparable
1947 to potential Phase IV scenarios.

1948 Unlike previous CRES experiments, where the tritium source could be co-located
1949 with the receiving antenna inside a waveguide transmission line, the tritium source
1950 in the FSCD is thermally isolated from the antenna array to avoid freeze-out of the
1951 tritium molecules. The tiny radiation power emitted by electrons requires a system noise
1952 temperature of ≈ 10 K or less, in order to detect events at a high enough efficiency to
1953 reach the neutrino mass sensitivity goals of the experiment. Achieving a system noise of
1954 10 K requires that the antenna array and amplifiers operate at cryogenic, liquid helium
1955 temperatures of ≈ 4 K, which significantly lowers the vapor pressure of molecular tritium.
1956 By keeping the molecular tritium isolated in an RF-transparent vessel the tritium gas can
1957 be kept at a relatively warmer temperature in the range of 30 K to avoid the accumulation
1958 of tritium on the experiment surfaces.

1959 **Data Acquisition and Reconstruction**

1960 A fundamental change in the data acquisition system for the FSCD is the shift from
1961 single to multi-channel reconstruction. This transition results in a significant increase in
1962 the data-generation rate, which is linearly related to the number of independent channels
1963 in the array. The larger data volume coincides with an increased demand for computer
1964 processing power based on the need for more precise signal reconstruction algorithms
1965 driven by the FSCD and Phase IV sensitivity goals. Therefore, the data acquisition
1966 system for the FSCD is likely to represent a significantly larger fraction of the experiment
1967 cost and complexity than previous CRES experiments.

1968 Each antenna in the array is connected to a cryogenic amplifier and down-converted
1969 from the 26 GHz CRES frequency using an IQ-mixer to reduce the size of the analysis
1970 window in which the tritium spectrum is measured. Using an LO with a frequency of
1971 approximately 25.80 GHz the antenna array signals can be digitized at a rate of 200 MHz,
1972 which is sufficient bandwidth to resolve the complete sideband spectrum produced by
1973 axial oscillations of electrons in the FSCD magnetic trap.

1974 Direct storage of the raw FSCD antenna array data is undesirable, since the estimated
1975 amount of raw data generated is $O(1)$ exabyte per year. The management and storage
1976 of such a large dataset is infeasible for a demonstrator experiment on the scale of the
1977 FSCD and would represent a large fraction of the budget for a Phase IV scale antenna
1978 array based CRES experiment. Therefore, a sub-goal of the FSCD experiment is the

¹⁹⁷⁹ development of real-time reconstruction methods that could reduce the raw data volume
¹⁹⁸⁰ by detecting and reconstructing CRES events in real-time. The ultimate goal would be
¹⁹⁸¹ a complete real-time reconstruction pipeline that takes raw voltages samples from the
¹⁹⁸² antenna array and returns estimates for the starting kinetic energies of CRES events in
¹⁹⁸³ the data.

¹⁹⁸⁴ The feasibility of a real-time reconstruction pipeline rests on the development of
¹⁹⁸⁵ computationally efficient algorithms that can be implemented without the need for
¹⁹⁸⁶ enormous computing resources. One challenge with the antenna array approach is that
¹⁹⁸⁷ the small radiation power of a single electron is distributed between each channel in
¹⁹⁸⁸ the array, such that reconstruction using only the information in a single channel is not
¹⁹⁸⁹ possible. Therefore, the simply performing the initial step in reconstruction — signal
¹⁹⁹⁰ detection — requires orders of magnitude more computational power than previous CRES
¹⁹⁹¹ experiments. This operation will then be followed by other, potentially more expensive,
¹⁹⁹² reconstruction steps that are required in order to determine the kinetic energy of the
¹⁹⁹³ electron.

¹⁹⁹⁴ **3.5 Pilot-scale Experiments**

¹⁹⁹⁵ **3.5.1 Choice of Frequency**

¹⁹⁹⁶ The optimal CRES frequency for Project 8 is that which can reach our target sensitivity
¹⁹⁹⁷ of 40 meV, while minimizing the cost and complexity of the overall experiment. The
¹⁹⁹⁸ magnitude of the background magnetic field determines the cyclotron frequency, which
¹⁹⁹⁹ affects the entirety of the CRES detection system design, specifying the operating
²⁰⁰⁰ frequency of the CRES experiments is one of the first steps towards developing a full
²⁰⁰¹ design.

²⁰⁰² **Scaling Laws**

²⁰⁰³ The Phase I and II experiments utilized a background magnetic field of 0.959 T provided
²⁰⁰⁴ by an NMR magnet. This magnetic field was selected primarily for convenience, however,
²⁰⁰⁵ the cyclotron frequencies for electrons near the tritium endpoint in a 0.959 T field ranges
²⁰⁰⁶ from 25 to 26 GHz, which is within the standard RF Ka-band. Therefore, microwave
²⁰⁰⁷ electronics specialized for these frequencies are easily obtainable for relatively low cost.
²⁰⁰⁸ The operating frequency for the large-scale experiments must be selected in a more
²⁰⁰⁹ rigorous manner due to the increased scale and complexity of the systems as well as the

2010 requirements of the 40 meV neutrino mass science goal.

2011 There is a bias towards lower frequencies in a large-volume experiment, due to the
2012 direct relationship between wavelength and the physical size of the compatible RF
2013 components like antennas and cavities. With a longer wavelength more volume can
2014 be surrounded by an array with fewer antennas, which reduces hardware and data-
2015 processing costs. Additionally, the size of a cavity experiment is directly proportional
2016 to the wavelength since this sets the physical dimensions of the cavity. Furthermore,
2017 it is easier to engineer a magnet that provides a uniform magnetic field across several
2018 cubic-meters of space at lower magnetic fields, which provides advantages in terms of
2019 cost-reduction and field uniformity.

2020 A concern with lower magnetic fields and frequencies is the scaling of the Larmour
2021 power equation, which is proportional to the square of the frequency. Naively, one would
2022 predict that the SNR would decrease with lower fields, however, two additional scaling
2023 laws that affect the noise power also come into play. Noise power is directly proportional
2024 to the required bandwidth, which decreases linearly with the magnetic field. Furthermore,
2025 at lower frequencies it is possible to purchase amplifiers with lower noise temperatures
2026 until approximately 300 MHz at which point this relationship tends to flatten. Therefore,
2027 it is expected that the SNR remains approximately constant as the frequency decreases.

2028 The SNR directly impacts the overall efficiency of the experiment through its effects
2029 on signal detection and energy resolution. Thus, the expectation that SNR remains the
2030 same at lower frequencies clearly biases large-scale experiments in this direction. One
2031 drawback of lower magnetic fields is the increased influence of external magnetic fields
2032 on the experiment. This includes magnetic fields from the building materials as well as
2033 variations in the earth's magnetic field. To deal with these affects a suitable magnetic
2034 field correction system will need to be devised, which includes constant monitoring of
2035 external fields.

2036 **Atomic Tritium Considerations**

2037 The pilot-scale experiments will be the first Project 8 experiments to combine CRES with
2038 atomic tritium, therefore, the optimal frequency should take into account the affect of the
2039 background magnetic field on the atom trap. The primary influence of the background
2040 field magnitude is through the rate of dipolar spin-flips caused by a spin exchange
2041 interaction between trapped atoms [58].

2042 Atomic tritium is a simple quantum system with a hyperfine structure given by the
2043 addition of the nuclear and atomic spins. The addition of two spins leads to a hyperfine

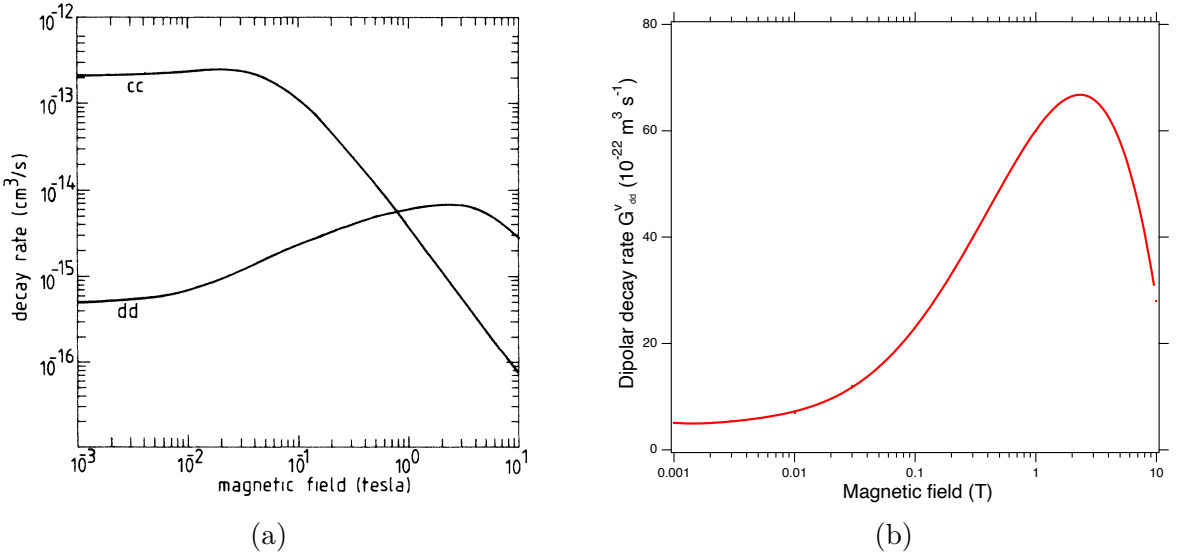


Figure 3.18. (a) A plot of the decay rate for the two-body dipolar spin exchange interaction for cc and dd state. (b) A plot of the decay rate of the dipolar spin exchange interaction for d+d states as a function of magnetic field magnitude. Lowering the magnetic field is key for reducing the losses from this interaction.

2044 structure with four states in the (m_s, m_I) basis [59]. The states with atomic spins directed
 2045 anti-parallel to the magnetic field have $m_s = -1/2$ and are labeled as the a and b states.
 2046 The a and b states are colloquially known as high-field seeking states, since their energy is
 2047 minimized when in regions of higher magnetic field. This leads to losses in the magnetic
 2048 trap as these atoms are drawn to higher fields away from the trap center. Alternatively,
 2049 the c and d states, with atomic spin $m_s = +1/2$, minimize their energy in low magnetic
 2050 fields because of the parallel alignment between spin and the magnetic field. Therefore,
 2051 these low-field seeking states tend to stay trapped significantly longer than the high-field
 2052 seeking states.

2053 It would be advantageous to prepare tritium atoms in purely c and d states before
 2054 trapping, however, even in this case losses still occur due to dipolar interactions between
 2055 pairs of c and d states leading to flipped atomic spins and subsequent losses from high-field
 2056 seeking atoms. The rate of these interactions depends on the magnitude of the background
 2057 magnetic field and is maximal for dd interactions around 1 T (see Figure 3.18). The rate
 2058 of losses from these interactions at 1 T requires atomic tritium production at a rate two
 2059 orders of magnitude larger than at 0.1 T, thus, requirements on the whole atomic tritium
 2060 system are significantly relaxed at lower magnetic fields, which provides an additional
 2061 argument for transitioning to lower frequencies with the pilot-scale experiments.

2062 3.5.2 Pilot-scale Experiment Concepts

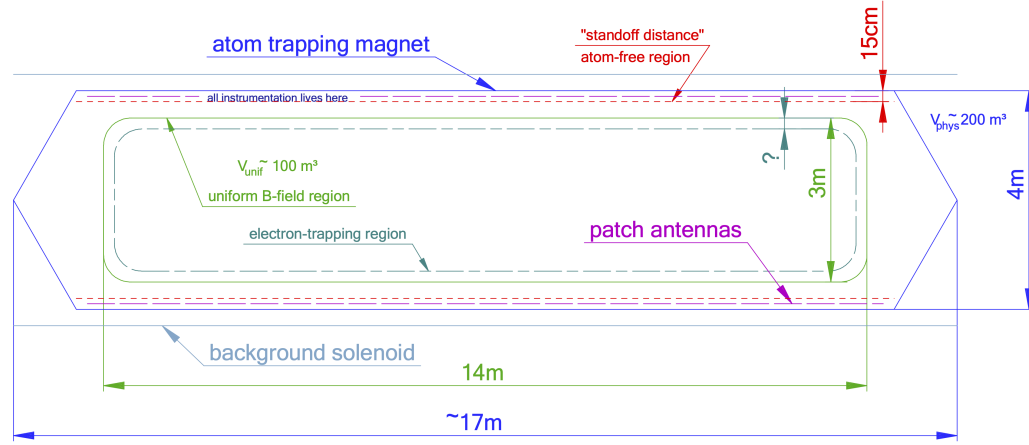


Figure 3.19. A conceptual sketch of a large-volume antenna array based CRES experiment to measure the neutrino mass.

2063 While the pilot-scale experiments are still in the early stages, enough is known to
 2064 sketch the general features of these experiments at the conceptual level.

2065 Pilot-scale Antenna Array CRES Experiment Concept

2066 A conceptual design for an antenna-based CRES experiment is shown in Figure 3.19.
 2067 A large solenoid magnet provides a uniform background magnetic field less than 0.1 T
 2068 in magnitude. Inside this region is the atom trapping magnet that generates a high
 2069 magnetic field at the walls, which decays exponentially towards the central region. Known
 2070 magnet designs that produce suitable atom trapping fields include Ioffe-Prichard traps,
 2071 which use conducting coils, as well as a Halbach array made from permanent magnets.
 2072 Either magnet choice produces a region of high magnetic fields, which excludes atoms
 2073 and allows for the placement of antennas inside the experiment.

2074 Inside this region an array of microstrip patch antennas is inserted to collect the
 2075 cyclotron radiation without providing a surface for atomic tritium recombination. Due
 2076 to the lower frequency of cyclotron radiation antennas of a larger size can be used,
 2077 which lowers the total number of antennas required to observe the experiment volume.
 2078 Because of this scaling, the lower frequency experiment uses a similar number of antennas
 2079 compared to a much smaller demonstrator experiment with a 1 T magnetic field.

2080 The atomic tritium beamline that supplies fresh tritium atoms to the experiment is
 2081 not shown in the figure. The general configuration would matches the one shown for the
 2082 pilot-scale cavity experiment (see Figure 3.20).

2083 **Pilot-scale Cavity CRES Experiment Concept**

2084 The pilot-scale cavity experiment includes both an atomic tritium system and cavity
2085 CRES system. The atomic system consists of a thermal atom cracker located at the
2086 start of an evaporatively cooled atomic beamline. The atomic tritium system provides a
2087 supply of tritium atoms to the trap with temperatures on the order of a few mK. Atoms
2088 at this temperature can be trapped magneto-gravitationally, which is the reason for the
2089 vertical orientation of the cavity. At these low magnetic fields the trapping requirements
2090 for electrons and atoms differ enough such that it is advantageous to decouple the the
2091 trapping potentials to avoid radioactive heating of the tritium atoms from excess trapped
2092 electrons. Electron trapping is provided by a set of magnetic pinch coils at the top and
2093 bottom of the cavity and a multi-pole Ioffe or Halbach magnet serves to contain the
2094 atoms.

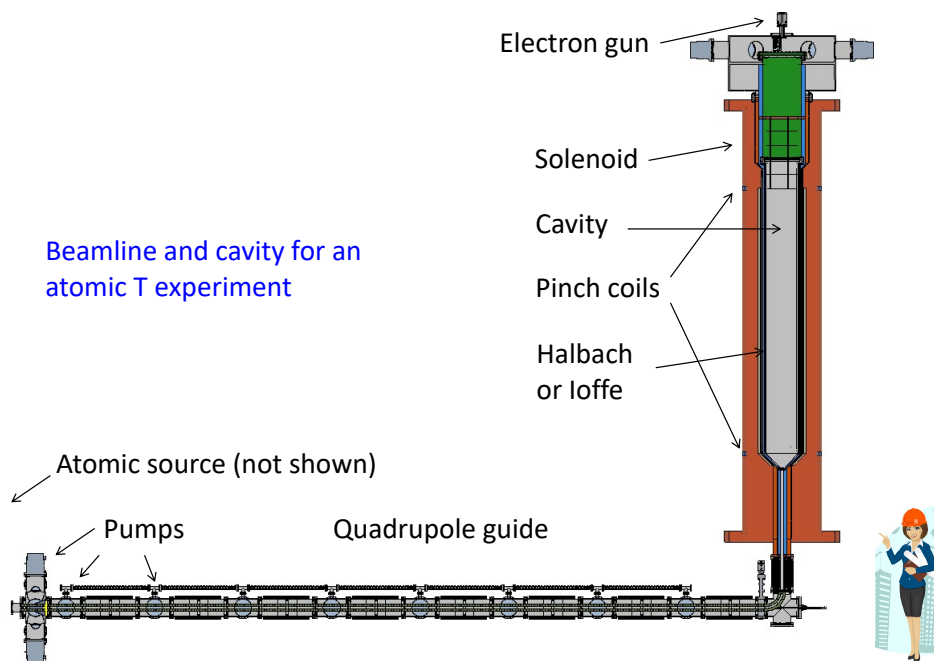


Figure 3.20. A conceptual sketch of a pilot-scale cavity CRES experiment with an atomic tritium beamline.

2095 The cavity design for the pilot-scale experiment consists of a large cylindrical cavity
2096 with a TE011 resonance of 325 MHz. Such a cavity is truly enormous, with a diameter
2097 of approximately 1.2 m and a height of 11 m. When an electron is produced inside
2098 the cavity with a cyclotron frequency that matches the TE011 resonant frequency it's
2099 cyclotron orbit couples the electron to the TE011, which drives a resonance in the cavity.
2100 These resonant fields can be read-out using an appropriate cavity coupling mechanism

2101 located at the center of the cavity. For more information on the cavity approach to
2102 CRES see Chapter 6.

2103 The bottom of the cavity has a cone termination to match the contour of the atom
2104 trapping magnet. This shape still allows for TE011 resonances with high internal Qs,
2105 which are required for good SNR in the cavity experiment. A small opening in the bottom
2106 of the cone serves as an entry point for the tritium atoms. To allow for calibration of
2107 the magnetic field inhomogeneities with an electron gun, the top of the cavity is left
2108 nearly completely open. Normally, this would drastically lower the Q-factor of the TE011
2109 mode, but a specially configured coaxial partition is inserted at the top. This termination
2110 scheme is designed to act as a perfect short for the TE011 mode since the circular shape
2111 of the partition matches the electric field boundary conditions for the TE011 mode.
2112 Simulations with HFSS have confirmed that this design results in a high quality TE011
2113 resonance despite the nearly completely open end.

2114 3.6 Phase IV

2115 The baseline CRES technology being pursued by the Project 8 collaboration are resonant
2116 cavities, which, due to their geometric properties, simple CRES signal structure, and low
2117 channel count, appear to be the better option for Phase IV. The current knowledge of the
2118 antenna array CRES approach reveals no technical obstacles that would preclude it as a
2119 baseline technology for Phase IV though it would most certainly be significantly more
2120 expensive. Therefore, antenna arrays represent a fallback approach if resonant cavities
2121 prove infeasible.

2122 The sensitivity of the pilot-scale atomic tritium experiment is estimated to be on
2123 the order of 0.1 eV, which means that increasing the sensitivity to reach the Phase IV
2124 goal will require an even larger experiment. Because of the direct coupling between the
2125 RF characteristics of a cavity and its geometry, the baseline plan is to build multiple
2126 copies of the pilot-scale experiment (see Figure 3.21) to obtain the required amount of
2127 volume rather than increase the size of the cavity beyond the pilot-scale. The built-in
2128 redundancy of this approach is useful in the sense that the experiment has no single
2129 point of failure, additionally, building several copies of the a pilot-scale experiment will
2130 minimize new engineering and design effort.

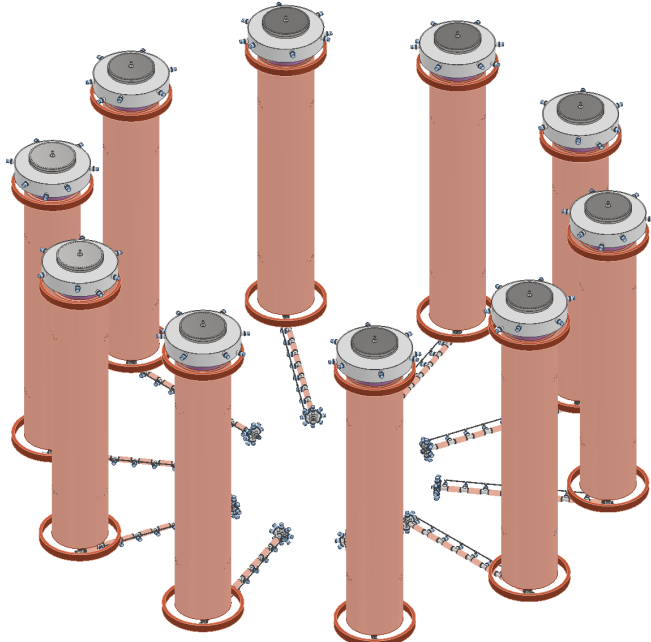


Figure 3.21. An illustration of a possible arrangement of ten pilot-scale cavity experiments for Phase IV. The experiments are arranged in a circle with an approximate diameter of 50 meters. Each atomic beamline connected to the bottom of each cavity is approximately 10 m in length. The cavities themselves are designed to operate at 325 MHz and are approximately 11 m tall. The circular arrangement of cavities has some advantages when it comes to cancellation of fringe fields from neighboring magnets, which is important due to the small magnetic field magnitudes consistent with these CRES frequencies. The advantage of ten independent atomic sources and cavities is that there is no single point of failure for the experiment. If an experiment goes down for repairs the other nine may continue running. Figure courtesy of Michael Huehn at UW-Seattle.

2131 **Chapter 4** |

2132 **Signal Reconstruction Techniques for An-**

2133 **tenna Array CRES and the FSCD**

2134 **4.1 Introduction**

2135 The transition from a waveguide CRES experiment to an antenna array CRES experi-
2136 ment introduces new challenges related to data acquisition, signal detection, and signal
2137 reconstruction caused by the multi-channel nature of the data. The development of signal
2138 reconstruction algorithms is crucial to the design of antenna array based experiments like
2139 the FSCD, because these algorithms directly influence the detection efficiency and energy
2140 resolution of the CRES experiment. In this Chapter I summarize my contributions to
2141 the development and analysis of signal reconstruction and detection algorithms for the
2142 FSCD experiment.

2143 In Section 4.2 I discuss the primary tool for this work, which is the Locust simulations
2144 package developed by the Project 8 experiment. Locust is used to simulate CRES events
2145 in the detector. Locust uses Kassiopeia to calculate particle trajectory solutions for
2146 electrons in the magnetic trap. The trajectories are then used to calculate the response
2147 of the antenna array to the cyclotron radiation produced by the electron, which results
2148 in signals that can be used to analyze the performance of different signal reconstruction
2149 algorithms. More recently, Project 8 has developed CREsana, which is a new simulations
2150 package that takes a more analytical approach to CRES signal simulations for antenna
2151 arrays. Although CREsana signals were not used for the signal reconstruction algorithm
2152 development detailed here, we introduce the software as it plays a role in the antenna
2153 array measurements presented in Section 5.4.

2154 In Section 4.3 I discuss the signal reconstruction and detection approaches analyzed
2155 for the FSCD experiment. In general there are two steps to signal reconstruction —
2156 detection and parameter estimation. With signal detection one is primarily concerned

2157 only with distinguishing between data that contains a signal versus data that contains only
2158 noise, whereas, with parameter estimation one is interested in extracting the kinematic
2159 parameters of the electron encoded in the cyclotron radiation signal shape. Due to
2160 the low signal power of electrons near the spectrum endpoint in the FSCD experiment,
2161 signal detection is a non-trivial problem. This is magnified by the need to maximize the
2162 detection efficiency of the experiment in order to achieve the neutrino mass sensitivity
2163 goals. My contributions to signal reconstruction analysis for the FSCD are focused on
2164 this signal detection component of reconstruction.

2165 After the discussion of various signal detection approaches, in Section 4.4 I present a
2166 more detailed analysis of the detection performance of three algorithms, which could be
2167 used to signal detection in the FSCD. This section was originally prepared for publication
2168 in JINST as a separate paper. The algorithms include a digital beamforming algorithm,
2169 a matched filter algorithm, and a neural network algorithm, which I analyze in terms of
2170 classification accuracy and estimated computational cost.

2171 **4.2 FSCD Simulations**

2172 Antenna array CRES and the FSCD requires a combination of different capabilities
2173 not often found in a single simulation tool. First of all, accurate calculations of the
2174 magneto-static fields produced by current-carrying coils are required in order to accurately
2175 model the magnetic trap and background magnets. The resulting magnetic fields must
2176 then be used to calculate the exact relativistic trajectory of electrons, which is required
2177 in order to calculate the electro-magnetic (EM) fields produced by the acceleration of
2178 the electron. Finally, the simulation has to model the interaction of the antenna and
2179 RF receiver chain with these EM-fields in order to produce the simulated voltage signals
2180 produced by the antenna array during the CRES event. At the time when Project 8 was
2181 developing this simulation capability, no single available simulation tool was known to
2182 adequately perform this suite of calculations, which prompted the development of custom
2183 simulation framework to simulate the FSCD. This simulation framework includes custom
2184 simulation tools developed by Project 8 as well as other open-source and proprietary
2185 software developed by third-parties.

2186 **4.2.1 Kassiopeia**

2187 Kassiopeia¹ is a particle tracking and static EM-field solver developed by the KATRIN
2188 collaboration for simulations of their spectrometer based on magnetic adiabatic collimation
2189 with an electrostatic filter [60]. Due to the measurement technique employed by the
2190 KATRIN collaboration, Kassiopeia is not designed to solve for the EM-fields produced by
2191 electrons in magnetic fields. However, it does provide efficient solvers for static electric
2192 and magnetic fields and charged particle trajectory solvers. Because of this, Project 8
2193 has incorporated parts of Kassiopeia into its own simulation framework.

2194 **Magnetostatic Field Solutions**

2195 The solutions to the electric and magnetic fields generated by a static configuration of
2196 charges and currents is given by Maxwell's equations in the limit where the time-dependent
2197 terms go to zero. In their static form Maxwell's equations [49] are

$$\nabla \cdot \mathbf{E} = \frac{\rho}{\epsilon_0} \quad (4.1)$$

$$\nabla \times \mathbf{E} = 0 \quad (4.2)$$

$$\nabla \cdot \mathbf{B} = 0 \quad (4.3)$$

$$\nabla \times \mathbf{B} = \mu_0 \mathbf{J}, \quad (4.4)$$

2198 where we can see that the electric and magnetic fields are now completely decoupled
2199 from each other. The solution for the magnetic field in this boundary value problem is
2200 given by the Biot-Savart law

$$\mathbf{B}(\mathbf{r}) = \frac{\mu_0}{4\pi} \int dr' \frac{r'^3 \mathbf{J}(\mathbf{r}') \times (\mathbf{r} - \mathbf{r}')}{|\mathbf{r}' - \mathbf{r}|^3}, \quad (4.5)$$

2201 which Kassiopeia uses a variety of numeric integration techniques to solve for a user
2202 defined current distribution.

2203 **Kassiopeia Simulation of the FSCD Magnetic Trap**

2204 The trap developed for the FSCD experiment utilizes six current carrying coils, which
2205 surround a cylindrical tritium containment vessel (see Figure 4.1). Some critical aspects
2206 of the trap design include the total trapping volume, the maximum trap depth, the

¹<https://github.com/KATRIN-Experiment/Kassiopeia>

steepness of the trap walls, as well as the radial and azimuthal uniformity of the magnetic fields.

The volume of the FSCD trap is a cylindrically shaped region with a radius of 5 cm and a length of 15 cm resulting in a roughly 1 L total trap volume. The trap volume is an important design feature, because it sets the volume of the experiment that is potentially usable for CRES measurements. Trapping a larger volume allows one to observe a larger number of tritium atoms, which increases the statistical power and sensitivity of the neutrino mass measurement. Due to the cost of constructing magnets with large and uniform magnetic fields it is important that the trap use as much of the available volume as possible to limit the overall cost of the experiment.

Coil	Radius (mm)	Z Pos. (mm)	Current (A×Turns)
1	50.0	-92.3	750.0
2	50.1	-56.9	-220.3
3	68.5	-19.5	-250.0
4	68.5	19.5	-250.0
5	50.1	56.9	-220.3
6	50.0	92.3	750.0

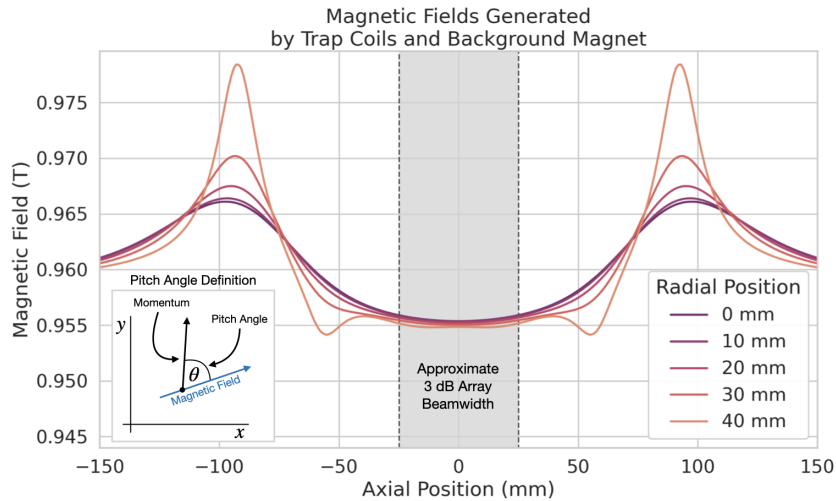
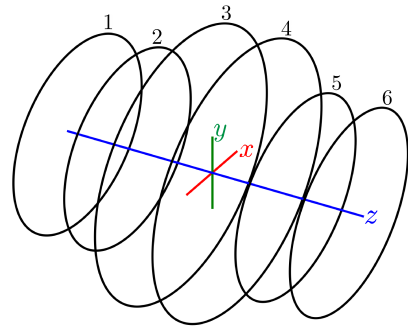


Figure 4.1. The geometry and parameters of the coils used to simulate the FSCD magnetic trap in Kassiopéia. Some axial profiles of the magnetic trap at different radial positions are shown to demonstrate the shape of the magnetic field and trap depth as a function of position. Calculation of the magnetic field profiles was graciously done by René Reimann.

The depth of the FSCD trap is approximately 10 mT when measured along the central axis, which is sufficient to trap electrons with pitch angles as small as 84° . The trap depth factors into the efficiency of the experiment by directly controlling the range

of electron pitch angles that can be trapped. If a higher fraction of pitch angles are trapped then, in principle, more decay events can be observed. However, the signals from electrons with small pitch angles are typically significantly harder to detect than larger pitch angles when using an antenna array, which increases the likelihood of not detecting the first track of the CRES event and harms the energy resolution of the experiment.

The steepness of the trap walls as well as any non-uniformities in the magnetic field contribute to the total energy resolution of the CRES measurement by causing uncertainty in the relationship between an electron's kinetic energy and it's cyclotron frequency. When an electron is trapped, it oscillates back and forth along the trap z-axis (see Figure 4.1) unless it is produced with a pitch angle of exactly 90° [61]. As the electron is reflected from the trap walls it experiences a change in the total magnetic field, which causes a modulation in the cyclotron frequency. This change in magnetic field from the trap introduces a correlation between the pitch angle and kinetic energy parameters of the electron that can reduce energy resolution. In order to mitigate this effect it is important to make the trap walls as steep as possible.

Particle Trajectory Solutions

The magnetic fields solved by direct integration of the electron's current density can be used by Kassiopeia to solve for the trajectory of electrons based on user specified initial conditions. Various distributions are available within Kassiopeia that can be sampled in order to replicate realistic event statistics, including uniform, Gaussian, and Lorentzian among others. In general, an electron has six kinematic parameters that define its trajectory, which are the three-dimensional coordinates of the initial position and the three components of the electron's momentum vector. However, when simulating CRES events it is more common to parameterize the electron's trajectory in terms of it's initial position, the kinetic energy, the pitch angle, and the initial direction of the component of the electron's momentum perpendicular to the magnetic field. This parameterization is completely equivalent to specify each component of the electrons initial position and momentum vectors.

From the initial parameters of the electron and the magnetic field, Kassiopeia solves for the trajectory of the electron. The direct approach proceeds by solving the motion of the electron using the Lorentz force equation, which takes the form of a set of differential equations

$$\frac{d\mathbf{r}}{dt} = \frac{\mathbf{p}}{\gamma m} \quad (4.6)$$

$$\frac{d\mathbf{p}}{dt} = e(\mathbf{E} + \frac{\mathbf{p} \times \mathbf{B}}{\gamma m}), \quad (4.7)$$

where \mathbf{r} is the position of the electron, \mathbf{p} is the electron's momentum, e is the charge of the electron, m is the electron's mass, and γ is the relativistic Lorentz term. To account for kinetic energy losses from radiation Kassiopeia includes an additional term in the momentum differential equation, which calculates the change in the electron's momentum induced by synchrotron radiation. Kassiopeia solves this pair of differential equations using numerical integration, however, the exact trajectory can be computationally intensive to solve. If the adiabatic approximation can be applied, then Kassiopeia can make use of a simpler set of equations that can be more readily solved numerically.

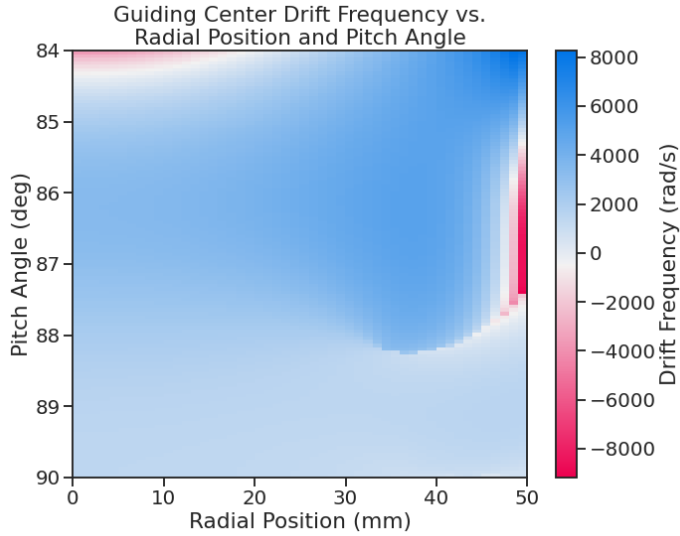


Figure 4.2. A map of the average ∇B -drift frequency for electrons trapped in the prototype FSCD trap shown in Figure 4.1. Negative drift frequencies indicate electrons that are drifting opposite to the standard direction, which means that they are close to escaping the magnetic trap.

Even though Kassiopeia is not directly capable of simulating the cyclotron radiation, it is still an invaluable CRES simulation tool, due to the accurate trajectory solutions for electrons in magnetic traps. With Kassiopeia it is possible to test the efficiency of a particular trap design and analyze features of the electron trajectories that are important to the position, track, and event reconstruction algorithms (see Section 4.3). One example of this for the FSCD is the analysis of the average ∇B -drift frequency as a function of the electrons radial position and pitch angle in the magnetic trap (see Figure 4.2). Radial gradients in the trap cause the guiding center of the electron to drift around the center of

the magnetic trap with an average frequency on the order of 10^3 rad/s. This frequency, while slow compared to the length of a typical CRES time-slice, is large enough to cause a significant loss in efficiency of certain signal reconstruction algorithms. Therefore, it is important to model the drift of the electron in the reconstruction algorithm in order to mitigate the effects of this motion on the reconstruction.

4.2.2 Locust

The Locust² software package [62] is the primary simulation tool developed and used by the Project 8 collaboration for CRES experiments. Locust simulates the responses of antennas and receiver electronics chain to rapidly time-varying electric fields using a flexible approach that allows one to choose from a variety of electric field sources and antennas. Similarly, one can simulate the receiver chain using a series of modular generators that include standard signal processing operations such as down-mixing and fast Fourier transforms (FFT). Since the primary focus of this chapter is the application of Locust to analyses of the FSCD, we shall describe only the most relevant aspects of the software rather than provide a comprehensive description.

Cyclotron Radiation Field Solutions

Simulating CRES events in the FSCD requires that we calculate the electric fields produced by the acceleration of the electron. In the general case, this can be a complicated question to answer, due to back-reaction forces on the electron from its own electric fields that occur when the electron is surrounded by conductive material such as a waveguide or cavity. However, in the case of the FSCD it is possible to ignore such effects and approximate the electron as radiating into a free-space environment.

The equations that describe the electromagnetic fields from a relativistic moving point particle are the Liénard-Wiechert field equations [63, 64], which are obtained by differentiating the Liénard-Wiechert potentials. In their full form the Liénard-Wiechert field equations are

$$\mathbf{E} = e \left[\frac{\hat{n} - \boldsymbol{\beta}}{\gamma^2(1 - \boldsymbol{\beta} \cdot \hat{n})^3 |\mathbf{R}|^2} \right]_{t_r} + \frac{e}{c} \left[\frac{\hat{n} \times [(\hat{n} - \boldsymbol{\beta}) \times \dot{\boldsymbol{\beta}}]}{(1 - \boldsymbol{\beta} \cdot \hat{n})^3 |\mathbf{R}|} \right]_{t_r} \quad (4.8)$$

$$\mathbf{B} = [\hat{n} \times \mathbf{E}]_{t_r}, \quad (4.9)$$

²https://github.com/project8/locust_mc/tree/master

2294 where e is the charge of the particle, \hat{n} is the unit vector pointing from the particle to the
 2295 position where the fields are calculated, β and $\dot{\beta}$ are the velocity and acceleration of the
 2296 particle divided by the speed of light (c), \mathbf{R} is the distance from the particle to the field
 2297 calculation position, and γ is the relativistic Lorentz term. The subscript t_r indicates
 2298 that the equations must be evaluated at the retarded time so that the time-delay from
 2299 the travel time of the electromagnetic radiation is correctly accounted for.

2300 The only required input to calculate the electric field at the position of an FSCD
 2301 antenna is the velocity and acceleration of the electron, which can be obtained from
 2302 Kassiopeia simulations. Therefore, when simulating a CRES event Locust first runs a
 2303 Kassiopeia simulation of the electron and calculates the electric field incident on the
 2304 antenna. The only difficulty with this approach is the determination of the retarded time.
 2305 The retarded time corresponds to the time that a photon, which has just arrived at an
 2306 antenna at the space-time position (t, \mathbf{r}) , was actually emitted by the electron at the
 2307 space-time position of $(t_r, \mathbf{r}_e(t_r))$. Defined in this way, finding the retarded time requires
 2308 solving

$$c(t - t_r) = |\mathbf{r} - \mathbf{r}_e(t_r)|, \quad (4.10)$$

2309 where the distance traveled by the photon between the measurement and retarded times
 2310 is equal to the distance between the antenna and the electron at the retarded time.
 2311 Locust solves Equation 4.10 using a built-in root finding algorithm to find the retarded
 2312 time, and thus the electric field produced by the electron at the position of each antenna
 2313 in the FSCD array.

2314 Antenna Response Modeling

2315 With the electric field it is possible, in principle, to calculate the resulting voltages pro-
 2316 duced in the antenna. However, direct simulation of the antenna itself is computationally
 2317 expensive since it would require the modeling of complex interactions of the electron's
 2318 electric fields with charge carriers in the conductive elements of the antenna. Direct
 2319 simulation of the antenna in Locust can be avoided by modeling the antenna response
 2320 using the antenna factor, or antenna transfer function, approach. The antenna factor
 2321 defines the voltage produced in the antenna terminal for an incident electric field [65],

$$A_F = \frac{V}{|\mathbf{E}|}, \quad (4.11)$$

where V is the voltage and $|\mathbf{E}|$ is the magnitude of the incident electric field. To obtain the antenna factor for the antennas developed for the FSCD Project 8 employs Ansys HFSS. HFSS is a commercially available finite element method electromagnetic solver widely used throughout the antenna engineering industry [66]. HFSS is capable of calculating the antenna factor and gain patterns for complex antenna designs and outputting the resulting quantities in the form of a text file that can be used as an input to the Locust simulation.

The antenna factor defines the steady-state response of the antenna to electromagnetic plane waves and is a function of the frequency of the radiation. Therefore, in order to apply the transfer function for the calculation of the antenna voltage response in the time domain, Locust models the antenna as a linear time-invariant system [67]. In this formalism the response of the system to the driving force is given by

$$y[n] = h * x = \sum_k h[k]x[n - k], \quad (4.12)$$

where $y[n]$ is the discretely sampled response, x is the driving force stimulus, and h is the finite impulse response (FIR) filter. When applied to the FSCD array, this formalism calculates the voltage time-series produced in each antenna by convolving the electric field time-series with the antenna FIR filter, which is obtained by performing a inverse Fourier transform on the transfer function from HFSS.

Radio-frequency Receiver and Signal Processing

After obtaining the voltage time-series by computing the electron trajectory and antenna response, Locust simulates the signal processing associated with the radio-frequency receiver chain. The standard receiver chain used in Locust simulations of the FSCD attempts to mimic the operations that would actually occur in hardware (see Figure 4.3).

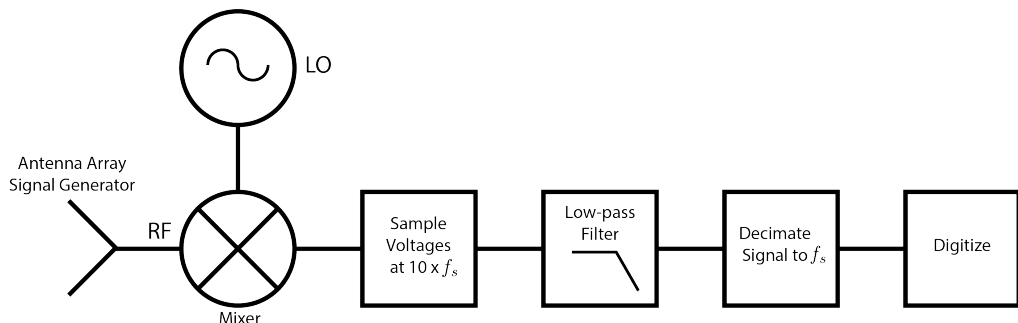


Figure 4.3. The receiver chain used by Locust when simulating CRES events in the FSCD.

2344 Frequency down-conversion is used in the FSCD to reduce the digitization bandwidth
 2345 required to read-out CRES data. According to the Nyquist sampling theorem [68], the
 2346 minimal sampling rate that guarantees no information loss for a signal with a bandwidth
 2347 Δf is given by

$$f_{\text{Nyq}} = 2\Delta f. \quad (4.13)$$

2348 The total bandwidth of CRES signal frequencies from tritium beta-decay ranges from 0
 2349 to 26 GHz in a 0.95 T magnetic field, therefore, direct digitization of CRES signals from
 2350 the FSCD would require sampling frequencies greater than 50 GHz, which is infeasible for
 2351 a real experiment. However, for the purposes of neutrino mass measurement we are only
 2352 interested in measuring the shape of the spectrum in the last 100 eV, which corresponds
 2353 to a frequency bandwidth of 5 MHz. Down-conversion is a technique for reducing the
 2354 base frequencies of signals in a bandwidth given by $[f_{\text{LO}}, f_{\text{LO}} + \Delta f]$ to the bandwidth
 2355 $[0, \Delta f]$, by performing the following multiplication

$$x(t) \rightarrow x(t)e^{-2\pi f_{\text{LO}} t}. \quad (4.14)$$

2356 In down-conversion the signal ($x(t)$) is multiplied by a sinusoidal signal with frequency
 2357 f_{LO} to reduce the absolute frequencies of the signals in the bandwidth. In the FSCD this
 2358 allows us to detect events in the last 100 eV of the tritium spectrum while sampling the
 2359 data far below 50 GHz. The standard bandwidth used in the FSCD is 200 MHz, which
 2360 allows for higher frequency resolution than the minimum sampling frequency for 100 eV
 2361 of energy bandwidth.

2362 Trying to directly simulate down-conversion with a frequency multiplication in Locust
 2363 would require the sampling of the electric fields at each antenna in the FSCD array with
 2364 a period of ≈ 20 ps, which is extremely slow computationally. To avoid this Locust
 2365 performs the down-conversion by intentionally under-sampling the electric fields with
 2366 a frequency of 2 GHz. Sampling below the Nyquist limit causes the higher frequency
 2367 components of the CRES signal to alias, however, Locust can remove these aliased
 2368 frequency peaks using a combination of low-pass filtering and decimation to recreate
 2369 frequency down-conversion. After filtering and decimation, Locust simulates digitization
 2370 by an 8-bit digitizer at a sampling frequency of 200 MHz to recreate the conditions of
 2371 the FSCD. The voltage offset and the digitizer range must be configured by the user
 2372 based on the characteristics of the simulation.

2373 **Data**

2374 The output of Locust simulations for the FSCD primarily consists of two data files. The
2375 first is the electron trajectory information calculated by Kassiopiea, which is output in
2376 the form of a `.root` file [69]. This file contains important kinematic information about
2377 the electron such as it's position and pitch angle as a function of time. The other file is
2378 produced by Locust and it contains the digitized signals acquired from each antenna in
2379 the FSCD array. The Locust output files conform to the Monarch specification developed
2380 by Project 8, which is based on the commonly used HDF5 file format, and matches the
2381 format of the files produced by the Project 8 data acquisition software. This makes it
2382 possible to use the same data analysis code to analyze both simulated and real data.

2383 **4.2.3 CRESana**

2384 Locust is the primary simulation tool used by Project 8 in the development and simulation
2385 of the FSCD. However, simulations of CRES events in larger antenna arrays (≥ 100
2386 antennas) using Locust can take several hours to complete, which is prohibitively long
2387 when one is performing a sensitivity analysis for a large scale antenna experiment. One
2388 of the reasons for Locust's slow operation is that the electric fields from the electron
2389 must be solved numerically for each time-step for each of the antennas in the array.
2390 These numerical solutions allow Locust to accurately simulate the electric fields from
2391 arbitrarily complicated electron trajectories at the cost of more computations and slower
2392 simulations. Therefore, an additional simulation tool that sacrifices some accuracy for
2393 computational efficiency would be extremely useful simulations and sensitivity analyses
2394 of larger antenna array experiments.

2395 To fill this need, Project has developed a new simulations package called CRESana³,
2396 specifically designed to perform analytical simulations of antenna array based CRES
2397 experiments. CRESana is not as flexible as Locust, but it provides a significant increase
2398 in simulation speed. It does this by using well-justified analytical approximations of the
2399 electrons motion in the magnetic field and the resulting electric fields from the electron's
2400 acceleration. The electric fields and signals generated by CRESana are consistent with
2401 theoretical calculations of the electron's radiation, and are test for accuracy using
2402 well-known test-case simulations and consistency checks.

³<https://github.com/MCFlowMace/CRESana>

2403 4.3 Signal Detection and Reconstruction Techniques for 2404 Antenna Array CRES

2405 Antenna Array CRES Signal Reconstruction

2406 A robust set of FSCD simulation tools are vital to the development of the analysis
2407 algorithms necessary for antenna array CRES to succeed. In order to perform CRES
2408 measurements using an antenna array, one must develop an algorithm that uses the
2409 multi-channel time-series obtained by digitizing the array to estimate the starting kinetic
2410 energies of electrons produced in the magnetic trap. This procedure consists of a multi-
2411 stage process of detecting a CRES signal then estimating the parameters of the electron
2412 that produced and is often referred to as simply CRES signal reconstruction.

2413 Compared with the signal reconstruction approaches of the Phase I and II CRES
2414 experiments, antenna array CRES requires a significantly different approach to signal
2415 reconstruction. In Phase I and II, CRES was performed using a waveguide gas cell that
2416 could be directly connected to a waveguide transmission line. The transmission line
2417 efficiently transmits the cyclotron radiation along its length to an antenna at either end
2418 of the waveguide. However, with an antenna array the electron is essentially radiating
2419 into free-space, therefore, the cyclotron radiation power collected by the array is directly
2420 proportional to the solid angle surrounding the electron that is covered with antennas.
2421 Because it is not practical to fully surround the magnetic trap with antennas, some of the
2422 cyclotron radiation power that would have been collected by the waveguide escapes into
2423 free-space. Furthermore, the power that is collected by the antenna array is split between
2424 every channel in the antenna array, which significantly lowers the signal-to-noise ratio
2425 (SNR) of CRES signals in a single antenna channel compared to a waveguide apparatus.
2426 Therefore, a suite of completely new signal reconstruction techniques are needed in order
2427 to perform CRES in the FSCD.

2428 Changes to the approach to CRES signal reconstruction are also motivated by the
2429 more ambitious scientific goals of the FSCD experiment. A measurement of the tritium
2430 beta-decay spectrum that is sensitive to neutrino masses as small as 40 meV requires that
2431 we measure the kinetic energies of individual electrons with a total energy broadening
2432 of 115 meV [70]. This resolution includes all sources of uncertainty in the electron's
2433 kinetic energy such as magnetic field inhomogeneities. This level of energy resolution is
2434 compatible only with an event-by-event signal reconstruction approach where the kinetic
2435 energies, pitch angles, and other parameters of the CRES events are estimated before

2436 constructing the beta-decay spectrum.

2437 The event-by-event approach is distinct from the analysis done for the Phase I and
2438 Phase II experiments where only the starting cyclotron frequency of the event was
2439 estimated by analyzing the tracks formed by the carrier frequency in the time-frequency
2440 spectrogram. These frequencies were then combined into a frequency spectrogram, which
2441 was converted to the beta-decay energy spectrum using an ensemble approach that
2442 averaged over all other event parameters. The ensemble approach to signal reconstruction
2443 results in poor energy resolution because other kinematic parameters such as pitch angle
2444 change the cyclotron carrier frequency due to changes in the average magnetic field
2445 experience by the electron, and it is therefore incompatible with the future goals of the
2446 Project 8 collaboration.

2447 Components of Reconstruction: Signal Detection and Parameter Estimation

2448 CRES signal reconstruction can be viewed as a two-step procedure consisting of signal
2449 detection followed by parameter estimation. In the former, one is concerned with
2450 identifying CRES signals in the data regardless of the signal parameters, whereas, in the
2451 latter one operates under the assumption that a signal is present and then estimates its
2452 parameters.

2453 More formally, signal detection is essentially a binary hypothesis test between the
2454 signal and noise data classes and parameter estimation describes a procedure of fitting a
2455 model to the observed data. While both of these processes are required for a complete
2456 reconstruction (see Figure 4.4), the focus of my work and this chapter is on the signal
2457 detection aspect of antenna array CRES signal reconstruction.

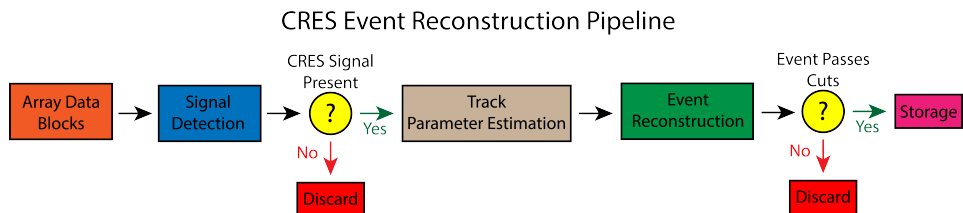


Figure 4.4. A high-level diagram depicting the process of CRES event reconstruction. The first step consists of identifying the presence of a signal in the data. This step is necessary to avoid the danger of performing a reconstruction of a false event, which would constitute a background contribution to the tritium spectrum measured by CRES.

2458 **Detection Theory**

2459 The problem of signal detection can be posed as a statistical hypothesis test [71]. For
2460 CRES signals, which are essentially vectors with added white Gaussian noise (WGN),
2461 one needs to choose between two hypotheses

$$\mathcal{H}_0 : \mathbf{y} = \boldsymbol{\nu} \quad (4.15)$$

$$\mathcal{H}_1 : \mathbf{y} = \mathbf{x} + \boldsymbol{\nu}, \quad (4.16)$$

2462 where \mathbf{y} is the CRES data vector, $\boldsymbol{\nu}$ is a sample of WGN, and \mathbf{x} represents the CRES
2463 signal. The hypothesis that the data contains only noise is labeled \mathcal{H}_0 and the hypothesis
2464 that the data contains a signal is labeled \mathcal{H}_1 .

2465 For illustrative purposes one can examine the case where one the first sample of
2466 data is used to distinguish between \mathcal{H}_0 and \mathcal{H}_1 . The value of the first data sample is
2467 distributed according to two gaussian distributions corresponding to \mathcal{H}_0 and \mathcal{H}_1 (see
2468 Figure 4.5). By setting a decision threshold on the value of this sample, one can choose
2469 the correct hypothesis with a probability given by the areas underneath the probability
2470 distribution curves. A true positive corresponds to correctly identifying that the data
2471 contains signal, whereas, a true negative means that one has correctly identified the data
2472 as noise. The rate at which the detector performs a true positive classification is given
2473 by the green region underneath $p(\mathbf{y}[0]; \mathcal{H}_0)$, and the rate at which the detector performs
2474 a true negative classification is given by the orange region underneath $p(\mathbf{y}[0]; \mathcal{H}_1)$. Two
2475 types of misclassifications are possible. Either we declare noise data as signal, which is
2476 call a false positive, or we declare signal data as noise, which is a false negative. Note
2477 that it is only possible to trade off these two types of errors by tuning the detection
2478 threshold. One cannot simultaneously reduce the rate of false positives without also
2479 increasing the rate of false negatives.

2480 The approach taken with CRES signals is to fix the rate of false positives by setting
2481 a minimum value for a detection threshold. The rate of false positives that is acceptable
2482 at the detection stage depends upon the rate of background events compatible with the
2483 sensitivity goals of the experiment. The ultimate goal of a neutrino mass measurement
2484 with 40 meV sensitivity in general has strict requirements on the number of background
2485 events, which requires a relatively high detection threshold to achieve. Consequently,
2486 the ideal signal detection algorithm is the one that achieves the maximum rate of true
2487 positives for a fixed rate of false positives, so that the detection efficiency of the experiment
2488 is maximized and potential sources of background are kept to a minimum.

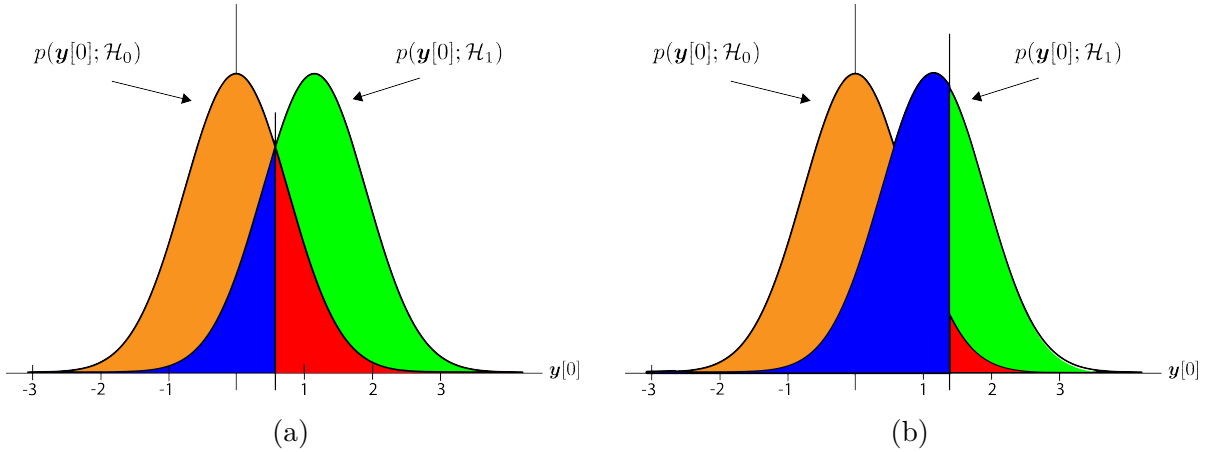


Figure 4.5. An illustration of two PDFs associated with a binary hypothesis test. The decision threshold is represented by the vertical line that partitions both distributions. The orange and red areas correspond to the true negative and false positive probabilities and the blue and green areas correspond to the false negative and true positive probabilities respectively. To decide between the two hypotheses we perform the likelihood ratio test specified by the Neyman-Pearson theorem. This approach achieves the highest true positive probability for a given false positive probability.

According to the Neyman-Pearson theorem [72], the statistical hypothesis test that maximizes the probability of detection for a fixed rate of false positives is the likelihood ratio test, which is formed by computing the ratio of the signal likelihood to the noise likelihood,

$$L(x) = \frac{P(\mathbf{y}; \mathcal{H}_1)}{P(\mathbf{y}; \mathcal{H}_0)} > \gamma. \quad (4.17)$$

Here, the likelihood of the hypotheses \mathcal{H}_0 and \mathcal{H}_1 are described by the probability distributions $P(\mathbf{y}; \mathcal{H}_0)$ and $P(\mathbf{y}; \mathcal{H}_1)$ respectively, and γ is the threshold for deciding \mathcal{H}_1 . The decision threshold is determined by integrating $P(\mathbf{y}; \mathcal{H}_0)$ such that

$$P_{\text{FP}} = \int_{\gamma}^{\infty} P(\tilde{\mathbf{y}}; \mathcal{H}_0) d\tilde{\mathbf{y}} = \alpha, \quad (4.18)$$

where α is the desired false positive detection rate given by the red colored areas shown in Figure 4.5. The true positive detection rate is given by the similar integral

$$P_{\text{TP}} = \int_{\gamma}^{\infty} P(\tilde{\mathbf{y}}; \mathcal{H}_1) d\tilde{\mathbf{y}}, \quad (4.19)$$

which corresponds to the green areas in Figure 4.5.

Changing the decision threshold allows one to trade-off between P_{TP} and P_{FP} as

appropriate for the given situation. It is common to summarize the relationship between P_{TP} and P_{FP} using the receiver operating characteristic (ROC) curve, which is obtained by evaluating the true positive and false positive probabilities as a function of the decision threshold value (see Figure 4.6). The ROC curve provides a convenient way to compare

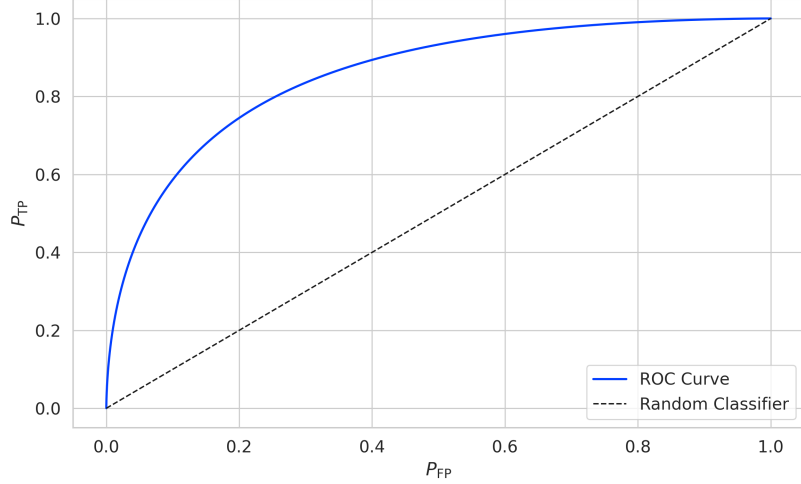


Figure 4.6. An example ROC curve formed by computing the P_{FP} and the P_{TP} for a given likelihood ratio test. As the decision threshold is increased P_{FP} decreases at the expense of a lower P_{TP} . The black dashed line indicates the lower bound ROC curve obtained by randomly deciding between \mathcal{H}_0 and \mathcal{H}_1 .

the performance of different signal detection algorithms. In general, a classifier with a higher the P_{TP} as a function of P_{FP} is desirable, which corresponds to a larger area underneath the respective ROC curve. A perfect classifier has an area underneath the curve of 1.0, however, such a classifier is almost never achievable in practice.

4.3.1 Digital Beamforming

Introduction to Beamforming

Beamforming refers to a suite of antenna array signal processing techniques that are designed to enhance the radiation or gain of the array in certain directions and suppress it in other direction [65]. Beamforming is of interest to Project 8 as a first level of signal reconstruction for the FSCD and other antenna array CRES experiments, which operates at the signal detection stage of reconstruction.

Beamforming is accomplished by performing a phased summation of the signals received by the antenna array. The beamforming phases are chosen such that the signals

2517 emitted by the array will constructively interfere at the point of interest (see Figure
 2518 4.7). As a consequence of the principle of reciprocity [73], when the array is operating in
 2519 receive mode, the signals emitted from a source at the same point will constructively
 interfere when summed. The origin of the phase delays in beamforming is the path-

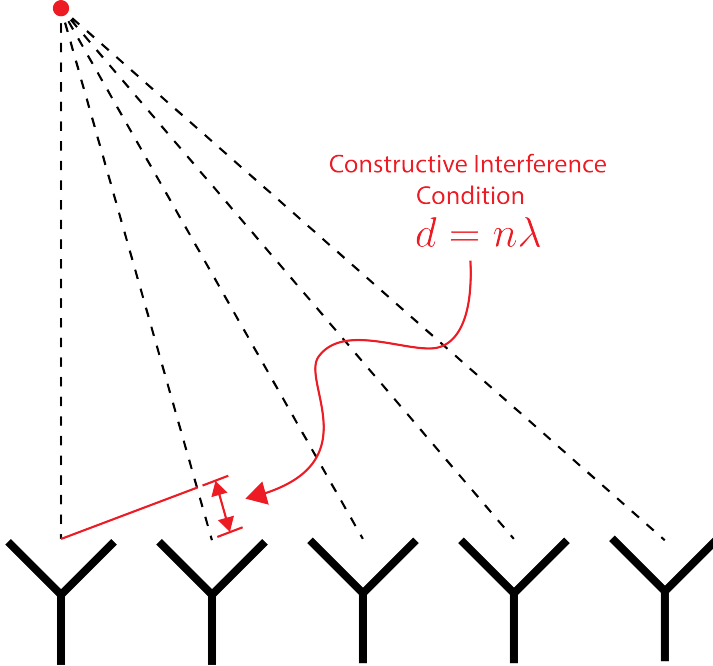


Figure 4.7. An illustration of the constructive interference condition which is the operating principle of digital beamforming using a uniform linear array as an example.

2520
 2521 length difference to the beamforming point between different antennas in the array. The
 2522 relationship between the phase delay and the path-length difference is given by the
 2523 familiar equation

$$\phi = \frac{2\pi d}{\lambda}, \quad (4.20)$$

2524 where ϕ is the phase delay, d is the path-length difference, and λ is the wavelength of
 2525 the radiation. In practice, one chooses the values of d by specifying the beamforming
 2526 positions of interest and then calculates the beamforming phases using Equation 4.20,
 2527 which is guaranteed to follow the constructive interference condition shown in Figure 4.7.

2528 Beamforming can be neatly expressed mathematically using the vector equation

$$y[n] = \Phi^T[n] \mathbf{x}[n], \quad (4.21)$$

2529 where $\mathbf{x}[n]$ is the array snapshot vector, $\Phi[n]$ is a vector of beamforming shifts, and
 2530 $y[n]$ is the resulting summed signal. The beamforming shifts consist of a set of complex

2531 numbers that contain the beamforming phase shift and an amplitude weighting factor,

$$\Phi[n] = [A_0[n]e^{-2\pi i \phi_0[n]}, A_1[n]e^{-2\pi i \phi_1[n]}, \dots, A_{N-1}[n]e^{-2\pi i \phi_{N-1}[n]}], \quad (4.22)$$

2532 where the set of magnitudes $A_i[n]$ are amplitude weighting factors and $\phi_i[n]$ are the phase
2533 shifts from the path-length differences. The index i is used to denote the antenna channel
2534 number. The amplitude weighting factor is the relative magnitude of the signal received
2535 by a particular antenna to the other antennas in the array, such that the antennas that
2536 receive signals with higher amplitude, due to being closer to the source, have more
2537 weight in the beamforming summation. The input and outputs signals beamforming
2538 are naturally expected to be functions of time as indicated by the index $[n]$, however, it
2539 is also possible to use time dependent beamforming phases that shift the beamforming
2540 position of the array over time.

2541 Digital beamforming is the type of beamforming algorithm of interest to Project 8 for
2542 CRES. Specifically, digital beamforming means that the beamforming phases are applied
2543 to the array signals in software rather than employing fixed beamforming phase shifts in
2544 the receiver chain hardware. The advantage of digital beamforming is that for a given
2545 series of array snapshots one can specify a large number of beamforming positions and
2546 effectively search for electrons by performing the beamforming summation associated
2547 with each point and applying a signal detection algorithm to identify the presence of a
2548 CRES signal.

2549 One of the most attractive features of digital beamforming is the spatial filtering
2550 effect, which is a direct consequence of the constructive interference condition used to
2551 define the beamforming phases. Spatial filtering allows for signals from multiple electrons
2552 at different positions in the trap to be effectively separated, because the constructive
2553 interference condition will force the signals from electrons at positions different from the
2554 beamforming position to cancel. This helps to reduce signal pile-up that could become
2555 an issue for large scale CRES experiments using a dense tritium source.

2556 The digital beamforming positions can be specified with arbitrary densities limited
2557 only by the available computational resources. This provides a very straight-forward way
2558 to estimate the position of the electron in the trap by using a dense grid of beamforming
2559 positions and maximizing the output power of the beamforming summation over this
2560 grid. This natural approach to position reconstruction is attractive due the requirements
2561 of an event-by-event signal reconstruction, which needs an accurate estimation of the
2562 exact magnetic field experienced by the electron in order to correctly estimate it's kinetic

2563 energy. Combined with an accurate map of the magnetic field inhomogeneities of the
 2564 trap obtained from calibrations, beamforming allows one to apply this magnetic field
 2565 correction with a spatial resolution that is a fraction of the cyclotron wavelength.

2566 **Laboratory Beamforming Demonstrations**

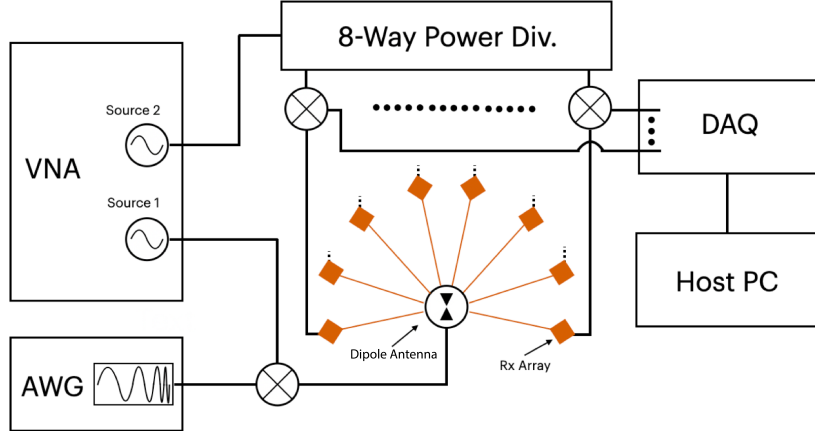


Figure 4.8. System level diagram of the laboratory setup used for beamforming demonstrations at Penn State. For more information on this system see Chapter 5. Signals near 26 GHz are fed to a dipole antenna using an arbitrary waveform generator (AWG) and vector network analyzer (VNA), which drive a mixer. The dipole radiation is collected by an array of antennas connected to the digitizer data acquisition (DAQ) system.

2567 As part of the development of antenna array CRES for the FSCD, an antenna
 2568 measurement setup was constructed at Penn State to serve as a testbed for antenna
 2569 prototypes and to perform laboratory validations of array simulations. This system
 2570 is discussed in more detail in Chapter 5. Early versions of the antenna measurement
 2571 system (see Figure 4.8 and Figure 4.9) were used to perform beamforming reconstruction
 2572 studies of a simple probe antenna to better understand the principles of beamforming
 2573 and confirm the estimated beamforming performance of Locust.

2574 Signals from an arbitrary waveform generator were up-converted to 26 GHz using a
 2575 mixer and a high-frequency source from a vector network analyzer and fed to the dipole
 2576 antenna through a balun. The radiation from the dipole antenna was received by an
 2577 array of horn antennas. The signals from the horn antennas were then down-converted
 2578 to baseband using a collection of mixers and an 8-way power divider. The signals were
 2579 then digitized and saved to a host computer for analysis.

2580 The data collected using the dipole and horn antenna array is reconstructed using the
 2581 beamforming reconstruction approach specified in Section 4.3.1. A two-dimensional grid

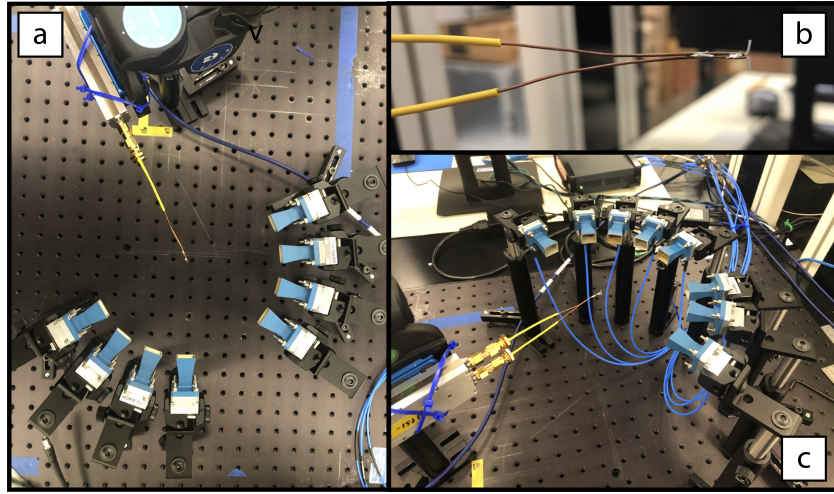


Figure 4.9. Photographs of the beamforming demonstration setup. In (a) I show a top-down view of the dipole antenna and the array of eight horn antennas. Manual repositioning of the horn antennas allows one to synthesize a full-circular antenna array. The dipole antenna is mounted on a camera tripod mount that allows for manual position tuning. (b) is a close up image of the dipole, which is manufactured from two segments of semi-rigid coaxial cable. (c) is another image of the dipole and array.

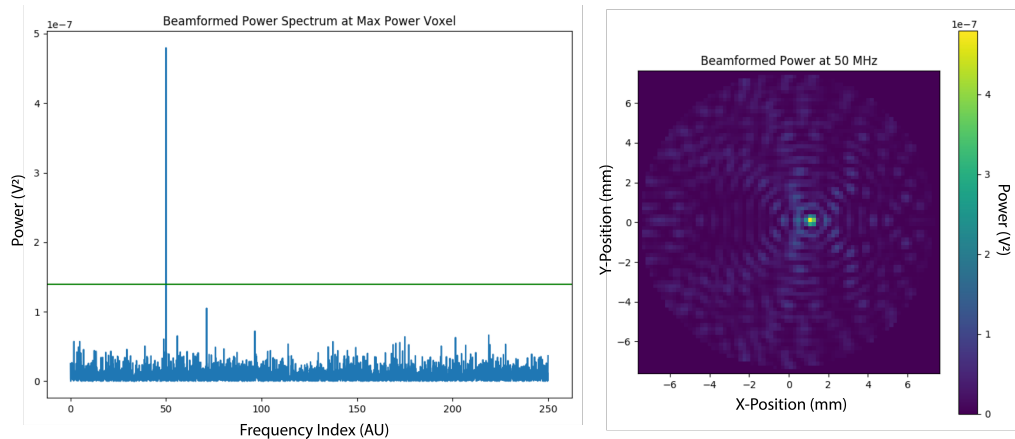


Figure 4.10. An example of digital beamforming reconstruction of a dipole antenna using a synthetic array of horn antennas. The beamforming image on the right is constructed by computing the time-averaged power of the summed signals for a two-dimensional grid of beamforming positions. In the image one can see a clear maximum that corresponds to the position of the dipole antenna. On the left I show the frequency spectrum of the time-series at the maximum power pixel. White gaussian noise is added to the signal to mimic a more realistic signal-to-noise-ratio. The signal emitted by the dipole is clearly visible as the high power peak in the frequency spectrum.

of xy-positions is defined and the beamforming phase shifts for each of these positions is calculated. The phased summation can be visualized by plotting the time-averaged power for each of the summations as a pixel in the resulting beamforming image (see Figure 4.10). White Gaussian noise (WGN) can be added to the data at this stage to simulate more realistic signal-to-noise ratios (SNR) if desired. The beamforming peak maxima is expected to have a Bessel function shape due to the circular symmetry of the array, and by analyzing the size of the beamforming maxima one can confirm that the beamforming reconstruction measurement has similar position resolution as expected from Locust simulations. Additionally, signal detection rates can be estimated from the data by comparing the magnitude of the beamforming signal peak in the frequency spectra to simulation.

2593 FSCD Beamforming Simulations

Using Locust simulations of the FSCD one can perform beamforming reconstruction studies using the simulated CRES signal data. As we mentioned in the previous section, the beamforming procedure begins by specifying a set of beamforming positions and corresponding beamforming shifts. The beamforming positions form a grid that covers the region of interest in the field of view of the antenna array. There are effectively an infinite number of ways to specify the grid positions, however, uniform square grids are the most commonly used due to their simplicity. In the FSCD experiment the number and pattern of the grid positions would be optimized to cover the most important regions of the trap volume to maximize detection efficiency while minimizing superfluous calculations.

The beamforming grids used for signal reconstruction with the FSCD consist of a set of points that cover a region of the two-dimensional plane formed by the perimeter of the antenna array. The axial dimension is left out of the beamforming grid because the electrons are assumed to occupy only an average axial position, which corresponds to the center of the magnetic trap. This is because it is impossible to resolve the axial position of the electron as a function of time due to the rapid axial oscillation frequencies of trapped electrons relative to the FSCD time-slice duration.

After beamforming, a summed time-series is obtained for each beamforming position that can be evaluated for the presence of a signal using a detection algorithm. A beamforming image is a visualization method that is equivalent to arranging the beamforming grid points according to their physical locations to form a three-dimensional matrix where the first two dimensions encode the XY-position of the beamforming point and the third dimension contains the summed time-series. The image is formed by taking the

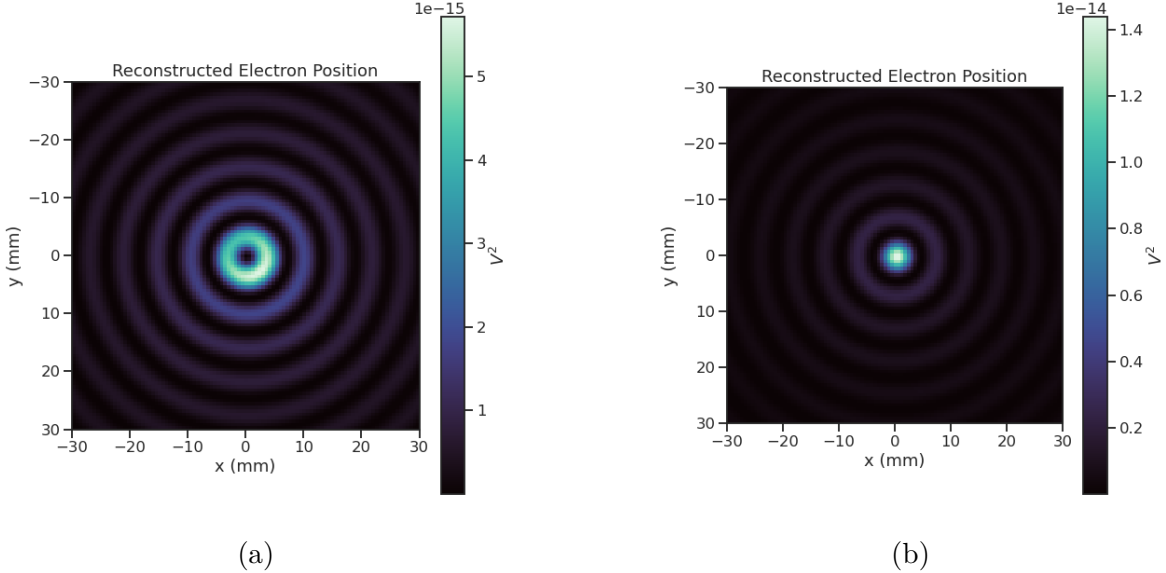


Figure 4.11. Beamforming images visualizing the reconstruction of an electron without (a) and with (b) the cyclotron phase correction. The images were generated using data from Locust simulations. The cyclotron phase refers to a phase offset equal to the relative azimuthal position of an antenna in the array. This phase offset is caused by the circular electron orbit and must be corrected for during reconstruction.

time-averaged power (see Figure 4.11). Beamforming images are purely for the purposes of visualization and are not particularly useful for signal detection or reconstruction.

If the beamforming phases consist only of the spatial phase component from Equation 4.20, then the resulting beamforming image contains a relatively high-power ring-shaped region that is centered on the position of the electron (see Figure 4.11a). The origin of this shape is an additional phase offset particular to a cyclotron radiation source. Essentially, the circular motion that produces the cyclotron radiation introduces a relative phase offset to the electric fields that is equal to the azimuthal position of the field measurement point. For example, if we have two antennas, one located at an azimuthal position of 0° and another located at an azimuthal position of 90° , then the CRES signals received by these antennas will be out of phase by 90° , which is the difference in their azimuthal positions. This phase offset can be corrected by adding an additional term to the beamforming phase equation that is equal to the azimuthal position of the antenna relative to the electron,

$$\phi_i[n] = \frac{2\pi d_i[n]}{\lambda} + \Delta\varphi_i[n], \quad (4.23)$$

where $\Delta\varphi_i$ is difference between the azimuthal position of the electron and the i -th antenna channel. Using the updated beamforming phases in the summation changes the

ring feature into a Bessel function peak whose maximum corresponds to the position of the electron. Including this cyclotron phase correction significantly improves the signal detection and reconstruction capabilities of beamforming by more than doubling the summed signal power and shrinking the beamforming maxima feature size.

The beamforming image examples in Figure 4.11 were produced using an electron located on the central axis of the magnetic trap, which do not experience ∇B -drift. However, for electrons produced at non-zero radial position the beamforming phases must be made time-dependent in order to track the position of the electron's guiding center over time. Without this correction the ∇B -drift causes the electron to move between beamforming positions, which effectively spreads the cyclotron radiation power over a wider area in the beamforming image (see Figure 4.12). This effect significantly

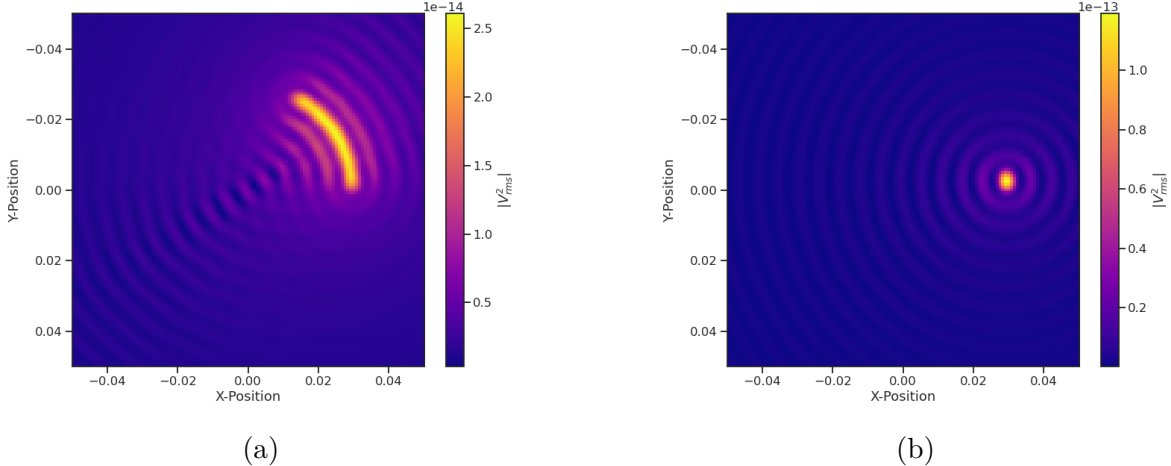


Figure 4.12. Beamforming images visualizing the reconstruction of an electron located off the central axis of the FSCD trap. In (a) we performing beamforming without the ∇B -drift correction, and in (b) we include the ∇B -drift correction.

reduces the power of the beamforming maxima and increases the size of the beamforming features, simultaneously harming detection efficiency and position reconstruction.

The ∇B -drift correction simply adds a circular time-dependence to the beamforming positions as a function of time,

$$r[n] = r_0 \quad (4.24)$$

$$\varphi[n] = \varphi_0 + \omega_{\nabla B} t[n], \quad (4.25)$$

where $\omega_{\nabla B}$ is the drift frequency and $t[n]$ is the time vector. In the ideal case the ∇B -drift frequencies from Figure 4.2 for the correct pitch angle and radial position would be used,

2649 however, it is not possible to know the electron's pitch angle a priori. In principle, one
 2650 could perform multiple beamforming summations for a given beamforming position using
 2651 different drift frequencies and choose the one that maximizes the summed power, but
 2652 this approach leads to a huge computational burden that would be impractical for a
 2653 real FSCD experiment. A compromise is to use an average value of $\omega_{\nabla B}$ obtained by
 2654 averaging over the drift frequencies for electrons of different pitch angle at a particular
 2655 radius. This approach keeps the computational cost of time-dependent beamforming to a
 2656 minimum while still providing a significant increase in the detection efficiency of digital
 2657 beamforming.

2658 **Signal Detection with Beamforming and a Power Threshold**

2659 Up to this point we have neglected any specific discussion of how digital beamforming is
 2660 used for signal detection and reconstruction. This is because, strictly speaking, digital
 2661 beamforming consists only of the phased summation of the array signals and cannot
 2662 be used alone for signal detection. The example beamforming images shown in Figure
 2663 4.11 and Figure 4.12 were produced using simulated data that contained no noise, which
 2664 significantly degrades the utility of analyzing the beamforming images for signal detection
 2665 and reconstruction.

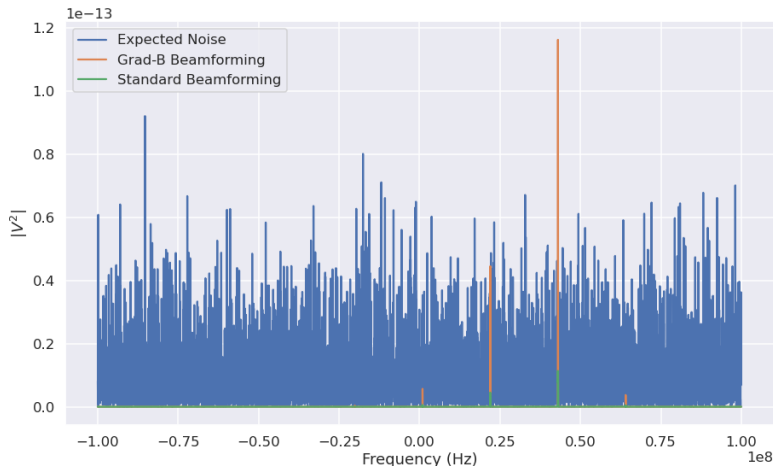


Figure 4.13. A plot of a typical frequency spectrum obtained by applying a Fourier transform to the time-series obtained from beamforming. The frequency spectra are plotted without noise on top of an example of a typical noise spectrum to visualize a realistic signal-to-noise ratio. In the example we see that without beamforming it would not be possible to detect anything since the signal amplitudes would be reduced by a factor of sixty relative to the noise. Additionally, we see that the ∇B -drift correction is needed to detect this electron since it comes from a simulation of an electron with a significant off-axis position.

2666 Digital beamforming as a detection algorithm is understood to mean digital beam-
 2667 forming plus a detection threshold placed on the amplitude of the frequency spectrum
 2668 obtained by applying a fast Fourier transform (FFT) to the summed time-series (see
 2669 Figure 4.13). This approach is most similar to the time-frequency spectrogram analysis
 2670 employed in previous CRES experiments, however, in principle any signal detection
 2671 algorithm could be used after the beamforming procedure. In Section 4.4 I analyze the
 2672 signal detection performance of the power threshold approach in detail.

2673 From the example frequency spectra in Figure 4.13 it is clear that without a re-
 2674 construction technique that coherently combines the signals from the full antenna our
 2675 ability to detect CRES signals will be drastically reduced. Because the CRES signals are
 2676 in-phase at the correct beamforming position the summed power increases as a function
 2677 of N^2 compared to a single antenna channel, where N is the number of antennas. It
 2678 is true that the noise power is also increased by beamforming, but, because the noise
 2679 is incoherent, its power only increases linearly. Consequently, the signal-to-noise ratio
 2680 (SNR) of the CRES signal increases linearly with the number of antennas, which greatly
 2681 improves detection efficiency compared to using only the information in a single antenna.

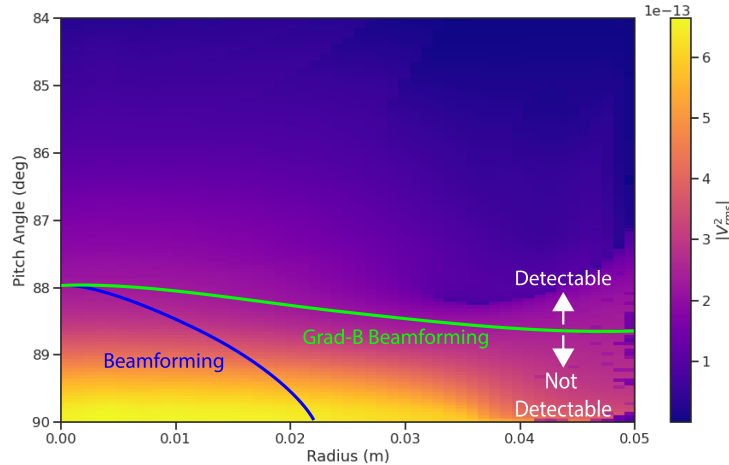


Figure 4.14. A plot of the total signal power received by the FSCD array from trapped electrons with different radial positions and pitch angles generated using Locust simulations. The lines on the plot indicate a 10 dB detection threshold above the mean value of the noise in the frequency spectrum. With static beamforming electrons with radial positions larger than about two centimeters are undetectable due to the change in the electron's position over time causing losses from beamforming phase mismatch. This is corrected by including ∇B -drift frequencies in the beamforming phases. Both beamforming techniques fail to detect electrons below $\approx 88.0^\circ$, since these signal are composed of several relatively weak sidebands that are comparable to the noise.

2682 The power threshold detection algorithm searches for high-power frequency bins that
 2683 should correspond to a frequency component of the CRES signal. In order to prevent
 2684 random noise fluctuations from being mistaken as CRES signals the power threshold
 2685 must be set high enough so that it is unlikely that random noise could be responsible. A
 2686 consequence of this is that many electrons that can be trapped will go undetected because
 2687 the modulation caused by axial oscillations leads to the cyclotron carrier power to falling
 2688 below the decision threshold. The time-dependent beamforming used to correct for the
 2689 ∇B -drift increases the volume of the magnetic trap where electrons can be detected,
 2690 but it is ineffective at increasing the range of detectable pitch angles (see Figure 4.14).
 2691 Fundamentally, this is because the power threshold only uses a fraction of the signal
 2692 power to detect electrons and ignores the power present in the frequency sidebands. In
 2693 the subsequent sections I examine two other signal detection algorithms that seek to
 2694 improve the detection efficiency of the FSCD by utilizing the more of the signal shape to
 2695 compute the detection test statistics.

2696 **4.3.2 Matched Filtering**

2697 **Introduction to Matched Filtering**

2698 The problem of CRES signal detection is the problem of detecting a signal buried in
 2699 WGN, which has been examined at great depth in the signal processing literature [71].
 2700 For a fully known signal in WGN the optimal detector is the matched filter, which means
 2701 that it achieves the highest true positive rate for a fixed rate of false positives. The
 2702 matched filter test statistic is calculated by taking the inner product of the data with
 2703 the matched filter template

$$\mathcal{T} = \left| \sum_n h^\dagger[n] y[n] \right|, \quad (4.26)$$

2704 where $h[n]$ is the matched filter template and $y[n]$ is the data. The matched filter test
 2705 statistic defines a binary hypothesis test in which the data vector is assumed to be an
 2706 instance of two possible data classes. By setting a decision threshold on the value of \mathcal{T} ,
 2707 one can classify a given data vector as belonging to two distinct hypotheses. Under the
 2708 first hypothesis the data is composed of pure WGN, and under the second hypothesis the
 2709 data is composed of the known signal with additive WGN. The matched filter template

2710 is obtained by rescaling the known signal in the following way

$$h[n] = \frac{x[n]}{\sqrt{\tau \sum_n x^\dagger[n]x[n]}}, \quad (4.27)$$

2711 where τ is the variance of the WGN and $x[n]$ is the known signal. Strictly speaking,
 2712 Equation 4.27 is only true for noise with a diagonal covariance matrix, however, in the
 2713 context of the FSCD we are justified in assuming this to be true. Defining the matched
 2714 filter templates in this way guarantees that the expectation value of \mathcal{T} is equal to one
 2715 when the data contains only noise, which is the standard matched filter normalization in
 2716 the signal processing literature.

2717 Although matched filters are canonically formulated in terms of a perfectly known
 2718 signal, it is still possible to apply the matched filter technique given imperfect information
 2719 about the signal provided that the signal is deterministic. From our discussion of CRES
 2720 simulation tools for the FSCD (see Section 4.2) we know that the shape of CRES signals
 2721 are completely determined by the initial parameters of the electron. The random collisions
 2722 with background gas molecules which cause the formation of signal tracks are the only
 2723 stochastic component of the CRES event after the initial beta-decay, therefore, it is
 2724 possible to develop a matched filter for the detection of CRES signal tracks which are fully
 2725 determined by the parameters of the electron after the initial beta-decay or subsequent
 2726 collision events.

2727 The matched filter test statistic for CRES signals is a modified version of Equation
 2728 4.26

$$\mathcal{T} = \max_{\mathbf{h}, m} |\mathbf{h} * \mathbf{y}| = \max_{\mathbf{h}, m} \left| \sum_k h^\dagger[k]x[m - k] \right|, \quad (4.28)$$

2729 where the matched filter inner product has been replaced with a convolution operation
 2730 and a maximization over the template and convolution delay (m). Replacing the inner
 2731 product with a convolution accounts for the fact that the start time of the CRES signal is
 2732 now an unknown parameter, in addition, we now perform a maximization of the matched
 2733 filter convolution over a number of different templates. Because the shape of the signal is
 2734 unknown we are forced to guess a number of different signal shapes to create a template
 2735 bank with which we can identify unknown signals by performing an exhaustive search.

2736 The template bank approach to matched filtering, while quite powerful, can quickly
 2737 become computationally intractable. This is especially true in the case of the FSCD
 2738 because of the large amount of raw data produced by the array that must be analyzed.
 2739 Specifically, the time-domain convolution specified by Equation 4.28 is particularly

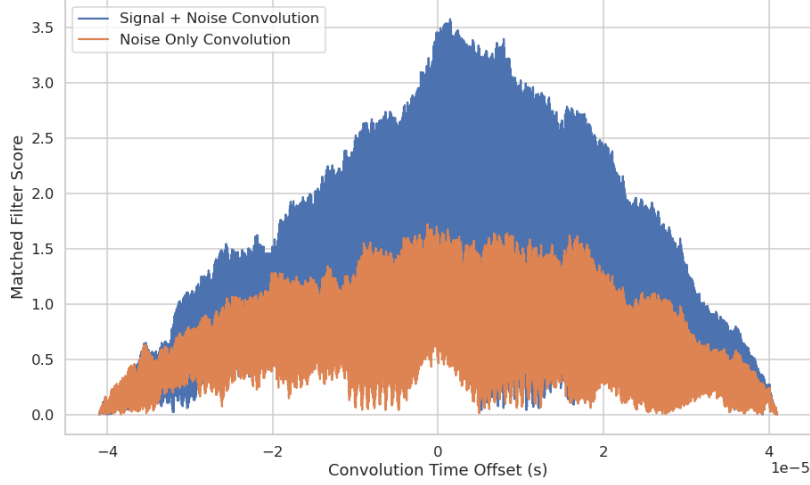


Figure 4.15. Example of a convolution of a CRES signal template with a segment of noisy data. A simulated CRES signal was simulated using Locust and normalized to create a matched filter template. When this template is convolved with noisy data the contains the matching signal the convolution output increases dramatically compared to data with only noise. The decreasing convolution output as the time offset of the convolution increases is caused by zero-padding of the data and template.

2740 computationally intensive and is a major barrier towards the implementation of a
 2741 matched filter for signal detection in an experiment like the FSCD. This can be avoided
 2742 by using the convolution theorem to replace the time-domain convolution with an inner
 2743 product in the frequency domain.

2744 The convolution theorem states that

$$\mathbf{f} * \mathbf{g} = \mathcal{F}^{-1}(\mathbf{F} \cdot \mathbf{G}) \quad (4.29)$$

2745 where \mathbf{f} and \mathbf{g} are discretely sampled time-series, \mathbf{F} and \mathbf{G} are the respective discrete
 2746 Fourier transforms, and \mathcal{F}^{-1} is the inverse discrete Fourier transform operator. The
 2747 convolution theorem allows us to perform the matched filter convolution by first com-
 2748 puting the Fourier transform of the template and data, then performing a point-wise
 2749 multiplication of the two frequency series, and finally performing the inverse Fourier
 2750 transform to obtain the convolution output. Because discrete Fourier transforms can be
 2751 performed extremely efficiently, the convolution theorem is almost always used in lieu of
 2752 directly computing the convolution.

2753 One thing to note here is that the convolution theorem for discrete sequences shown
 2754 here, is technically valid only for circular convolutions, which is not directly specified
 2755 in Equation 4.28. However, because typical CRES track lengths are much longer than

2756 the Fourier analysis window and also that the frequency chirp rates are small compared
2757 to the time-slice duration, it is relatively safe to use circular convolutions to evaluate
2758 matched filter scores for CRES signals, which allows us to apply the convolution theorem
2759 to compute matched filter scores using the frequency representation of the data and
2760 matched filter template.

2761 **Matched Filter Analysis of the FSCD**

2762 The optimality provided by the matched filter makes it a useful algorithm for analysis
2763 of CRES experiment designs for sensitivity analyses, since it indicates the best possible
2764 detection efficiency achievable by an experiment configuration. The standard approach to
2765 performing these studies involves generating a large number of simulated electron signals
2766 that span the kinematic parameter space of electrons in the magnetic trap. In general,
2767 electrons have six kinematic parameters along with an additional start time parameter.

2768 In order to limit the number of simulations required to evaluate the detection efficiency
2769 the standard approach is to fix the starting axial position, starting azimuthal position,
2770 starting direction of the perpendicular component of the electron's momentum, and event
2771 start time to reduce the parameter space to starting radial position, starting kinetic
2772 energy, and starting pitch angle. The fixed variables are true nuisance parameters that do
2773 not affect the detection efficiency estimates for the FSCD design, because they manifest
2774 as phases which are marginalized during the calculation of the matched filter score.

2775 Across radial position, kinetic energy, and pitch angle one defines a regular grid of
2776 parameters and uses Locust to simulate the corresponding signals (see Figure 4.16). This
2777 grid of simulated signals can be used to estimate the likelihood of detecting signals,
2778 because the matched filter score specifies the shape of the PDF that defines the detection
2779 probability and the size of the template bank influences the likelihood of a good match
2780 between a template and a random signal.

2781 The matched filter approach can also be used to estimate the achievable energy
2782 resolution of the experiment by using a dense grid of templates generated with parameters
2783 close to the unknown signal (see figure 4.17). Because matched filter templates with
2784 similar parameters have signal shapes that are also similar, templates with incorrect
2785 parameters can have nearly identical matched filter scores as the correct template. Since
2786 only one sample of noise is included in a sample of real data, one cannot guarantee that
2787 the best matching template corresponds to the ground truth parameters of the signal.
2788 This introduces uncertainty into the signal parameter estimation that manifests as an
2789 energy broadening. Dense grids of matched filter templates allows one to quantify this

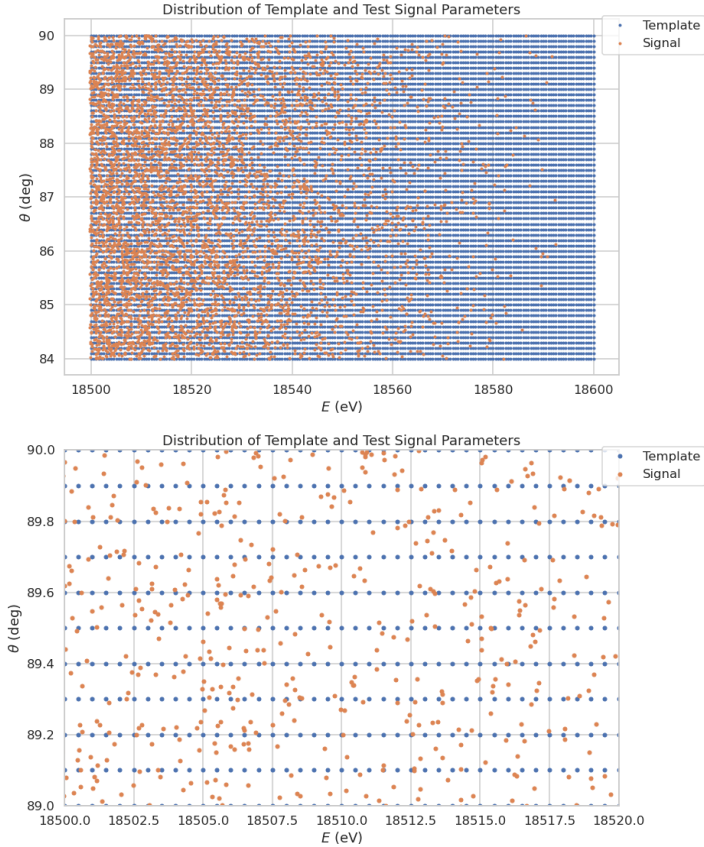


Figure 4.16. An example two-dimensional parameter distribution of a matched filter template bank and random test signals. θ refers to the pitch angle of the electron and E is the kinetic energy. The template bank forms a regular grid of in pitch angle and energy, whereas, the test signals are uniformly distributed in pitch angle and follow the tritium beta-decay kinetic energy distribution. This is why there are fewer test signals at higher energies. The need for high match across the full parameter space prevents one from reducing the density of templates in this low activity region. A zoomed in version of the template bank illustrates the relative density of templates and signals needed for match $> 90\%$.

broadening by analyzing the parameter space of templates with matched filter scores close to the ground truth. This approach is analogous to maximum likelihood estimation and is one key component of a complete sensitivity analysis for an antenna array CRES experiment.

A key parameter for describing the performance of a matched filter template bank at signal detection is match, which we define as the average ratio of the highest matched filter score for a random signal to the matched filter score for a perfectly matching

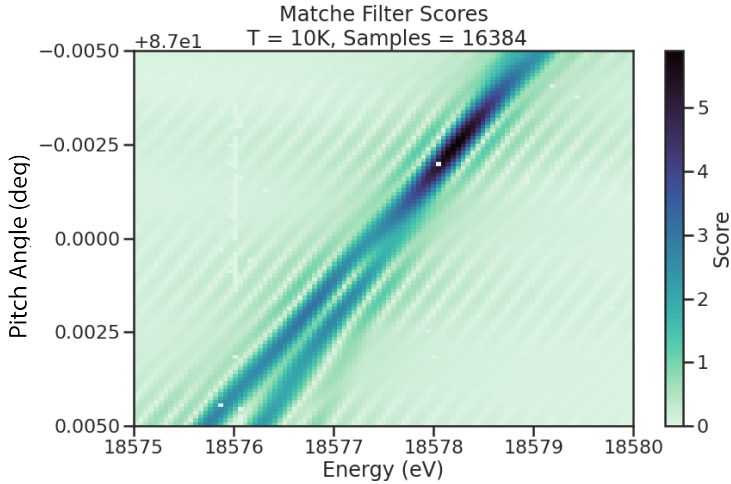


Figure 4.17. The matched filter scores of a dense grid of templates in pitch angle energy space. Dense template grids allow one to estimate the kinetic energy of the electron by identifying the best matching template. The uncertainty on this value is proportional to the space of templates that also match the test signal well. In the worst case matched filter templates can be completely degenerate where templates with different parameters match a signal with equal likelihood.

2797 template. In equation form this is

$$\text{Match} \equiv \Gamma = \frac{\mathcal{T}_{\text{best}}}{\mathcal{T}_{\text{ideal}}}, \quad (4.30)$$

2798 where $\mathcal{T}_{\text{best}}$ is the matched filter score of the best fitting template in the bank and $\mathcal{T}_{\text{ideal}}$ is
 2799 the hypothetical matched filter score one would measure if the signal perfectly matched
 2800 the template. Generally, one desires an average match as close to one as possible, however,
 2801 the average match value is an exponential function of the number of templates in the
 2802 template bank (see Figure 4.18). This behavior is observed for dense matched filter grids
 2803 like the one in Figure 4.17. A dense grid was used to calculate the average value of match
 2804 for different template bank sizes shown in Figure 4.18.

2805 The exponential relationship between match and template bank size is also evident
 2806 for template banks that cover a wide range of parameters, such as the template bank
 2807 visualized in Figure 4.16. Since no prior knowledge of the signal parameters is available,
 2808 one has no choice but to use a template bank that covers a large range of parameters for
 2809 signal detection. Achieving a high average match in this scenario can easily overwhelm
 2810 the available computational resources, so in practice only a limited number of templates
 2811 could be used at the detection stage. Therefore, accurately modeling the effects of match
 2812 is key to correct sensitivity calculations.

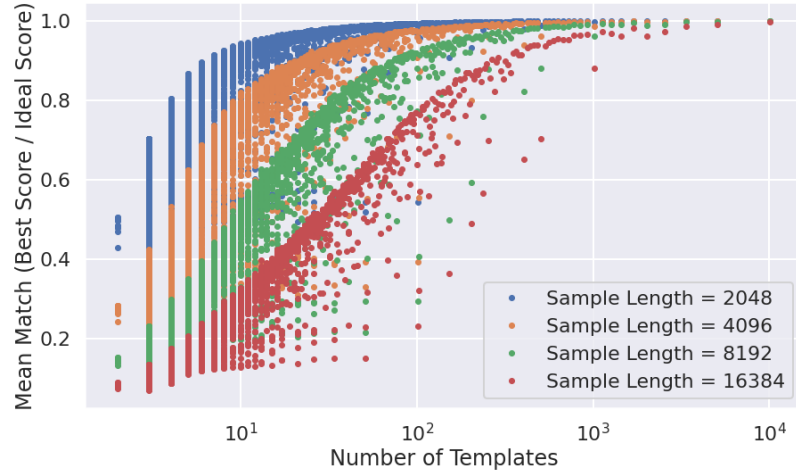


Figure 4.18. The mean match of the dense template grid shown in Figure 4.17 for different numbers of templates. Grids of different sizes were obtained by decimating a dense grid of templates and the average match for each grid was computed using the same set of randomly distributed test signals. Plotting the mean match against the size of the grid allows one to visualize the exponential relationship between match and template bank size. The noise in each curve is caused by sampling effects from the decimation algorithm. In general, longer templates are harder to than shorter templates.

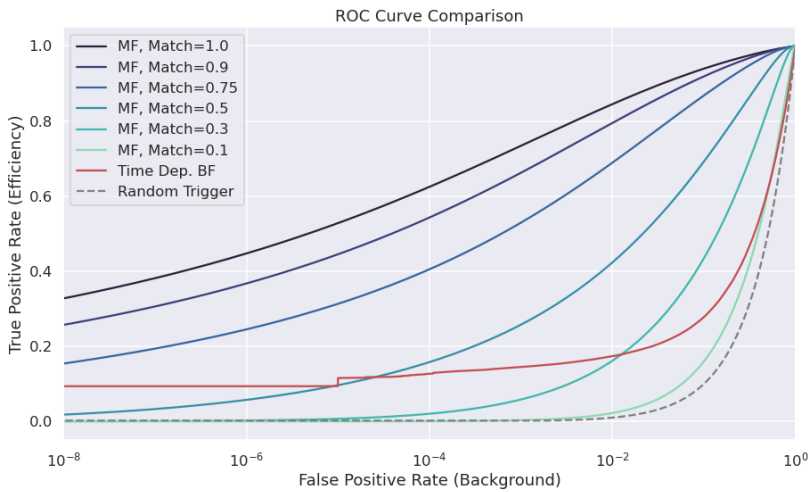


Figure 4.19. Matched filter template bank ROC curves as a function of mean match. One can see that for low match a matched filter is on average worse than the more straight forward beamforming detection approach.

2813 The effect of match on the detection efficiency of the matched filter template bank can
2814 be summarized using the ROC curve (see Figure 4.19). A single ROC curve is obtained
2815 by averaging over the PDFs that describe the detection probabilities of each individual
2816 template. The matched filter score for a template follows a Rician distribution with a
2817 mean value equal to the matched filter score multiplied by the match ratio between the
2818 template and signal. Therefore, the distribution that describes the average matched filter
2819 score when there is a signal in the data is obtained by averaging over the distributions
2820 for every template, whose expectation values are multiplied by the average match ratio.

2821 The distribution of the matched filter score when there is no signal in the data follows
2822 a Rayleigh distribution. Therefore, a trials penalty, which is the statistical penalty one
2823 pays for randomly checking many templates in order to avoid a random match between
2824 noise and a template, is included by computing the joint distribution of N_{template} Rayleigh
2825 distributions, where N_{template} is the size of the template bank. For more information on
2826 the calculation of matched filter template bank ROC curves please refer to Section 4.4.

2827 An alternative way to visualize the detection performance for each algorithm is to
2828 specify a minimum acceptable false positive rate at the trigger level. This is equivalent
2829 to specifying a minimum threshold on the value of the matched filter score or the size of
2830 a frequency peak for a beamforming power threshold trigger. One can then draw regions
2831 of detectable signals as a function of the electron's pitch angle and radial position (see
2832 Figure 4.20). A kinetic energy shift is equivalent to an overall frequency shift of the
2833 signal and should have no effect on the detection probability assuming sufficient density
2834 of matched filter templates in the energy dimension. A electron is declared "detectable"
2835 for the regions in Figure 4.20 if the signal has at least 50% probability of falling above the
2836 decision threshold of the respective classifier. One can see that the parameter space of
2837 detectable signals is greatly expanded beyond the beamforming power threshold trigger
2838 with a matched filter (MF) or deep neural network (DNN) (see Section 4.3.3). Plots such
2839 as Figure 4.20 are useful for visualization, but, since the handling of detection likelihood
2840 is not sufficiently rigorous, the detection probability boundaries are not well-suited to
2841 sensitivity estimates.

2842 **Optimized Matched Filtering Implementation for the FSCD**

2843 The biggest practical obstacle to the implementation of a matched filter template bank
2844 detection approach is oftentimes the computational cost associated with exhaustively
2845 calculating the matched filter scores of the template bank, and the FSCD is no exception
2846 in this regard. At a basic level computing a matched filter score requires the convolution

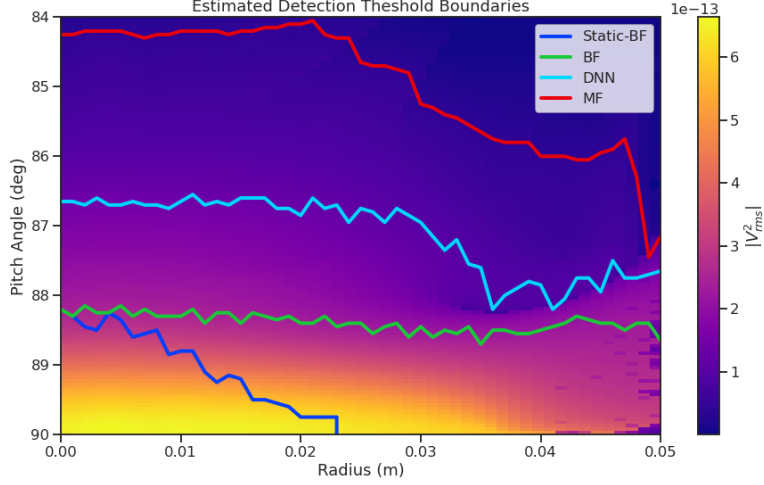


Figure 4.20. Boundaries of detectable electrons in pitch angle kinetic energy space for a series of different signal detection algorithms. A detectable signal is defined as a signal that is above a consistent decision with at least 50% probability. This non-rigorous treatment of detection probability is primarily useful for the visualization the relative increases in detection performance provided by the different algorithms. The static beamforming (Static-BF) algorithm is the digital beamforming algorithm introduced above without the ∇B -drift correction. The DNN algorithm refers to a convolutional neural network classifier trained to detect CRES signals (see Section 4.3.3).

of two vectors, which can be performed very efficiently by computers if the convolution theorem and fast Fourier transforms (FFT) are utilized. Furthermore, one can consider applying digital beamforming as a pre-processing step to reduce the dimensionality of the data before the matched filter is applied. In order to understand the relative gain in computational efficiency offered by these optimizations we analyze the total number of floating-point operations (FLOP) of several matched filter implementations in big O notation that utilize different combinations of optimizations.

A direct implementation of a matched filter as specified by Equation 4.28 involves the convolution of N_{ch} signals of length N_s with template signals of length N_t . As a uniform metric we shall compare the FLOP of the various matched filter implementations on a per-template basis, since each implementation scales linearly with the number of templates. The direct convolution approach to matched filtering costs

$$O(N_{\text{ch}}) \times O(N_s \times N_t) \quad (4.31)$$

FLOP per-template, whose cost is dominated by the $O(M \times N)$ convolution operation. The computational cost of the direct matched filter approach can be significantly

2861 reduced by exploiting the convolution theorem and FFT algorithms. If we restrict
 2862 ourselves to signals and templates that contain equal numbers of samples then the
 2863 convolution can be calculated by Fourier transforming both vectors, performing the
 2864 point-wise multiplication, and then performing the inverse Fourier transform to obtain
 2865 the convolution result. The FFT algorithm is able to compute the Fourier transform
 2866 utilizing only $O(N \log N)$ operations compared to $O(N^2)$ for a naive Fourier transform
 2867 implementation. This optimization results in a computational cost per-template of

$$O(N_{\text{ch}}) \times O(N_s \log N_s) \quad (4.32)$$

2868 A typical signal vector in the FSCD contains $O(10^4)$ samples in which case the FFT
 2869 reduces the computational cost of the matched filter by a factor of $O(10^3)$. This large
 2870 reduction in computational cost implies that a direct implementation of a matched filter
 2871 is completely infeasible in the FSCD due to resource constraints.

2872 Rather than relying solely on the matched filter it is tempting to consider using
 2873 digital beamforming as an initial step in the signal reconstruction for the purposes of
 2874 data reduction. The primary motivation is to reduce the dimensionality of the data by
 2875 a factor of N_{ch} by combining the array outputs coherently into a single channel. One
 2876 can view the beamforming operation as a partial matched filter, in the sense that the
 2877 matched filter convolution contains the beamforming phased summation along with a
 2878 prediction of the signal shape. By separating beamforming from the signal shape one
 2879 hopes to reduce the overall computational cost by effectively shrinking the number of
 2880 templates and reducing the number of operations required to check each one.

2881 The nature of this optimization requires that we account for the number of templates
 2882 used for pure matched filtering versus the hybrid approach. To first order, the total
 2883 number of templates at the trigger stage is a product of the number of guesses for each
 2884 of the electron's parameters

$$N_T = N_E \times N_\theta \times N_r \times N_\varphi, \quad (4.33)$$

2885 where N_E is the number of kinetic energies, N_θ is the number of pitch angles, N_r is the
 2886 number of starting radial positions, and N_φ is the number of starting azimuthal positions.
 2887 The starting axial position and cyclotron motion phase are not necessary to include in
 2888 the template bank since these parameters manifest themselves as the starting phase of
 2889 the signal, which is effectively marginalized when using a FFT to compute the matched
 2890 filter convolution. Therefore, the total number of operations required by a matched filter

2891 to detect a signal in a segment of array data is on the order of

$$O(N_T) \times O(N_{ch}) \times O(N_s \log N_s) \quad (4.34)$$

2892 With the hybrid approach we attempt to remove the spatial parameters from the
2893 template bank by using beamforming to combine the array signals into a single channel.
2894 Beamforming explicitly assumes a starting position, which allows us to only use matched
2895 filter templates that span the two-dimensional space of kinetic energy and pitch angle.
2896 The total computational cost of the hybrid method is directly proportional to the number
2897 of beamforming positions. For the time-dependent beamforming defined in Section 4.3.1,
2898 the number of beamforming positions is given by

$$N_{BF} = N_r \times N_\varphi \times N_{\omega_{\nabla B}}, \quad (4.35)$$

2899 where N_r and N_φ are the same spatial parameters encountered in the pure matched
2900 filter template bank and $N_{\omega_{\nabla B}}$ is the number of ∇B -drift frequency assumptions. If a
2901 unique drift frequency is used for each pitch angle then the hybrid approach is effectively
2902 equivalent to a pure matched filter in the number of operations. The key efficiency gain
2903 of the hybrid approach is to exploit the relatively small differences in $\omega_{\nabla B}$ for electrons
2904 of different pitch angles by using only a small number of average drift frequencies.

2905 The total number of operations for the hybrid approach can be expressed as a sum of
2906 the operations required by the beamforming and matched filtering steps,

$$O(N_{BF}) \times O(N_{ch} N_s) + O(N_{BF}) \times O(N_E N_\theta) \times O(N_s \log N_s). \quad (4.36)$$

2907 The first product in the sum is the number of operations required by beamforming,
2908 which is simply the number of beamforming points times the computational cost of the
2909 beamforming matrix multiplication, and the second product is the computational cost
2910 of matched filtering the summed signal generated by each beamforming position. To
2911 compare this to pure matched filtering we take the ratio of Equations 4.34 and 4.36 to
2912 obtain

$$\Gamma_{BFMF} = \frac{O(N_{\omega_{\nabla B}})}{O(N_E N_\theta) \times O(\log N_s)} + \frac{O(N_{\omega_{\nabla B}})}{O(N_{ch})}. \quad (4.37)$$

2913 This expression can be simplified by observing that $O(N_E N_\theta) \times O(\log N_s) \gg O(N_{ch})$,

2914 which means that the ratio of computational cost for the two methods can be reduced to

$$\Gamma_{\text{BFMF}} \approx \frac{O(N_{\omega_{\nabla B}})}{O(N_{\text{ch}})}. \quad (4.38)$$

2915 If we limit ourselves to a number of estimated drift frequencies of $O(1)$ then we see that
2916 the estimated computational cost reduction of the hybrid approach is of $O(N_{\text{ch}})$. This is
2917 quite a large reduction considering that the FSCD antenna array contains sixty antennas
2918 in the baseline design.

2919 The main drawback of the hybrid approach is that the limited number of allowed
2920 drift frequency guesses can lead to detection efficiency loss due to phase mismatch. The
2921 degree of phase error from an incorrect drift frequency is proportional to the length of
2922 the array data vector used by the signal detection algorithm. For signals with lengths
2923 equal to the baseline FSCD Fourier analysis window of 8192 samples, typical phase errors
2924 from using an average versus the exact ∇B -drift frequency are on the order of a few
2925 percent in terms of the signal energy. This has a relatively small impact on the overall
2926 detection efficiency, however, future experiments with antenna array CRES will want to
2927 balance optimizations such as these during the design phase to keep experiment costs to
2928 a minimum while still achieving scientific goals.

2929 Kinetic Energy and Pitch Angle Degeneracy

2930 More accurate modeling of a matched filter requires that we consider the effects of
2931 mismatched signals and template, since this more accurately reflects the real-world usage
2932 of a matched filter where many incorrect templates are convolved with the data until the
2933 matching template is found. One way to study this is to use the grid of simulated signals
2934 to compute the matched filter scores between mismatched signals and templates and
2935 evaluate the matched filter scores under this scenario. What one finds when performing
2936 this analysis is that templates for kinetic energies and pitch angles that do not match
2937 the underlying signal can have matched filter scores that are indistinguishable from the
2938 matched filter score of the correct template (see Figure 4.21 and Figure 4.21).

2939 This degeneracy in matched filter score is the result of correlations between the kinetic
2940 energy of the electron and the pitch angle caused by changes in the average magnetic field
2941 experienced by an electron for different pitch angles. While in principle helpful for the
2942 purposes of signal detection these correlations are unacceptable since they greatly reduce
2943 the energy resolution of the experiment by causing electrons with specific kinetic energy
2944 to templates across a wide range of energies. It is important to emphasize that this

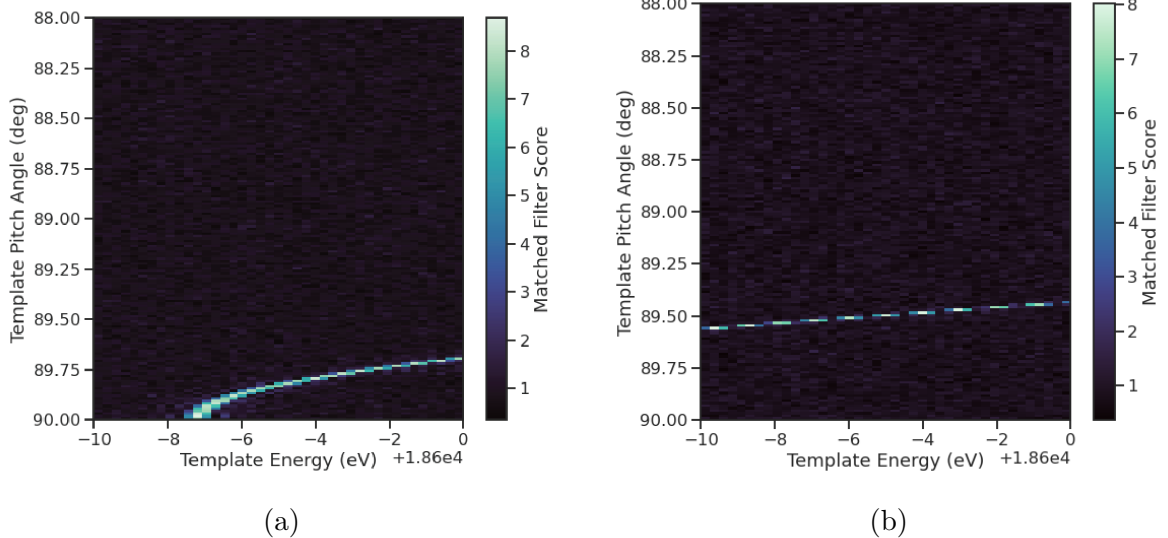


Figure 4.21. Two example illustrations of the correlation between kinetic energy and pitch angle imparted by the shape of the FSCD magnetic trap. The correlations manifest themselves as degeneracies in the matched filter score where multiple matched filter templates have the same matched filter for a particular signal. These degeneracies are a sign that the magnetic trap must be redesigned in order to break the correlation between pitch angle and kinetic energy.

2945 degeneracy cannot be fixed by implementing a different signal reconstruction algorithm.
 2946 As revealed by the matched filter scores the shapes of the signals for different parameters
 2947 are identical. Resolving this degeneracy between pitch angle and energy requires the
 2948 design of a new magnetic trap with steeper walls so that the average magnetic field
 2949 experienced by an electron is less dependent on pitch angle.

2950 **4.3.3 Machine Learning**

2951 Machine learning is a vast and rapidly developing field of research [74]. In this Section
 2952 we shall attempt to provided a brief introduction to some of the concepts and techniques
 2953 of machine learning that were applied to CRES signal detection rather than attempt a
 2954 comprehensive overview.

2955 **Introduction to Machine Learning**

2956 Digitization of the FSCD antenna array generates large amounts of data that must be
 2957 rapidly processed to enable real-time signal detection and reconstruction. While digital
 2958 beamforming combined with a power threshold is relatively computationally inexpensive,
 2959 it is relatively ineffective at detecting CRES signal with small pitch angles, since it relies

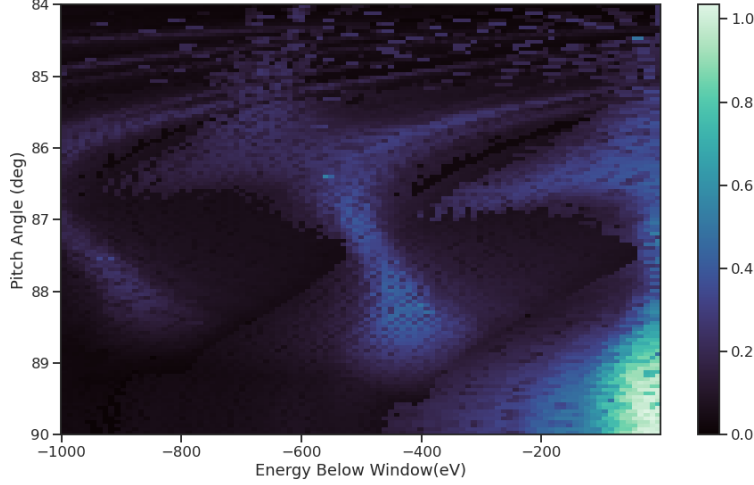


Figure 4.22. A visualization of the correlation between energy and pitch angle in the FSCD magnetic trap. The image is formed by computing the match of the best template from a grid consisting of pitch angles from 84 to 90 degrees in steps of 0.05 degrees, kinetic energies from 17574 to 18574 eV, located at 2 cm from the central axis, and simulated for a length of three FSCD time-slices. The signals used to compute the best matching template consisted of a grid from 84 to 90 degrees in steps of 0.05 degrees, kinetic energies from 18550 to 18575 eV in steps of 0.25 eV, located 2 cm from the central axis, and simulated for three FSCD time-slices. The colored regions of the plot show how well signals with lower energy can match those of higher energy for the FSCD magnetic trap, which is proportional to the achievable energy resolution of the FSCD design.

2960 on a visible frequency peak above the noise. On the other hand, a matched filter is able
 2961 to detect signals with a significantly larger range of parameters, however, the exhaustive
 2962 search of matched filter templates can be computationally expensive. Machine learning
 2963 based triggering algorithms have been used successfully in many different high-energy
 2964 physics experiments [75] and recent developments have shown success in the detection
 2965 of gravitational wave signals using machine learning techniques [76, 77] in place of the
 2966 more traditional matched filtering method. This motivates the exploration of machine
 2967 learning as a potential CRES signal detection algorithm.

2968 There are several different approaches to machine learning, but the one most important
 2969 to our discussion here is the supervised learning approach. In supervised machine learning
 2970 one uses a differentiable model or function that is designed to map the input data to the
 2971 appropriate label [74]. The data is represented as a multidimensional matrix of floating
 2972 point values such as an image or a time-series, and the label is generally a class name
 2973 such as signal or noise for classification problems or a continuous value like kinetic energy
 2974 in the case of regression problems.

2975 In supervised learning the model is trained to map from the data to the correct label
2976 by evaluating the output of the model using a training dataset consisting of a set of
2977 paired data and labels. To evaluate the difference between the model output and the
2978 correct label a loss function is used to quantify the error between the model prediction
2979 and the ground truth. For example, a common loss function in regression problems is the
2980 squared error loss function, which quantifies error using the squared difference between
2981 the model output and label.

2982 Using the outputs of the loss function the next step in supervised learning is to
2983 compute the gradient of error with respect to the model parameters in a process called
2984 backpropagation. Using the model parameter gradients the last step in the supervised
2985 learning process is to perform an update of the parameter values in order to minimize
2986 the error in the model predictions across the whole dataset. This loop is performed many
2987 times while randomly shuffling the dataset until the error converges to a minimum value
2988 at which point the training procedure has finished. It is standard practice to monitor
2989 the training procedure by evaluating the performance of the model using a separate
2990 validation dataset that matches the statistical distribution of the training data and to
2991 check the performance of the model after training using yet another dataset called the
2992 test dataset. These practices help to guard against overtraining which is a concern for
2993 models with many parameters.

2994 Convolutional Neural Networks

2995 A popular class of machine learning models are neural networks. A neural network is
2996 essentially a function composed of a series of linear operations called layers which take a
2997 piece of data typically represented as a matrix, multiplies the elements of the data by a
2998 weight, and then sums these products to produce an output matrix. Neural networks
2999 composed of purely linear operations are unable to model complex non-linear behavior,
3000 therefore, non-linear activation functions are applied to the outputs of each of the layers
3001 to increase the ability of the neural network to model complex relationships between the
3002 data.

3003 Neural networks are typically composed of at least three layers, but with the present
3004 capabilities of computer hardware they more often contain many more than this. The
3005 first layer in a neural network is called the input layer, because it takes the data objects
3006 as input, and the last layer in a neural network is known as the output layer. The
3007 output layer is trained by machine learning to map the data to a desired output using
3008 the supervised learning procedure described in Section 4.3.3. In between the input and

3009 the output layer are typically several hidden layers that receive inputs from and transmit
3010 outputs to other layers in the neural network model. The term deep neural network
3011 (DNN) refers to those neural networks that have at least one hidden layer, which have
3012 proven to be extremely powerful tools for pattern recognition and function approximation.

3013 An important type of DNN are convolutional neural networks (CNN) that typically
3014 contain several layers which perform a convolution of the input with a set of filters. These
3015 convolution operations are typically accompanied by layers that attempt to down-sample
3016 the data along with the standard neural network activation functions. A standard CNN
3017 is composed of several convolutional layers at the beginning of the network and ends
3018 with a series of fully-connected neural network layers at the output. Intuitively, one
3019 can imagine that the convolutional layers are extracting features from the data that
3020 fully-connected layers use to perform the classification or regression task.

3021 **Deep Filtering for Signal Detection in the FSCD**

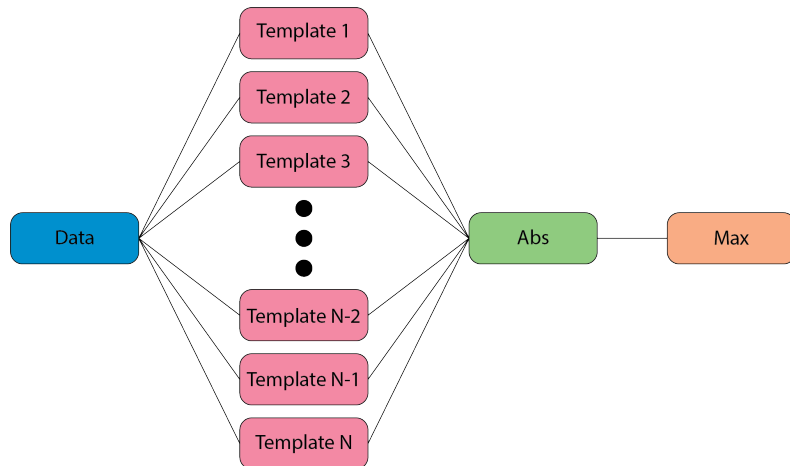


Figure 4.23. A representation of a matched filter template bank as a convolutional neural network. The network has a single layer composed of the templates, which act as convolutional filters. The activation of the neural network is an absolute value followed by a max operator.

3022 CNNs have been extremely influential in the field of computer vision, particularly tasks
3023 such as image segmentation and classification, but have also been applied in numerous
3024 experimental physics contexts. Given the particular challenge posed by signal detection
3025 and reconstruction in the FSCD we are interested in exploring the potential of machine
3026 learning as an effective algorithm for real-time signal detection, since this application
3027 requires both high efficiency and fast evaluation.

3028 In the machine learning paradigm signal detection is equivalent to a binary classifi-

cation problem between the signal and noise data classes, and my investigation focuses specifically on the application of CNNs to signal detection in the FSCD, which is motivated by relatively recent demonstrations of CNNs achieving classification accuracies for gravitational wave time-series signals comparable to a matched filter template bank. In this framework it is possible to interpret the matched filter as a type of CNN composed of a single convolutional layer with the templates making up the layer filters (see Figure 4.23). Since this neural network has no hidden layers, it is not a DNN like we have been discussing so far, but we can attempt to construct a proper CNN that attempts to reproduce the classification performance of the matched filter network.

The name deep filtering refers to this scheme of replacing a matched filter template bank with a DNN. The reason why one might want to do this is that it may be possible to exploit redundancies and correlations between templates that may allow one to perform signal detection with similar accuracy but with fewer computations, which is important for real-time detection scenarios like the FSCD experiment. In Section 4.4 we perform a detailed comparison of the signal detection performance of a CNN to beamforming and a matched filter template bank.

Deep filtering is conceptually a simple technique. Similar to a matched filter template bank a large number of simulated CREs signals are generated and used to train a model to distinguish between signal and noise data (see Figure 4.24). In order to reduce the dimensionality of the input FSCD data a digital beamforming summation is applied to the raw time-series data generated by Locust to compress the 60-channel data to a single time-series. CREs signal have a sparse frequency representation and experiments training CNN's on time-series and frequency series data found that models trained on frequency spectrum data performed significantly better, therefore, an FFT is applied to the summed time-series before being normalized and fed to the classification model.

The data used to train the model consists of an equal proportion of signal and noise frequency spectra. Unique samples of WGN are generated and added to the signals during training time to avoid having to pre-generate and store large samples of noise data. The binary cross-entropy loss function combined with the ADAM optimizer proved effective at training the models to classify CREs data. A simple hyperparameter optimization was performed by manually tuning model, loss function, and optimizer parameters. The model and training loops were implemented in python using the PyTorch deep learning framework. Standard machine learning best practices were followed when training the models, such as overtraining monitoring using a validation dataset. Models were trained until the training loss and accuracy converged and then evaluated using a separate test

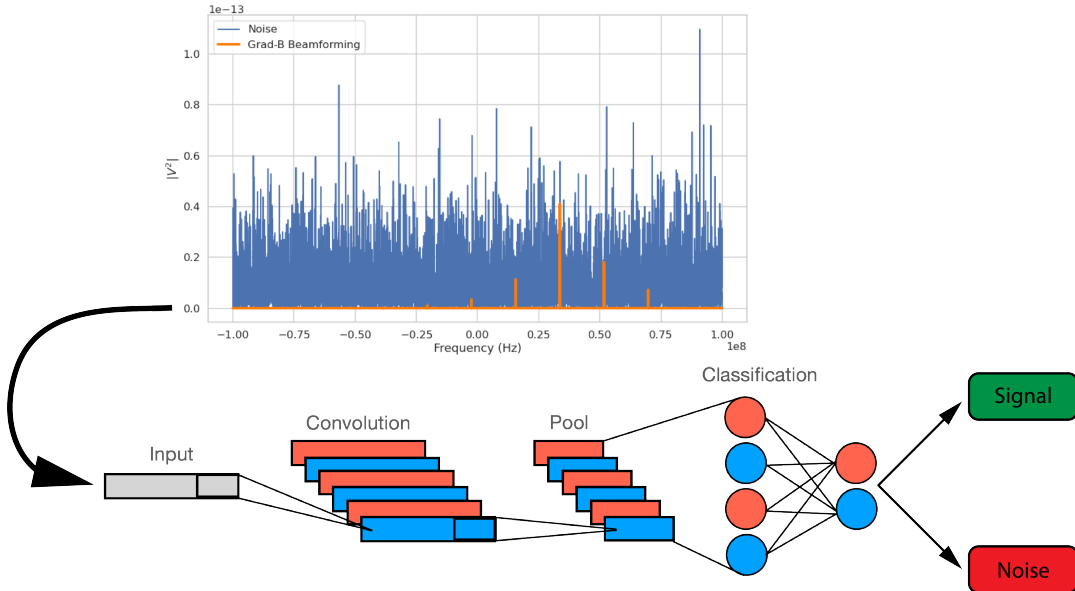


Figure 4.24. A graphical depiction of CRES signal detection using a CNN. A noisy segment of data is converted to a frequency series using digital beamforming and a FFT. The complex-valued frequency series is input into a trained CNN model that classifies the data as signal or noise using a decision threshold on the CNN output.

3064 data set.

3065 The classification results of the test dataset are used to quantify the relationship
 3066 between the true positive rate and the false positive rate for the model. The true positive
 3067 rate is analogous to detection efficiency and the false positive rate is a potential source of
 3068 background in the detector. One can limit the rate of false positives using a sufficiently
 3069 high threshold on the model output at the cost of a lower detection efficiency (see Figure
 3070 4.25 and Figure 4.26). As expected, the performance of the model at signal classification
 3071 is negatively effected the noise power, which is quantified by the noise temperature.

3072 **4.4 Analysis of Signal Detection Algorithms for the An-** 3073 **tenna Array Demonstrator**

3074 This section contains an early version of the manuscript for the triggering paper prepared
 3075 for publication in JINST. In it I present a relatively detailed analysis of the signal
 3076 detection performance of the three signal detection approaches discussed so far using a
 3077 population of simulated CRES signals generated with Locust. The focus of the paper is
 3078 on the performance of the signal detection algorithms for pitch angles below 88.5° where

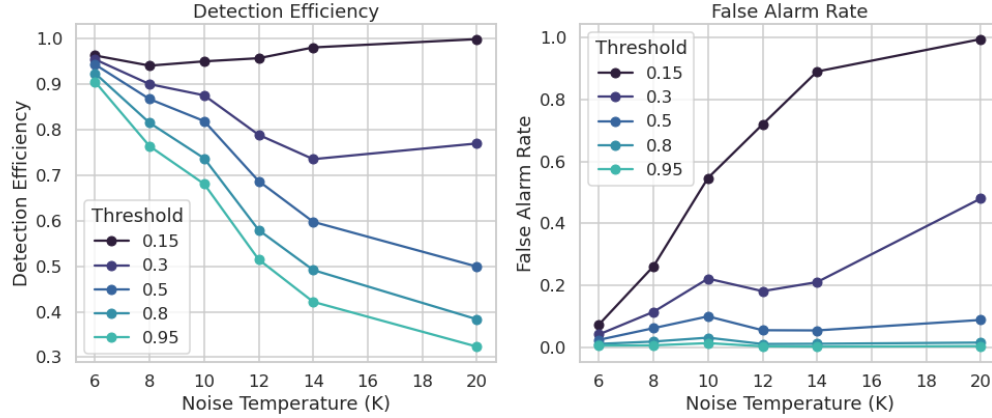


Figure 4.25. The detection efficiency and false alarm rate (false positive rate) as a function of the decision threshold for different values of the noise temperature. The model is trained to output a value close to one for data that contains a signal and outputs a value near zero when the data contains only noise. One sees that a lower decision threshold will have a high detection efficiency at the cost of a high rate of false alarms.

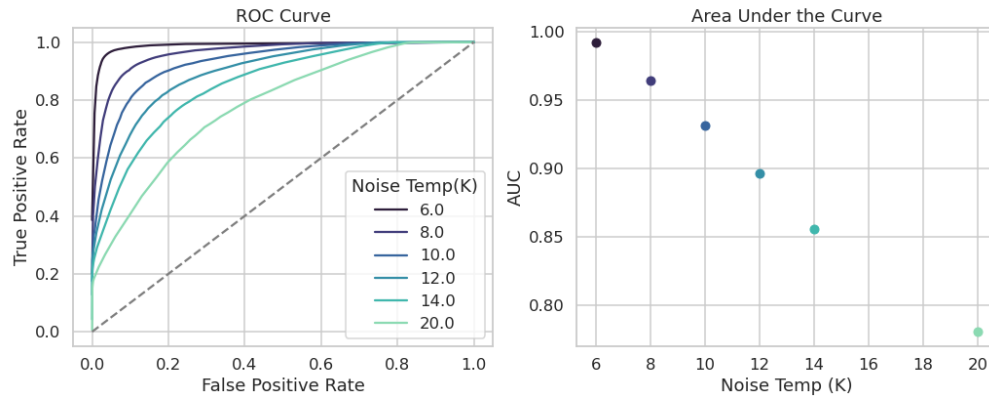


Figure 4.26. ROC curves for a CNN model classifying CRES signals. One can see that the area under the curve, which is a figure of merit that describes the performance of the classifier, is roughly linearly dependent with the noise temperature.

3079 the beamforming power threshold begins to fail.

3080 4.4.1 Introduction

3081 Cyclotron Radiation Emission Spectroscopy (CRES) is a technique for measuring the
 3082 kinetic energies of charged particles by observing the frequency of the cyclotron radiation
 3083 that is emitted as they travel through a magnetic field [40]. The Project 8 Collaboration
 3084 is developing the CRES technique as a next-generation approach to tritium beta-decay
 3085 endpoint spectroscopy for neutrino mass measurement. Recently, Project 8 has used

3086 CRES to perform the first ever tritium beta-decay energy spectrum and neutrino mass
3087 measurement [42, 43].

3088 Previous CRES measurements have utilized relatively small volumes of gas that are
3089 directly integrated with a waveguide transmission line, which transmits the cyclotron
3090 radiation emitted by the trapped electrons to a cryogenic amplifier. While this technology
3091 has had demonstrable success, it is not a feasible option for scaling up to significantly
3092 larger measurement volumes. In particular, the goal of the Project 8 Collaboration
3093 is to use CRES combined with atomic tritium to measure the neutrino mass with a
3094 40 meV sensitivity. Achieving this sensitivity goal will require a multi-cubic-meter scale
3095 measurement volume in order to obtain the required event statistics in the tritium
3096 beta-spectrum endpoint region; hence, there is a need for new techniques to enable large
3097 volume CRES measurements for future experiments.

3098 One approach is to surround a large volume with an array of antennas that together
3099 collect the cyclotron radiation emitted by trapped electrons [41, 78]. A promising
3100 array design is an inward-facing uniform cylindrical array that surrounds the tritium
3101 containment volume. Increasing the size of the antenna array, by adding additional
3102 rings of antennas along vertical axis, allows one to grow the experimental volume until a
3103 sufficient amount of tritium gas can be observed by the array. A challenging aspect of
3104 this approach is that the total radiated power emitted by an electron near the tritium
3105 spectrum endpoint is on the order of 1 fW or less, which is then distributed between
3106 all the antennas in the array. Consequently, detecting the presence of a CRES signal
3107 and determining the electron's kinetic energy requires reconstructing the entire antenna
3108 array output over the course of the CRES event, posing a significant data acquisition
3109 and signal reconstruction challenge.

3110 Project 8 has developed a triggering system to enable real-time identification of CRES
3111 events using an antenna array [79]. Previous measurements with the CRES technique
3112 have utilized a threshold on the frequency spectrum formed from a segment of CRES
3113 time-series data. This algorithm relies on the detection of a frequency peak above the
3114 thermal noise background, which limits the kinematic parameter space of detectable
3115 electrons. Due to the limitations of this power threshold, Project 8 has been investigating
3116 alternative signal identification approaches, including both matched filtering and machine
3117 learning based classifiers, to improve the detection efficiency of the experiment. In
3118 order to evaluate the relative gains in detection efficiency that come from utilizing
3119 these alternative algorithms, we develop analytical models for the power threshold and
3120 matched filter signal classifier performance applicable to an antenna array based CRES

3121 detector. In addition, we implement and test a basic convolutional neural network (CNN)
 3122 as a first step towards the development of neural-network based classifiers for CRES
 3123 measurements. These results allow us to compare the estimated detection efficiencies of
 3124 each of these methods, which we weigh against the associated computational costs for
 3125 real-time applications.

3126 The outline of this paper is as follows. In Section 4.4.2 we give an overview of a
 3127 prototypical antenna array CRES experiment, and describe the major steps involved
 3128 in the proposed approach to real-time signal identification. In Section 4.4.3 we develop
 3129 models for the power threshold and matched filter algorithms, and introduce the machine
 3130 learning approach and CNN architecture. In Section 4.4.4 we describe our process for
 3131 generating simulated CRES signal data and the details of training the CNN. Finally,
 3132 in Section 4.4.5 we perform a comparison of the signal classification accuracy of the
 3133 three approaches and discuss the relevant trade-offs in terms of detection efficiency and
 3134 computational cost.

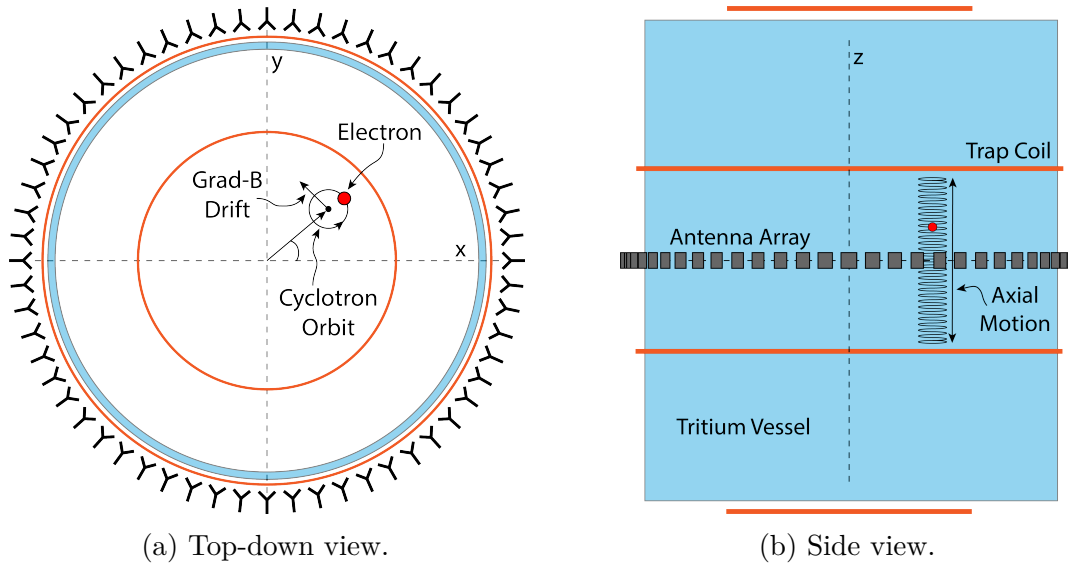


Figure 4.27. An illustration of the conceptual design for an antenna array CRES tritium beta-decay spectrum measurement. The antenna array geometry consists of a 20 cm interior diameter with 60 independent antenna channels arranged evenly around the circumference. The nominal antenna design is sensitive to radiation in the frequency range of 25-26 GHz, which corresponds to the cyclotron frequency of electrons emitted near the tritium beta-spectrum endpoint in a 1 T magnetic field. The array is located at the center of the magnetic trap produced by a set of current-carrying coils. The nominal magnetic trap design is capable of trapping electrons up to 5 cm away from the central axis of the array and traps electrons within an approximately 6 cm long axial region centered on the antenna array.

3135 **4.4.2 Signal Detection with Antenna Array CRES**

3136 **4.4.2.1 Antenna Array and DAQ System**

3137 In order to explore the potential of antenna array CRES for neutrino mass measurement,
3138 the Project 8 Collaboration has developed a conceptual design for a prototype antenna
3139 array CRES experiment [41, 78], called the Free-space CRES Demonstrator or FSCD,
3140 which could be used as a demonstration of the antenna array measurement technique
3141 (see Figure 4.27). The FSCD utilizes a single ring of antennas, which is the simplest
3142 form of a uniform cylindrical array configuration, to surround a radio-frequency (RF)
3143 transparent tritium gas vessel. A prototype version of this antenna array has been built
3144 and tested by the Project 8 collaboration to validate simulations of the array radiation
3145 pattern and beamforming algorithms [44]. In the FSCD the antenna array is positioned
3146 at the center of the magnetic trap formed by a set of electro-magnetic coils that are
3147 designed to produce a magnetic trap with flat central region and steep walls both radially
3148 and axially.

3149 When a beta-decay electron is trapped its motion consists of three primary components.
3150 The component with the highest frequency is the cyclotron orbit whose frequency is
3151 determined by the size of the background magnetic field. The FSCD design assumes
3152 a background magnetic field value of approximately 0.96 T, which results in cyclotron
3153 frequencies for electrons with kinetic energies near the tritium beta-spectrum endpoint
3154 from 25 to 26 GHz. The component with the next highest frequency is the axial oscillation
3155 experienced by electrons with pitch angles of less than 90° [61]. The flat region of the
3156 FSCD magnetic trap extends approximately 3 cm above and below the antenna array
3157 plane causing electrons to move back and forth as they are reflected from the trap walls.
3158 Typical oscillation frequencies are on the order of 10's of MHz, which results in an
3159 oscillation period that is $O(10^3)$ smaller than the duration of a typical CRES event.
3160 Therefore, when reconstructing CRES events we treat the electron as occupying only an
3161 average axial position at the center of the magnetic trap, since we are not able to resolve
3162 the axial position as a function of time. The component of motion with the smallest
3163 frequency is ∇B -drift caused by radial field gradients in the trap, producing an orbit of
3164 the electron around the central axis of the trap with a frequency on the order of a few
3165 kHz, dependent on the pitch angle and the radial position of the electron.

3166 The data acquisition (DAQ) system digitizes the signals from the antenna array and
3167 combines thee data streams into a time-ordered matrix of array snapshots that can be
3168 used by the reconstruction algorithms. The FSCD DAQ system design [79] is divided into

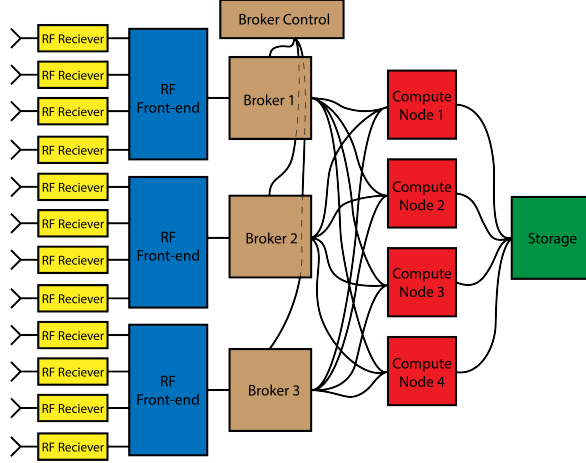


Figure 4.28. A high-level diagram of the DAQ system architecture envisioned for the FSCD.

3169 three layers 4.28. The first layer is the RF front-end, which includes the antenna array,
 3170 the RF receiver boards, and the digitization electronics. The receiver board contains an
 3171 amplifier, RF mixer, and bandpass filter to enable down-conversion, and is followed by
 3172 the digitization electronics that sample the CRES signals at 200 MHz. In order to achieve
 3173 an adequate signal-to-noise ratio to detect CRES events, the DAQ system for the antenna
 3174 array demonstrator must have a total system noise temperature of ≈ 10 K, which we
 3175 can achieve by using low-noise amplifiers and operating at cryogenic temperatures. After
 3176 digitization, the array data must be reorganized from individual data streams sorted
 3177 by channel into array snapshots sorted by time. In order to solve this data transfer
 3178 and networking problem the second layer of the DAQ system consists of a set of broker
 3179 computer nodes that reorganize the array data into time-ordered chunks. This approach
 3180 allows us accommodate different data transfer requirements by scaling the number of
 3181 broker nodes in this layer accordingly. Next, the broker layer distributes these chunks
 3182 of array data to the final layer of the DAQ system, which consists of a set of identical
 3183 reconstruction nodes that perform the calculations required for CRES reconstruction.
 3184 Similar to the broker layer, the number of reconstruction nodes can be increased or
 3185 decreased depending on the amount of computer power required for real-time CRES
 3186 reconstruction.

3187 The design of the FSCD DAQ system is intended to enable a significant portion of
 3188 the CRES event reconstruction to occur in real-time. The motivation for this comes from
 3189 the fact that the FSCD antenna array generates approximately 1 exabyte of raw data
 3190 per year of operation. Therefore, in order to reduce the data-storage requirements, it is
 3191 ideal to perform at least some of the CRES event reconstruction in real-time so that it

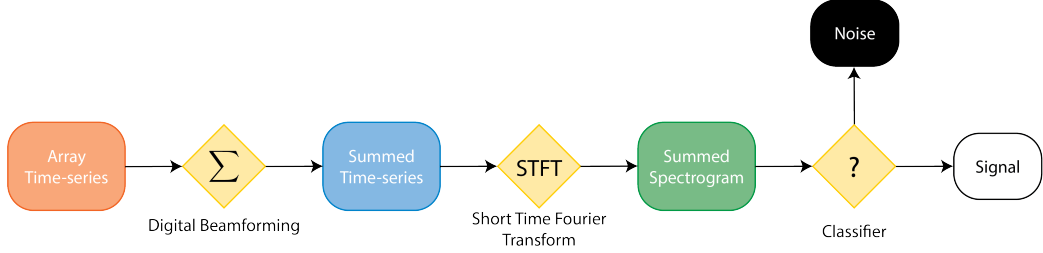


Figure 4.29. A block diagram illustration of the real-time triggering algorithm proposed for antenna array CRES reconstruction.

is possible to save a reduced form of the data for offline analysis. The first step of the real-time reconstruction would be a real-time signal detection algorithm, which is the focus of this paper. Our approach consists of three main operations performed on the time-series data blocks including digital beamforming, a short time Fourier transform (STFT), and a binary classification algorithm to distinguish between signal and noise data (see Figure 4.29).

4.4.2.2 Real-time Signal Detection

The first step in the real-time detection algorithm is digital beamforming, which is a phased summation of the signals received by individual antennas in the array (see Figure 5.21). The phase shifts correspond to the path length differences between a spatial position and each individual antenna such that, when there is an electron located at the beamforming position, all the signals received by the array constructively interfere. Since we do not know ahead of time where an electron will be produced in the detector, we define a grid of beamforming positions that cover the entire region where electrons can be trapped and perform a phased summation for each of these points for every time-step in the array data block. As we saw in Section 4.4.2.1, the axial oscillation of the electrons prevents us from resolving it's position along the Z-axis of the trap, therefore our beamforming grid need only cover the possible positions of the electron in the two-dimensional plane defined by the antenna array.

The equation defining digital beamforming can be expressed as

$$\mathbf{y}[n] = \Phi^T[n]\mathbf{x}[n], \quad (4.39)$$

where $\mathbf{x}[n]$ is array snapshot vector at the sampled time n , $\Phi[n]$ is the matrix of beamforming phase shifts, and $\mathbf{y}[n]$ is summed output vector that contains the voltages for each of the summed channels that correspond to a particular beamforming position.

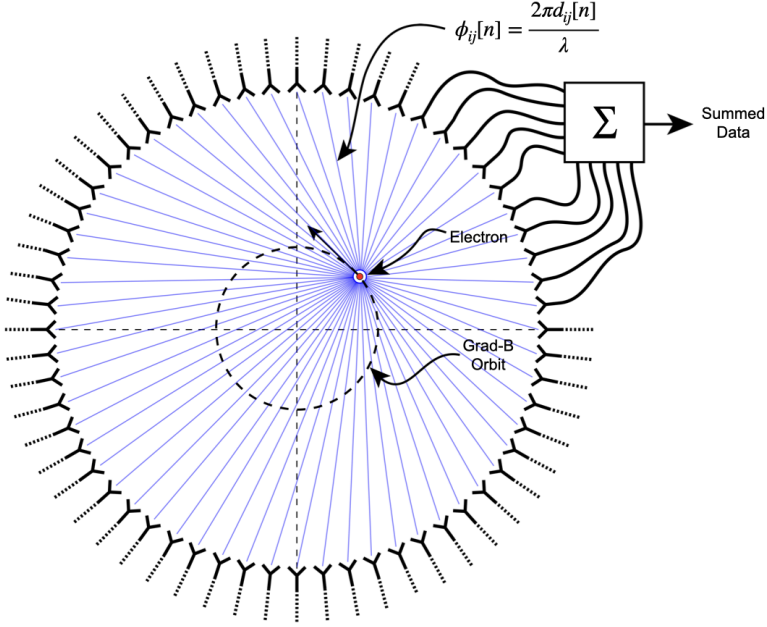


Figure 4.30. An illustration of the digital beamforming procedure. The blue lines indicate the various distances from the beamforming position to the antenna. In the situation depicted the actual position of the electron matches the beamforming position, so we should expect constructive interference when the phase shifted signals are summed. To prevent the electron's ∇B -motion from moving the electron off of the beamforming position, the beamforming phase include a time-dependence to follow the trajectory of the electron in the magnetic trap.

3215 The elements of the beamforming phase shift matrix can be expressed as a weighted
 3216 complex exponential

$$\Phi_{ij}[n] = A_{ij}[n] \exp(2\pi i \phi_{ij}[n]), \quad (4.40)$$

3217 where the indices i and j label the beamforming and antenna positions respectively. The
 3218 weight A_{ij} accounts for the relative power increase for antennas that are closer to the
 3219 position of the electron, and ϕ_{ij} is the total beamforming phase shift for the j -th antenna
 3220 at the i -th beamforming position.

3221 The beamforming phase shift is a sum of two terms

$$\phi_{ij}[n] = \frac{2\pi d_{ij}[n]}{\lambda} + \theta_{ij}[n], \quad (4.41)$$

3222 where the first term is the phase shift originating from the path length difference ($d_{ij}[n]$)
 3223 between the beamforming and antenna positions, which are represented by the vectors
 3224 (r_j, θ_j) and $(r_i, \theta_i[n])$, and the second term is the angular separation ($\theta_{ij}[n]$) of the two
 3225 positions. The angular separation enters into the beamforming phase due to an effect

3226 caused by the circular orbit of the electron that produces radiation whose phase is linearly
 3227 dependent on the relative azimuthal position of the antenna [80,81]. The time-dependence
 3228 of the beamforming phases is intended to correct for the effects of ∇B -drift, which cause
 3229 the guiding centers of electrons to orbit the center of the magnetic trap. By including a
 3230 linear time-dependence in the azimuthal beamforming position,

$$\theta_i[n] = \omega_{\nabla B} t[n] + \theta_{i,0}, \quad (4.42)$$

3231 where $\omega_{\nabla B}$ is the azimuthal grad-B drift frequency, $t[n]$ is the time vector and, $\theta_{i,0}$ is the
 3232 starting azimuthal position, we can configure the beamforming phases to effectively track
 3233 the XY-position of the guiding center over the event duration. Predicting accurate values
 3234 of $\omega_{\nabla B}$ for a specific trap and set of kinematic parameters will be done by simulations,
 3235 which are performed using the Kassiopeia software package [60] by Project 8.

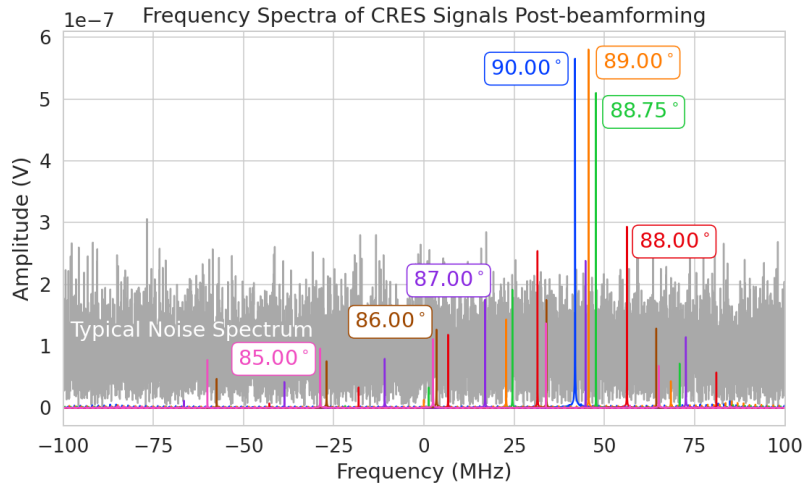


Figure 4.31. Frequency spectra of simulated CRES signals post-beamforming. The signal of a 90° electron consists of a single frequency component that is easy to detect with a power threshold on the frequency spectrum. This power threshold is still effective for signals with relatively large pitch angles such as 89.0° and 88.75° , which are composed of a main carrier and a few small sidebands. Signals with smaller pitch angles, below about 88.5° , tend to be dominated by sidebands such that no single frequency component can be reliably distinguished from the noise with a power threshold.

3236 After digital beamforming, we apply a short-time Fourier transform (STFT) to the
 3237 summed time-series to obtain the frequency spectrum representation of the signals (see
 3238 Figure 4.31). From the detection perspective, the frequency representation of the CRES
 3239 data is advantageous compared to the time domain, because the frequency spectra of
 3240 CRES signals are well-approximated by a frequency and amplitude modulated sinusoidal

whose carrier frequency increases as a linear chirp. The modulation is caused by the axial oscillation of the electron in the magnetic trap and produce frequency spectra that are well-described by a small number of frequency components. The linear chirp is caused by the energy loss due to cyclotron radiation, which results in a relatively slow increase in the frequency components of the CRES signal over time. During the standard Fourier analysis window for the FSCD of 40.96 μ sec, we expect a typical CRES signal to increase in frequency by approximately 15 kHz, which is smaller than the frequency bin width given the 200 MHz sample rate. Therefore when considering a single frequency spectrum it is justifiable to neglect the effects of the linear frequency chirp.

In the cases where the electron's pitch angle is $\gtrsim 88.5^\circ$, the majority of the signal power is contained in a single frequency component, with the remaining signal power contained in a small number of sidebands proportional to the electron's axial modulation (see Figure 4.31). In these cases detection is relatively straight-forward by implementing a power threshold on the STFT, since the amplitude of the main signal peak is distinct from the thermal noise spectrum. However, as the pitch angle of the electron is decreased below 88.5° , the modulation index of the signal increases causing the maximum amplitude of the frequency spectrum to be comparable to typical noise fluctuations. At this point, the power threshold trigger is no longer able to distinguish between signal and noise leading to a reduction in detection efficiency. The neutrino mass sensitivity of the FSCD is directly linked to the overall detection efficiency. And, because the distribution of electron pitch angles is effectively uniformly distributed across the range of pitch angles that can be trapped, the overall detection efficiency is directly influenced by the range of pitch angles that have detectable signals. Therefore, utilizing a signal detection algorithm that can more effectively identify signals with pitch angles less than 88.5° will improve both detection efficiency and ultimately the neutrino mass sensitivity of the FSCD and other CRES experiments.

Modeling the detection performance of alternative signal detection algorithms for the FSCD requires that we pose the signal detection problem in a consistent manner. The approach we take is to perform a binary hypothesis test on the frequency spectra generated by the STFT. Mathematically, this is expressed as,

$$\mathcal{H}_0 : y[n] = \nu[n] \quad (4.43)$$

$$\mathcal{H}_1 : y[n] = x[n] + \nu[n]. \quad (4.44)$$

Where under hypothesis \mathcal{H}_0 , the vector representing the frequency spectrum ($y[n]$) is

composed of pure white Gaussian noise (WGN) represented by $\nu[n]$, and under hypothesis \mathcal{H}_1 the frequency spectrum is composed of a CRES signal ($x[n]$) with added WGN. The dominant source of noise in a FSCD-like experiment is expected to be thermal Nyquist-Johnson noise, which is well approximated by a WGN distribution. In order to decide between these two hypotheses we follow the standard Neyman-Pearson approach by performing a log-likelihood ratio test between the probability distributions of the signal classifier output under \mathcal{H}_1 and \mathcal{H}_0 [71]. The output of the log-likelihood ratio test is called the test statistic, which is used to assign the data as belonging to the noise (\mathcal{H}_0) or signal (\mathcal{H}_1) classes by setting a decision threshold on the value of the test statistic.

In practice, we select the decision threshold by finding the value of the test statistic that guarantees an acceptable rate of false positives and then attempt to maximize the signal detection probability under that fixed false positive rate. Because the signal classifier will be used to evaluate the spectra of $O(10^2)$ beamforming positions every 40.96 μ sec, we will require the signal classifiers to operate with decision thresholds that provide false positive rates significantly smaller than 1%. This reduces the burden placed on later stages of the CRES reconstruction chain to reject these false positives and decreases the overall likelihood of reconstructing a false event. Below, we calculate the probability distributions that allow us characterize how different detection algorithms will perform for CRES signals in an FSCD experiment.

4.4.3 Signal Detection Algorithms

4.4.3.1 Power Threshold

The power threshold detection algorithm uses the maximum amplitude of the frequency spectra as the detection test statistic. To model the performance of this approach, consider first the case where the signal is pure WGN. For a single bin in the frequency spectrum, the probability that the amplitude falls below a specific threshold value is given by the Rayleigh cumulative distribution function (CDF),

$$\text{Ray}(x; \tau) = 1 - \exp(-|x|^2/\tau), \quad (4.45)$$

where the complex amplitude of the frequency bin is x , and τ is the WGN variance. Because the noise samples for each frequency bin are independent and identically distributed (IID), the probability that every bin in the frequency spectrum falls below the

3301 threshold is the joint CDF formed by the product of each individual frequency bin CDF,

$$F_0(x; \tau, N_{\text{bin}}) = \text{Ray}(x; \tau)^{N_{\text{bin}}}. \quad (4.46)$$

3302 The PDF for the power threshold classifier can then be obtained by differentiating the
 3303 CDF.

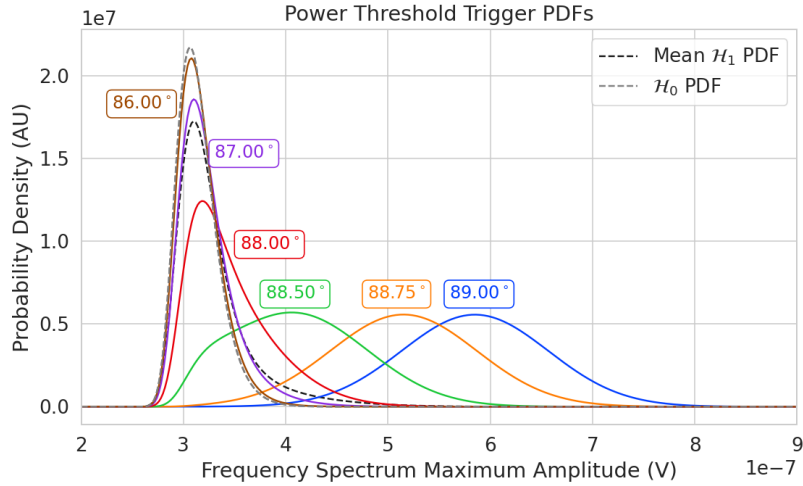


Figure 4.32. PDFs of the power threshold test statistic for CREs signals with various pitch angles as well as the PDF for the noise-only signal case. The average PDF computed for pitch angles ranging from 85.5 to 88.5° is also shown. As the pitch angle is decreased the signal PDF converges towards the noise PDF which indicates that the power threshold trigger is unable to distinguish between small pitch angle signals and noise.

3304 The probability distribution for the power threshold classifier under \mathcal{H}_1 is formed in
 3305 a similar way, but the frequency bins that contain signal must be treated separately. For
 3306 a frequency bin that contains both signal and noise we can describe the probability that
 3307 the amplitude of the bin will fall below our threshold using the Rician CDF,

$$\text{Rice}(x; \tau, \nu) = 1 - Q_1 \left(\frac{|\nu|}{\sqrt{2\tau}}, \frac{|x|}{\sqrt{2\tau}} \right), \quad (4.47)$$

3308 where the parameter $|\nu|$ defines the noise-free amplitude of the signal and Q_1 is the
 3309 Marcum Q-function. This time the CDF that describes the probability that the entire
 3310 spectrum falls below the decision threshold is the product of both signal and noise CDFs,

$$F_1(x; \tau, \nu, N_{\text{bin}}, N_s) = \text{Ray}(x; \tau)^{N_{\text{bin}} - N_s} \prod_{k=0}^{N_s} \text{Rice}(x; \tau, \nu_k). \quad (4.48)$$

3311 The first half of Equation 4.48 is the contribution from the bins in the frequency spectrum
 3312 that contain only noise, and the second half is the product of the Rician CDFs for the
 3313 frequency bins that contain signal peaks with a noise-free amplitude of $|\nu_k|$. In Figure
 3314 4.32 we show plots of example PDFs under \mathcal{H}_1 and \mathcal{H}_0 .

3315 4.4.3.2 Matched Filtering

3316 The shape of a CRES signal is completely determined by the initial conditions of the
 3317 electron as it is emitted from beta-decay, which implies that it is possible to apply
 3318 matched filtering as a signal detection algorithm. With a matched filter one uses the
 3319 shape of the known signal, which is called a template, to filter the incoming data by
 3320 computing the convolution between the signal and the data [71]. For cases where the
 3321 signal is buried in WGN, the matched filter is the optimal detector in that it achieves
 3322 the maximum probability of a true detection for a fixed false positive rate. Since CRES
 3323 signals have an unknown shape but are deterministic, we can apply a matched filter by
 3324 using simulations to generate a large number of signal templates called a template bank,
 3325 which spans the parameter space of possible signals. Then at detection time, we use the
 3326 template bank to identify signals by performing the matched filter convolution for each
 3327 template in an exhaustive search.

3328 As we saw from the frequency spectra in Figure 4.31, CRES signals are highly periodic
 3329 in nature. In such cases, it is advantageous to utilize the convolution theorem to replace
 3330 the matched filter convolution with an inner product in the frequency-domain. With the
 3331 convolution theorem, the matched filter test statistic that describes the detection of a
 3332 signal buried in WGN using a matched filter template bank is given by

$$\mathcal{T} = \max_{\mathbf{h}} \left| \sum_{n=0}^{N_{\text{bin}}} h^\dagger[n] y[n] \right|, \quad (4.49)$$

3333 where $h^\dagger[n]$ is the complex conjugate of the signal template. For the case when our
 3334 template bank consists of only a single template it is possible to derive an exact analytical
 3335 form for the PDF describing the matched filter test statistic. First, we derive PDF under
 3336 the signal hypothesis, where the equation describing the matched filter test statistic, also
 3337 known as the matched filter score, becomes

$$\mathcal{T} = \left| \sum_{n=0}^{N_{\text{bin}}} h^\dagger[n] y[n] \right|. \quad (4.50)$$

3338 Each noisy frequency bin represented by $y[n]$ is the sum between value of the signal
 3339 at that bin and complex WGN, which means that $y[n]$ is itself Gaussian distributed.
 3340 Therefore, the value of the inner product between the template and the data is also a
 3341 complex Gaussian variable; and, since the matched filter score is the magnitude of this
 3342 inner product, it must follow a Rician distribution.

3343 We can derive the equation for the Rician PDF by expressing the matched filter
 3344 template \mathbf{h} in terms of the corresponding simulated signal, which we write as \mathbf{x}_h to
 3345 distinguish from the signal in the data. Using the standard normalization and assuming
 3346 uncorrelated WGN, the matched filter templates can be written as

$$\mathbf{h} = \frac{\mathbf{x}_h}{\sqrt{\tau|\mathbf{x}_h|^2}} \quad (4.51)$$

3347 where τ is the noise variance. Inserting this into Equation 4.49 and expressing the data
 3348 as a sum between a signal and a WGN vector yields,

$$\mathcal{T} = \frac{1}{\sqrt{\tau|\mathbf{x}_h|^2}} \left| \sum_{n=1}^{N_{\text{bin}}} x_h[n] (x[n] + \nu[n]) \right|. \quad (4.52)$$

3349 Next, we transform the expression by isolating the randomly distributed components
 3350 giving

$$\mathcal{T} = \frac{\left| \sum_{n=1}^{N_{\text{bin}}} x_h[n] x[n] \right|}{\sqrt{\tau|\mathbf{x}_h|^2}} + \frac{1}{\sqrt{\tau|\mathbf{x}_h|^2}} \left| \sum_{n=1}^{N_{\text{bin}}} x_h[n] \nu[n] \right|. \quad (4.53)$$

3351 The first term of 4.53 can be simplified by using the Cauchy-Schawrz inequality to express
 3352 the magnitude of the inner product in terms of the magnitudes of the signal and template
 3353 as well as an orthogonality constant which we call "match" (Γ). Using this we obtain,

$$\mathcal{T} = |\mathbf{h}| |\mathbf{x}| \Gamma + \frac{1}{\sqrt{\tau|\mathbf{x}_h|^2}} \left| \sum_{n=1}^{N_{\text{bin}}} x_h[n] \nu[n] \right|. \quad (4.54)$$

3354 The second term is a sum of Gaussian distributed variables, which we should expect also
 3355 follows a Gaussian distribution. Each of the samples $\nu[n]$ is described by

$$\nu[n] \sim \mathcal{N}(0, \tau), \quad (4.55)$$

3356 where $\mathcal{N}(0, \tau)$ is a complex Gaussian distribution with zero mean and variance τ . There-

3357 fore,

$$\frac{x_h[n]}{\sqrt{\tau|\mathbf{x}_h|^2}}\nu[n] \sim \mathcal{N}\left(0, \frac{x_h[n]^2}{|\mathbf{x}_h|^2}\right), \quad (4.56)$$

$$\sum_{n=1}^{N_{\text{bin}}} \frac{x_h[n]}{\sqrt{\tau|\mathbf{x}_h|^2}}\nu[n] \sim \mathcal{N}\left(0, \frac{\sum_{n=1}^{N_{\text{bin}}} x_h[n]^2}{|\mathbf{x}_h|^2}\right) = \mathcal{N}(0, 1), \quad (4.57)$$

$$|\mathbf{h}||\mathbf{x}|\Gamma + \sum_{n=1}^{N_{\text{bin}}} \frac{x_h[n]}{\sqrt{\tau|\mathbf{x}_h|^2}}\nu[n] \sim \mathcal{N}(|\mathbf{h}||\mathbf{x}|\Gamma, 1). \quad (4.58)$$

3358 We see that \mathcal{T} is magnitude of a complex variable with mean $|\mathbf{h}||\mathbf{x}|\Gamma$ and variance one. In
3359 order to simply the expression a bit further, we define the quantity $\mathcal{T}_{\text{ideal}} = |\mathbf{h}||\mathbf{x}|\Gamma$, which
3360 we call the ideal matched filter score, because it represents the value of the matched
3361 filter inner product that we would expect if no noise was present in the signal. We can
3362 write the matched filter test statistic as the magnitude of a two-dimensional vector in
3363 the complex plane

$$\mathcal{T} = |(\mathcal{T}_{\text{ideal}} + n_r, n_i)|, \quad (4.59)$$

3364 where n_r and n_i are the real and imaginary components of the noise each with variance
3365 $1/2$, which is modeled by a Rician distribution with shape factor $\mathcal{T}_{\text{ideal}}$. Therefore, the
3366 probability distribution of the matched filter test statistic is given by,

$$P_1(x; \mathcal{T}_{\text{ideal}}) = 2x \exp(- (x^2 + \mathcal{T}_{\text{ideal}}^2)) I_0(2x\mathcal{T}_{\text{ideal}}), \quad (4.60)$$

3367 where I_0 is the zeroth-order modified Bessel function.

3368 The shape of the matched filter score distribution is controlled by the parameter
3369 $\mathcal{T}_{\text{ideal}}$, which is effectively the value of the matched filter score if the data contained no
3370 noise. Without noise, the data vector reduces to the signal, \mathbf{x} , in which case Equation
3371 4.50 becomes the magnitude of an inner product between two vectors. We can write
3372 the magnitude of an inner product in terms of the lengths of the individual vectors and
3373 a constant that describes the degree of orthogonality between them. Applying this to
3374 Equation 4.50, we obtain

$$\mathcal{T}_{\text{ideal}} = |\mathbf{h}^\dagger \cdot \mathbf{x}| = |\mathbf{h}| |\mathbf{x}| \Gamma \quad (4.61)$$

3375 where Γ describes the orthogonality between \mathbf{h} and \mathbf{x} . From the point of view of matched
3376 filtering, we can interpret Γ as describing how well the template matches the underlying
3377 signal in the data.

3378 The matched filter score PDF under the noise hypothesis can be readily obtained

3379 from Equation 4.60 by setting the value of $\mathcal{T}_{\text{ideal}}$ to zero, since the data contains no signal
 3380 in the noise case. Doing this, we obtain the Rayleigh distribution that describes the
 3381 matched filter score under \mathcal{H}_0 ,

$$P_0(x) = 2x \exp(-x^2). \quad (4.62)$$

3382 Equations 4.60 and 4.62 describe the behavior of the matched filter test statistic
 3383 under \mathcal{H}_0 and \mathcal{H}_1 for a single template. However, defining a PDF that describes the
 3384 matched filter test statistic in the case of multiple templates is in general a mathematically
 3385 intractable problem, since there is no guarantee of orthogonality between matched filter
 3386 templates. This leads to correlations between the matched filter scores of different
 3387 templates because only one sample of noise is used to compute the matched filter scores
 3388 of the template bank. In order to proceed, we need to make the simplifying assumption
 3389 that we can treat the matched filter scores as IID variables, which allows to ignore
 3390 correlations between templates. The overall effect of this will be an underestimate of the
 3391 performance of the matched filter, since we are under counting the number of templates
 3392 that could contribute a detectable score.

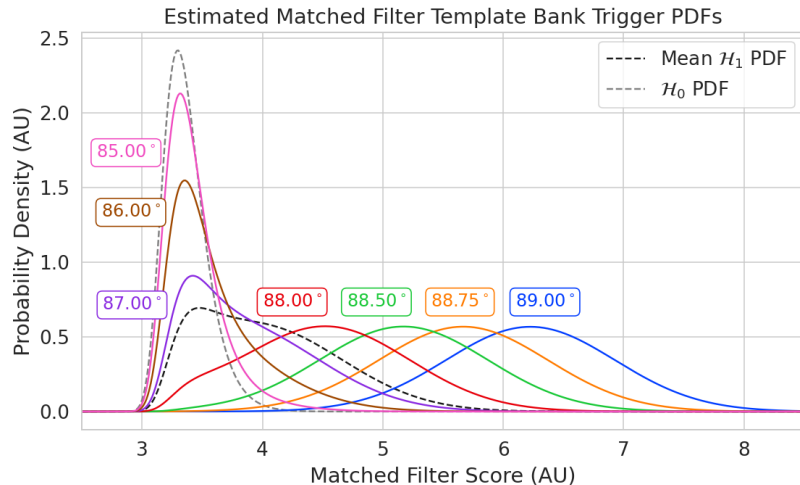


Figure 4.33. Plots of the estimated PDFs for the matched filter template bank test statistic for CRES signals with various pitch angles as well as the estimated PDF for the noise only signal case. We assume an estimated number of templates of 10^5 and perfect match between signal and template i.e. $\Gamma_{\text{best}} = 1$. The mean PDF includes signals ranging from $85.5 - 88.5^\circ$ in pitch angle. There is a much larger distinction between the signal PDFs at small pitch angle compared to the power threshold indicating a higher detection efficiency for these signals.

3393 For \mathcal{H}_0 we model the probability that the matched filter score falls below our threshold

3394 using the CDF obtained by integrating Equation 4.62. Because we are assuming that
 3395 the matched filter scores using different templates are independent, the probability that
 3396 the matched filter score for all templates falls below a threshold value is the joint CDF
 3397 formed by multiplying the CDF for each template. Under \mathcal{H}_0 this is

$$F_0(x) = \left(1 - e^{-x^2}\right)^{N_t}, \quad (4.63)$$

3398 where x is the matched filter score threshold and N_t is the number of templates. We
 3399 should expect that the distribution describing the matched filter template bank maximum
 3400 score depends on N_t , because with more templates there is a greater chance of a random
 3401 match between the template and data.

3402 For \mathcal{H}_1 , we start by denoting the CDF of the best matching template as $F_{\text{best}}(x; \mathcal{T}_{\text{best}})$,
 3403 and treat the matched filter scores for all other templates as negligible ($\mathcal{T}_{\text{ideal}} \approx 0$). Then
 3404 we form the joint CDF by combining the distributions for all templates used during
 3405 detection. Since we are exhaustively checking the matched filter scores, the number of
 3406 templates checked will be a randomly distributed variable that ranges from zero to the
 3407 total number of available templates. If we assume that signals are uniformly distributed
 3408 across the parameter space spanned by the template bank then on average we check
 3409 $(N_t - 1)/2 \approx N_t/2$ templates for each inference. Therefore, the estimated CDF under \mathcal{H}_1
 3410 is

$$F_1(x; \mathcal{T}_{\text{best}}) = F_{\text{best}}(x; \mathcal{T}_{\text{best}}) \left(1 - e^{-x^2}\right)^{N_t/2}. \quad (4.64)$$

3411 In Figure 4.33 we show plots of the estimated matched filter template bank classifier
 3412 PDFs under both \mathcal{H}_0 and \mathcal{H}_1 .

3413 4.4.3.3 Machine Learning

3414 In this paper we focus on Convolutional Neural Networks (CNN) as an example of
 3415 a machine learning based signal classifier. CNNs are constructed using a series of
 3416 convolutional layers, each composed of a set of filters that are convolved with the input
 3417 data. The individual convolutional filters can be viewed as matched filter templates that
 3418 are learned from a set of simulated data rather than being directly generated. This opens
 3419 the possibility of finding a more efficient representation of the matched filter templates
 3420 during the training process that can potentially reduce computational cost at inference
 3421 time while still offering good classification performance.

3422 The machine learning approach is distinct from both the power threshold and matched
 3423 filtering in that we do not attempt to manually engineer a test statistic that is computed

3424 from the data for classification. Instead, we attempt calculate the test statistic by
 3425 constructing a differentiable function that maps the complex frequency series generated
 3426 by the STFT to a binary classification as either signal or noise. The test statistic for the
 3427 machine learning classifier can be expressed as

$$\mathcal{T} = G(\mathbf{y}; \boldsymbol{\Omega}) \quad (4.65)$$

3428 where \mathbf{y} is the noisy data vector and $G(\mathbf{y}; \boldsymbol{\Omega})$ is the machine learning model parameterized
 3429 by the weights $\boldsymbol{\Omega}$. By using supervised learning on a labeled set of training signals, we
 3430 can modify the function parameters to learn the mapping from the data to the likelihood
 3431 of \mathbf{y} belonging to either \mathcal{H}_1 or \mathcal{H}_0 .

Table 4.1. A summary of the CNN model layers and parameters. The output of each 1D-Convolution and Fully Connected layer is passed through a LeakyReLU activation function and re-normalized using batch normalization before being passed to the next layer in the model. The output of the final Fully Connected layer in the model is left without activation so that the model outputs can be directly passed to the Binary Cross-entropy loss function used during training.

Layer	Type	Input Channels	Output Channels	Parameters
1	1D-Convolution	2	15	($N_{\text{kernel}} = 4$, $N_{\text{stride}} = 1$)
2	Maximum Pooling	15	15	($N_{\text{kernel}} = 4$, $N_{\text{stride}} = 4$)
3	1D-Convolution	15	20	($N_{\text{kernel}} = 4$, $N_{\text{stride}} = 1$)
4	Maximum Pooling	20	20	($N_{\text{kernel}} = 4$, $N_{\text{stride}} = 4$)
5	1D-Convolution	20	25	($N_{\text{kernel}} = 4$, $N_{\text{stride}} = 1$)
6	Maximum Pooling	25	25	($N_{\text{kernel}} = 4$, $N_{\text{stride}} = 4$)
7	Fully Connected	3200	512	NA
8	Fully Connected	512	64	NA
9	Fully Connected	64	2	NA

3432 The CNN architecture used for this work is summarized by Table 4.1. No strategic
 3433 hyper-parameter optimization approach was implemented beyond the manual testing
 3434 of different CNN architecture variations, so this particular model is best viewed as a
 3435 proof-of-concept rather than a rigorously optimized design. Numerous model variations
 3436 were tested, some with significantly more layers and convolutions filters per layer, as
 3437 well as others that were even smaller than the architecture in Table 4.1. Ultimately, the
 3438 model architecture choice was driven by the motivation to find the minimal model whose
 3439 classification performance was still comparable to the larger CNN's tested, because of
 3440 the importance of minimizing computational cost in real-time applications. It is possible
 3441 that more sophisticated machine learning models could improve upon the classification

3442 results achieved here, but we leave this investigation for future work.

3443 4.4.4 Methods

3444 4.4.4.1 Data Generation

3445 To test the triggering performance of the classifiers, simulated CRES signals were
3446 generated using the Locust simulations package [62, 80] developed by the Project 8
3447 collaboration. Locust uses the separately developed Kassiopeia package to calculate the
3448 magnetic fields produced by a user defined set of current carrying coils along with any
3449 specified background magnetic fields, resulting in a magnetic trap. Next, Kassiopeia
3450 calculates the trajectory of an electron in this magnetic field starting from a set of user
3451 specified initial conditions. The Locust software then uses the electron trajectories from
3452 Kassiopeia to calculate the resulting electromagnetic fields using the Liénard-Wiechert
3453 equations, and determine the voltages generated in the antenna array with the antenna
3454 transfer function. Locust then simulates the down-conversion, filtering, and digitization
3455 steps resulting in the simulated CRES signals for an electron.

3456 The shape of the received CRES signal is determined by the initial kinematic parameters,
3457 including the starting position of the electron, the starting kinetic energy of the
3458 electron, and the pitch angle. For the studies performed here we constrain ourselves to a
3459 single initial electron position located at $(x, y, z) = (5, 0, 0)$ mm, and using this starting
3460 position we generate two datasets by varying the initial kinetic energy and the starting
3461 pitch angle. The first dataset consists of a two-dimensional square grid of kinetic energy
3462 and pitch angle spanning an energy range from 18575-18580 eV with a spacing of 0.1 eV,
3463 and pitch angles from 85.5-88.5° with a spacing of 0.001°, resulting in 153051 signals with
3464 a unique energy-pitch angle combination. This dataset is intended to represent a matched
3465 filter template bank. The second dataset was generated by randomly sampling uniform
3466 probability distributions covering the same parameter space to produce approximately
3467 50000 signals randomly parameterized in energy and pitch angle. This dataset provides
3468 the training and test data for the machine learning approach, and acts as a representative
3469 sample of signals to evaluate the performance of the matched filter template bank.

3470 Each signal was simulated for a duration of 40.96 μ s, which is equivalent to 8192
3471 samples at the FSCD digitization rate, and begins at time $t = 0$ s for all simulations.
3472 This duration represents a single frequency spectrum generated by the STFT. The output
3473 of the Locust simulation is a matrix of array snapshots with size given by the number of
3474 channels times the event length ($N_{\text{ch}} \times N_{\text{sample}}$), which we pre-process using the digital

beamforming summation and STFT described in Section 4.4.2.2. The ∇B -drift correction uses the exact value of $\omega_{\nabla B}$, obtained from the Cassiopeia simulation of that electron. In practice, an average value for $\omega_{\nabla B}$ could be used, because there is limited variation in drift frequency across this parameter space.

4.4.4.2 Template Number and Match Estimation

The estimated PDF for the matched filter template bank depends on the score of the best matching template or equivalently the match of the best template (Γ_{best}) as well as the number of templates. One expects that with a higher number of templates the average value of Γ_{best} will increase, however, there is a point of diminishing returns at which more templates will not significantly increase match, but will still increase the likelihood of false positives. Therefore, it is desirable to use the minimum number of templates that provide an acceptable mean value of Γ_{best} .

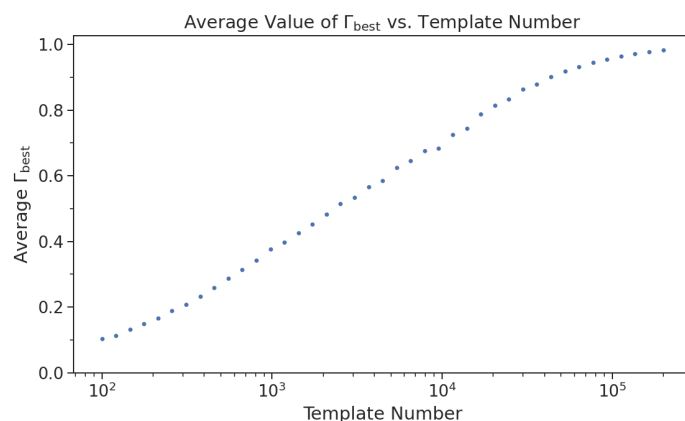


Figure 4.34. The mean match of the matched filter template bank to a test set of randomly parameterized signals as a function of the number or density of templates. The parameter space includes pitch angles from $85.5 - 88.5^\circ$ and energies from $18575 - 18580$ eV.

To quantify the relationship between match and template number, we calculated the mean match of the random dataset to a selection of templates obtained from the regularly spaced dataset. The results are shown in Figure 4.34, where we find that the average value of Γ_{best} is an exponential function of the number of templates. From this plot we select the desired value of mean match at which we would like to evaluate the matched filter PDF and can infer the required number of templates.

3493 **4.4.4.3 CNN Training and Data Augmentation**

3494 To prepare the data for training the model, we split the random dataset in half to create
3495 distinct training and test datasets. Additionally, a randomly selected 20% of the training
3496 data is isolated for use as a validation set during the training loop. The size of the
3497 training, validation, and test datasets are then tripled by appending two additional copies
3498 of the data to increase the sample size of the dataset after data augmentation. The
3499 data is loaded with no noise, which is added to each data batch during the training
3500 phase by generating a new noise sample from a complex WGN distribution. In order to
3501 ensure an even split between signal and noise data we append to the noise-free signals an
3502 equal number of empty signals composed of all zeros. Therefore, as the data is randomly
3503 shuffled during training, on average an equal number of empty signals will be included
3504 with the training signals. After adding the sample of WGN to the data batch, the empty
3505 signals represent the noise-only data that the model must distinguish from signal data.

3506 As the training signals are loaded we apply a unique random phase shift as the
3507 first form of data augmentation. Since the data is generated using the same initial
3508 axial position and cyclotron orbit phase, the randomization is an attempt to prevent
3509 overtraining on these features. During each training epoch the data is randomly shuffled
3510 and split into batches of 2500 signals. Each batch of signals is then circularly shifted
3511 by a random number of frequency bins to simulate a kinetic energy shift from -75 to
3512 20 eV to simulate a training dataset with a larger energy range. Next, a sample of
3513 complex WGN, consistent with the expected 10 K Nyquist-Johnson noise expected for
3514 the FSCD, is generated and added to the signal, which prevents overtraining on noise
3515 features. As a final step, the data is renormalized by the standard deviation of the noise
3516 so that the range of values in the data is close to $[-1, 1]$, which helps ensure well-behaved
3517 back-propagation.

3518 The Binary Cross-entropy loss function is used to compute the loss for each batch of
3519 data and the model weights are updated using the ADAM optimizer with a learning rate
3520 of 5×10^{-3} . After each training epoch, the loss and classification accuracy of the validation
3521 dataset are computed to monitor for overtraining. It was noticed that the relatively high
3522 noise power and the fact that a new sample of noise was used for each batch together
3523 provided a strong form of regularization, since no evidence of over-training was observed
3524 even after several thousand epochs. Typically, the loss and classification accuracy of
3525 the model converged after a few hundred training epochs, but the training loop was
3526 extended to 3000 epochs to attempt to achieve the best possible performance. The
3527 training procedure generally took about 24 hrs using a single NVIDIA V100 GPU [82].

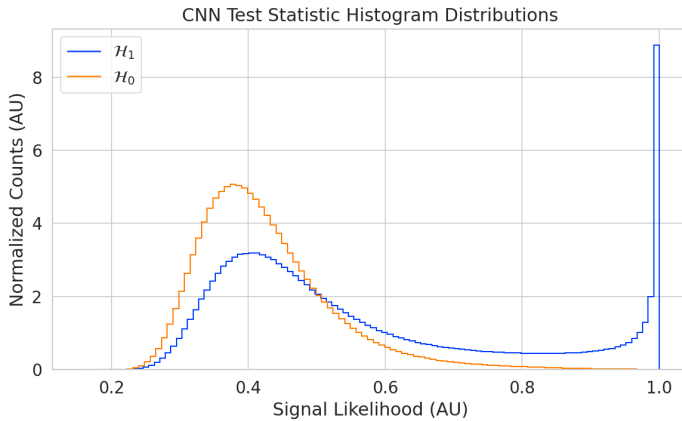


Figure 4.35. Histograms of the trained CNN model output from the test dataset. The blue histogram shows the model outputs for signal data. The oddly shaped peak near the end is the result of the softmax function mapping the long tail of the raw output distribution to the range $[0, 1]$.

After training the model, we use it to classifying the test dataset and generate histograms of the model outputs for both classes of data. The data augmentation procedure for the evaluation of the test data mirrors the training procedure without the validation split. Since a random circular shift and a new sample of WGN is added to each batch, the testing evaluation loop is run for 100 epochs to get a representative sample of noise and circular shifts. The model outputs for each batch are passed through a softmax activation and then combined into histograms, which we show in Figure 4.35.

4.4.5 Results and Discussion

4.4.5.1 Trigger Classification Performance

Using the matched filter and power threshold CDFs, along with the classification results from the CNN, we compare detection performance by computing receiver operating characteristic (ROC) curves. Specifically, we compare the detection performance averaged over the full signal parameter space in order to get a measure of the overall detection efficiency achieved by each algorithm. For the power threshold and matched filter algorithms, we obtain the mean ROC curve by taking the average over all signals in the regularly spaced dataset. In the case of the matched filter, we examine two cases using different numbers of templates, which have different values of mean match. The ROC curve describing the CNN is obtained by forming a histogram of the network outputs for each class of signal and from this computing the estimated CDFs and ROC curve.

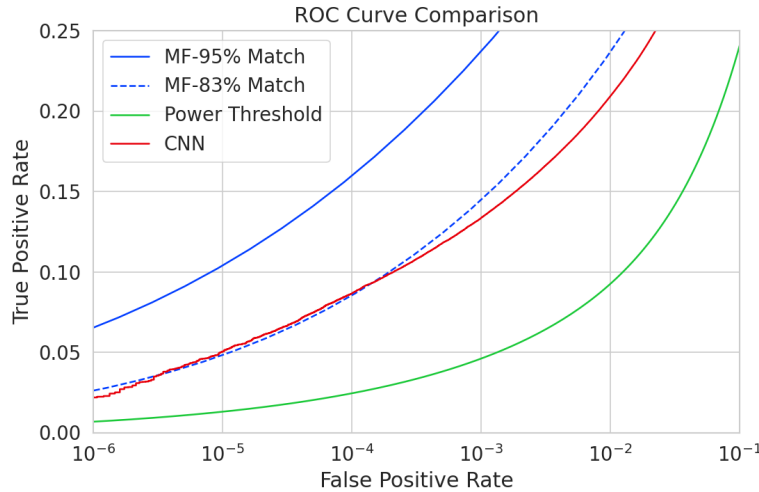


Figure 4.36. ROC curves describing the detection efficiency or true positive rates for the three signal classification algorithms examined in this paper.

3547 In Figure 4.36, we show the ROC curves obtained for each of the detection algorithms,
 3548 visualized in terms of true positive rate and false positive rate.

3549 The true positive rate of a signal classifier is equivalent to its detection efficiency, and
 3550 we see that for the population of signals with pitch angles $< 88.5^\circ$ the power threshold
 3551 has a consistently lower detection efficiency than the CNN and the matched filter. This
 3552 result could have been predicted from the visualization of signal spectra in Figure 4.31,
 3553 where we see that there is no way to distinguish between a noise peak and a signal peak
 3554 with high confidence at small pitch angles. The CNN offers a significant and consistent
 3555 increase in detection efficiency over the power threshold approach, with the relative
 3556 improvement in detection efficiency increasing as the false positive rate decreases. If
 3557 we compare the CNN to the matched filter, we see that the performance of the tested
 3558 network is roughly equivalent to a matched filter detector with an average match of
 3559 about 83%, which uses approximately 20000 matched filter templates. The overall best
 3560 detection efficiency is achieved by the matched filter classifier if a large enough template
 3561 bank is used. We show in the plot the ROC curve for a matched filter template bank
 3562 with 95% average match, which is achieved with approximately 100000 templates. Since
 3563 the matched filter is known to be statistically optimal for detecting a known signal in
 3564 WGN, it is somewhat expected that this algorithm has the highest detection efficiency.

3565 A potentially impactful difference between the matched filter and CNN algorithms is
 3566 that the CNN relies upon convolutions as its fundamental calculation mechanism, whereas
 3567 our implementation of a matched filter utilizes an inner product. Since convolution is

3568 a translation invariant operation, the detection performance of CNN can be extended
3569 to a wider range of CRES event kinetic energies with less cost than the matched filter,
3570 a feature that we exploited during the CNN training by including circular translations
3571 of the CRES frequency spectra in the training loop. Increasing the range of kinetic
3572 energies detectable by a matched filter requires a proportional increase in the number of
3573 templates, which directly translates into increased computational and hardware costs.
3574 From a practical perspective, the detection algorithm is always limited by the available
3575 computational hardware, so estimating the relative costs is a key factor in determining
3576 their feasibility. Below we perform a more detailed analysis of the relative costs of each
3577 of the detection algorithms.

3578 4.4.5.2 Computational Cost and Hardware Requirements

3579 In the process of investigating triggering approaches for an antenna array CRES experi-
3580 ment, we have uncovered a strong tension between detection efficiency and computational
3581 resources. To relate the computational cost estimates to actual costs, we compare the
3582 theoretical amount of computer hardware required to implement the signal classifiers
3583 for real-time detection in an FSCD experiment. To do this we shall utilize order of
3584 magnitude estimates of the theoretical peak performance values for currently available
3585 Graphics Processing Units (GPUs) as a metric. This approach will underestimate the
3586 amount of required hardware, since it is unlikely that any CRES detection algorithm
3587 could reach the theoretical peak performance of the hardware.

3588 Of the three detection algorithms tested, the power threshold classifier is the least
3589 expensive. It requires that we check whether the amplitude of each frequency bin in
3590 the STFT is below or above our decision threshold. The STFT combined with digital
3591 beamforming produces $N_{\text{bin}}N_b$ frequency bins that must be checked every N_{bin}/f_s seconds.
3592 This requires approximately $O(10^{10})$ FLOPS to check in real-time. Current generations of
3593 GPUs have peak theoretical performances in the range of $O(10^{13}) - O(10^{14})$ FLOPS [83],
3594 dependent on the required floating-point precision of the computation. Therefore, the
3595 entire computational needs of a real-time triggering system using a power threshold
3596 classifier, including digital beamforming and generation of the STFT, could be met by a
3597 single high-end GPU or a small number of less powerful GPUs. Since triggering is only
3598 one step of the full real-time signal reconstruction approach, limiting the computational
3599 cost of this stage is ideal. However, we have seen that the power threshold classifier does
3600 not provided sufficient detection efficiency across the entire range of possible signals,
3601 which is the primary motivation for exploring more complicated triggering solutions.

3602 As discussed, the computational cost of the matched filter approach requires counting
3603 the number of templates that must be checked for each frequency spectra produced by the
3604 STFT. Computing the matched filter scores requires $O(N_b N_t N_{\text{bin}})$ operations, since for
3605 each of the N_b beamforming positions we must multiply N_t templates with a data vector
3606 that has length N_{bin} . The time within which we must perform this calculation is equal
3607 to N_{bin}/f_s to keep up with the data generation rate. To cover the 5 eV kinetic energy
3608 range spanned by the template bank, we saw that 10^4 to 10^5 templates are required in
3609 order to match or exceed the detection efficiency of the CNN. If the number of templates
3610 scales linearly with then kinetic energy range of interest as expected, then we would
3611 require 10^5 to 10^6 matched filter templates with this more realistic range of energies.
3612 Considering this, the estimated computational cost of the matched filter is between
3613 $O(10^{15})$ to $O(10^{16})$ FLOPS, which is $O(10^2)$ to $O(10^3)$ high-end GPUs.

3614 Lastly, we have the CNN classifier. To estimate the computational cost we simply
3615 sum the number of convolutions and matrix multiplications specified by the network
3616 architecture shown in Table 4.1. Each convolutional layer consists of $N_{\text{in}} N_{\text{out}} N_{\text{kernel}} L_{\text{input}}$
3617 floating-point operations, where N_{in} is the number of input channels, N_{out} is the number
3618 of output channels, N_{kernel} is the size of the convolutional kernel, and L_{input} is the length
3619 of the input vector, and the fully connected layers each contribute $N_{\text{in}} N_{\text{out}}$ operations.
3620 Summing all the neural network layers we estimate that the CNN would require $O(10^6)$
3621 floating point operations for each frequency spectra; therefore, the total computation
3622 cost of the CNN trigger is this cost times the number of beamforming positions per the
3623 data acquisition time, which is $O(10^{13})$ FLOPS or $O(10^0)$ GPUs.

3624 Compared with the matched filter approach the CNN requires $O(100)$ to $O(1000)$
3625 fewer GPUs to implement, dependent on the exact number of templates used in the
3626 template bank. The 100 eV kinetic energy range is motivated by the application of these
3627 detection algorithms to an FSACD-like neutrino mass measurement experiment. However,
3628 if a significantly larger range of kinetic energies is required, a CNN may be the preferred
3629 detection approach despite the lower average detection efficiency due to computational
3630 cost considerations. The low estimated computational cost of the CNN is directly related
3631 to the small network size.

3632 Additional experiments with larger CNNs, generated by increasing the depth and
3633 width of the neural network, and we observed that these changes provided minimal
3634 ($\lesssim 1\%$) improvement in the classification accuracy of the model. A potential reason
3635 for this could be the sparse nature of the signals in the frequency domain and the low
3636 SNR which makes for a challenging dataset to learn from. Future work could investigate

3637 modifications to the neural network architecture such as sparse convolutions, which may
3638 improve the classification accuracy of the model or further reduce the computational
3639 costs of this approach. Alternatively, more complicated CNN architectures such as a
3640 ResNet [84] or VGG model [85] may provide improved classification performance over a
3641 basic CNN. An additional promising area of investigation are recurrent neural networks,
3642 which may be able to exploit the time-ordered features of the STFT for more accurate
3643 signal detection if the electron signals last for multiple Fourier transform windows.

3644 Our estimate of the computational cost of the matched filter is somewhat naive if
3645 we notice that the majority of the values that make up a CRES frequency spectra are
3646 zero (see Figure 4.31). Therefore, the majority of operations in the matched filter inner
3647 product are unnecessary, and we could instead evaluate the matched filter inner product
3648 using only the $\lesssim 10$ frequency peaks that make up CRES signal. This optimization
3649 reduces the number of operations required to check each template by a factor of $O(100)$
3650 to $O(1000)$, which brings the estimated computational cost of the matched filter in
3651 line with the CNN. Although this level of sparsity results in a multiplication with very
3652 low arithmetic complexity, the resulting sparse matched filter algorithm is still likely
3653 to be constrained by memory access speed rather than compute speed. Ultimately, the
3654 comparison of the relative computational and hardware costs between the matched filter
3655 and CNN will depend on the efficiency of the software implementation and hardware
3656 support for neural network and sparse matrix calculations.

3657 **4.4.6 Conclusion**

3658 Increasing the detection efficiency and overall event rate of the CRES technique represents
3659 a key developmental path towards new scientific results and broader applications of the
3660 CRES technique. It is what motivates both the antenna array detection approach and
3661 the development of real-time signal reconstruction algorithms. We have demonstrated
3662 that significant gains in the detection efficiency of the CRES technique are achievable
3663 by utilizing triggering algorithms that account for the specific shape of CRES signals in
3664 the detector. These algorithms emphasize the need for accurate and fast methods for
3665 CRES simulation, since they directly contribute to the success of matched filter methods
3666 by providing a way to generate expected signal templates and also serve as a source of
3667 training data for machine learning approaches.

3668 The improvements in detection efficiency offered by these alternative approaches to
3669 triggering are crucial to the success of efforts to develop scalable technologies for CRES
3670 measurement, since they provide a significant increase in the detectable parameter space

3671 of CRES events, which allows for a better utilization of the larger detection volume.
3672 While we have focused on the real-time detection of CRES signals from antenna arrays,
3673 these same signal classifiers could be used in CRES experiments utilizing a different
3674 detector technologies, since the same principles of signal detection will apply. For example,
3675 previous CRES measurements by the Project 8 collaboration that utilized a waveguide
3676 gas cell, could have improved their detection efficiency by employing a matched filter
3677 or neural network classifier to identify trapped electrons with pitch angles that are too
3678 small to be detected by the power threshold approach. Furthermore, alternative CRES
3679 detector technologies such as resonant cavities [41] could also see similar improvements
3680 in detection efficiency, which is of crucial importance to future efforts by the Project 8
3681 collaboration to utilize CRES to measure the neutrino mass.

Chapter 5

Antenna and Antenna Measurement System Development for the Project 8 Experiment

5.1 Introduction

The FSCD and antenna array CRES represent an innovative approach to beta-decay spectroscopy. While much can be learned from simulations about the systematics of CRES with antenna arrays, laboratory measurements and demonstrations provide critical inputs to sensitivity and simulation models as well as provide a means for calibration and commissioning of the experiment. Therefore, a robust program of antenna and antenna measurement hardware development is important to the success of the FSCD and the development of antenna array CRES more broadly.

In this chapter we summarize the development of an antenna measurement system at Penn State to implement and test the techniques of antenna array CRES on the bench-top, in order to support the efforts of the Project 8 collaboration. In Section 5.2 we provide an introduction to some fundamental parameters and concepts related to antenna measurements as well as an overview of the Penn State antenna measurement system hardware. In Section 5.3 we include the manuscript of a paper [81] which details the design and characterization of a specialized antenna developed to mimic the electric fields emitted by an electron in a CRES experiment. This antenna, called the Synthetic Cyclotron Antenna (SYNCA), is intended as a calibration tool for antenna arrays developed for CRES measurements. Lastly, in Section 5.4 we summarize a set of prototype FSCD antenna array measurements with the SYNCA [44], which we use to validate the simulated performance of the antenna array and estimate systematic errors associated with the antenna array.

3707 5.2 Antenna Measurements for CRES experiments

3708 5.2.1 Antenna Parameters

3709 Antenna characterization measurements are intended to validate simulations of the
3710 antenna array performance, which ultimately informs the neutrino mass sensitivity of
3711 the experiment. In this section, I shall summarize a few fundamental concepts relating
3712 to antennas and antenna measurement, before introducing how Project 8 uses antenna
3713 measurement for the development of antenna array CRES.

3714 5.2.1.1 Radiation Patterns

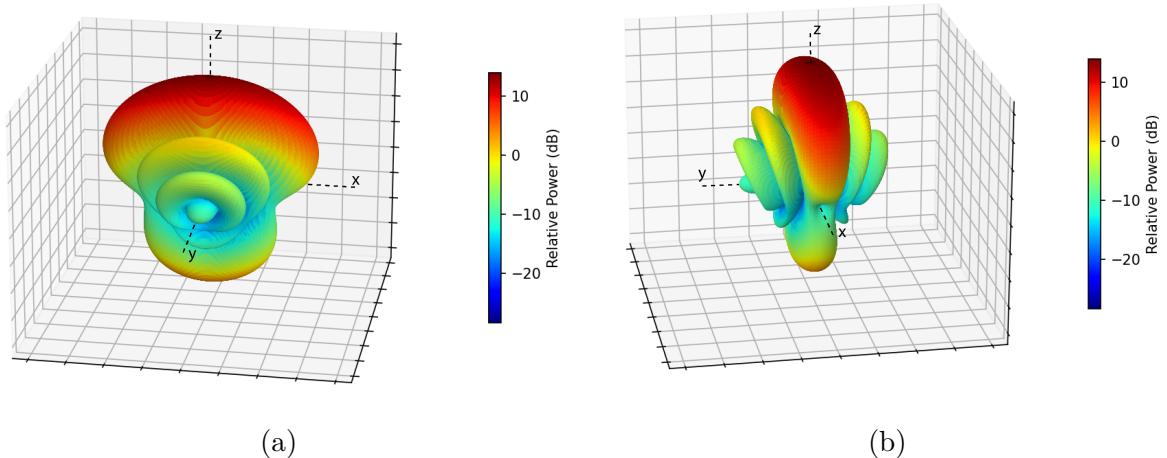


Figure 5.1. An example radiation pattern generated using HFSS simulations. The color and radial distance of the surface from the origin indicate the relative magnitude of radiation power emitted by the antenna in that direction. The primary goal of most antenna measurements is typically to measure the antenna pattern, which is used to derive many useful antenna performance parameters.

3715 Antennas are conductive structures designed to carry alternating electric currents
3716 in order to transmit energy in the form of electro-magnetic (EM) waves [65]. Perhaps
3717 the most fundamental way to characterize an antenna, is to map out the radiated power
3718 density as a function of position, which is called the radiation pattern (see Figure 5.1).
3719 We find the radiation power density by calculating the time-averaged Poynting vector for
3720 all positions surrounding the antenna, which in equation form is

$$\mathbf{W}(x, y, z) = \langle \mathbf{E}(x, y, z, t) \times \mathbf{H}^*(x, y, z, t) \rangle_t, \quad (5.1)$$

3721 where $\mathbf{E}(x, y, z, t)$ and $\mathbf{H}(x, y, z, t)$ are the time-dependent electric and magnetic fields
 3722 produced by the antenna [49]. The radiation power density has units of W/m^2 and is
 3723 more typically called the energy flux density in physics applications, since it is a measure
 3724 of the amount of energy passing through a unit area over time.

3725 Because the radiation power density is a measure of power per unit area, its value
 3726 in a particular direction will depend on the distance from the antenna at which we are
 3727 measuring. This is undesirable for practical applications A related quantity, which is
 3728 distance independent, is the energy flux per unit solid angle or radiation intensity, which
 3729 is computed directly from the radition power density by multiplying by the squared
 3730 distance from the antenna. Specifically,

$$U = r^2 W(x, y, z), \quad (5.2)$$

3731 where r is the distance from the antenna to the field measurement point. The radiation
 3732 intensity is typically defined in regions where the Poynting vector consists only of a radial
 3733 component where it is safe to treat as a scalar quantity.

3734 5.2.1.2 Directivity and Gain

3735 Since the radiation intensity is a measure of average power per unit solid angle, it is
 3736 independent of distance and more useful as feature for antenna measurement. However,
 3737 most antenna measurements are performed in terms of the directly related directivity
 3738 and gain quantities. Directivity is defined as the ratio between the radiation intensity at
 3739 particular point on the radiation pattern to the average radiation intensity computed
 3740 over all solid angles [65]. The equation that relates the radiation intensity to directivity
 3741 is

$$D = \frac{U}{U_0} = \frac{4\pi U}{P_{\text{rad}}}, \quad (5.3)$$

3742 where U_0 is the average radiation intensity over all solid angles, which simply the total
 3743 radiated power (P_{rad}) divided by 4π . Closely related to directivity is concept of gain,
 3744 which accounts for energy losses that occur inside then antenna when attempting to
 3745 transmit or receive a signal. The antenna gain is given by

$$G = \frac{4\pi U}{P_{\text{in}}}, \quad (5.4)$$

3746 where P_{in} is the total power delivered to the antenna. Gain can be thought of as the ratio
 3747 of the antenna's radiation intensity to that of a hypothetical isotropic, lossless radiator.

3748 The maximum values of gain and directivity exhibited by the main lobe of the antenna
 3749 pattern as well as the ratio between the gain of the main lobe and any side-lobes are
 3750 important figures of merit used to evaluate antenna designs.

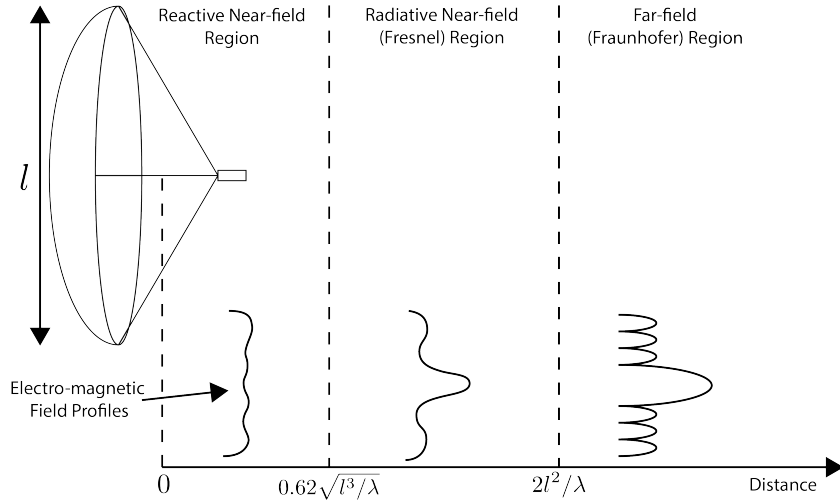


Figure 5.2. An illustration of the three field regions important for the analysis of an antenna system. Very close to the antenna the electric fields are primarily reactive so there is no radiation. If a receiving antenna were placed in this region most of the energy would be reflected back to the transmitter. Outside of the reactive near-field is the radiative near field. At these distances the antenna does radiate, but the radiation pattern is not well-defined since it changes based on the distance of the receiving antenna. It is only in the far-field region where the radiation pattern becomes constant as a function of distance, which is where the majority of antenna engineering is assumed to take place. The antenna arrays developed by Project 8 for CRES measurements operate in the radiative near-field due to the importance of limiting power loss from free-space propagation, which complicates the design of the antenna system.

3751 5.2.1.3 Far-field and Near-field

3752 Radiation patterns are only well-defined in regions where the shape of the radiation
 3753 pattern is independent of distance. The region where this approximation is valid is called
 3754 the "far-field", and in this region we can treat the EM fields from the antenna as spherical
 3755 plane waves. A rule of thumb for antennas is that the far-field approximation is valid
 3756 when the condition

$$R > \frac{2l^2}{\lambda} \quad (5.5)$$

3757 is met. In this expression, R is the distance from the antenna, l is the largest characteristic
 3758 dimension of the antenna, and λ is the wavelength of the radiation (see Figure 5.2).

3759 The region very close to the antenna is called the reactive near-field, because in this
 3760 region the reactive component of the EM field is dominant. Unlike radiative electric

3761 fields, the reactive electric and magnetic fields are out of phase from each other by
 3762 90° , since they are the result of electrostatic and magnetostatic effects coming from the
 3763 self-capacitance and self-inductance of the antenna. The reactive fields are unable to
 3764 transfer energy a significant distance from the antenna and are thus completely negligible
 3765 for most antenna applications. The limit of the reactive near-field for an electrically-large
 3766 antenna is typically taken to be

$$R < 0.62\sqrt{l^3/\lambda}. \quad (5.6)$$

3767 The unique application of antennas by Project 8 is somewhat limited by reactive near-
 3768 field effects in the form of a maximum radial position for electrons inside the uniform
 3769 cylindrical antenna array. If electrons are too close to the edge of the array than reactive
 3770 near-field effects leads to a large reduction in the received power and consequently
 3771 detection efficiency. This leads to a significant volume inside of the antenna array that
 3772 is unsuitable for CRES lowering the volumetric efficiency of the antenna array CRES
 3773 technique relative to a cavity experiment.

3774 In between the reactive near-field and the far-field is the radiative near-field region.
 3775 In this region the fields are primarily radiative, however we are still too close to the
 3776 antenna for the spherical plane wave approximation to apply. Therefore, interference
 3777 effects between EM waves emitted from different points on the antenna occur causing the
 3778 shape of the radiation pattern to change as a function of distance from the antenna. If we
 3779 evaluate the far-field distance limit for the FSCD one finds an estimated far-field distance
 3780 of 43 cm, which is a factor of four larger than the radius of the antenna array designed for
 3781 the experiment. Consequently, we expect near-field effects to influence the performance
 3782 of the antenna array highlighting the importance of calibration and characterization
 3783 measurements.

3784 5.2.1.4 Polarization

3785 The polarization of an EM wave defines the spatial orientation of the electric field
 3786 oscillations in the plane perpendicular to the direction of the propagation, and is defined
 3787 in terms of orthogonal polarization components. In our application, one analyzes the
 3788 properties of radiation propagating along the radial (\hat{r}) direction away from the antenna,
 3789 which implies that the electric fields can be described as a linear combination of orthogonal
 3790 polarization components

$$\mathbf{E}_{\text{tot}} = E_x \hat{x} + E_y \hat{y} + E_z \hat{z}, \quad (5.7)$$

³⁷⁹¹ in Cartesian coordinates, or

$$\mathbf{E}_{\text{tot}} = E_\theta \hat{\theta} + E_\phi \hat{\phi}, \quad (5.8)$$

³⁷⁹² in spherical coordinates.

³⁷⁹³ In general, one defines partial radiation patterns, directivities, and gains so that the
³⁷⁹⁴ performance of the antenna for the desired polarization can be analyzed. The radiation
³⁷⁹⁵ pattern defined in terms of partial patterns is

$$U_{\text{tot}} = U_\phi + U_\theta, \quad (5.9)$$

³⁷⁹⁶ where U_ϕ and U_θ are the radiation intensities in a particular direction for the respective
³⁷⁹⁷ polarization components. Similarly, a quantity such as gain can be written in terms of
³⁷⁹⁸ partial gains,

$$G_{\text{tot}} = G_\phi + G_\theta = \frac{2\pi U_\phi}{P_{\text{in}}} + \frac{2\pi U_\theta}{P_{\text{in}}}. \quad (5.10)$$

³⁷⁹⁹ If we view an electron performing a circular orbit in the XY-plane from the side, that
³⁸⁰⁰ is, along the X or Y axes, then we would observe the electron to be performing a linear
³⁸⁰¹ oscillation perpendicular to the viewing axis. From this intuitive picture, we can predict
³⁸⁰² that the primary polarization of electric fields from CRES events to be linearly polarized
³⁸⁰³ in the $\hat{\phi}$ direction when viewed with an antenna positioned in the XY-plane.

³⁸⁰⁴ 5.2.1.5 Antenna Factor and Effective Aperture

³⁸⁰⁵ A useful way to characterize the performance of an antenna is to measure the electric
³⁸⁰⁶ field magnitude required to produce a signal with an amplitude of one volt in the antenna
³⁸⁰⁷ terminals. This ratio between the magnitude of the incoming electric field and the
³⁸⁰⁸ magnitude of the signal produced by the antenna is called the antenna factor, which is
³⁸⁰⁹ written as

$$A_F = \frac{|\mathbf{E}_{\text{in}}|}{V_{\text{ant}}}, \quad (5.11)$$

³⁸¹⁰ where A_F is the antenna factor, E_{in} is the incoming electric field, and V_{ant} is the magnitude
³⁸¹¹ of the voltage produced by the antenna.

³⁸¹² The antenna factor can be expressed in terms of the antenna's gain through a related
³⁸¹³ quantity called the effective aperture. The effective aperture defines for a given incident
³⁸¹⁴ radiation power density (W/m^2) the power that is received by the antenna. Therefore,

3815 the effective aperture gives the equivalent area of the antenna,

$$A_{\text{eff}} = \frac{P_{\text{rec}}}{P_{\text{in}}} = \frac{\lambda^2}{4\pi} G, \quad (5.12)$$

3816 where the received power is P_r and the total incoming power is P_{in} .

3817 If we express the incident power in terms of the magnitude of the Poynting vector,
3818 then

$$|\mathbf{S}_{\text{in}}| = |\mathbf{E}_{\text{in}}|^2 / \eta_0, \quad (5.13)$$

3819 where η_0 is the impedance of free-space, which relates the magnitudes of the electric and
3820 magnetic fields in a vacuum, and is defined by

$$\eta_0 = \frac{|\mathbf{E}|}{|\mathbf{H}|} = \sqrt{\frac{\epsilon_0}{\mu_0}}. \quad (5.14)$$

3821 The total received power by the antenna can therefore be expressed as

$$P_{\text{rec}} = |\mathbf{S}_{\text{in}}| A_{\text{eff}} = |\mathbf{S}_{\text{in}}| \frac{\lambda^2}{4\pi} G = \frac{|\mathbf{E}_{\text{in}}|^2 \lambda^2 G}{4\pi \eta_0}. \quad (5.15)$$

3822 To relate this to the antenna factor recall that we can relate the voltage produced by
3823 the antenna to the received power with

$$P_{\text{rec}} = \frac{V_{\text{ant}}^2}{Z} = \frac{|\mathbf{E}_{\text{in}}|^2}{A_F^2 Z}, \quad (5.16)$$

3824 where Z is the system impedance. Setting Equations 5.15 and 5.16 equal to each other,
3825 we obtain the following expression for antenna factor in terms of gain

$$A_F = \sqrt{\frac{4\pi\eta_0}{ZG\lambda^2}} = \frac{9.73}{\lambda\sqrt{G}}. \quad (5.17)$$

3826 The second expression in Equation 5.17 is obtained by evaluating the constant terms
3827 assuming a system impedance of 50Ω .

3828 We have gone through the effort of expressing the antenna factor in terms of gain
3829 to highlight that the majority of antenna parameters that we care to measure for a
3830 CRES experiment can be obtained from the radiation or gain pattern of the antenna.
3831 The antenna factor is a particularly important parameter for CRES measurements
3832 due to its relevance to antenna array simulations with the Locust software [62, 80].
3833 Specifically, Locust simulates the trajectory of an electron in a magnetic trap by running

3834 the Kassiopeia software package [60] and then uses the Liénard-Wiechert equations [63, 64]
3835 to calculate the electric fields that are incident on the antenna.

3836 To compute the response of the antenna to the electric field, Locust relies upon
3837 linear time-invariant system theory, which computes the response of the antenna (i.e. the
3838 voltage time series generated by the antenna) using a convolution between the electric field
3839 time-series and the antenna impulse response. This approach is necessary for correctly
3840 modeling the antenna response to the electric field due to the broadband and non-
3841 stationary nature of the electric fields from CRES events. Since antenna measurements
3842 take place under steady-state conditions, parameters such as the radiation pattern, gain,
3843 and antenna factor are defined in the frequency domain. However, by performing an
3844 inverse Fourier transform on the antenna factor we can obtain the antenna impulse
3845 response, which allows us to simulate CRES events in the antenna array demonstrator
3846 experiment.

3847 **5.2.2 Antenna Measurement Fundamentals**

3848 **5.2.2.1 Friis Transmission Equation**

3849 The antenna factor, sometimes called the antenna transfer function, is used to model
3850 how the antenna will respond to electric fields emitted from a CRES event. Therefore,
3851 being able to measure the antenna transfer function of the antenna array is a key step
3852 in the commissioning and calibration phases of an antenna array CRES experiment. A
3853 common approach to antenna characterization is to perform a two antenna transmit-
3854 receive measurement where an antenna with a known gain is used to characterize the
unknown gain of the antenna under test (see Figure 5.3).

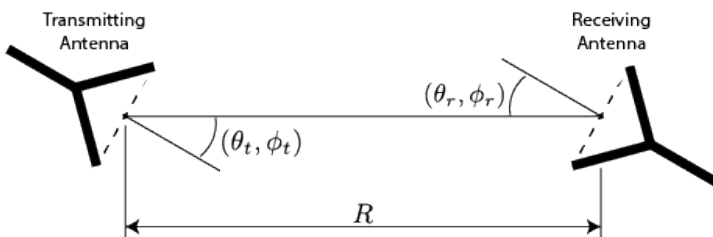


Figure 5.3. An illustration of the Friis measurement technique commonly used for antenna characterization measurements.

3855
3856 To analyze this two antenna setup we seek to calculate the amount of power from
3857 the transmitting antenna that we will detect with the receiving antenna. Using our
3858 understanding of antenna gain, we can calculate the power density transmitted by an

3859 antenna in a direction (θ_t, ϕ_t) at frequency f and distance R , which is given by

$$w_t = \frac{P_t}{4\pi R^2} G_t(\theta_t, \phi_t, f). \quad (5.18)$$

3860 Here, P_t is the total power delivered to the transmitting antenna and $G_t(\theta_t, \phi_t, f)$ is
3861 the value of the transmitting antenna gain. The power density is the power per unit
3862 area, so to calculate the total power delivered to the receiving antenna we multiply the
3863 transmitted power density by the effective area of the receiving antenna,

$$P_r = w_t A_{eff,r} = P_t \frac{G_t(\theta_t, \phi_t, f) G_r(\theta_r, \phi_r, f) c^2}{(4\pi R f)^2}, \quad (5.19)$$

3864 where $G_r(\theta_r, \phi_r, f)$ is the gain of the receiving antenna. Equation 5.19 is called the Friis
3865 transmission equation [86], which is of fundamental importance for antenna measurements,
3866 since it allows one to measure the gain of an unknown antenna by measuring the power
3867 received from an antenna with a known gain pattern. Alternatively, if no antenna with a
3868 known gain pattern is available, two identical antennas with unknown gain patterns can
3869 be used.

3870 5.2.2.2 S-Parameters and Network Analyzers

3871 Instead of directly measuring the power received by the antenna under test, it is more
3872 common to measure the ratio of the received power to the transmitted power,

$$\frac{P_r}{P_t} = \frac{G_t(\theta_t, \phi_t, f) G_r(\theta_r, \phi_r, f) c^2}{(4\pi R f)^2}. \quad (5.20)$$

3873 This power ratio can be easily measured using a vector network analyzer (VNA), which
3874 automates a significant fraction of the measurement process. Network analyzers are
3875 used to measure the scattering or S-parameters of a multi-port RF device [87], which
3876 describes how waves are scattered between the device ports. The antenna measurements
3877 we have been considering can be modeled as a two-port microwave device that we can
3878 characterize by measuring how incident voltage waves are transmitted or reflected (see
3879 Figure 5.4). We can write the scattered waves (V_1^- and V_2^-) in terms of the incident (V_1^+
3880 and V_2^+) waves using the scattering matrix

$$\begin{pmatrix} V_1^- \\ V_2^- \end{pmatrix} = \begin{pmatrix} S_{11} & S_{12} \\ S_{21} & S_{22} \end{pmatrix} \begin{pmatrix} V_1^+ \\ V_2^+ \end{pmatrix}, \quad (5.21)$$

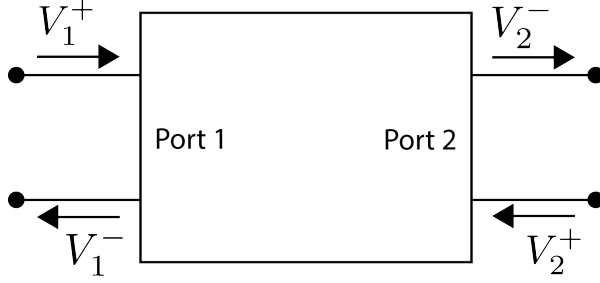


Figure 5.4. Illustration of a two-port S-parameter measurement setup. S-parameters characterize how incoming waves of voltage or power scatter off of the RF device under test. This allows you to measure important properties of the device. In particular, we can use this framework to model a two antenna radiation pattern measurement, which we can then automate using a VNA.

3881 where the elements of the matrix are the device S-parameters. It is assumed that,
 3882 when exciting the device from a particular port, that all other ports in the network are
 3883 terminated at the system impedance. This ensures that the incident waves from other
 3884 ports in the network are zero. Therefore, the S-parameters are the ratios between the
 3885 scattered and incident waves,

$$S_{ij} = \frac{V_i^-}{V_j^+}. \quad (5.22)$$

3886 Alternatively, S-parameters can be defined as the ratio of the scattered and incident
 3887 power, which is proportional to the ratio of the squared voltage waves. Returning to
 3888 our antenna measurement setup, we see that measuring the ratio of the received to the
 3889 transmitted power is equivalent to measuring the ratio of power being scattered from port
 3890 1 to port 2 in a RF network. Therefore, measuring an antenna's gain can be accomplished
 3891 quite easily, by using a VNA to perform a two port S_{21} measurement.

3892 5.2.2.3 Antenna Array Commissioning and Calibration Measurements

3893 Up to this point we have been discussing calibration and commissioning measurements
 3894 as they apply to a single antenna. While these measurements play an important role
 3895 in validating the radiation patterns of the individual array elements, the ultimate goal
 3896 is to use a phased array of these antennas. Therefore, we must also consider antenna
 3897 measurement techniques that apply to the whole array system.

3898 By measuring the gain of each individual array element we can predict the features of
 3899 the signals received during a CRES event using the antenna factor (see Section 5.2.1.5).
 3900 However, unpredictable changes to the antenna performance can be introduced by the
 3901 incorporation of the antennas into the circular array geometry, therefore, we employ both

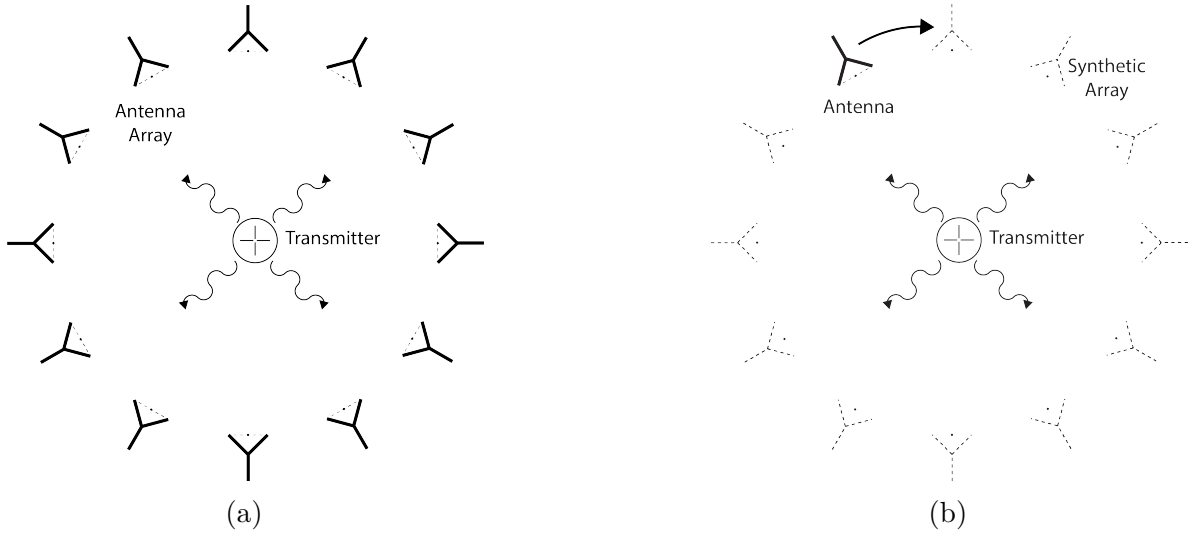


Figure 5.5. Two measurement approaches to characterizing an antenna array for CRES measurements. The full-array approach (a) requires a complete antenna array with all the associated hardware. The synthetic array approach (b) utilizes a single antenna and a set of rotation/translation stages to reposition the transmitter or the receiving antenna to synthesize the signals that would be received by the full-array. This approach reduces the cost and complexity of array measurements. A down-side of the synthetic array approach is that multi-channel effects such as reflections cannot be measured. Utilizing both the full-array and the synthetic array is a powerful way to quantify the impact of errors from the multi-channel array.

3902 individual antenna and full-array measurements in the commissioning of the FSCD to
 3903 account for these effects.

3904 There are two main approaches to array measurements that could be used for
 3905 characterization and calibration (see Figure 5.5). One approach is to construct the
 3906 complete array and use an omni-directional transmitting antenna to measure the power
 3907 received by each channel in the antenna array. In Section 5.3 we describe the development
 3908 of an omni-directional transmitter that also mimics the radiation phase characteristics of a
 3909 CRES event, which is useful because the entire array can be tested without repositioning.
 3910 Alternatively, a full antenna array can be synthesized by repeatedly moving and measuring
 3911 a single array element. This approach is ideal for identifying if different channels in the
 3912 antenna array are affecting each other through multi-path interference by comparing the
 3913 measurement results of the synthetic array to the real array.

5.2.3 The Penn State Antenna Measurement System

The development of antenna array based CRES requires the capability to test and calibrate different antenna array designs to validate the performance of the as-built antenna array before and during the experiment. With these aims in mind we developed an antenna measurement system at Penn State specifically designed to mimic the characteristics of the antenna experiment designed for demonstration of the antenna array CRES technique by the Project 8 collaboration.

The Penn State antenna measurement system utilizes a two antenna measurement configuration with a stationary reference antenna and a test antenna mounted on a set of motorized translation and rotation stages (see Figure 5.6). The antenna measurement system can be operated in two distinct modes, one focused on the characterization of the radiation patterns of prototype antennas and the other focused on the validation of data-acquisition (DAQ) and CRES signal reconstruction techniques to bridge the gap between real measurements and simulation. In both measurement configurations it is critical to isolate the antennas from the environment so that multi-path reflections do not negatively influence the measurement results. For this reason we surround the measurement volume with microwave absorber foam (AEMI AEC-1.5) specifically designed to attenuate microwave radiation near the 26 GHz measurement range of the system.

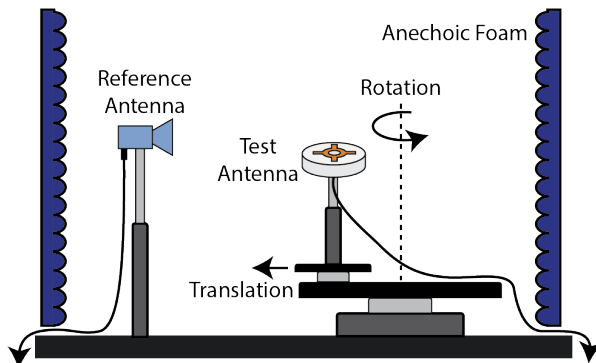


Figure 5.6. Illustration of the antenna measurement system developed for the Project 8 Collaboration. The reference and test antennas can be connected to different data acquisition configurations depending on the measurement goals. The reference antenna is typically a standard horn antenna and the test antenna is mounted on a set of translation stages for positioning. Automated translation stages allow for relatively painless data-taking enabling synthetic antenna array measurements using only a single receiving antenna. Anechoic foam designed to mitigate RF reflections surrounds the setup.

In the first measurement configuration the reference antenna is typically a well-

characterized horn antenna as pictured, since horn antennas have well-known and stable radiation patterns making them ideal as standard references. For characterization measurements, the test antenna represents the antenna-under-test whose pattern we wish to characterize. Mounting the test antenna on motorized rotation and translation stages allows us to automate the procedure significantly speeding up the radiation pattern measurement process.

In the second measurement configuration one is interested in recreating the conditions of an antenna array CRES experiment as it concerns the antenna array and DAQ system. In this case, the reference antenna is a prototype FSCD antenna, which will be used to construct the antenna array in the FSCD experiment, and the test antenna is a specially designed synthetic cyclotron antenna (SYNCA) as picture in Figure 5.6. The SYNCA is designed such that the radiation pattern mimics that of a CRES electron so that the signals received by the prototype CRES array antenna mimic what is expected for a real CRES experiment.

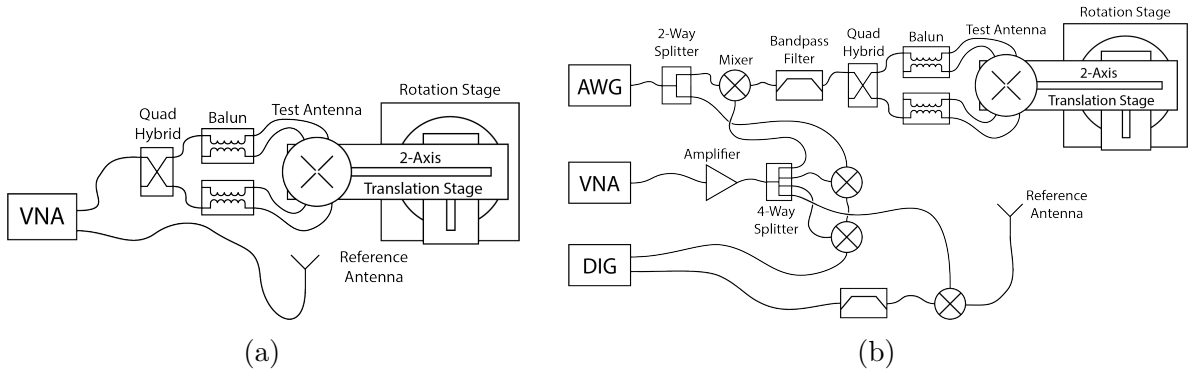


Figure 5.7. Diagrams of two measurement system configurations. Configuration (a) utilizes a VNA and is more suited to antenna characterization. Configuration (b) utilizes an AWG and VNA as a signal generation system and digitizer to collect measurement data, which is more suited to simulating CRES measurements. The transmission chain utilizes a quadrature hybrid and a pair of baluns to drive the cross-dipole variant test antenna developed for synthetic CRES measurements.

In Figure 5.7 we show two high-level system diagrams of the Penn State antenna measurement system that depict the important system components and the connections between them. The two configurations of the measurement system utilize different hardware. For characterization and radiation pattern measurements, one prefers the configuration shown in Figure ???. In this case a vector network analyzer (VNA) is used as both the transmission source and data acquisition system and it is relatively easy to calibrate over a wide range of frequencies. Whereas, if one is more interested in recreating

what would take place in the FSCD experiment then the configuration shown in Figure ?? is preferable, since this system effectively mimics the receiver chain envisioned for the FSCD experiment.

The characterization configuration utilizes a network analyzer (Keysight N5222A) with two independent sources and four measurement ports as the primary measurement tool. A standard reference antenna is connected to one measurement port, and the test antenna is connected to a separate port. The typical reference antenna used for these studies is a Pasternack PF9851 horn antenna . In the measurement shown, the test antenna represents a SYNCA antenna, which requires a transmission chain consisting of quadrature hybrid coupler (Marki QH-0226) connected to two baluns (Marki BAL-0026) to generate feed signals with the appropriate phases. The VNA measures the radiation pattern by performing a transmission S-parameter measurement, which can be used with the knowledge of the reference antenna's radiation pattern to determine the radiation pattern of the test antenna (see Section 5.2.1).

The second configuration is more complicated and incorporates more hardware components in order to more closely mimic the DAQ system envisioned for the FSCD experiment. The basic approach is to produce CRES-like radiation and use an antenna combined with a realistic RF receiver chain to acquire the signals. On the transmit side, an arbitrary waveform generator (AWG, RIGOL DG5252) is used to generate a waveform that mimics a CRES signal at a baseband frequency up to 250 MHz. This frequency is then up-converted to the CRES signal frequency band of 25.8 to 26.0 GHz using a mixer (Marki MM1-0832L) and a bandpass filter (K&L Microwave 3C62-25900/T200-K/K) to reject unwanted mixing components outside out of the 200 MHz CRES signal band. The local oscillator signal for mixing is provided by one of the VNA sources configured to run in a continuous wave setting. On the receive side, a prototype antenna is used to detect the radiation emitted by the test antenna, which is down-converted and filtered using the same mixer and bandpass filter as the transmission chain. Lastly, data acquisition is performed using a 14-bit ADC sampling at 500 MSa/s (CAEN DT530) to digitize the down-converted signals.

In order to distribute the LO to all mixers a 4-way power splitter (MiniCircuits ZC4PD-18263-S+) along with an amplifier (Marki APM-6848) is used to drive the four mixers used in the measurement system. A limitation of using the VNA as an LO source is that there is no control of the LO phase when a measurement is triggered by the control script, which leads to a random phase offset between acquisitions. This makes it impossible to perform synthetic array measurements, which require strict control over

3990 the starting phase of the transmitted signal. In order to monitor the random phase of the
3991 LO, a 2-way power splitter (MiniCircuits Z99SC-62-S+) is used to split the signal from
3992 the AWG between the transmission path and a LO monitoring path. The LO monitoring
3993 path consists of an up-conversion and down conversion using two mixers connected by a
3994 coaxial cable, and monitors the relative phase of the LO using a channel on the digitizer
3995 to sample this path. A phase shift in the LO will lead to a proportional phase shift in
3996 the mixed signal, which is measured and removed from the received signals.

3997 The test antenna is mounted on a set of motorized stages, which are identical for
3998 both measurement configurations. A rotational stage (ThorLabs PRMTZ8) is used as
3999 the base layer with additional translation stages mounted on top of this. The rotational
4000 stage is ideal for measuring a complete azimuthal scan of the test antenna's radiation
4001 pattern as well as for moving a SYNCA antenna in circular motion to recreate the
4002 symmetry of the FSCD antenna array. On top of the rotational stage we mount two
4003 linear translation stages (ThorLabs MTS50-Z8 and MTS25-Z8) in a cross-wise manner
4004 so that the test antenna can be moved along two perpendicular axes. Using the linear
4005 stages in combination with the rotational stage allows one to fine-tune the positioning of
4006 the test antenna so that it can be perfectly aligned with the central axis of the array.
4007 A LabView script was developed to automate the measurement of a full 360° radiation
4008 pattern and control the measurement electronics. Data from these acquisitions is stored
4009 on university provided cloud storage.

4010 **5.3 Development of a Synthetic Cyclotron Antenna (SYNCA) 4011 for Antenna Array Calibration**

4012 This section is the manuscript of the publication [81] detailing the development of a
4013 Synthetic Cyclotron Antenna (SYNCA) for antenna array characterization measurements
4014 by the Project 8 collaboration.

4015 **5.3.1 Introduction**

4016 Neutrinos are the most abundant standard model fermions in our universe, but due to
4017 weak interaction cross-sections with other particles, neutrinos are particularly difficult
4018 to study. Consequently, many fundamental properties of neutrinos are still unknown
4019 including the absolute scale of the neutrino mass [31]. Direct, kinematic measurements of
4020 the neutrino mass are particularly valuable due to their model independent nature [37].

4021 To date the most sensitive direct neutrino mass measurements have been performed by
 4022 the KATRIN collaboration [88], which measures the molecular tritium β -decay spectrum
 4023 to infer the neutrino mass. Current data from neutrino oscillation measurements [31]
 4024 allow for neutrino masses significantly smaller than the design sensitivity of the KATRIN
 4025 experiment; therefore, there is a need for new technologies for performing direct neutrino
 4026 mass measurements to probe lower neutrino masses.

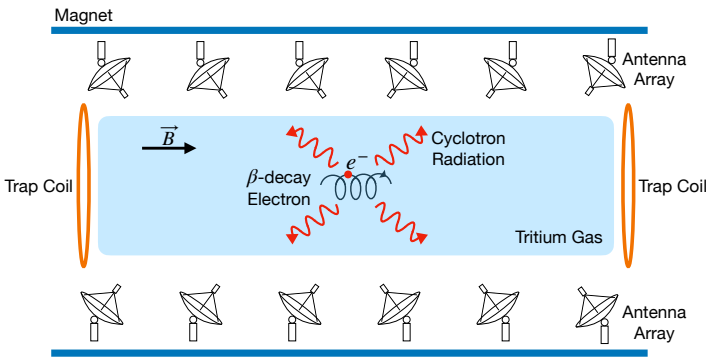


Figure 5.8. A sketch of an antenna array large-volume CRES experiment. Electrons from β -decays are confined in a magnetic field using a set of trap coils. The cyclotron radiation produced by the motion of the trapped electrons can be detected by a surrounding antenna array to determine the electron energies. Measuring the energies of many electrons produces a β -decay spectrum.

4027 The Project 8 collaboration is developing new methods for neutrino mass measurement
 4028 based on Cyclotron Radiation Emission Spectroscopy (CRES) [56, 89–91], with the goal
 4029 of measuring the absolute scale of the neutrino mass with a 40 meV/c² sensitivity [?, 37].
 4030 This sensitivity goal will require the development of two separate technical capabilities.
 4031 First is the development of an atomic tritium source, which avoids significant spectral
 4032 broadening due to molecular final states [55]. Second is the technology for performing
 4033 CRES in a multi-cubic-meter experimental volume with high combined detection and
 4034 reconstruction efficiency, which is required in order to obtain sufficient event statistics
 4035 near the tritium spectrum endpoint.

4036 One approach for a large-volume CRES experiment is to use an array of antennas,
 4037 which surrounds a volume of tritium gas, to detect the cyclotron radiation produced
 4038 by the β -decay electrons when they are trapped in a background magnetic field using a
 4039 set of magnetic trapping coils (see Figure 5.8). Project 8 has developed a conceptual
 4040 experiment design to study the feasibility of this approach. The design consists of a
 4041 single circular array of antennas with a radius of 10 cm and 60 independent channels
 4042 positioned around the center of the magnetic trap. The motivation behind this antenna

array design is to first develop an understanding of the antenna array approach to CRES with a small scale experiment before attempting to scale the technique to large volumes by using multiple antenna rings to construct the full cylindrical array. The development of the antenna array approach to CRES has largely proceeded through simulations using the Locust software package [80, 92], which is used to model the fields emitted by CRES events and predict the signals received by the surrounding antenna array. To validate these simulations, a dedicated test stand is being constructed to perform characterization measurements of the prototype antenna array developed by Project 8 (see Figure 5.9) and benchmark signal reconstruction methods using a specially designed transmitting calibration probe antenna.

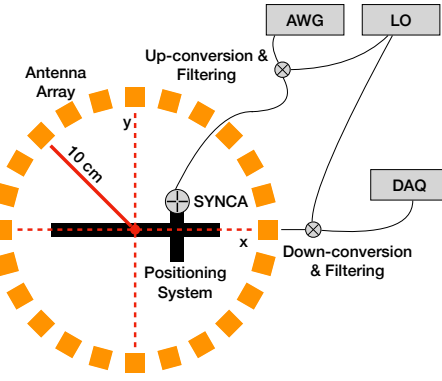


Figure 5.9. A schematic of the antenna array test stand. The circular antenna array has a radius of 10 cm with 60 independent channels (limited number shown for clarity). The test stand includes an arbitrary waveform generator (AWG), local oscillator (LO), and data acquisition (DAQ) hardware. Finally, a specialized Synthetic Cyclotron Antenna (SYNCA) is used to inject signals to test the antenna array.

We call this probe antenna the Synthetic Cyclotron Antenna or SYNCA. The SYNCA is a novel antenna design that mimics the cyclotron radiation generated by individual charged particles trapped in a magnetic field, which will be used in the antenna test stand to perform characterization measurements, simulation validation, and reconstruction benchmarking. This paper provides an overview of the design, construction, and characterization measurements of the SYNCA performed in preparation for its usage as a transmitting calibration probe.

In Section 5.3.2 we provide a description of the cyclotron radiation field characteristics that we recreate with the SYNCA. In Section 5.3.3 we give an overview of the simulations performed to develop an antenna design that mimics the characteristics of cyclotron radiation. In Section 5.3.4 we outline characterization measurements to validate that the fields generated by the SYNCA match simulation, and finally in Section 5.3.5 we

4065 demonstrate an application of the SYNCA to test phased array reconstruction techniques
 4066 on the bench-top.

4067 5.3.2 Cyclotron Radiation Phenomenology

4068 To understand the cyclotron radiation phenomenology that the SYNCA should mimic,
 4069 we consider a charged particle moving at relativistic speed in the presence of an external
 4070 magnetic field (see Figure 5.10). In the special case we shall examine, the entirety of
 4071 the electron's momentum is directed perpendicular to the magnetic field; therefore, the
 4072 trajectory of the electron is confined to the cyclotron orbit plane. Because the momentum
 4073 vector is oriented perpendicular to the magnetic field, electrons with these trajectories
 4074 are said to have pitch angles of 90°.

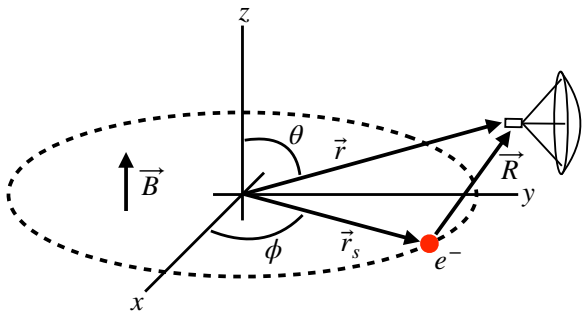


Figure 5.10. An electron (red dot) performing cyclotron motion in the x-y plane. The resulting cyclotron radiation is observed by an antenna located at the field point of interest.

4075 The cyclotron radiation fields generated by this circular trajectory are those which
 4076 we aim to reproduce with the SYNCA. We can describe the electromagnetic (EM) fields
 4077 using the Liénard-Wiechert equations [49, 80], which in non-covariant form express the
 4078 electric field as

$$\vec{E} = e \left[\frac{\hat{n} - \vec{\beta}}{\gamma^2 (1 - \vec{\beta} \cdot \hat{n})^3 |\vec{R}|^2} \right]_{t_r} + \frac{e}{c} \left[\frac{\hat{n} \times [(\hat{n} - \vec{\beta}) \times \dot{\vec{\beta}}]}{(1 - \vec{\beta} \cdot \hat{n})^3 |\vec{R}|} \right]_{t_r}, \quad (5.23)$$

4079 where e is the particle's charge, $\hat{n} = (\vec{r} - \vec{r}_s)/|\vec{r} - \vec{r}_s|$ is the unit vector pointing from the
 4080 electron to the field measurement point, $\vec{\beta} = \dot{\vec{r}}_s/c$ is the velocity of the particle divided
 4081 by the speed of light, and γ is the relativistic Lorentz factor. The equation is meant to
 4082 be evaluated at the retarded time as indicated by $t_r = t - |\vec{R}|/c$, which accounts for the
 4083 time delay due to the finite speed of light between the point where the field was emitted
 4084 and the point where the field is detected.

4085 We would like to simplify Equation 5.23 it at all possible. As a first step we analyze
 4086 the relative magnitudes of the electric field polarization components. Consider an electron
 4087 following a circular cyclotron orbit in a uniform magnetic field whose guiding center
 4088 is positioned at the origin of the coordinate system. The equation of motion can be
 4089 expressed as

$$\vec{r}_s = (r_c \cos \omega_c t_r) \hat{x} + (r_c \sin \omega_c t_r) \hat{y}. \quad (5.24)$$

4090 For single antenna located along the y -axis at position $\vec{r} = r_a \hat{y}$ we are interested in the
 4091 incident electric fields from the electron. The electric field is given by Equation 5.23,
 4092 which we evaluate in the regime where $r_a \gg r_c$. This limit can be justified by comparing
 4093 the radius of the cyclotron orbit for an electron with the tritium beta-spectrum endpoint
 4094 energy of 18.6 keV in a 1 T magnetic field to the typical ($r_a \simeq 100$ mm) radial position
 4095 of the receiving antenna. We find that the cyclotron orbit has a radius of 0.46 mm which
 4096 is approximately a factor of 200 smaller than the typical antenna radial position. In this
 4097 regime we can make the approximation $\vec{R} \simeq r_a \hat{y}$ and the expression for the electric field
 4098 at the antenna's position becomes

$$\vec{E} = \frac{e}{\gamma^2 r_a^2} \frac{\hat{x}(\frac{r_c \omega_c}{c} \sin \omega_c t_r) + \hat{y}(1 - \frac{r_c \omega_c}{c} \cos \omega_c t_r)}{(1 - \frac{r_c \omega_c}{c} \cos \omega_c t_r)^3} - \frac{e}{cr_a} \frac{\hat{x}(\frac{r_c^2 \omega_c^3}{c^2} - \frac{r_c \omega_c^2}{c} \cos \omega_c t_r)}{(1 - \frac{r_c \omega_c}{c} \cos \omega_c t_r)^3}. \quad (5.25)$$

4099 Since the receiving antenna is part of a circular array of antennas, it is useful to rewrite
 4100 Equation 5.25 in terms of the azimuthal ($\hat{\phi}$) and radial (\hat{r}) polarizations. Making use of
 4101 the fact that for an antenna located at $R = r_a \hat{y}$ that $\hat{\phi} = -\hat{x}$ and $\hat{r} = \hat{y}$ we find

$$\vec{E} = \hat{\phi} E_\phi + \hat{r} E_r \quad (5.26)$$

$$E_\phi = \frac{e}{(1 - \frac{r_c \omega_c}{c} \cos \omega_c t_r)^3} \left[-\frac{\frac{r_c \omega_c}{c} \sin \omega_c t_r}{\gamma^2 r_a^2} + \frac{\omega_c \left(\frac{r_c^2 \omega_c^2}{c^2} - \frac{r_c \omega_c}{c} \cos \omega_c t_r \right)}{cr_a} \right] \quad (5.27)$$

$$E_r = \frac{e(1 - \frac{r_c \omega_c}{c} \sin \omega_c t_r)}{\gamma^2 r_a^2 (1 - \frac{r_c \omega_c}{c} \cos \omega_c t_r)^3}. \quad (5.28)$$

4102 For the purposes of designing a synthetic cyclotron radiation antenna we are interested
 4103 in the dominant electric field polarization emitted by the electron. The antenna is being
 4104 designed to mimic the cyclotron radiation produced by electrons with kinetic energies of
 4105 approximately 18.6 keV in a 1 T magnetic field [55]. Since the relativistic beta factor for
 4106 an electron with this kinetic energy is $|\vec{\beta}| \simeq \frac{1}{4}$, the approximations $\gamma \simeq 1$ and $\frac{r_c \omega_c}{c} \simeq \frac{1}{4}$ are
 4107 justified. Inserting these expressions into the equations for the electric field components

⁴¹⁰⁸ above simplifies the comparison of the magnitudes of the two components. Additionally,
⁴¹⁰⁹ we compare the time-averaged magnitudes to evaluate the root mean squared electric
⁴¹¹⁰ field ratio. The time-averaged ratio of the radial and azimuthally polarized electric fields
⁴¹¹¹ with the above simplifications is given by

$$\frac{\langle |E_r| \rangle}{\langle |E_\phi| \rangle} = \frac{8 - \sqrt{2}}{\left| 1 - \frac{r_a}{r_c} \frac{1-2\sqrt{2}}{8} \right|} \simeq \frac{r_c}{r_a} \frac{8(8 - \sqrt{2})}{2\sqrt{2} - 1} = 0.13, \quad (5.29)$$

⁴¹¹² where we have made use of the fact that for these magnetic fields and kinetic energies
⁴¹¹³ the cyclotron radius is much smaller than the radius of the antenna array.

⁴¹¹⁴ From Equation 5.29 we see that the time-averaged azimuthal polarization is larger than
⁴¹¹⁵ the radial polarization by about a factor of 8, which makes it the dominant contribution
⁴¹¹⁶ to the electric fields at the position of the antenna. We must also consider the directivity
⁴¹¹⁷ of the receiving antenna which can have a gain that is disproportionately large for a
⁴¹¹⁸ specific polarization component. Because the E_ϕ component is dominant, the receiving
⁴¹¹⁹ antenna array is designed with an azimuthal polarization, which negates the voltages
⁴¹²⁰ induced in the antenna from the radially polarized fields. Therefore, we conclude that
⁴¹²¹ for the purpose of designing the SYNCA antenna it is acceptable to approximate the
⁴¹²² electric fields from Equation 5.23 as purely azimuthally or ϕ -polarized. The simplified
⁴¹²³ expression for the electric field received by an antenna becomes

$$\vec{E} = E_\phi \hat{\phi} = \frac{e \frac{r_c \omega_c}{c}}{4r_a r_c} \left[\frac{\frac{r_c \omega_c}{c} - \cos \omega_c t - \frac{4r_c}{r_a} \sin \omega_c t}{(1 - \frac{r_c \omega_c}{c} \cos \omega_c t)^3} \right]_{t_r} \hat{\phi}, \quad (5.30)$$

⁴¹²⁴ where the radius of the cyclotron orbit is called r_c , the cyclotron frequency is called ω_c ,
⁴¹²⁵ and the radial position of the receiving antenna is called r_a . Equation 5.30 has been
⁴¹²⁶ evaluated in the non-relativistic limit where $\gamma \simeq 1$, which is justified by the fact that
⁴¹²⁷ $|\vec{\beta}| \simeq \frac{c}{4}$ for an electron with an 18.6 keV kinetic energy in a 1 T magnetic field.

⁴¹²⁸ This rather complicated expression can be simplified using Fourier analysis. Assuming
⁴¹²⁹ a background magnetic field of 1 T and a kinetic energy of 18.6 keV we calculate
⁴¹³⁰ numerically the electric field using Equation 5.30 and apply a discrete Fourier Transform
⁴¹³¹ to visualize the frequency spectrum (see Figure 5.11).

⁴¹³² We observe that the azimuthally polarized electric field is periodic with a base cyclotron
⁴¹³³ frequency of 25.898 GHz corresponding to the highest power frequency component in
⁴¹³⁴ Figure 5.11. The frequency spectrum reveals that the signal is composed of a constant
⁴¹³⁵ term with zero frequency and a series of harmonics separated by 25.898 GHz. Therefore,

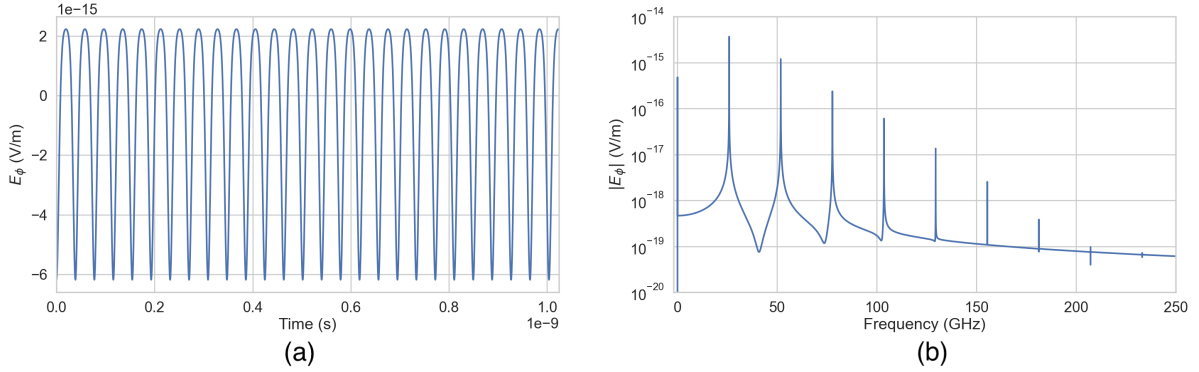


Figure 5.11. A plot of the numeric solution to Equation 5.31. The time-domain representation of the signal (a) is composed of a zero frequency term and a series of harmonics separated by the main cyclotron frequency as shown in the plot of the frequency spectrum (b). We can see that the relative amplitude of the harmonics beyond $k = 7$ are smaller than the main carrier by a factor of about 10^{-5} and are completely negligible.

we can represent the azimuthal electric fields from the electron as a linear combination of pure sinusoids with frequencies given by $\omega_k = k\omega_c$ ($k \in 0, 1, 2, \dots$) and amplitudes extracted from the Fourier representation. Using this representation we can transform the equation for the azimuthally polarized electric fields in Equation 5.30 into

$$E_\phi = \frac{e^{\frac{r_c \omega_c}{c}}}{4r_a r_c} \sum_{k=0}^7 A_k e^{i\omega_k t_r}, \quad (5.31)$$

where we have truncated the sum over harmonics at the 7th order for completeness. The amplitudes A_k are dimensionless complex numbers, which encode the relative powers of the harmonics as well as the starting overall phase of the cyclotron radiation. Because magnitude of the relative amplitudes exponentially decreases for higher harmonics, it is usually sufficient to consider only the terms up to $k = 4$ where the relative amplitude of the harmonics has decreased from the main carrier by a factor of approximately 100. However, for completeness we include harmonics up to 7th order in Equation 5.31. The range of frequencies to which the receiving antenna array in the antenna test stand is sensitive is defined by the antenna's transfer function. The receptive bandwidth for the antennas used in the test stand is a range of frequencies with a bandwidth on the order of a few GHz centered around the main cyclotron carrier frequency of 25.898 GHz. Therefore, the higher order harmonics as well as the zero frequency term can be ignored when considering only the signals that will be received by the antenna array.

Considering only the 1st order harmonic term from Equation 5.31, which represents the portion of the electric field that will be detected by the array, and evaluating this at

4155 the retarded time we obtain the following for the ϕ -polarized electric fields

$$E_\phi \propto \cos \left(\omega_c \left(t - |\vec{R}|/c \right) - \Delta \right), \quad (5.32)$$

4156 where the arbitrary phase Δ is defined by $A_k = |A_k|e^{i\Delta}$. We are interested in the
 4157 characteristics of the amplitude of the electric field as a function of the radial distance
 4158 component ($|\vec{R}|$) of the retarded time. In particular, the maximum of E_ϕ occurs when
 4159 the argument of the cosine function is equal $n\pi$ where $n \in \{0, \pm 2, \pm 4, \dots\}$; however, the
 4160 solutions where n is negative can be discarded since they represent unphysical negative
 4161 overall phases. Applying this condition to Equation 5.32 gives a condition on the radial
 4162 position of the maximum of E_ϕ

$$\omega_c(t - |\vec{R}|/c) - \Delta = n\pi, \quad (5.33a)$$

$$|\vec{R}| = \frac{c}{\omega_c} ((\omega_c t - \Delta) - n\pi), \quad (5.33b)$$

4163 which is a function of time in the frame of the moving electron (t). Equation 5.33 can
 4164 be further simplified by noticing that the azimuthal position of the electron ($\phi_e(t)$) as a
 4165 function of time is defined by $\phi_e(t) = \omega_c t - \Delta$ which reduces Equation 5.33 to

$$|\vec{R}| = \frac{c}{\omega_c} (\phi_e(t) - n\pi). \quad (5.34)$$

4166 Equation 5.34 represents an archimedian spiral which is formed when plotting the
 4167 amplitude of E_ϕ in the x-y plane. The solution where $n = 0$ represents the leading edge
 4168 of the radiation spiral which propagates outward from the electron at the speed of light.
 4169 The additional solutions for $n > 0$ represent the persistent spiral at radii inside the
 4170 leading edge of the radiated fields that have not yet been detected by the receiver at the
 4171 current time. In Figure 5.12a we show the expected spiral pattern for the maxima of the
 4172 cyclotron radiation.

4173 In particular, we note that for the circular array geometry of the test stand, depicted
 4174 as the series of circles in Figure 5.12a, each antenna receives a linearly polarized wave
 4175 with a phase offset that corresponds to the azimuthal angle for that antenna element.
 4176 Therefore, as we show in Figure 5.12b, when the relative phase of the received signal is
 4177 plotted as a function of the receiving antenna's azimuthal position the result is also an
 4178 Archimedean spiral.

4179 Based on these analytical calculations we can characterize the magnitude, polarization,
 4180 and phase of the signals received by the antenna array using three criteria. These criteria

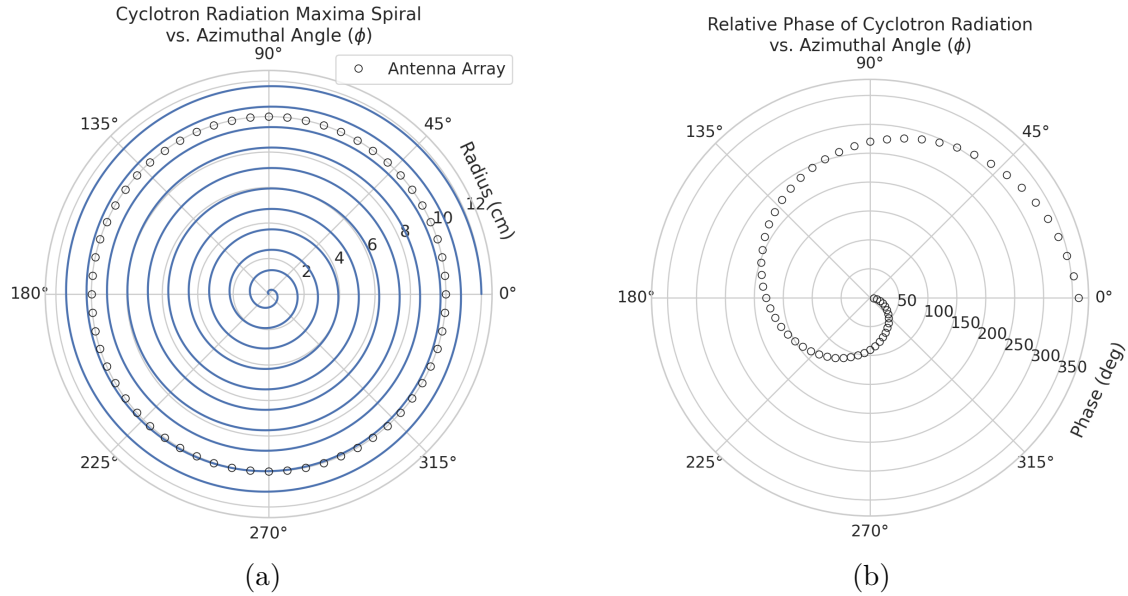


Figure 5.12. The amplitude maxima of the cyclotron radiation form an Archimedean spiral as the radiation propagates outward from the cyclotron orbit center (a). A circular antenna array located at a fixed radius from the orbit center will receive electric fields with equal magnitude in each of its channels, but the phase of the electric field incident on each array channel will be linearly out of phase from its neighbor antennas by an amount equal to the angular separation of the two channels (b).

are the basis of comparison for the radiation produced by the SYNCA and cyclotron radiation emitted by electrons and will be used to evaluate the performance of antenna designs. The criteria are:

1. Electric fields that are ϕ -polarized near $\theta = 90^\circ$
2. Uniform time-averaged electric field magnitudes around the circumference of a circle centered on the antenna
3. Electric fields whose phase is equal to the azimuthal angle at the point of measurement plus a constant

The Locust simulation package [92] can be used to directly simulate the EM fields generated by electrons performing cyclotron motion to validate the analytical calculations. Locust simulates the EM fields by first calculating the trajectory of the electrons in the magnetic trap using the Kassiopeia software package [93]. The trajectory can then be used to solve for the EM fields using the Liénard-Wiechert equations directly with no approximations. The resulting electric field solutions drive a receiving antenna by

4195 convolving the time-domain fields with the finite-impulse response filter of the antenna
 4196 or they can be examined directly to study the field characteristics that the SYNCA must
 4197 reproduce. In the next section we compare the radiation field patterns for electrons
 4198 simulated with Locust to patterns from a SYNCA antenna design.

4199 **5.3.3 SYNCA Simulations and Design**

4200 One potential SYNCA design is the crossed-dipole antenna [94]. A crossed-dipole antenna
 4201 consists of two dipole antennas, one of which is rotated 90° with respect to the other,
 4202 which are fed with signals that are out of phase from the opposite dipole by 90° (see
 Figure 5.13). This arrangement causes the signals fed to each arm of the dipole to be

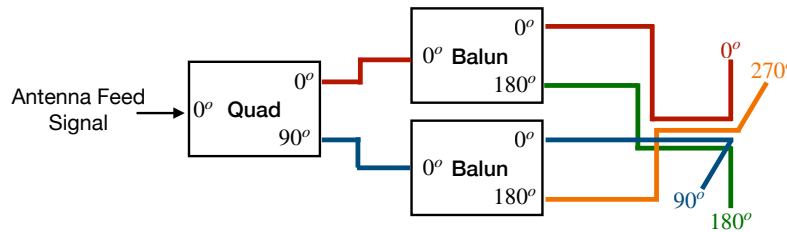


Figure 5.13. An idealized crossed-dipole antenna consists of two electric dipole antennas oriented perpendicular to each other and is fed with four signals with a quadrature phase relationship. An example antenna feed circuit is shown which is composed of a chained combination of a quadrature hybrid-coupler (Quad) and two baluns.

4203
 4204 out of phase from each of the neighboring arms by 90°, which mirrors the spatial phase
 4205 relationship of cyclotron radiation fields.

4206 A potential drawback of this design is that standard crossed-dipole antennas do not
 4207 radiate uniform electric fields near the $\theta = \pi/2$ plane. Typical crossed-dipole antennas
 4208 use dipole arm lengths equal to $\lambda/4$ or larger [94], where λ is the wavelength at the
 4209 desired operating frequency. Such large arm lengths cause the electric field magnitude
 4210 to vary significantly around the circumference of the antenna. However, making the
 4211 antenna electrically small by shrinking the arm length can improve the antenna pattern
 4212 uniformity.

4213 In general, the criterion for an electrically small antenna is that the largest dimension
 4214 of the antenna (D) obey $D \lesssim \lambda/10$ [65]. In our application, we are attempting to mimic
 4215 the cyclotron radiation emitted by electrons produced from tritium β -decay with energies
 4216 near the spectrum endpoint. For a background magnetic field of 1 T, the corresponding

⁴²¹⁷ cyclotron frequency of tritium endpoint electrons is approximately 26 GHz. Therefore, the
⁴²¹⁸ electrically small condition would require that the largest dimension of the crossed-dipole
⁴²¹⁹ antenna be smaller than 1.2 mm.

⁴²²⁰ A crossed-dipole antenna with an overall size of 1.2 mm is challenging to fabricate due
⁴²²¹ to the small dimensions of the dipole arms that, in practice, are fragile and unsuitable
⁴²²² for use as a calibration probe. To mitigate some of the challenges with the fabrication
⁴²²³ of such a small antenna, a variant crossed-dipole antenna design using printed circuit
⁴²²⁴ board (PCB) technology (see Figure 5.14) was developed in partnership with an antenna
prototyping company, Field Theory Consulting ¹.

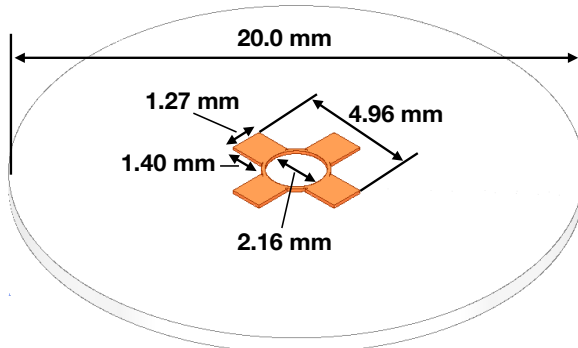


Figure 5.14. A model of the PCB crossed-dipole antenna with dimensions. The design has an inside diameter of 2.16 mm for the central circular trace, which is 0.13 mm wide. The dipole arms each have a width of 1.27 mm and protrude beyond the circular trace by 1.40 mm, which gives an overall width of 4.96 mm for the length of the antenna PCB trace from end-to-end. The overall size of the antenna is 20.0 mm the majority of which is the PCB dielectric material. This design was observed in simulation to maintain the field characteristics of the idealized crossed-dipole while being simpler to fabricate due to the increased size of the antenna.

⁴²²⁵
⁴²²⁶ The PCB crossed-dipole design uses four rectangular pads to represent the dipole arms,
⁴²²⁷ which are connected by a thin circular trace. The circular trace both adds mechanical
⁴²²⁸ stability to the antenna and improves the azimuthal uniformity of the electric fields
⁴²²⁹ compared to a more standard crossed-dipole geometry. Furthermore, the circular trace
⁴²³⁰ allows for a greater separation between dipole arms than standard crossed-dipoles, which
⁴²³¹ is required to accommodate the coaxial connections to each pad. The pads each contain
⁴²³² a through-hole solder joint to connect coaxial transmission lines using hand soldering.
⁴²³³ The antenna PCB has no ground plane on the bottom layer as this was observed in
⁴²³⁴ simulation to significantly distort the radiation pattern in the plane of the PCB. The
⁴²³⁵ only ground planes present in the model are the outer conductors of the four coaxial

¹<https://fieldtheoryinc.com/>

4236 transmission lines which feed the antenna. These are left unterminated on the bottom of
4237 the PCB dielectric material.

4238 The antenna design development utilized a combination of Locust electron simula-
4239 tions and antenna simulations using ANSYS HFSS [66], a commercial finite-element
4240 electromagnetic simulation software. Two antenna designs were simulated: an idealized
4241 electrically small crossed-dipole antenna with an arm length of 0.40 mm and an arm
4242 separation of 0.05 mm, as well as a PCB crossed-dipole antenna with the dimensions
4243 shown in Figure 5.14. Plotting the magnitude of the electric fields generated by the
4244 antennas across a 10 cm square located in the same plane as the respective antennas
4245 reveals the expected cyclotron spiral pattern (see Figure 5.15) which closely matches
4246 the prediction for simulated electrons. The spiral pattern demonstrates that the electric
4247 fields have the appropriate phases to mimic cyclotron radiation, which fulfills SYNCA
criterion 3 identified in Section 5.3.2.

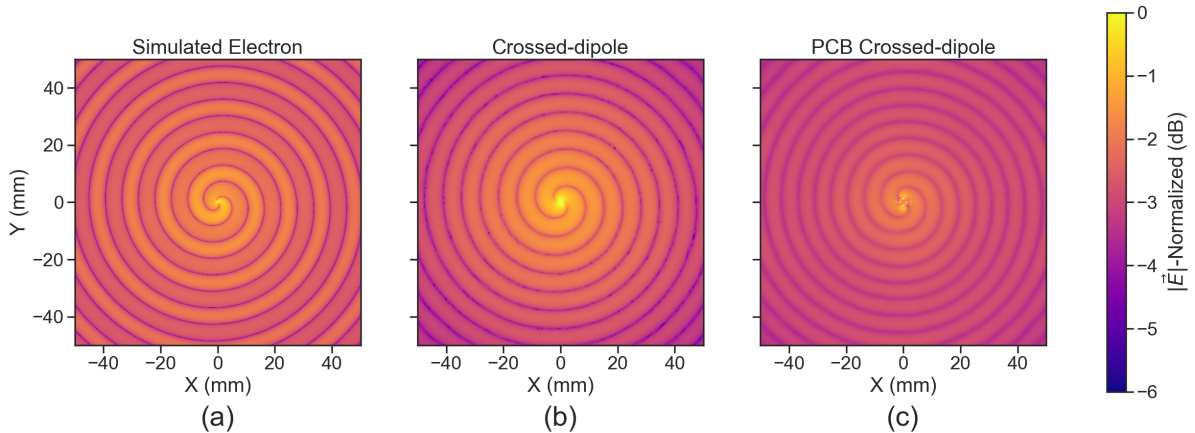


Figure 5.15. A comparison of the electric field magnitudes, normalized by the maximum value of the electric field in each simulation, plotted on a 10 cm square to visualize the Archimedean spirals formed by the electron (a), the crossed-dipole antenna (b), and a PCB crossed-dipole antenna (c). The matching patterns indicate that the electric fields have similar phase characteristics. These images were generated using Locust simulations for the electron and ANSYS HFSS for both antennas.

4248
4249 As we can see from Figure 5.16, the crossed-dipole antenna, which uses an idealized
4250 geometry, exhibits good agreement with simulation. The antenna has a maximum
4251 deviation from a simulated electron of approximately 0.5 dB in the total electric field, 1
4252 dB for the ϕ -polarized electric field and 1 dB for the θ -polarized electric field.

4253 In comparison, the pattern of the PCB crossed-dipole antenna, because the simulation
4254 incorporates the geometry of the coax transmission lines, exhibits some distortion from
4255 the idealized cross-dipole simulations. The vertically oriented ground planes of the coax

4256 lines introduce more θ -polarized electric fields than are observed for simulated electrons
 4257 near $\theta = 90^\circ$. The significant θ -polarized field minimum is still present but shifted
 4258 to approximately $\theta = 65^\circ$. The θ -polarized field deviations of the PCB crossed-dipole

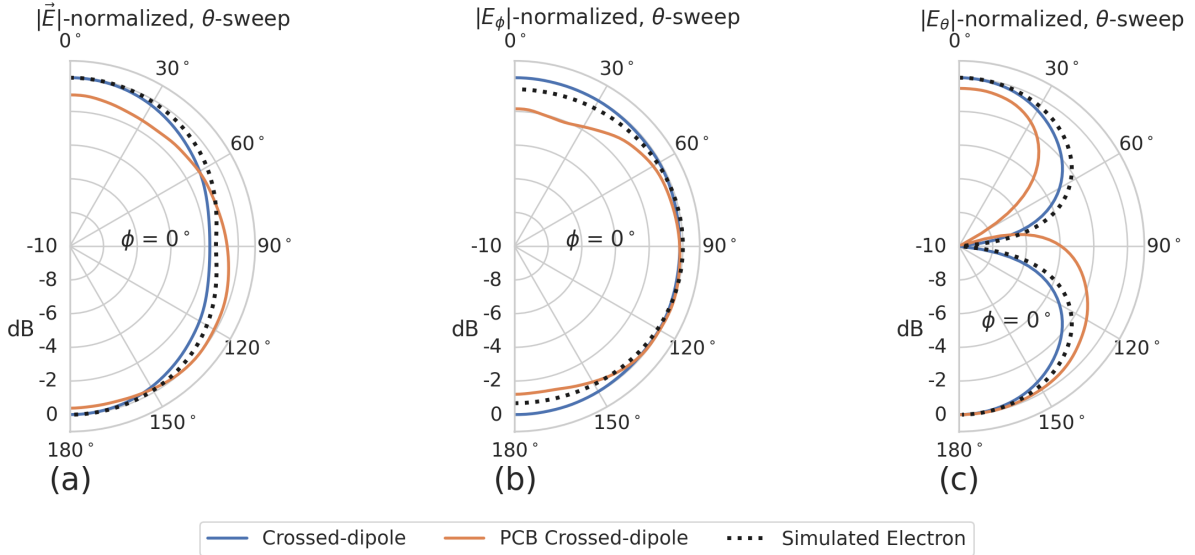


Figure 5.16. A comparison of the normalized electric field magnitudes for the ideal crossed-dipole, PCB crossed-dipole, and a simulated electron as a function of the polar angle (θ). (a) Shows the total electric field, (b) shows the ϕ -polarized electric field component, and (c) shows the θ -polarized electric field component. These images were generated using Locust simulations for the electron and ANSYS HFSS for both antennas.

4258
 4259 antenna should not greatly impact the performance of the antenna because the receiving
 4260 antenna array is primarily ϕ -polarized. Therefore deviations in the θ -polarized fields
 4261 will be suppressed due to the polarization mismatch. More importantly, the ϕ -polarized
 4262 electric field pattern generated by the PCB crossed-dipole closely matches simulated
 4263 electrons across the polar angle range of $50^\circ < \theta < 150^\circ$. In this region the PCB crossed-
 4264 dipole differs by less than 0.5 dB from simulated electrons. This range greatly exceeds
 4265 the beamwidth of the receiving antenna array which is designed to be most sensitive
 4266 to fields produced near $\theta = 90^\circ$. Therefore, we conclude that the PCB crossed-dipole
 4267 antenna generates a ϕ -polarized radiation pattern that fulfills SYNCA criterion 1 from
 4268 Section 5.3.2.

4269 The final SYNCA criterion is related to the uniformity of the electric fields when
 4270 measured azimuthally around the antenna. As we saw for real electrons in Section 5.3.2
 4271 it is expected that the magnitude of the electric field be completely uniform as a function
 4272 of the azimuthal angle due to the symmetry of the cyclotron orbit. In Figure 5.17 we plot
 4273 the total electric field as a function of azimuthal angle for an electron, the crossed-dipole

antenna, and the PCB crossed-dipole antenna. The crossed-dipole antenna exhibits

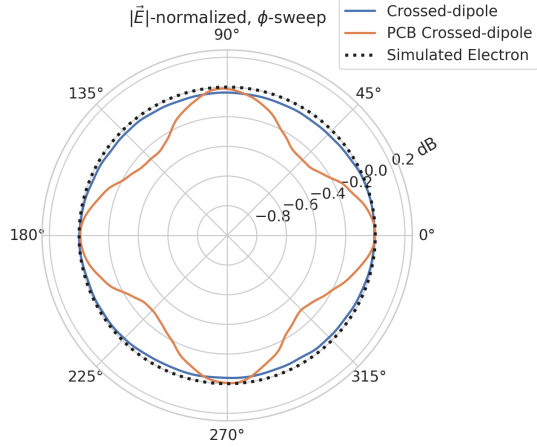


Figure 5.17. A comparison of the normalized electric field magnitudes for the crossed-dipole, PCB crossed-dipole, and a simulated electron as a function of the azimuthal angle (ϕ) evaluated at $\theta = 90^\circ$. This image was generated using Locust simulations for the electron and ANSYS HFSS for both antennas.

4274

4275 perfect uniformity around the azimuthal angle, whereas the PCB crossed-dipole has a
 4276 small periodic deviation with a maximum difference of 0.3 dB caused by the coaxial
 4277 transmission lines below the PCB. Such a small deviation from uniformity is acceptable
 4278 since it is smaller than the expected variation in uniformity caused by imperfections in
 4279 the antenna fabrication process, which modifies the antenna shape in an uncontrolled
 4280 manner by introducing solder blobs with a typical size of a few tenths of a millimeter on
 4281 the dipole arms (see Figure 5.18). Additionally, the SYNCA will be separately calibrated
 4282 to account for azimuthal differences in the electric field magnitude. Therefore we see
 4283 from the simulated performance of the PCB crossed-dipole antenna that this antenna
 4284 design meets all three of the SYNCA criteria.

4285

5.3.4 Characterization of the SYNCA

4286 Two SYNCAs were manufactured using the PCB crossed-dipole design (see Figure 5.18).
 4287 The antenna PCB (Matrix Circuit Board Materials, MEGTRON 6) is connected to
 4288 four 2.92 mm coaxial connectors (Fairview Microwave, SC5843) using semi-rigid coax
 4289 (Fairview Microwave, FMBC002), which also physically support the antenna PCB. The
 4290 antenna PCB consists only of two layers which correspond to the copper antenna trace
 4291 and the PCB dielectric. Each coax line is connected to the associated dipole arm using
 4292 through-hole soldering and phase matched to ensure that the electrical length of each
 4293 of the transmission lines is identical at the operating frequency. The antenna PCB is

4294 further reinforced using custom cut polystyrene foam blocks, which have an electrical
 4295 permittivity nearly identical to air. A custom 3D printed mount is included at the base
 4296 of the antenna to support the coax connectors and to provide a sturdy mounting base.

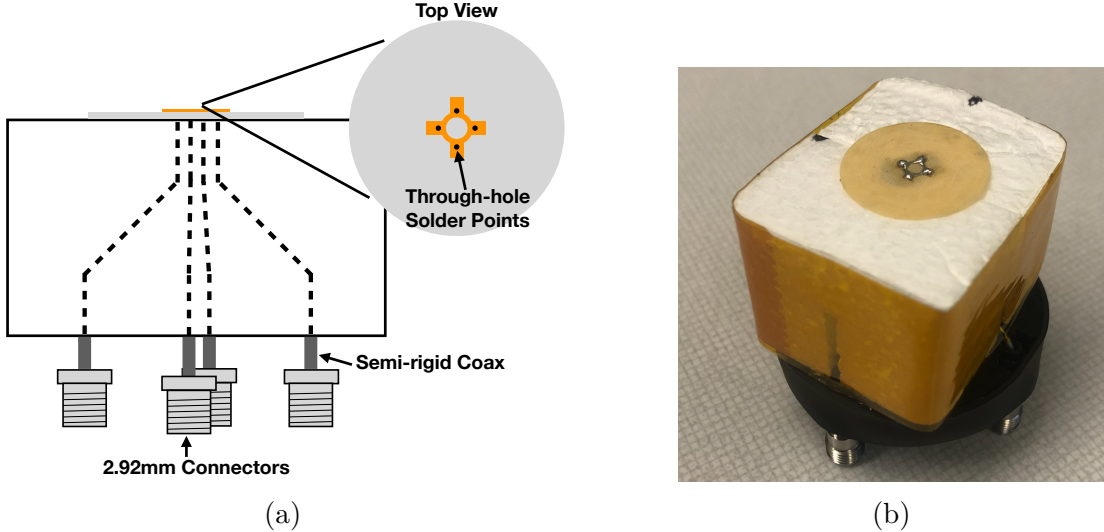


Figure 5.18. (a) A cartoon schematic which highlights the routing of the semi-rigid coax transmission lines. (b) A photograph of a SYNCA constructed using the modified crossed-dipole PCB antenna design. Visible in the photograph of the SYNCA are four blobs of solder which are an artifact of the SYNCA's hand-soldered construction. These solder blobs are the most significant deviation from the SYNCA design shown in Figure 5.14 and are responsible for a significant fraction of the irregularities seen in the antenna pattern.

4297 Characterization measurements were performed using a Vector Network Analyzer
 4298 (VNA) to measure the electric field magnitude and phase radiated by the SYNCA to
 4299 verify the radiation pattern (see Figure 5.19). The VNA is connected to the SYNCA
 4300 at one port through a hybrid-coupler whose outputs are connected to two baluns to
 4301 generate the signals with the appropriate phases to feed the SYNCA (see Figure 5.13).
 4302 The other port of the VNA is connected to a single reference horn antenna that serves
 4303 as a field probe. To position the SYNCA, a combination of translation and rotation
 4304 stages are used to characterize the antenna's fields across the entire radiation pattern
 4305 circumference. This measurement scheme is equivalent to measuring the fields generated
 4306 by the SYNCA using a full circular array of probe antennas.

4307 The antenna measurement space is surrounded by RF anti-reflective foam to isolate
 4308 the measurements from the lab environment (see Figure 5.19b) and remaining reflections
 4309 are removed using the VNA's time-gating feature. The SYNCA is affixed to the stages
 4310 by a custom RF transparent mount made of polystyrene foam. The coaxial cables deliver

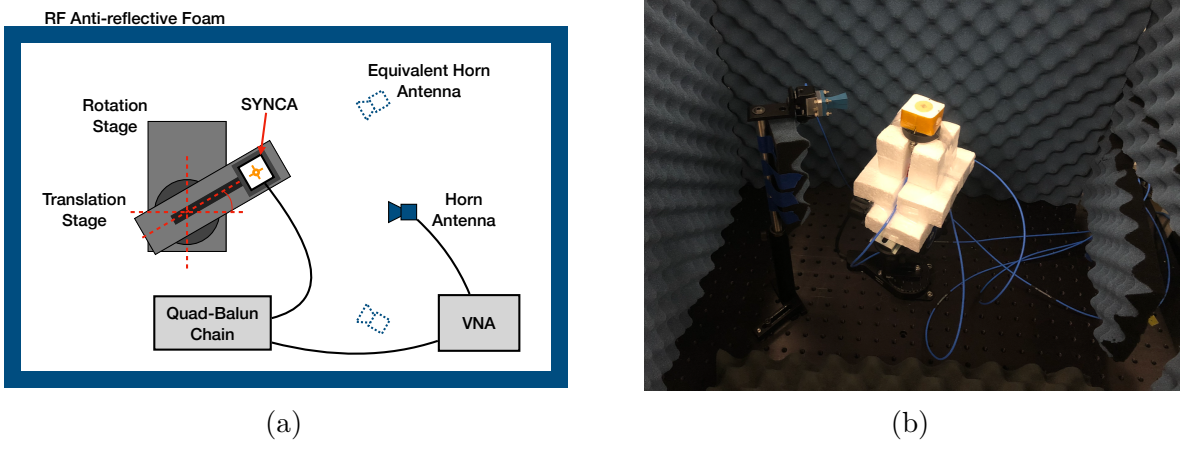


Figure 5.19. A schematic of the VNA characterization measurements (a). This setup allows for antenna gain and phase measurements across a full 360° of azimuthal angles using a motorized rotation stage and control of the radial position of the SYNCA using a translation stage. A photo of the setup in the lab is shown in (b).

the antenna feed signals generated by the VNA to the SYNCA while still allowing unrestricted rotation. The horn antenna probe is nominally positioned in the plane formed by the antenna PCB ($\theta = 90^\circ$ or $z = 0$ mm) at a distance of 10 cm from the SYNCA, to match the expected position of the antenna array relative to the SYNCA in the antenna array test stand. The horn antenna can be manually raised or lowered to different relative vertical positions to characterize the radiation pattern at different polar angles.

Several 360° scans were performed with probe vertical offsets of -10.0 mm, -5.0 mm, 0.0 mm, 5.0 mm, and 10.0 mm relative to the antenna PCB plane. These probe offsets cover a 2 cm wide vertical region centered on the SYNCA PCB, approximately equal to ± 6 degrees of polar angle. The measurements show that the SYNCA is generating fields with nearly isotropic magnitude across the probed region. The standard deviation of the electric field magnitude measured around the antenna circumference is approximately 2.9 dB for a typical rotational scan. The presence of a significant pattern null is noted near 45° (see Figure 5.20), which we attribute to small imperfections in the antenna PCB that could be introduced from the hand soldered terminations connecting the coax cables to the antenna. There is no significant difference in the radiation pattern when measured across the 2 cm vertical range. The measured relative phases closely follow the expectation for an electron, being linear with the measurement rotation angle and forming the expected spiral pattern. Other than the small phase imperfections there is

4331 a slight sinusoidal bias to the phase data, which we determined is the result of a small
 4332 ($\lesssim 1$ mm) offset of the antenna's phase center from the rotation axis of the automated
 4333 stages.

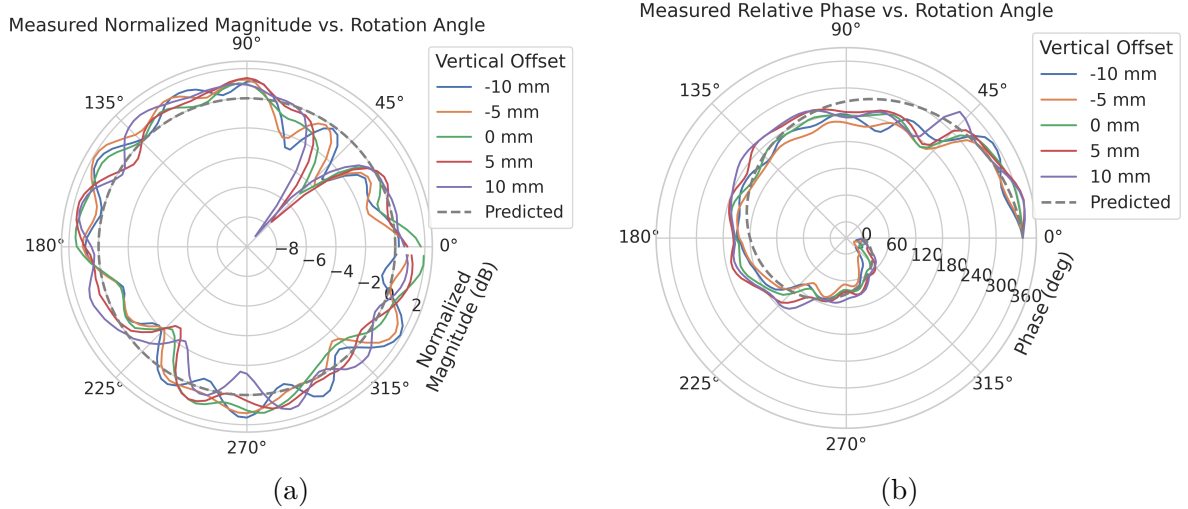


Figure 5.20. Linear interpolations of the measured electric field magnitude (a) and phase (b). The data was acquired using a VNA at 120 points spaced by 3 degrees from 0 to 357 degrees of azimuthal angle. The different color lines indicate the vertical offset of the horn antenna relative to the SYNCA PCB and the dashed line shows the expected shape from electron simulations. No significant difference in the antenna pattern is observed for the measured vertical offsets.

4344 The characterization measurements confirm the simulated performance of the SYNCA.
 4345 As expected the fields generated by the antenna are nearly isotropic in magnitude, ϕ -
 4346 polarized, and are linearly out of phase around the circumference of the antenna as
 4347 predicted for cyclotron radiation in Section 5.3.2. Small imperfections in the magnitude
 4348 and phase of the antenna are expected, particularly at the antenna's high operating
 4349 frequency of 26 GHz where small geometric changes can have significant impacts on
 4350 electrical properties. However, calibration through careful characterization measurements
 4351 can be used to remove the majority of these pattern imperfections, including the relatively
 4352 large pattern null near 45°, which will allow for the usage of the SYNCA as a test source
 4353 for free-space CRES experiments utilizing antenna arrays. In the next section we use the
 4354 VNA measurements obtained here as a calibration for signal reconstruction using digital
 4355 beamforming.

4346 5.3.5 Beamforming Measurements with the SYNCA

4347 Digital beamforming is a standard technique for signal reconstruction using a phased
 4348 array [95]. The SYNCA, since it exhibits the same cyclotron phases as a trapped electron,
 4349 can be used to perform simulated CRES digital beamforming reconstruction experiments
 4350 on the bench-top without the need for the magnet, cryogenics, and vacuum systems
 4351 required by a full CRES experiment. The fields received by the individual elements
 4352 of the antenna array will have phases dependent on the spatial position of the source
 4353 relative to the antennas. Therefore, a simple summation of the received signals will fail
 4354 to reconstruct the signal due to destructive interference between the individual channels
 4355 in the array. However, applying a phase shift associated with the source's spatial position
 4356 removes phase differences and results in a constructive summation of the channel signals
 4357 (see Figure 5.21). We can summarize the digital beamforming operation succinctly using
 4358 the following equation

$$y[t_n] = \sum_{m=0}^{N-1} x_m[t_n] A_m e^{i\phi_m}, \quad (5.35)$$

4359 where $y[t_n]$ represents the summed array signal at time t_n , $x_m[t_n]$ is the signal received
 4360 by channel m at time t_n , ϕ_m is the phase shift applied to the signal received at channel
 4361 m , and A_m is an amplitude weighting factor that accounts for the different signal power
 4362 received by individual channels. By changing the digital beamforming phases, the point
 4363 of constructive interference can be scanned across the sensitive region of the array to

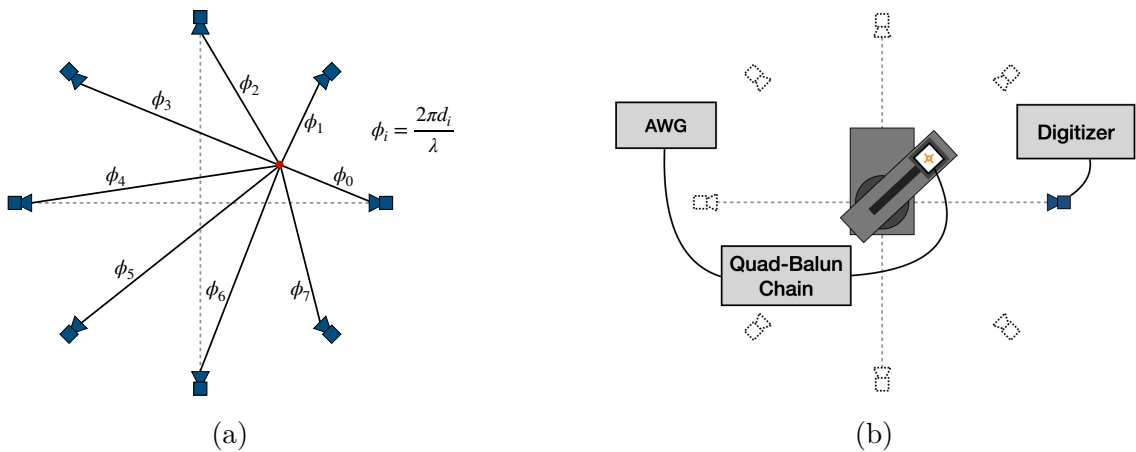


Figure 5.21. (a) A depiction of the relative phase differences for signals received by a circular antenna array from an isotropic source. The phases correspond to a unique spatial position.
 (b) A schematic of the setup used to perform digital beamforming.

4364 search for the location of a radiating source, which is identified as the point of maximum
 4365 summed signal power above a specified threshold. The digital beamforming phases consist
 4366 of two components,

$$\phi_m = 2\pi d_m/\lambda + \theta_m, \quad (5.36)$$

4367 where d_m is the distance from the m -th array element to the source, and θ_m is the
 4368 relative angle between the source position and the m -th antenna. The first component is
 4369 the standard digital beamforming phase that corresponds to the spatial position of the
 4370 source, and the second component is the cyclotron phase that corresponds to the relative
 4371 azimuthal phase offset.

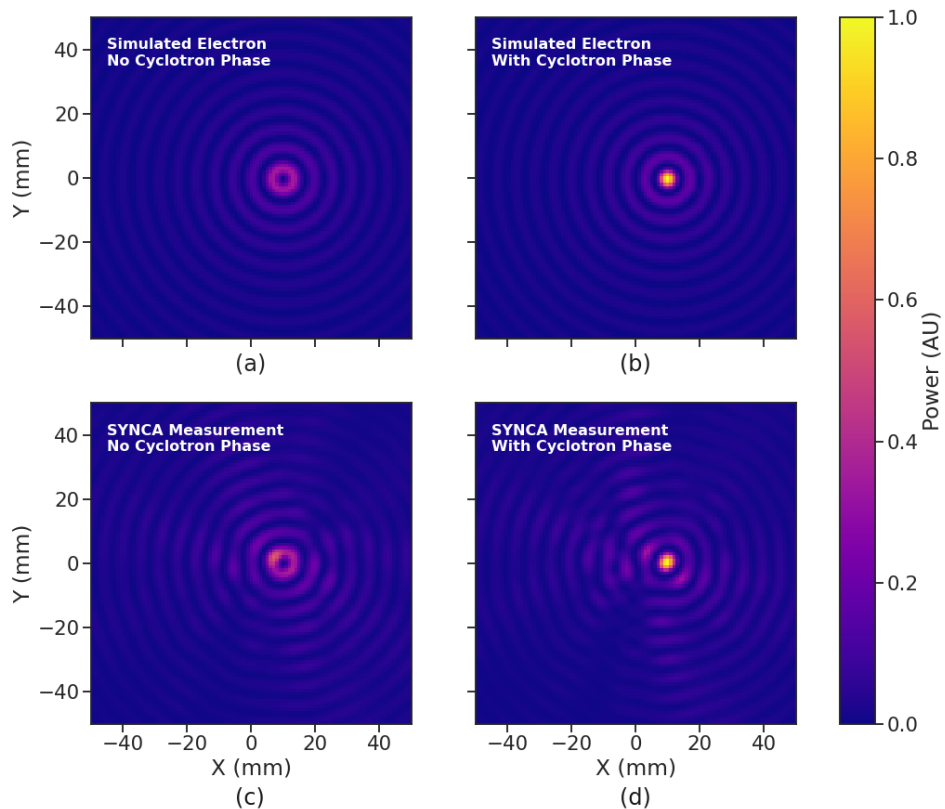


Figure 5.22. Digital beamforming maps generated using a simulated 60 channel array and electron simulated using the Locust package. (a) and (b) show the beamforming maps for simulated electrons without the cyclotron spiral phases and with the cyclotron spiral phases respectively. (c) and (d) show the beamforming maps produced from SYNCA measurements. We observe good agreement between simulated electrons and the SYNCA measurements.

4372 With a small modification to the hardware used to characterize the SYNCA (see
 4373 Figure 5.19), we can perform a digital beamforming reconstruction of a synthetic CRES

4374 event. By replacing the VNA with an arbitrary waveform generator (AWG), the SYNCA
4375 can be used to generate cyclotron radiation with an arbitrary signal structure, which
4376 can then be detected by digitizing the signals received by the horn antenna. Rotational
4377 symmetry allows us to use the rotational stage of the positioning system to rotate the
4378 SYNCA to recreate the signals that would have been received by a complete circular
4379 array of antennas.

4380 Using this setup, signals from a 60 channel circular array of equally spaced horn
4381 antennas were generated with the SYNCA positioned 10 mm off the central array axis,
4382 reconstructed using digital beamforming, and compared to Locust simulation (see Figure
4383 5.22). When the cyclotron spiral phases are not used, which is equivalent to setting θ_m
4384 in Equation 5.36 to zero, the SYNCA's position is reconstructed as a relatively faint ring
4385 as predicted by simulation. However, when the appropriate cyclotron phases are used
4386 during the beamforming procedure, both the simulated electron and the SYNCA appear
4387 as a single peak of high relative power corresponding to the source position. Therefore,
4388 we observe good agreement between the simulated and SYNCA reconstructions. While it
4389 may seem that for the case with no cyclotron phase corrections the ring reconstructs the
4390 position of the electron as effectively as beamforming with the cyclotron phase corrections,
4391 it is important to note that the simulations and measurements were generated without a
4392 realistic level of thermal noise. The larger maxima region and lower signal power, which
4393 occurs without the cyclotron phase corrections, significantly reduce the probability of
4394 detecting an electron in a realistic noise background.

4395 To bound the beamforming capabilities of the synthetic array of horn antennas, we
4396 performed a series of beamforming reconstructions where the SYNCA was progressively
4397 moved off the central axis of the array (see Figure 5.23). To extract an estimate of the
4398 position of the SYNCA using the digital beamforming image we apply a 2-dimensional
4399 (2D) Gaussian fit to the image data and extract the estimated centroid value. We find
4400 that the synthetic horn antenna array reconstructs the position of the SYNCA with a
4401 1σ -error of 0.3 mm with no apparent trend across the 30 mm measurement range. This
4402 reconstruction error is an order of magnitude larger than mean fit position uncertainty
4403 of 0.02 mm indicating that systematic effects related to the SYNCA positioning system
4404 could be contributing additional uncertainty to the measurements. Note that the current
4405 mean reconstruction error of 0.3 mm is a factor of 20 smaller than the full width at half
4406 maximum of the digital beamforming peak (6 mm), which could be interpreted as a naive
4407 estimate of the position reconstruction performance of this technique. Because these
4408 measurements are intended as a proof-of-principle demonstration, we do not investigate

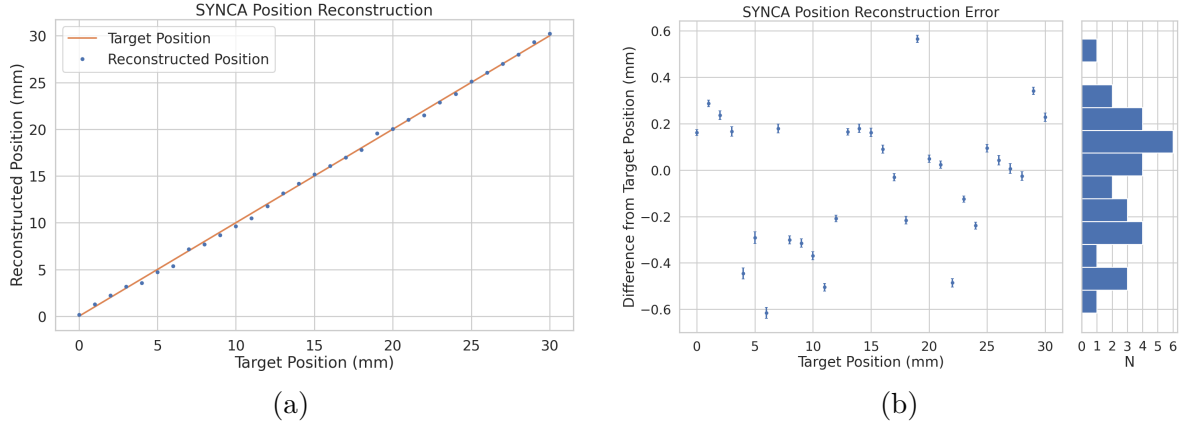


Figure 5.23. A plot of the SYNCA’s reconstructed position using the synthesized horn-antenna array and digital beamforming. (a) Shows the reconstructed position of the SYNCA compared with the target position indicated by the positioning system readout. (b) Shows the reconstruction error, which is the difference between the target and reconstructed positions. The error bars in (b) are the uncertainty in the mean position of the 2D Gaussian used to fit the digital beamforming reconstruction peak obtained from the fit covariance matrix. The mean fit position uncertainty of 0.02 mm is an order of magnitude smaller than the typical reconstruction error of 0.3 mm obtained by calculating the standard deviation of the difference between the reconstructed and target position.

4409 potential sources of systematic errors further; however, we expect that a similar and
 4410 more thorough investigation will be performed using the Project 8 antenna array test
 4411 stand, where typical reconstruction errors can be used to estimate the energy resolution
 4412 limits of antenna array designs.

4413 5.3.6 Conclusions

4414 In this paper we have introduced the SYNCA, which is a novel antenna design that
 4415 emits radiation that mimics the unique properties of the cyclotron radiation generated by
 4416 charged particles moving in a magnetic field. The characterization measurements of the
 4417 SYNCA validated the simulated performance of the PCB crossed-dipole antenna design.
 4418 Additionally, the SYNCA was used to estimate the position reconstruction capabilities
 4419 of a synthesized array of horn antennas and experimentally reproduced the simulated
 4420 digital beamforming reconstruction of electrons.

4421 While the SYNCA performs well, there exist discrepancies in the phase and magnitude
 4422 of the radiation pattern compared to the simulated SYNCA design that are related to
 4423 the small geometric differences in the soldered connections. Future design iterations that
 4424 replace the soldered connections with a fully surface mount design could improve the

4425 radiation pattern at the cost of some complexity and expense. Furthermore, improving
4426 the design of the antenna PCB and mounting system would allow the antenna to be
4427 inserted into a cryogenic and vacuum environment where in-situ antenna measurement
4428 calibrations could be performed.

4429 The discrepancies in the radiation pattern and phases exhibited by the as-built
4430 SYNCA should not greatly impact its performance as a calibration probe. Both magni-
4431 tude and phase variations can be accounted by applying the SYNCA characterization
4432 measurements as a calibration to the data collected by the antenna array test stand. The
4433 separate calibration of the SYNCA radiation does not impact the primary goals for the
4434 antenna array test stand which are array calibration and signal reconstruction algorithm
4435 performance characterization, because it can be performed with standard reference horn
4436 antennas with well understood characteristics.

4437 The SYNCA antenna technology advances the CRES technique by providing a
4438 mechanism to characterize free-space antenna arrays for CRES measurements without
4439 the need for a magnet and cryogenics system, which would be required for calibration
4440 using electron sources. Both the Project 8 collaboration as well as future collaborations
4441 which are developing antenna array based CRES experiments can make use of SYNCA
4442 antennas as an important component of their calibration and commissioning phases.

4443 **5.4 FSCD Antenna Array Measurements with the SYNCA**

4444 **5.4.1 Introduction**

4445 Using the SYNCA we can perform full-array measurements of prototype versions of
4446 the FSCD antenna array to test its performance with a realistic cyclotron radiation
4447 source (see Figure 5.24). The goal is to check how the measured power received by
4448 the array compares to FSCD simulations as a function of the radial and axial position
4449 of the SYNCA. These measurements are intended to validate the antenna research
4450 and development by Project 8, which has been driven primarily by simulations with
4451 Locust [62] and CREsana (see Section 4.2.3), and identify any discrepancies with these
4452 simulations tools. This knowledge will provide confidence in the simulations necessary
4453 for the analysis of the sensitivity of larger antenna array based CRES experiment designs
4454 to the neutrino mass.

4455 As shown in Section 5.3, the SYNCA does have some radiation pattern imperfections
4456 that complicate the comparison between measurement and simulation data. One way to

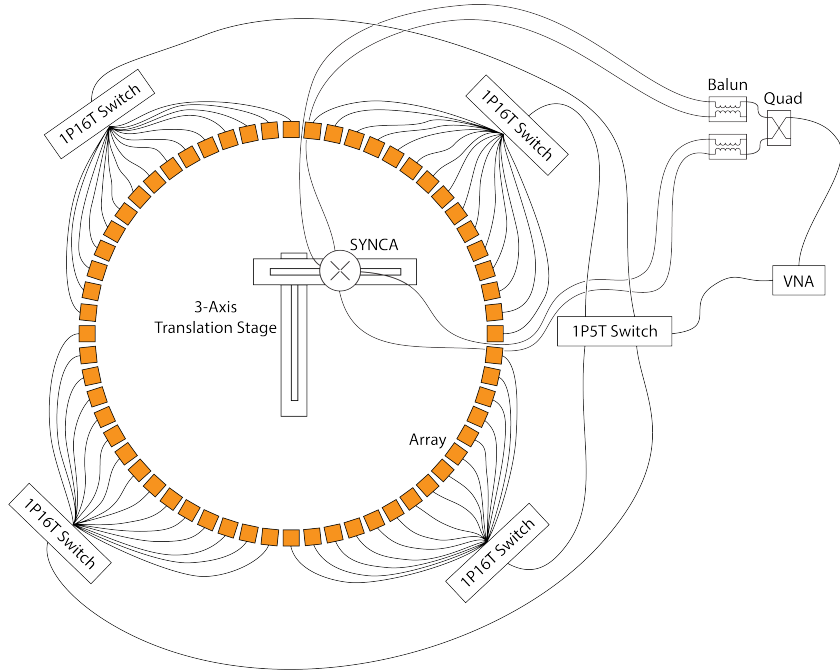


Figure 5.24. A diagram of the array measurement system used to test the prototype FSCD antenna array. A VNA is used as the primary measurement tool, which is connected to the array through a series of switches. The other port of the VNA connects to the SYNCA through the quad-balun chain used to provide the SYNCA feed signals. During measurements the SYNCA is positioned inside the center of the antenna array and translated to different radial and axial positions using a 3-axis manual translation stage setup.

disentangle some of the effects of these imperfections is to perform an additional set of measurements using a synthetic antenna array setup along with the SYNCA antenna. Since the synthetic array setup uses only a single array antenna, the data should be free of errors associated with individual antenna differences and multi-path interference, which are two error sources being tested with the full-array setup. By comparing the synthetic array data to the FSCD array data and to simulation data one can evaluate the significance of these effects relative to the errors introduced by SYNCA imperfections.

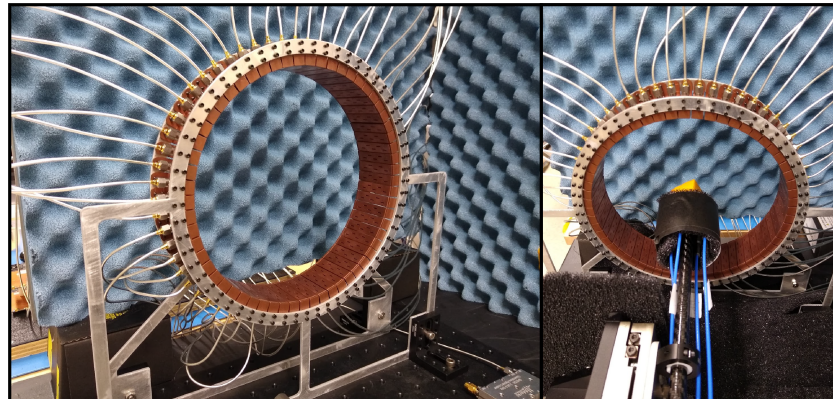
5.4.2 Measurement Setups

5.4.2.1 FSCD Array Setup

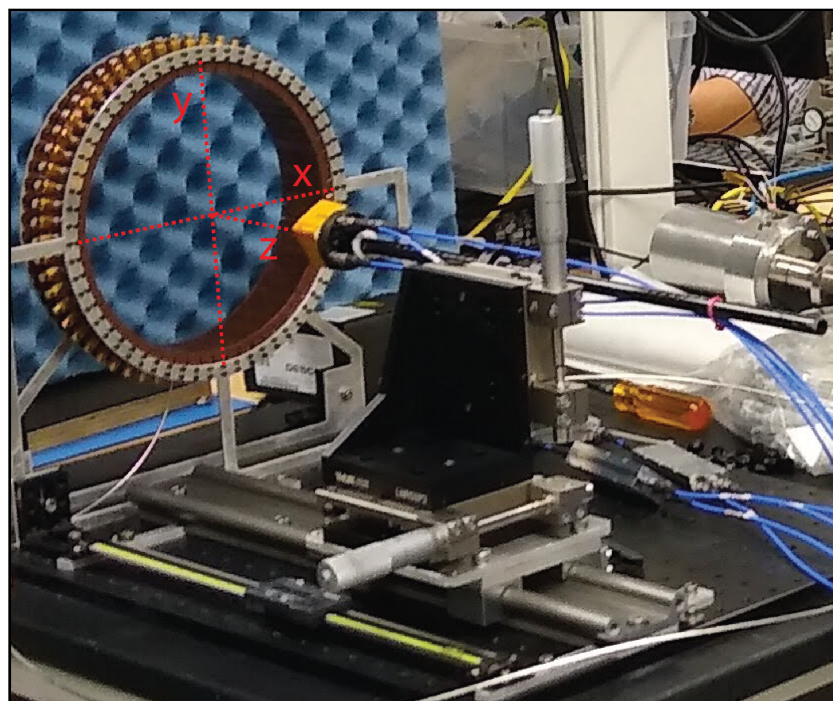
The antenna design that composes the array is the 5-slot waveguide antenna developed for the FSCD experiment (see Figure 5.25a). The antenna is 5 cm long and is constructed out of WR-34 waveguide with a 2.92 mm coax connector located at the center of the antenna. Copper flanges located on both ends of the antenna are used to mount the



(a)



(b)



(c)

Figure 5.25. Photos of the prototype FSCD antenna (a), the FSCD array and SYNCA (b), and the translation stages and coordinate system used to position the SYNCA (c).

4470 antenna in the array support structure. The antennas are supported by two circular steel
4471 brackets that can be bolted to both ends of the waveguide to construct the circular array
4472 (see Figure 5.25b). The antenna array consists of sixty identical waveguide antennas
4473 with a radius of 10 cm. The array is mounted perpendicular to an optical breadboard
4474 surface using a pair of the steel brackets, which provide sufficient space for the coaxial
4475 cable connections and allows for easy positioning of the SYNCA antenna. The SYNCA is
4476 mounted on the end of a carbon fiber rod attached to a set of manual translation stages,
4477 which are used to move the SYNCA antenna to different positions inside the array (see
4478 Figure 5.25c). The stages allow for independent motion in three different axes and can
4479 position the SYNCA at radial distances up to 5 cm from the center.

4480 Data acquisition is accomplished using a two-port VNA in combination with a series
4481 of microwave switches that allow the VNA to connect to each channel in the array . The
4482 first port of the VNA is connected to the quad-balun chain used to feed the SYNCA (see
4483 Section 5.3), and the second port of the VNA connects to a 1P5T microwave switch. The
4484 1P5T switch is connected to four separate 1P16T switch boards that connect directly
4485 to the array. The data acquisition is controlled by a python script running on a lab
4486 computer, which is connected to the VNA and an Arduino board programmed to control
4487 the microwave switches. The script uses the switches to iteratively connect each of the
4488 antennas in the array to the VNA. The VNA is configured to load a specific calibration
4489 file for each antenna channel and performs the measurements of all available S-parameters.
4490 The separate calibration files is an attempt to remove phase and magnitude errors caused
4491 by different propagation through the RF switches. Array measurements were performed
4492 for the set of SYNCA positions consisting of radial (x-axis) positions from 0 to 50 mm in
4493 5 mm steps and axial (z-axis) positions from 0 to 50 mm in 5 mm steps resulting in 121
4494 array measurements. At each SYNCA position we measured the two-port S-parameter
4495 matrix using a linear frequency sweep from 25.1 to 26.1 GHz with 101 discrete frequencies.

4496 5.4.2.2 Synthetic Array Setup

4497 A photograph of the setup used to perform the synthetic array measurements is shown
4498 in Figure 5.26. One important difference between this setup and the FSCD array setup
4499 is that the synthetic array measurements were performed with a waveform generator and
4500 digitizer instead of a VNA. The electronics configuration is identical to the diagram in
4501 Figure 5.7b. Despite the differences, one is still able to compare the measured phases of
4502 the synthetic array and the relative magnitude of the power, since the digitized signal
4503 power is directly proportional to S21.

4504 The arbitrary waveform generator in the setup is configured to produce a 64 MHz
4505 sine wave signal that is up-converted to 25.864 GHz using a mixer and the VNA source.
4506 This signal is passed through a bandpass filter and fed to the SYNCA quad-balun chain.
4507 A single FSCD antenna is positioned 10 cm from the SYNCA and aligned vertically so
4508 that the center of the 5-slot waveguide is in the plane of the SYNCA PCB (see Figure
5.26). This position corresponds to $z = 0$ in Figure 5.25c. The SYNCA is rotated

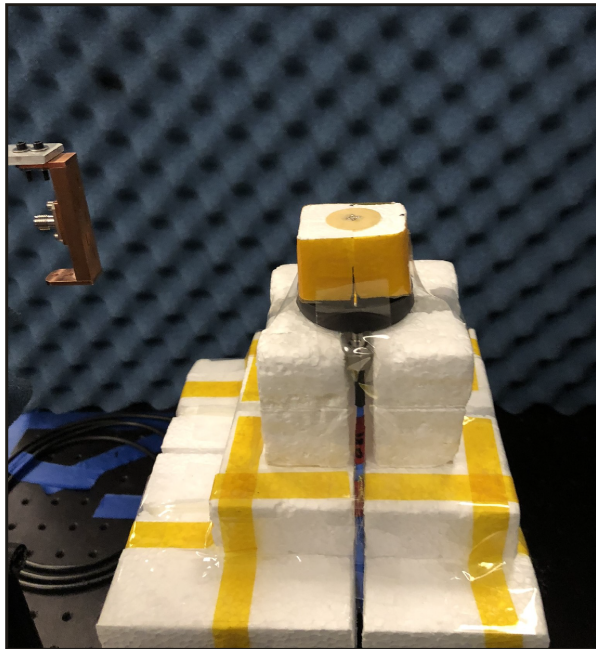


Figure 5.26. A photo of the FSCD antenna and the SYNCA in the synthetic array measurement setup at Penn State.

4509
4510 in three degree steps to synthesize an antenna array with 120 channels. This channel
4511 count is more than could physically fit in a 10 cm radius array, but there is no cost to
4512 over-sampling. Additionally, over-sampling allows for a check of the smoothness of the
4513 antenna array radiation pattern. The signals from the FSCD antenna are down-converted
4514 using the second mixer connected to the VNA source before being digitized at 250 MHz
4515 and saved to disk. Several synthetic array measurement scans were performed by using
4516 the linear translation stage to change the radial position of the SYNCA. In total eight
4517 scans were taken from 0 to 35 mm using a radial position step size of 5 mm.

4518 **5.4.3 Simulations, Analysis, and Results**

4519 The Locust and CREsana simulation packages utilize the antenna transfer functions
4520 to calculate the power that would be received by each antenna from a CREs electron.

4521 The equivalent quantity in the measurement setup is the S21 matrix element, which
4522 indicates the ratio of the power received by an antenna in the array to the amount of
4523 power delivered to the SYNCA. Therefore, the analysis focuses on comparing the relative
4524 magnitudes and phase of the S21 parameters measured by the VNA as a function of
4525 the array channel and the SYNCA position. Additionally, we apply a beamforming
4526 reconstruction to the S21 data to evaluate how the summed power and beamforming
4527 images change as a function of the position of the SYNCA.

4528 **5.4.3.1 Simulations**

4529 Simulations for the FSCD array measurements were performed using CREsana, which
4530 performs analytical calculations of the EM-fields produced by an electron at the position
4531 of the antennas. At each sampled time CREsana computes the electric field vector at the
4532 antenna positions, which is projected onto the antenna polarization axis to obtain the
4533 co-polar electric field. The magnitude of the co-polar electric field is then multiplied by
4534 a flat antenna transfer function to calculate the corresponding voltage signal. CREsana
4535 simulations exploit the flat transfer functions of the FSCD antennas, which allows the
4536 electric field to be multiplied by the antenna transfer function rather than performing
4537 the full FIR calculation. These calculations produce a voltage time-series for each of the
4538 antennas in the array that can be compared to the laboratory measurements.

4539 CREsana was configured to simulate a 90° electron in a constant background magnetic
4540 field of ≈ 0.958 T with a kinetic energy of 18.6 keV. These parameters were chosen
4541 in order to mimic a CRES event near the tritium beta-decay spectrum endpoint in
4542 the FSCD experiment. The constant background magnetic field guarantees that the
4543 guiding center of the electron is stationary across the duration of the simulation which is
4544 consistent with the SYNCA in the laboratory measurements. Simulations were performed
4545 with the electron's guiding center at radial positions from 0 to 45 mm in steps of 1 mm
4546 and axial positions from 0 to 30 mm in steps of 1 mm. The simulations generated time
4547 series consisting of 8192 samples at 200 MHz for the sixty channel FSCD antenna array
4548 geometry.

4549 **5.4.3.2 Phase Analysis**

4550 Correct modeling of the signal phases is fundamental to reconstruction for both beam-
4551 forming and matched filter approaches. The beamforming reconstruction relies on a
4552 signal phase model developed from Locust simulations, which allows one to predict the

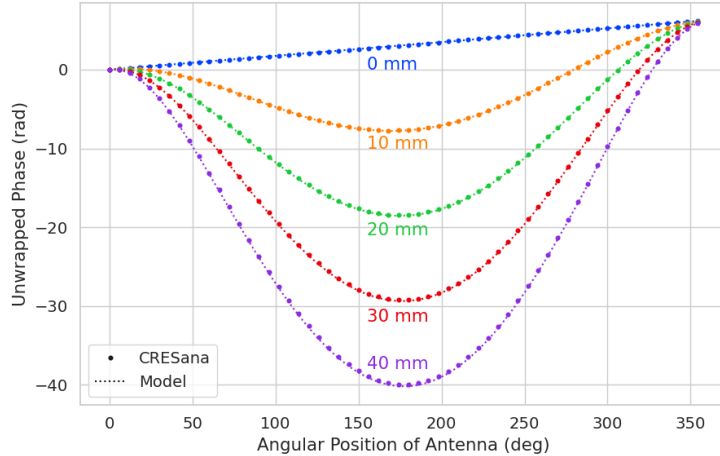


Figure 5.27. The unwrapped phases of signals received by the FSCD antenna array from an electron with a 90° pitch angle located in the plane of the antenna array. The data points indicated the phases extracted from simulation and the dashed lines show the model predictions.

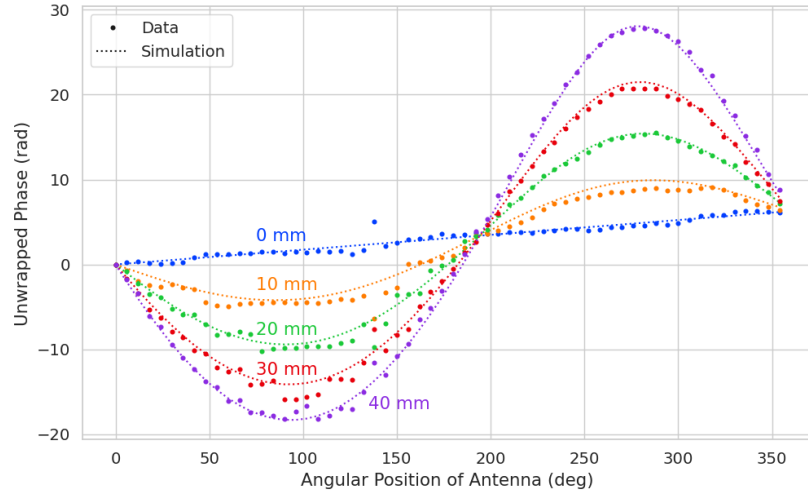
4553 relative signal phases for a specific magnetic trap and electron position. The equation
 4554 for the model is

$$\phi_{ij}(t) = \frac{2\pi d_{ij}(t)}{\lambda} + \theta_{ij}(t), \quad (5.37)$$

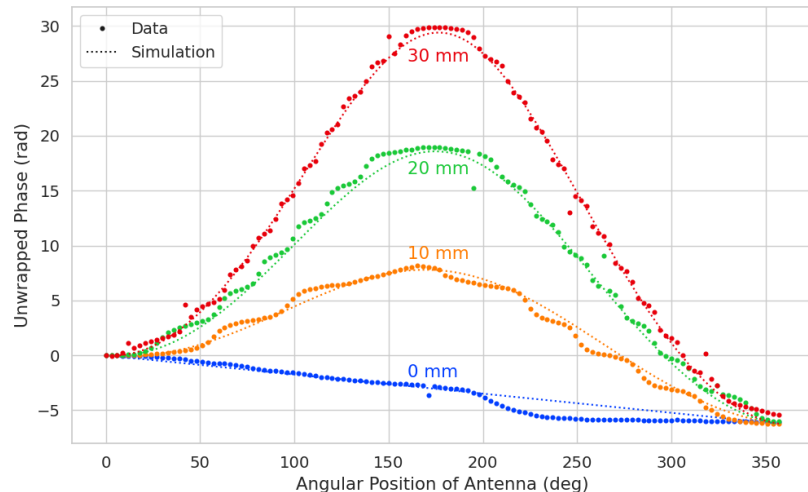
4555 where $d_{ij}(t)$ is distance between the assumed electron position and the antenna position,
 4556 and $\theta_{ij}(t)$ is the angular separation between the electron and antenna positions. For
 4557 details on the components of the phase model see Section 5.3.2. In Figure 5.27 we
 4558 compare the phases predicted by Equation 5.37 to phases extracted from CRESana
 4559 simulations of an electron located in the plane of the antenna array at a series of radial
 4560 positions. One observes excellent agreement between the model and simulation.

4561 The measured signal phases from the FSCD array and synthetic array are shown
 4562 in Figures 5.28a and 5.28b compared to the signal phase model. The axial position of
 4563 the SYNCA in both plots is $z = 0$ mm, such that the plane of the PCB is aligned with
 4564 the center of the FSCD antenna. The data shown in Figure 5.28a corresponds to the
 4565 S-parameters measured at 25.80 GHz which is the frequency closest to the one used in
 4566 the synthetic array setup. The different slope and sinusoidal phases exhibited by Figure
 4567 5.28a and 5.28b reflects differences in the coordinate system for each setup. In general,
 4568 we see that the phase model predicts the large scale features of the phases quite well,
 4569 but there are some small scale deviations or errors from the phase model that do not
 4570 appear to be present in simulation.

4571 A comparison of the phase errors, which are the difference between measurement and



(a)



(b)

Figure 5.28. Plots of the measured unwrapped phases from the FSCD array (a) and the synthetic array (b) compared to the model predictions for a series of radial positions. The different phases of the sinusoidal phase oscillations in the two plots reflects differences in the coordinate systems of the measurements.

4572 model is shown in Figure 5.29. The FSCD array data is referred to as the JUGAAD
 4573 data in the plot legend, which is an alternative name for the FSCD array setup.

4574 The phase error at $R = 0$ in Figure 5.29 forms a smooth curve, with the exception of
 4575 an outlier data point caused by a bug in the data acquisition script. One can attribute
 4576 the observed phase error at this position to imperfections in the antenna pattern of the
 4577 SYNCA. As the SYNCA is moved away from $R = 0$ mm one observes that the phase

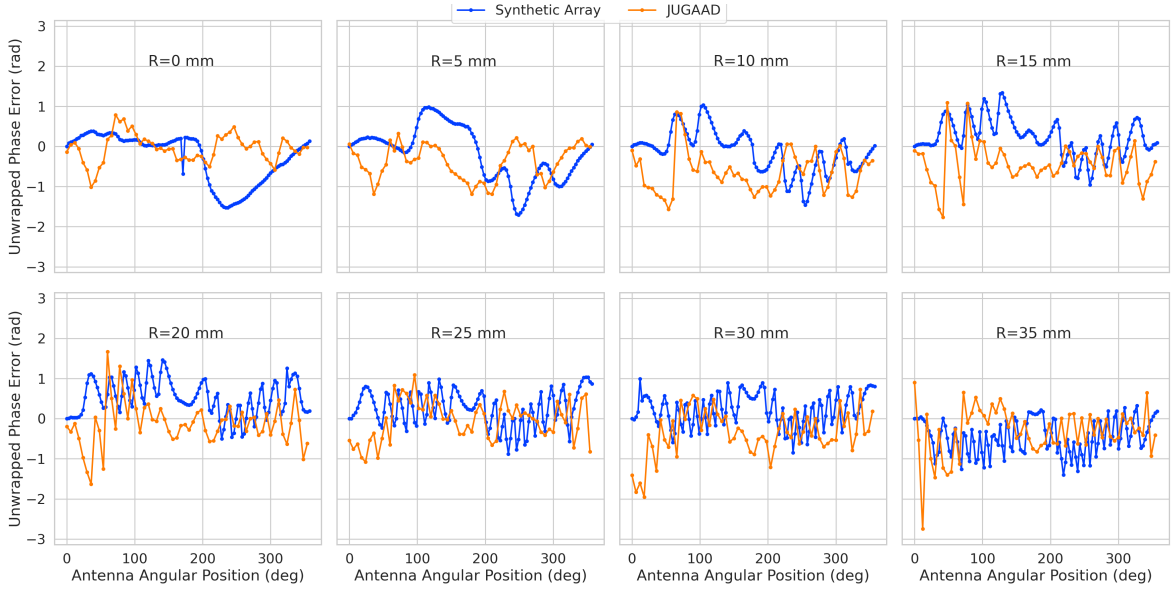


Figure 5.29. The phase errors between the measurement and model for the synthetic array (blue) and the FSCD array (orange) for a series of radial positions. The label JUGAAD refers to an alternative name for the FSCD array setup. As the SYNCA is translated off-axis phase errors with progressively higher oscillation frequency enter into the measurements.

4578 error exhibits oscillations whose frequency increases as a function of the radial position
 4579 of the SYNCA. These oscillations have the appearance of a diffraction pattern, which
 4580 is particularly clear for the radii ≥ 15 mm, due to the bilateral symmetry of the phase
 4581 error peaks around 180° .

4582 One can observe a higher average variance in the phase errors measured for the FSCD
 4583 array compared to the synthetic array. This is best seen by comparing the curves at
 4584 $R \leq 15$ mm where the smooth synthetic array curves are distinct from the relatively
 4585 noisy FSCD array errors. The extra noise in the FSCD array is most likely caused by
 4586 differences in the radiation patterns of the antennas that make up the array as well as
 4587 differences in the transmission lines through the switch network that introduce additional
 4588 phase errors into the measurement. Since the synthetic array measurements use only
 4589 a single antenna, these extra error terms are not present, which explains the relatively
 4590 smoother phase error curves. Despite the extra phase errors in the FSCD array, it is still
 4591 possible to observe a similar phase error oscillation effect as the SYNCA is moved away
 4592 from $R = 0$ mm.

4593 The diffraction pattern exhibited by the phase error oscillations is more easily observed
 4594 by plotting the phase errors in a two-dimensional map, which is done in Figures 5.30a and
 4595 5.30b. For the synthetic array ones observes a relatively clear diffraction pattern

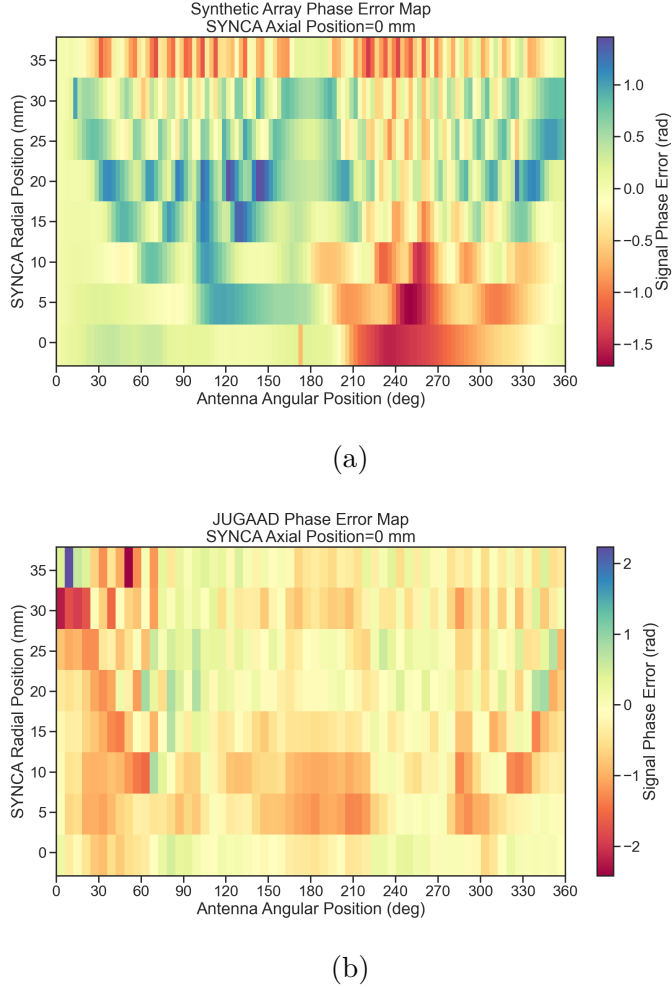


Figure 5.30. Two dimensional plots of the phase errors for the synthetic array (a) and the FSCD (JUGAAD) array (b). In both plots we observe evidence of a similar diffraction pattern with bilateral symmetry, but the FSCD array measurements have an additional phase error contribution from the different antennas and paths through the switch network.

that emerges as the SYNCA is moved radially. The bilateral symmetry of the diffraction patterns is due to the bilateral symmetry of the circular synthetic array around the translation axis of the SYNCA. A similar pattern is also visible in the FSCD array data, although, it is obscured by the additional phase error that results from the multi-channel array.

The physical origin of the phase error diffraction pattern is attributed to interference effects arising from path-length differences between the individual slots in the FSCD antenna and the SYNCA transmitter. Since we are operating in the radiative near-field of the FSCD antenna, the path length differences between the slots introduce a significant change in the summation of the signals that occurs inside the waveguide, which causes

4606 the radiation pattern of the antenna to change as a function of distance. Therefore, when
4607 the SYNCA is positioned off-axis the different path-lengths from the SYNCA to each
4608 antenna results in different radiation patterns leading to the observed diffraction pattern.

4609 This near-field effect is not present in simulations, because in order to simplify the
4610 calculations we assume that the far-field approximation can be applied to the FSCD
4611 antennas. This means that the radiation pattern and antenna transfer functions are
4612 independent of the distance between the transmitter and the receiving antenna. In
4613 principle, we can account for these near-field effects with a more detailed simulation of
4614 the FSCD antennas either in CRESana or Locust, which would result in an additional
4615 term in the beamforming phase model. However, this would increase the computational
4616 intensity of the simulation software. In the next section we briefly discuss the impact of
4617 these near-field effects on the measured magnitude of the signals.

4618 5.4.3.3 Magnitude Analysis

4619 Exactly as for the signal phase, one can use simulations to construct a model that
4620 describes the magnitude of the signals received by each channel in the antenna array.
4621 By examining the results of simulations or by analyzing the Liénard-Wiechert equation
4622 one can show that radiation pattern from a 90° pitch angle electron in a magnetic field
4623 is omni-directional. Therefore the relative magnitudes of the signals received by each
4624 channel will be determined by the free-space power loss, which is proportional to the
4625 inverse distance between the assumed electron position and the antenna.

4626 A consequence of this is that the signals produced in the array for electrons off the
4627 central axis will have larger amplitudes for the antennas closer to the electron compared
4628 to those which are further away. The amplitudes of the signals received by the array
4629 from an electron located at a series of radial positions are shown in Figure 5.31.

4630 One expects to see a similar trend in the signal magnitudes in both the FSCD and
4631 synthetic arrays. The normalized signal magnitudes extracted from the full and synthetic
4632 array setups for a series of radial SYNCA positions are shown in Figure 5.32. The data
4633 corresponds to a SYNCA axial position of $z = 0$ mm and at a frequency 25.86 GHz. One
4634 complication is that the radiation pattern of the SYNCA is not perfectly omni-directional,
4635 which causes the measured magnitudes at $R = 0$ mm to diverge from the perfectly flat
4636 behavior exhibited by electrons.

4637 As the SYNCA is moved off-axis one observes a similar increase in the number of
4638 magnitude peaks in the synthetic array data that one would expect from a diffraction
4639 pattern, although this trend is not as stark compared to the phase data. Noticeably,

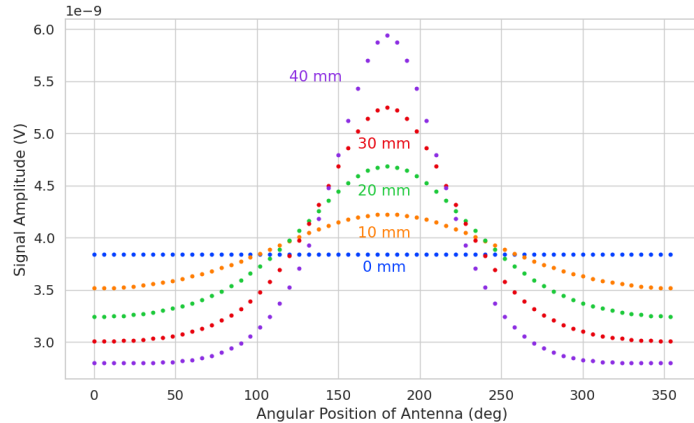


Figure 5.31. The amplitude of the signals from CRESana for the FSCD array from a 90° electron. As the electron is moved from $R = 0$ the signals begin to have unequal amplitudes depending on the distance from the electron to the antenna.

there does not appear to be a set of channels with disproportionately larger amplitude at large R , which would be expected based on the trends from CRESana.

Comparing the magnitudes of the synthetic array to the FSCD array in Figure 5.32 we see that there is a similar amount of variability in the magnitudes at $R = 0$ mm, although there is potentially more small scale error in the magnitude curve caused by channel differences in the FSCD array. We observe a similar trend in the number of magnitude error peaks in the FSCD array data to the synthetic array data, which mirrors the diffraction effect observed in the phase data. The diffraction effect can be visualized more clearly by plotting a similar two-dimensional map of the magnitudes (see Figure 5.33).

The fact that one observes a similar diffraction pattern in the signal magnitudes as a function the SYNCA position reinforces the conclusions from the phase analysis that near-field effects are having a significant impact on the radiation pattern of the FSCD array. These near-field effects lead to changes in the magnitude and phase of the radiation pattern of the FSCD antenna as a function of distance. If left uncorrected these errors reduce detection efficiency by causing power loss in the beamforming or matched filter reconstruction due to phase mismatch. We explore the impact of these phase and magnitude errors on beamforming in the next section.

5.4.3.4 Beamforming Characterization

Errors in the signal magnitudes and phases lead to errors in signal reconstruction. For example, a matched filter reconstruction requires accurate knowledge of the signals in

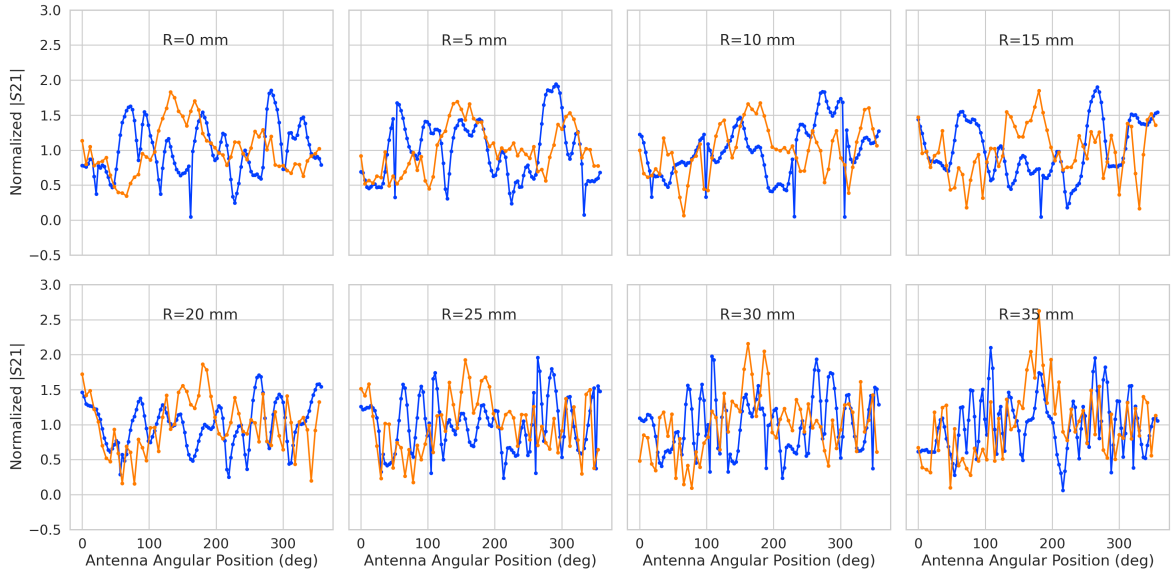
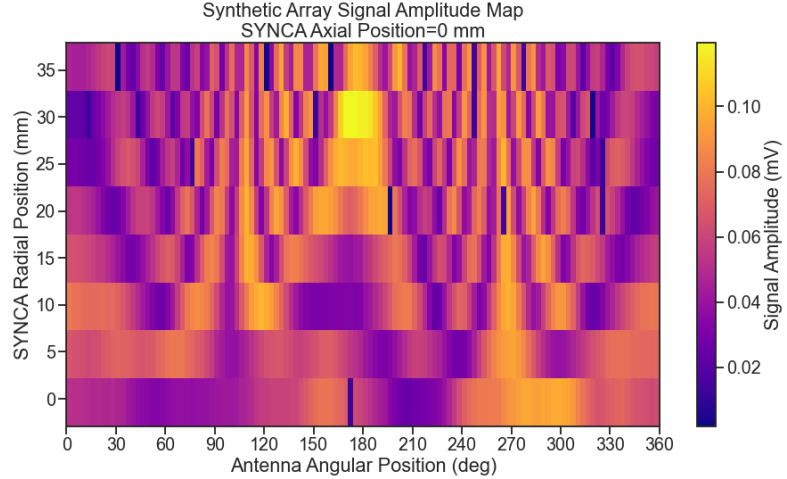


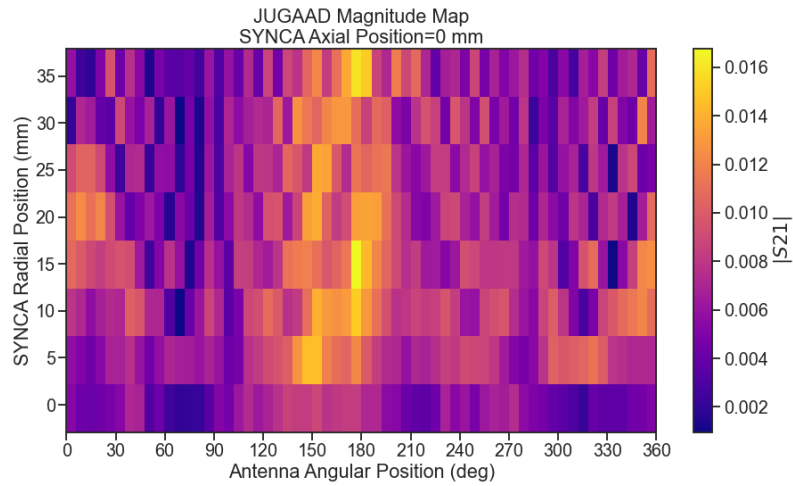
Figure 5.32. The normalized magnitudes of the S21 parameters measured in the FSCD (orange) and synthetic array (blue) setups. The dominant observed behavior as a function of radius is the increase in the number of magnitude peaks, which was noted in the phase error curves. There does not appear to be a strong change in the relative amplitude of a group of antennas as predicted by CRESana.

4661 each channel to achieve optimal performance. Uncorrected errors leads to mismatches
 4662 between the template and signal, which reduces detection efficiency and introduces
 4663 uncertainty in the parameter estimation. In this section, we analyze the beamformed
 4664 signal amplitude as a function of the position of the SYNCA to quantify the impact of
 4665 the phase and magnitude errors on signal reconstruction. Because of the imperfections
 4666 in the SYNCA source, it is inappropriate to directly compare the beamformed signal
 4667 amplitude of the FSCD array or synthetic array. Such a comparison would not allow
 4668 one to disentangle losses that occur because of the antenna array from those that occur
 4669 because of the source. Therefore, we focus on comparing the beamforming of the FSCD
 4670 array to the synthetic array.

4671 The first method of comparison is to analyze the images generated by applying the
 4672 beamforming reconstruction specified in Section 4.3.1 to the FSCD and synthetic array
 4673 data (see Figure 5.34). The beamforming grid consisting of a square 121×121 grid
 4674 spanning a range of -60-mm to 60 mm in the x and y dimensions. The beamforming
 4675 images formed from the synthetic array produces a three-dimensional matrix where each
 4676 grid position contains a summed time series. A single beamforming image is formed from
 4677 this data matrix by taking the mean over the time dimension. In the case of the FSCD



(a)



(b) The two-dimensional maps showing the diffractive pattern exhibited by the FSCD and synthetic array signal magnitudes.

Figure 5.33.

array, the VNA generates frequency domain data such that each grid position contains a summed frequency series produced by the VNA sweep. For this data a single image is formed by averaging in the frequency domain.

There is a clear difference between the synthetic and FSCD array beamforming images, which is the additional faint beamforming maxima located directly opposite the maxima corresponding to the SYNCA position. The images in Figure 5.34 were generated with data collected at a SYNCA radial position of 15 mm, which agrees well with the observed beamforming maximum in both images. We observe that the faint beamforming peak is

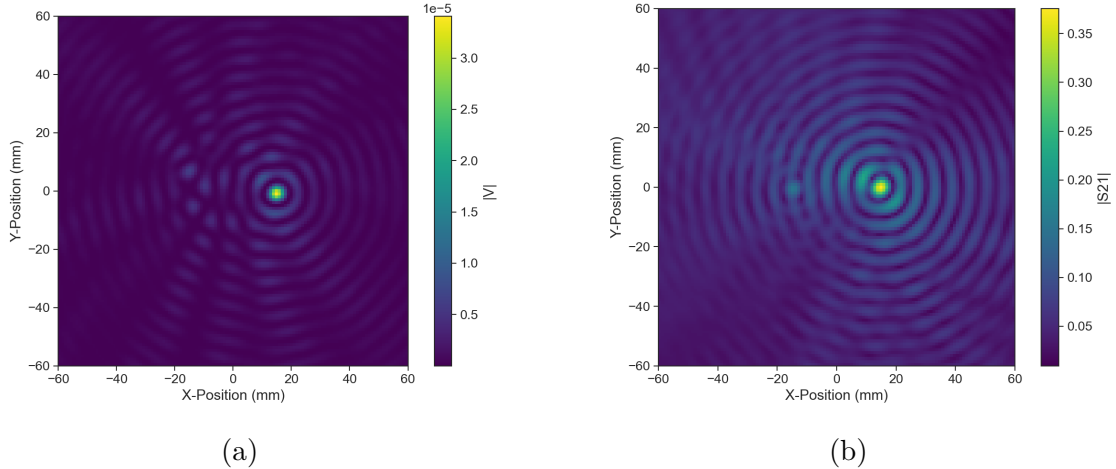


Figure 5.34. Beamforming images from the synthetic array (a) and FSCD array (b) setups with the SYNCA positioned 15 mm off the central axis. In both images we see a clear maxima that corresponds to the true SYNCA position. However, in the FSCD array there is an additional faint peak located at the opposite position of the beamforming maximum. This additional peak is the mirror of the true peak and is the result of reflections between antennas in the FSCD array.

located directly opposite of the true beamforming maximum similar to a mirror image. Therefore, the origin of this additional feature appears to be reflections between the two sides of the circular antenna array that are not present for the synthetic array since only a single physical antenna is used.

From the beamforming images we extract the maximum amplitude, which we plot as a function of the radial position of the SYNCA (see Figure 5.35). The phase errors we observed in the FSCD and synthetic arrays leads to power loss at the beamforming stage due to phase mismatches between the signals at different channels. This power loss can be quantified by comparing the signal amplitude obtained from beamforming to the amplitude which would be obtained from an ideal summation. We perform the ideal summation by phase shifting each array channel to the same phase and then summing. The comparison between the beamforming and ideal sums is shown in Figure 5.35, where we observe that both the synthetic and FSCD arrays experience power losses from the beamforming summation.

The beamforming power loss can be quantified using the ratio of the beamforming to ideal signal amplitudes. Computing this ratio as a function of SYNCA radial position radius for the FSCD and synthetic arrays we find that the FSCD array has a uniformly smaller beamforming amplitude ratio, which means that the FSCD array has a larger beamforming power loss (see Figure 5.36). The primary contributions to the beamforming

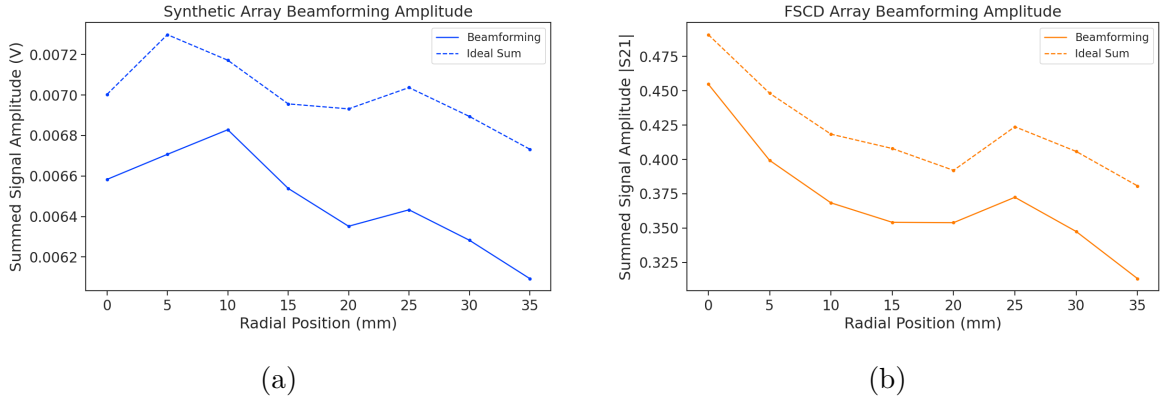


Figure 5.35. A comparison of the maximum signal amplitude obtained by beamforming to the signal amplitude obtained with an ideal summation as a function of the radial position of the SYNCA. The amplitudes for the synthetic array are shown in (a) and the FSCD array are shown in (b). In both setups we observe that the signal amplitudes obtained from beamforming are smaller than the signal amplitude that could be attained with the ideal summation without phase mismatch.

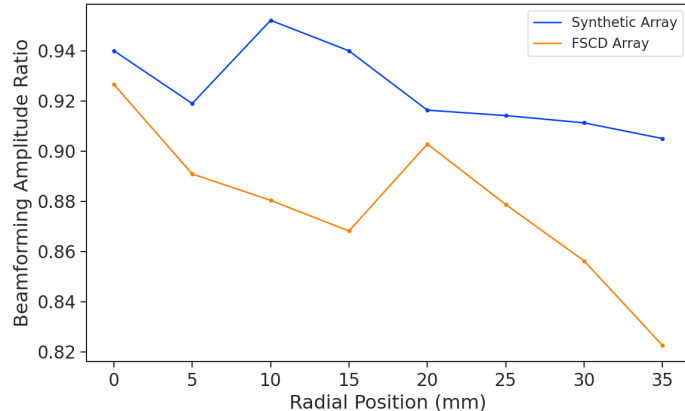


Figure 5.36. The ratio of the beamforming signal amplitude to the ideal signal amplitude for the FSCD and synthetic arrays. We see that the FSCD array has a larger power loss from phase error compare to the synthetic array which indicates that calibration errors associated with the multiple channels as well as reflections are impacting the signal reconstruction.

power loss in the synthetic array are phase errors from the SYNCA and phase errors from the FSCD antenna near-field. Both of these phase errors contribute to beamforming losses in the FSCD array, but there are clearly additional phase errors in the FSCD array measurements contributing to the smaller ratio. Two potential error sources include phase differences in the different antenna channels that could not be corrected by calibration as well as reflections between antennas in the array. The total effect of these additional phase errors is to reduce the beamforming amplitude ratio by about 5% from the beamforming

4712 ratio of the synthetic array. Therefore, we estimate that if no effort is made to correct
4713 these phase errors in an FSCD-like experiment, then we expect approximately a 10%
4714 total signal amplitude loss from a beamforming signal reconstruction.

4715 **5.4.4 Conclusions**

4716 The estimated power loss of a beamforming reconstruction obtained from this analysis
4717 provides valuable inputs to sensitivity calculations of a FSCD-like antenna array exper-
4718 iment to measure the neutrino mass, since it helps to bound systematic uncertainties
4719 from the antenna array and reconstruction pipeline. This power loss lowers the estimated
4720 detection efficiency of the experiment since some of the signal power is lost due to
4721 improper combining between channels and also increases the uncertainty in the electron's
4722 kinetic energy by contributing to errors in the estimation of the electron's cyclotron
4723 frequency.

4724 If these reconstruction losses prove unacceptable there are steps that can be taken
4725 to mitigate their effects. Some examples include the development of a more accurate
4726 antenna simulation approach that can reproduce the observed near-field interference
4727 patterns of the FSCD antennas and the implementation of a calibration approach that
4728 allows for the relative phase delays of the array to be measured without changing or
4729 disconnecting the antenna array configuration.

Chapter 6

Development of Resonant Cavities for Large Volume CRES Measurements

6.1 Introduction

The cavity approach was originally an alternative CRES measurement technology under consideration by the Project 8 collaboration for the Phase IV experiment. After pursuing an antenna array based CRES demonstrator design for several years, the increasing costs and complexity of the antenna arrays led to a reconsideration of the baseline technology for the ultimate CRES experiment planned by Project 8. Currently, a cavity based CRES experiment is the preferred technology choice for future experiments by the Project 8 collaboration including the Phase IV experiment.

In this chapter I provide a brief summary of resonant cavities and sketch out the key features of a cavity based CRES experiment. In Section 6.2 I provide a brief introduction to cylindrical resonant cavities and the solutions for the electromagnetic fields in the cavity volume.

In Section 6.3 I describe the main components of a cavity based CRES experiment, including the background and trap magnets, cavity geometry and design, and cavity coupling considerations. I also discuss some relevant trade-offs between an antenna array and cavity CRES experiment, and highlight some reasons for the transition of Project 8 to the development of a cavity based experiment.

Finally, in Sections 6.4 and 6.5, I present the design and development of an open mode-filtered cavity that could be used in a cavity based CRES experiment with atomic tritium. The results of the cavity simulations are confirmed by laboratory measurements of a proof-of-principle prototype that demonstrates key features of the design.

6.2 Cylindrical Resonant Cavities

Resonant cavities are sealed conductive containers, which allows us to describe the electromagnetic (EM) fields contained in the cavity volume as a superposition of resonant modes [87]. The field shapes of the resonant modes are determined by Maxwell's equations and the boundary conditions enforced by the cavity geometry. Of interest to Project 8 for CRES measurements are cylindrical cavities due to their ease of construction and integration with atom and electron trapping magnets.

6.2.1 General Field Solutions

Consider a long segment of conducting material with a cylindrical cross-section (see Figure 6.1). A geometry such as this can be used as a waveguide transmission line to transfer EM energy from point to point, or, if conducting shorts are inserted on both ends of the cylinder, the waveguide becomes a resonant cavity.

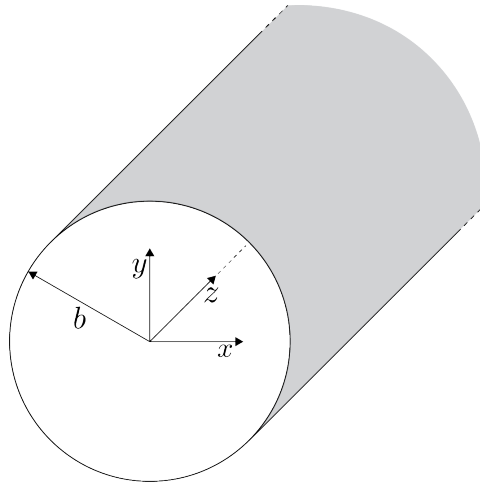


Figure 6.1. Geometry of a cylindrical waveguide with radius b .

The fields allowed inside a cylindrical cavity are determined by the boundary conditions of the cylindrical geometry. The general approach to solving the fields begins by assuming solutions to Maxwell's equations of the form

$$\mathbf{E}(x, y, z) = (\mathbf{e}(x, y) + \hat{z}e_z(x, y))e^{-i\beta z}, \quad (6.1)$$

$$\mathbf{H}(x, y, z) = (\mathbf{h}(x, y) + \hat{z}h_z(x, y))e^{-i\beta z}. \quad (6.2)$$

The solutions assume a harmonic time dependence of the form $e^{i\omega t}$ and propagation

4770 along the positive z-axis. The functions $\mathbf{e}(x, y)$ and $\mathbf{h}(x, y)$ represent the transverse
 4771 (\hat{x}, \hat{y}) components of the electric and magnetic fields respectively, and $e_z(x, y)$, $h_z(x, y)$
 4772 represent the longitudinal components. The version of Maxwell's equations in the case
 4773 where there are no source terms can be written as a pair of coupled differential equations,

$$\nabla \times \mathbf{E} = -i\omega\mu\mathbf{H}, \quad (6.3)$$

$$\nabla \times \mathbf{H} = i\omega\epsilon\mathbf{E}, \quad (6.4)$$

4774 where ϵ and μ are the permittivity and permeability of the material inside the waveguide
 4775 or cavity. Using the field solutions from Equations 6.1 and 6.2 one can solve for the
 4776 transverse components of the fields in terms of the longitudinal fields. Because we
 4777 are interested in cylindrical cavities it is advantageous to write the field solutions in
 4778 cylindrical coordinates. After performing this transformation the set of four equations
 4779 for the transverse field components are,

$$H_\rho = \frac{i}{k_c^2} \left(\frac{\omega\epsilon}{\rho} \frac{\partial E_z}{\partial\phi} - \beta \frac{\partial H_z}{\partial\rho} \right), \quad (6.5)$$

$$H_\phi = \frac{-i}{k_c^2} \left(\omega\epsilon \frac{\partial E_z}{\partial\rho} + \frac{\beta}{\rho} \frac{\partial H_z}{\partial\phi} \right), \quad (6.6)$$

$$E_\rho = \frac{-i}{k_c^2} \left(\beta \frac{\partial E_z}{\partial\rho} + \frac{\omega\mu}{\rho} \frac{\partial H_z}{\partial\phi} \right), \quad (6.7)$$

$$E_\phi = \frac{i}{k_c^2} \left(-\beta \frac{\partial E_z}{\partial\phi} + \omega\mu \frac{\partial H_z}{\partial\rho} \right), \quad (6.8)$$

4780 where k_c is the cutoff wavenumber defined by $k_c^2 = k^2 - \beta^2$ with $k = \omega\sqrt{\mu\epsilon}$ being the
 4781 wavenumber of the EM radiation.

4782 This set of equations can be used to solve for a variety of different modes that can be
 4783 obtained by setting conditions on E_z and H_z . For cylindrical cavities two types of modes
 4784 are allowed, which correspond to solutions where $E_z = 0$ and $H_z = 0$ respectively.

4785 6.2.2 TE and TM Modes

4786 The TE family of modes corresponds to the case where $E_z = 0$. This implies that H_z is
 4787 a solution to the Helmholtz wave equation

$$(\nabla^2 + k^2)H_z = 0. \quad (6.9)$$

4788 For solutions of the form $H_z(\rho, \phi, z) = h_z(\rho, \phi)e^{-i\beta z}$, Equation 6.9 can be solved using
 4789 the standard technique of separation of variables. Rather than reproduce the derivation
 4790 here we shall simply quote the solutions for the transverse fields [87], which are

$$H_\rho = \frac{-i\beta}{k_{c_{nm}}} (A \sin n\phi + B \cos n\phi) J'_n(k_{c_{nm}}\rho) e^{-i\beta_{nm}z}, \quad (6.10)$$

$$H_\phi = \frac{-i\beta n}{k_{c_{nm}}^2 \rho} (A \cos n\phi - B \sin n\phi) J_n(k_{c_{nm}}\rho) e^{-i\beta_{nm}z}, \quad (6.11)$$

$$E_\rho = \frac{-i\omega\mu n}{k_{c_{nm}}^2 \rho} (A \cos n\phi - B \sin n\phi) J_n(k_{c_{nm}}\rho) e^{-i\beta_{nm}z}, \quad (6.12)$$

$$E_\phi = \frac{i\omega\mu}{k_{c_{nm}}} (A \sin n\phi + B \cos n\phi) J'_n(k_{c_{nm}}\rho) e^{-i\beta_{nm}z}. \quad (6.13)$$

4791 One can observe that the solutions have a periodic dependence on ϕ , and radial profiles
 4792 given by the Bessel functions of the first kind. The integer indices n and m arise from
 4793 continuity conditions on the EM fields in the azimuthal and radial directions. For the
 4794 TE modes $n \geq 0$ and $m \geq 1$. $k_{c_{nm}}$ is the cutoff wavenumber for the TE_{nm} mode given by

$$k_{c_{nm}} = \frac{p'_{nm}}{b}, \quad (6.14)$$

4795 where b is the radius of the cavity or waveguide and p'_{nm} is the m -th root of the derivative
 4796 of the n -th order Bessel function (see Table 6.1).

Table 6.1. A table of the values of p'_{nm} .

n	p'_{n1}	p'_{n2}	p'_{n3}
0	3.832	7.016	10.174
1	1.841	5.331	8.536
2	3.054	6.706	9.970

4797 The TM mode family corresponds to the case where $H_z = 0$, and $(\nabla^2 + k^2)E_z = 0$.
 4798 Again, we assume solutions of the form $E_z(\rho, \phi, z) = e_z(\rho, \phi)e^{-i\beta z}$, for which the general
 4799 form of the solutions is the same as for the TE modes. However, the different boundary
 4800 conditions for the TM modes results in particular solutions with a different from, which
 4801 we shall quote here without derivation. The transverse fields of the TM modes are given
 4802 by

$$H_\rho = \frac{-i\omega\epsilon n}{k_{c_{nm}}^2 \rho} (A \cos n\phi - B \sin n\phi) J_n(k_{c_{nm}}\rho) e^{-i\beta_{nm}z}, \quad (6.15)$$

$$H_\phi = \frac{-i\omega\epsilon}{k_{c_{nm}}} (A \sin n\phi + B \cos n\phi) J'_n(k_{c_{nm}}\rho) e^{-i\beta_{nm}z} \quad (6.16)$$

$$E_\rho = \frac{-i\beta}{k_{c_{nm}}} (A \sin n\phi + B \cos n\phi) J'_n(k_{c_{nm}}\rho) e^{-i\beta_{nm}z}, \quad (6.17)$$

$$E_\phi = \frac{-i\beta n}{k_{c_{nm}}^2 \rho} (A \cos n\phi - B \sin n\phi) J_n(k_{c_{nm}}\rho) e^{-i\beta_{nm}z}, \quad (6.18)$$

which one may notice are the same solutions as the TE modes with H and E flipped.
 The cutoff wavenumber for the TM modes is given by, $k_{c_{nm}} = p_{nm}/b$, where the values of p_{nm} correspond to the m -th zero of the n -th order Bessel function (see Table 6.2).

Table 6.2. A table of the values of p_{nm} .

n	p_{n1}	p_{n2}	p_{n3}
0	2.405	5.520	8.654
1	3.832	7.016	10.174
2	5.135	8.417	11.620

6.2.3 Resonant Frequencies of a Cylindrical Cavity

A cylindrical cavity is constructed by taking a section of cylindrical waveguide and shorting both ends with conductive material. This means that the electric fields inside a cylindrical cavity are exactly those we derived in Section 6.2.2 with the additional condition that the electric fields must go to zero at $z = 0$ and $z = L$ (see Figure 6.2).

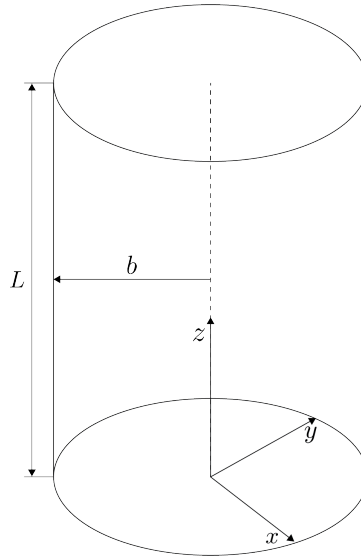


Figure 6.2. The geometry of a cylindrical cavity with length L and radius b .

4811 The transverse electric field solutions for a cylindrical waveguide are of the form

$$\mathbf{E}(\rho, \phi, z) = \mathbf{e}(\rho, \phi) (A_+ e^{-i\beta_{nm}z} + A_- e^{i\beta_{nm}z}), \quad (6.19)$$

4812 where A_+ and A_- are arbitrary amplitudes of forward and backward propagating waves.

4813 In order to enforce that \mathbf{E} is zero at both ends of the cavity we require that

$$\beta_{nm}L = 2\pi\ell, \quad (6.20)$$

4814 where $\ell = 0, 1, 2, 3, \dots$. Using this constraint on the propagation constant we can solve

4815 for the resonant frequencies of the TE_{nml} and the TM_{nml} modes in a cylindrical cavity.

4816 For the TE modes the resonant frequencies are

$$f_{nml} = \frac{c}{2\pi\sqrt{\mu_r\epsilon_r}} \sqrt{\left(\frac{p'_{nm}}{b}\right)^2 + \left(\frac{\ell\pi}{L}\right)^2}, \quad (6.21)$$

4817 and the frequencies of the TM modes are

$$f_{nml} = \frac{c}{2\pi\sqrt{\mu_r\epsilon_r}} \sqrt{\left(\frac{p_{nm}}{b}\right)^2 + \left(\frac{\ell\pi}{L}\right)^2}. \quad (6.22)$$

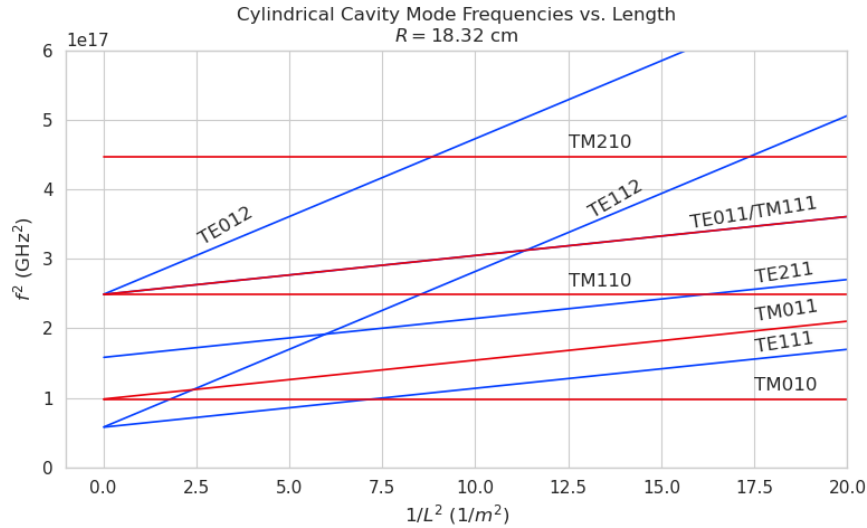


Figure 6.3. Relation of mode frequency to cavity length for a cylindrical cavity with a radius of 18.32 cm.

4818 6.2.4 Cavity Q-factors

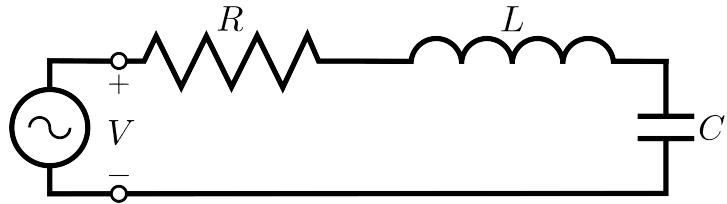


Figure 6.4. A series RLC circuit.

4819 The resonant behavior of cylindrical cavities can be modeled as a series RLC circuit
 4820 (see figure 6.4). The input impedance of the circuit can be obtained by applying
 4821 Kirchhoff's laws to calculate the impedance of the equivalent circuit. For a series RLC
 4822 circuit the input impedance is

$$Z_{\text{in}} = \left(\frac{1}{R} + \frac{1}{i\omega L} + i\omega C \right). \quad (6.23)$$

4823 The resistance in the circuit represents all sources of loss in the cavity, which is primarily
 4824 caused by the finite conductivity of the cavity walls. The inductor and capacitor represent
 4825 the energy stored in the cavity in the form of electric and magnetic fields. If the circuit
 4826 is being driven by an external power source we can write the input power in terms of the
 4827 circuit input impedance and the source voltage

$$P_{\text{in}} = \frac{1}{2} Z_{\text{in}} |I|^2 = \frac{1}{2} |I|^2 \left(\frac{1}{R} + \frac{1}{i\omega L} + i\omega C \right). \quad (6.24)$$

4828 The resistor introduces a loss into the system with a power given by

$$P_{\text{loss}} = \frac{1}{2} |I|^2 R, \quad (6.25)$$

4829 and the capacitor and inductor store energies given by

$$W_e = \frac{1}{4} \frac{|I|^2}{\omega^2 C}, \quad (6.26)$$

$$W_m = \frac{1}{4} |I|^2 L, \quad (6.27)$$

4830 respectively. Using these expressions we can write the input power and input impedance

4831 expressions in terms of the lost power and stored energy

$$P_{\text{in}} = P_{\text{loss}} + 2i\omega(W_m - W_e), \quad (6.28)$$

$$Z_{\text{in}} = \frac{P_{\text{loss}} + 2i\omega(W_m - W_e)}{\frac{1}{2}|I|^2}. \quad (6.29)$$

4832 The condition for resonance in the RLC circuit is that the stored magnetic energy
 4833 is equal to the stored electric energy ($W_e = W_m$). When this occurs $Z_{\text{in}} = R$, which is a
 4834 purely real impedance, and $P_{\text{in}} = P_{\text{loss}}$. The resonant frequency of the circuit can be
 4835 determined from the condition $W_e = W_m$ from which one finds that

$$\omega_0 = \frac{1}{\sqrt{LC}}. \quad (6.30)$$

4836 An important performance parameter for any resonant system is the Q-factor, which
 4837 quantifies the quality of the resonator as the ratio of the stored energy multiplied by the
 4838 resonant frequency to the average energy lost per second. For the series RLC circuit, the
 4839 Q-factor is given by the expression

$$Q_0 = \omega \frac{W_e + W_m}{P_{\text{loss}}} = \frac{1}{\omega_0 RC}, \quad (6.31)$$

4840 from which one observes that as the resistance of the RLC circuit is decreased the quality
 4841 factor of the resonator increases. From the perspective of cylindrical cavities this implies
 4842 that as one decreases the resistance of the cavity walls it is expected that the Q-factor of
 4843 the cavity should increase, which is indeed the case. In certain applications where a high
 4844 Q is desireable it is possible to manufacture a cavity out of superconducting materials in
 4845 order to minimize the power losses of the system.

4846 The Q-factor of the resonator also determines with bandwidth (BW) of the system.
 4847 A cavity with a high Q-factor will resonant with a smaller range of frequencies than a
 4848 cavity with a low Q-factor. To see this we can examine the behavior of the RLC circuit
 4849 when driven by frequencies near the resonance. For a frequency $\omega = \omega_0 + \Delta\omega$, where
 4850 $\Delta\omega = \omega - \omega_0 \ll \omega_0$, we can write the input impedance as

$$Z_{\text{in}} = R + i\omega L \left(\frac{\omega^2 - \omega_0^2}{\omega^2} \right), \quad (6.32)$$

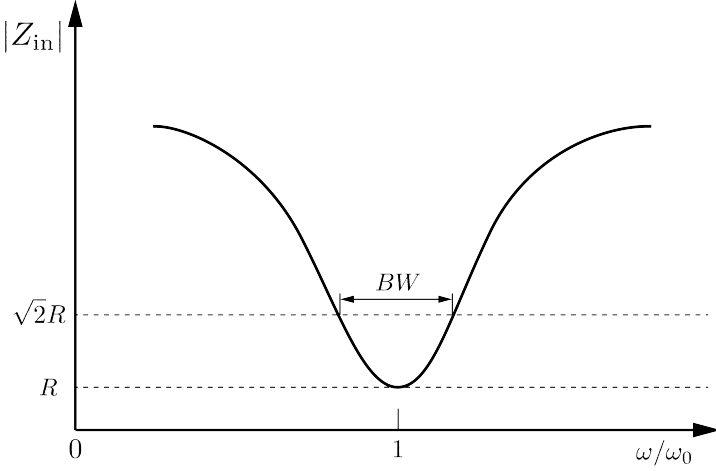


Figure 6.5. Illustration of the behavior of the input impedance of the series RLC circuit as a function of the driving frequency. The BW is proportion to the width of the resonance, which is inversely proportional to Q.

and by expanding $(\omega^2 - \omega_0^2)/\omega^2$ to first order in $\Delta\omega$, we obtain

$$Z_{in} \approx R + i \frac{2RQ_0\Delta\omega}{\omega_0}. \quad (6.33)$$

Therefore, the magnitude of the input impedance near the resonance is given by

$$|Z_{in}| = R \sqrt{1 + 4Q_0^2 \frac{\Delta\omega^2}{\omega^2}}, \quad (6.34)$$

from which we observe that for the series RLC circuit the input impedance is minimized at the resonant frequency, which corresponds to the maximum input power (see Figure 6.5). The half-power BW is the range of frequencies over which the input power drops to half the input power on resonance. This occurs when $|Z_{in}| = \sqrt{2}R$, which corresponds to $\Delta\omega/\omega = BW/2$. Using Equation 6.34 one can find that

$$2R^2 = R^2(1 + Q_0^2 BW^2), \quad (6.35)$$

which implies

$$BW = \frac{1}{Q_0} \quad (6.36)$$

It is important to emphasize that the Q-factor defined here, Q_0 , is technically the unloaded Q. It reflects the quality of the cavity or resonant circuit without the influence of any external circuitry. In practice, however, a cavity is invariably coupled to an

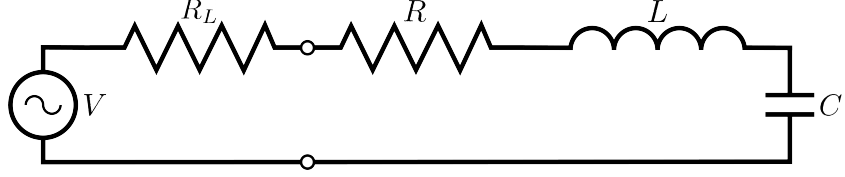


Figure 6.6. A series RLC circuit coupled to an external circuit with input impedance R_L .

4862 external circuit to drive a cavity resonance or to measure the energy of a resonant mode.
 4863 Coupling a cavity to an external circuit changes the Q by loading the equivalent cavity
 4864 RLC circuit (see Figure 6.6). The Q-factor of the cavity when it is loaded by an external
 4865 circuit is called the loaded Q, which is the quantity that one actually measures when
 4866 exciting a resonance in the cavity. Using the series RLC circuit model one can see that
 4867 the load resistor in Figure 6.6 will add in series with the resistor in the circuit for a total
 4868 equivalent resistance of $R + R_L$. Therefore, the loaded Q is given by

$$Q_L = \frac{1}{\omega_0(R + R_L)C}, \quad (6.37)$$

4869 from which one observes that the loaded Q is always less than the intrinsic Q of the
 4870 cavity.

4871 The amount of coupling that is desireable depends on the specific application of
 4872 the resonator. If one wants a resonator that is particular frequency selective than it
 4873 makes sense to limit the amount of coupling to the cavity to maintain a small BW,
 4874 alternatively, if a larger BW is need one can increase the cavity coupling by tuning the
 4875 input impedance of the external circuit. The critical point, where maximum power is
 4876 transferred between the cavity and the external circuit, occurs when the input impedance
 4877 of the cavity matches the input impedance of the external transmission line. For the
 4878 series RLC circuit on resonance, this matching condition corresponds to

$$Z_0 = Z_{in} = R, \quad (6.38)$$

4879 where Z_0 is the impedance of the transmission line. The loaded Q at this critical point
 4880 is, therefore,

$$Q_L = \frac{1}{2\omega_0 Z_0 C} = \frac{Q_0}{2}. \quad (6.39)$$

4881 One can described the degree of coupling between the cavity and an external circuit by

4882 defining a coupling factor, g , such that,

$$g = \frac{Q_0}{Q_L} - 1. \quad (6.40)$$

4883 When $g = 1$ then $Q_L = Q_0/2$, and the cavity is said to be critically coupled as we
4884 described. If $Q_L < Q_0/2$, then the cavity is undercoupled to the transmission line,
4885 corresponding to $g < 1$. Alternatively, if $Q_L > Q_0/2$, then $g > 1$, and the cavity is
4886 overcoupled to the transmission line. Various specialized circuits can be used to tune the
4887 input impedance of the external circuit as seen by the cavity to achieve a wide range of
4888 different coupling factors based on the desired application of the cavity.

4889 6.3 The Cavity Approach to CRES

4890 6.3.1 A Sketch of a Molecular Tritium Cavity CRES Experiment

4891 Resonant cavities can be used to perform CRES measurements, and they represent the
4892 current preferred technology by the Project 8 collaboration. The basic approach to a
4893 neutrino mass measurement using a resonant cavity and molecular tritium beta-decay
source is illustrated by Figure 6.7.

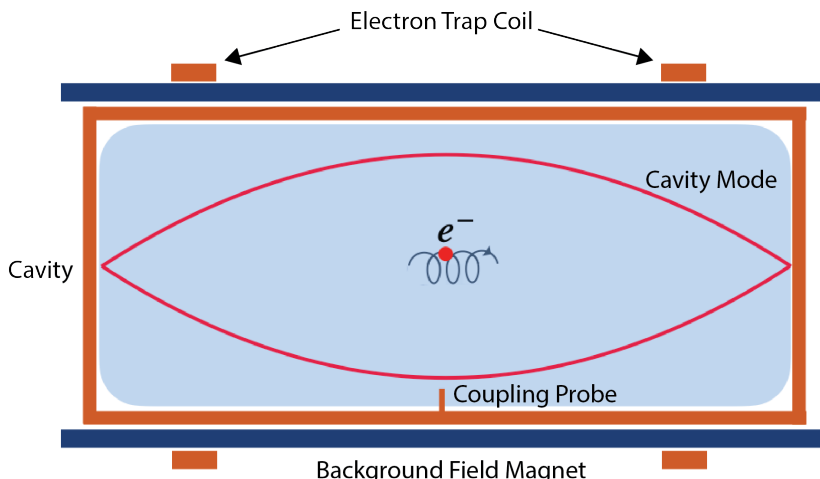


Figure 6.7. A cartoon depiction of a cavity CRES experiment. A metallic cavity filled with tritium gas is inserted into a uniform background magnetic field to perform CRES measurements. Electrons from beta-decays inside the cavity can be trapped and used to excite a resonant mode(s). By coupling to the cavity mode with a suitable probe one can measure the cyclotron frequency of the electron and perform CRES.

4894

4895 At the core of the experiment is a large resonant cavity filled with tritium gas. The
4896 filled cavity is then placed in a uniform magnetic field provided by a primary magnet
4897 that provides the background magnetic field. The value of the background magnetic field
4898 sets the range of cyclotron frequencies for electrons emitted near the tritium spectrum
4899 endpoint. When a beta-decay electron is produced in the cavity it is trapped using a set
4900 of magnetic pinch coils that keep electrons inside the cavity volume.

4901 Electrons trapped inside the cavity do not radiate in the same way as electrons
4902 in free-space. Effectively, the same boundary conditions that were used to derive the
4903 resonant modes of a cylindrical cavity in Section 6.2 apply to the radiation of the electron
4904 as well. The coupling of an electron performing cyclotron motion in a cavity has been
4905 studied in detail for measurements of the electron’s magnetic moment [96–98] If an
4906 electron is emitted with a kinetic energy that corresponds to a cyclotron frequency that
4907 matches a resonant frequency of the cavity, then energy radiated by the electron excites
4908 a corresponding resonance in the cavity. The strength of the electron’s coupling to the
4909 cavity is given to first order by the dot product between the electrons trajectory and
4910 the electric field vector of the resonant mode. Additional effects, such as the Purcell
4911 enhancement [99], alter the emitted power from the free-space Larmor equation [50]. If an
4912 electron is moving with a cyclotron frequency that is far from any resonant modes in the
4913 cavity, then radiation from the electron is suppressed. One can interpret this somewhat
4914 surprising effect as the metallic walls of the cavity reflecting the radiated energy back to
4915 the electron.

4916 Detecting an electron in the cavity is accomplished by coupling the cavity to an
4917 external transmission line that leads to an amplifier and RF receiver chain [100]. The
4918 coupling of the cavity resonance to the amplifier occurs through a coupling probe or
4919 aperture designed to read-out the excitation of the mode(s) excited by the electron. For
4920 CRES measurements, the placement of a wire antenna coupling probe inside the cavity
4921 volume leads to unacceptable losses of tritium atoms due to recombination to molecular
4922 tritium on the antenna surface, therefore, apertures are the preferred coupling method
4923 for cavity CRES experiments.

4924 One of the attractive features of the CRES technique for neutrino mass measurement
4925 is the gain in statistics that comes from the differential nature of the tritium spectrum
4926 measurement. Initially, this seems incompatible with cavities, due to the narrow reso-
4927 nances of cavity modes giving relatively small bandwidth. However, by intentionally
4928 over-coupling to a single cavity mode one can achieve bandwidths of a few 10’s of MHz
4929 (see Section 6.2), which is sufficient for a measurement of the tritium spectrum endpoint

4930 region.

4931 **6.3.2 Magnetic Field, Cavity Geometry, and Resonant Modes**

4932 **Magnetic Field and Volume Scaling**

4933 For a CRES experiment, cylindrical cavities are a natural choice since they match
4934 the geometry of standard solenoid magnets, which are needed in order to produce the
4935 background magnetic field for CRES measurements. Furthermore, the cylindrical shape is
4936 compatible with a Halbach array, which is the leading choice of atom trapping technology
4937 for future atomic tritium experiments by the Project 8 collaboration. Cylindrical
4938 cavities also benefit from well-established machining practices that are able to achieve
4939 high geometric precision at large lengths scales. More exotic cavity designs are under-
4940 consideration and there are on-going efforts to investigate the potential advantages these
4941 may have over the standard cylindrical geometry.

4942 As we saw in Section 6.2, the physical dimensions of the cavity are directly coupled
4943 to the resonant frequencies of the cavity. This dependency links the size of the cavity to
4944 the magnitude of the background magnetic field, because the magnetic field determines
4945 the cyclotron frequencies of trapped electrons. Specifically, as the size of the cavity is
4946 increased to accommodate larger volumes of tritium gas, the frequencies of the resonant
4947 modes decrease proportionally. This requires that the magnetic field also decrease in
4948 order to maintain coupling between electrons and the desired cavity mode.

4949 The required cavity size is ultimately determined by the required statistics in the
4950 tritium spectrum endpoint region. Because the gas density must be kept below a certain
4951 level to ensure that electrons have sufficient time to radiate before scattering, larger
4952 volumes become the only way to achieve higher event statistics. To achieve the sensitivity
4953 goals of Phase III and IV cavity volumes on the order of several cubic-meters are required,
4954 which pushes one towards frequencies in the range of 100's of MHz.

4955 **Single-mode Cavity CRES**

4956 It is tempting to consider maintaining a high magnetic field, while still increasing the size
4957 of the cavity, in order to increase the radiated power from trapped electrons for better
4958 SNR. However, if one were to maintain the same magnetic field while increasing the
4959 size of the cavity, the electrons would begin to couple to higher order modes with more
4960 complicated transverse geometries. The danger with this approach is that a complicated
4961 mode structure could introduce systematic errors into the CRES signals. Example

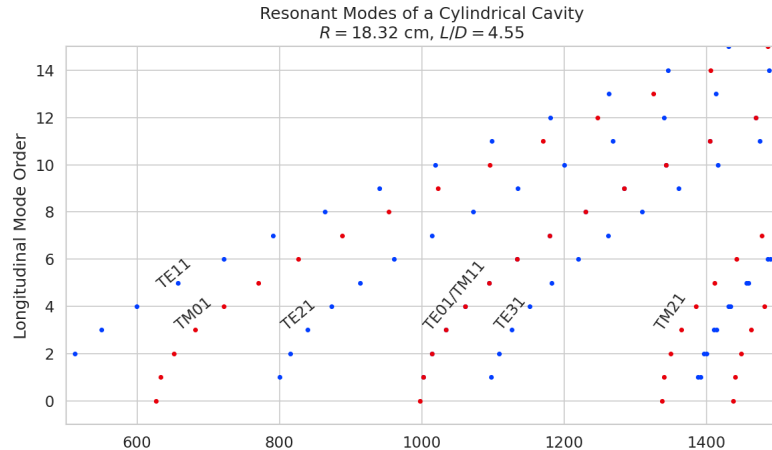
4962 systematics include unpredicted mode hybridization or changes in the mode shapes from
4963 imperfections in the cavity construction, which would prevent reconstruction of the
4964 electron's starting kinetic energies with adequate resolution. For this reason, it is ideal
4965 to operate with magnetic fields that give cyclotron frequencies near the fundamental
4966 frequency of the cavity, where the mode structure is relatively simple (see Figure 6.8).
4967 In this frequency region it is possible to perform CRES by coupling to only a single
4968 resonant mode, however, it is currently an open question if a single mode measurement
4969 will provide enough information about an individual electron's position to reconstruct
4970 the full event. Regardless, developing a solid understanding of the CRES phenomenology
4971 when an electron is coupling to a single mode will be a necessary step towards a future
4972 multi-mode cavity experiment.

4973 Considerations for Resonant Mode Selection

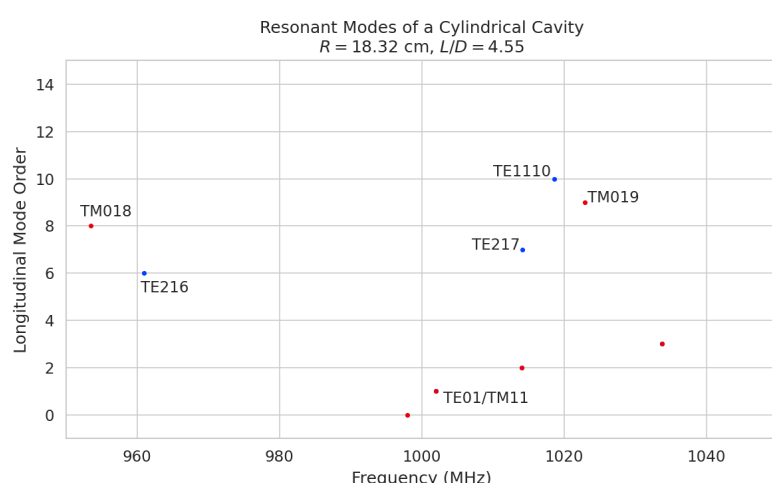
4974 A single-mode cavity experiment begs the question, which resonant mode is best for
4975 CRES measurements? There is an immediate bias towards low order TE_{nm} and TM_{nm}
4976 modes due to the multi-mode considerations discussed above. Additionally, there is a
4977 preference towards modes with longitudinal index $\ell = 1$ with a single antinode along the
4978 vertical axis of the cylindrical cavity. The reason for this is that there is a phase change
4979 in the electric fields between antinodes that leads to modulation effects that destroy the
4980 carrier frequency signal information.

4981 A second consideration for mode selection is the volumetric efficiency of the mode.
4982 Volumetric efficiency can be thought of as an integral over the volume of the cavity
4983 weighted by the relative amplitude of the mode. From the perspective of simply maximiz-
4984 ing the volume useable for CRES measurements this integral would be as close to unity
4985 as possible. However, there is a requirement to reconstruct the position of the electrons
4986 inside the cavity volume so that the local magnetic fields can be used to convert the
4987 measured cyclotron frequency to a kinetic energy. With a single mode this necessarily
4988 requires a variable transverse mode amplitude, which lowers the volumetric efficiency, so
4989 that position of the electron in the cavity can be estimated from the average amplitude
4990 of the CRES signal. Longitudinal indices of $\ell = 1$ have an advantage in volumetric
4991 efficiency over higher order ℓ modes, since there are only two longitudinal nodes, one at
4992 each end of the cavity. Therefore, the average coupling strength of trapped electrons as
4993 they oscillate axially is higher for $\ell = 1$ modes.

4994 The longitudinal variation in the mode strength is ultimately critical for achieving the
4995 energy resolution required for neutrino mass measurements. Correcting for the change in



(a)



(b)

Figure 6.8. Examples of the resonant mode frequencies of a cylindrical cavity. This cavity has a radius of 18.32 cm and a length to diameter ratio of 4.55.

the average magnetic fields experienced by electrons with different pitch angles requires that information on the axial motion of the electron be encoded into the CRES signal. The longitudinal variation in the mode amplitude leads to amplitude modulation of the CRES signal with a frequency proportional to the electron's pitch angle.

An additional factor for mode selection is the intrinsic or unloaded Q of the mode. In terms of SNR it is advantageous to use a mode with a very high Q_0 , which is then highly overcoupled to achieve the necessary bandwidth to cover the tritium endpoint spectrum. This scheme leads to a decoupling of the physical cavity temperature from the effective noise temperature after the amplifier, which allows us to achieve adequate SNR without

5005 the requirement of cooling the entire cavity to single Kelvin temperatures.

5006 An example of a resonant mode that exhibits these traits is the TE₀₁₁ mode. At present
5007 the TE₀₁₁ mode is the preferred resonance for a single-mode cavity CRES experiment
5008 by the Project 8 collaboration. TE₀₁₁ is a low order mode located in a region relatively
5009 far from other cavity modes. Furthermore, the separation of the TE₀₁₁ mode can be
5010 improved by various mode-filtering techniques discussed in Section 6.4.2 below. TE₀₁₁
5011 consists of a single longitudinal antinode that can provide pitch angle information in the
5012 form of amplitude modulation, and has an electric field with a radial profile given by the
5013 J'_0 Bessel function allowing for radial position estimation. Lastly, the TE₀₁₁ mode has a
5014 relatively high intrinsic Q compared to nearby modes, which helps with SNR. Unloaded
5015 Q's greater than 80000 are achievable for a 1 GHz TE₀₁₁ resonance using a copper walled
5016 cavity.

5017 **6.3.3 Trade-offs Between the Antenna and Cavity Approaches**

5018 The choice between cavities and antennas for large-scale CRES measurements is not
5019 without trade-offs. Both the antenna array and cavity approaches are relatively immature
5020 techniques, at present there are no known obstacles that would prevent either approach
5021 from being used for a large scale neutrino mass experiment. The preference for cavities
5022 is largely driven by important practical considerations that could make a cavity based
5023 experiment significantly cheaper than an antenna experiment of similar size and scope.
5024 However, the switch to cavities also introduces new challenges less relevant to the
5025 antenna array, which must be solved in order for Project 8 to achieve its neutrino mass
5026 measurement goals.

5027 One of the major relative drawbacks of the antenna array approach is the size and
5028 complexity of the data-acquisition system. A large-scale antenna array experiment
5029 requires $O(100)$ antennas independently digitized at rates of $O(10)$ to $O(100)$ MHz. Since
5030 there is insufficient information in a single antenna channel to detect or reconstruct the
5031 CRES signal, the entire array output must be processed during the signal reconstruction.
5032 Because data storage becomes an issue with these data volumes, there is a real-time
5033 signal reconstruction requirement that allows one to detect CRES signals buried in the
5034 thermal noise. As we discuss in Section 4.4, the computational cost of these real-time
5035 detection algorithms are potentially quite large for even a small scale antenna array
5036 experiment. However, the operating principle of a cavity experiment allows the CRES
5037 signal to be detected using only a single read-out channel digitized at rates of $O(10)$ MHz,
5038 which reduces the cost of the data acquisition system by many orders of magnitude.

5039 From an engineering perspective, the simple geometry and thin-walls of a cylindrical
5040 cavity are simpler to interface with the cryogenic and magnetic subsystems needed for a
5041 CRES experiment. Whereas, the antenna array requires careful design and engineering
5042 to accommodate the antenna array and receiver electronics in proximity to the trapping
5043 magnets. Additionally, due to near-field interference effects, the antenna array is unable
5044 to reconstruct CRES events within the reactive near-field distance of the antennas.
5045 Because atom trapping requirements require magnetic fields which correspond to cyclotron
5046 frequencies for endpoint electrons less than 1 GHz, the required stand-off distance leads to
5047 a significant loss in useable experiment volume, necessitating larger and more expensive
5048 magnets.

5049 Another advantage to the cavity approach is the relatively compact sideband structure,
5050 which is a result of the low modulation index for cavity CRES signals. The axial motion
5051 in an antenna array experiment leads to frequency modulation and sidebands. The shape
5052 of the sideband structure is determined by the modulation index, $h = \frac{\Delta f}{f_a}$, where Δf
5053 is the size of the frequency deviation and f_a is the axial frequency. The large electron
5054 traps required for a cubic-meter-scale experiment leads to high modulation indices, which
5055 causes the signal spectrum to be made up of numerous low power sidebands that make
5056 reconstruction and detection challenging. This behavior was observed in simulations
5057 of the FSCD in which carrier power decreased with pitch angle due to the increase in
5058 modulation index (see Figure 4.31). For cavities, however, the modulation index remains
5059 near $h = 1$ even for very long magnetic traps due to the high phase velocity in cavities
5060 relative to the axial velocity of the electron. This results in an almost ideal spectrum
5061 shape that has a strong carrier frequency with a few sidebands whose relative amplitudes
5062 encode pitch angle information.

5063 A downside of the cavity approach is the apparent difficulty of estimating the position
5064 of the electron using only the coupling of the electron to a single mode. The amplitude of
5065 the TE₀₁₁ mode is completely independent of the azimuthal coordinate, therefore, position
5066 reconstruction using the TE₀₁₁ mode is only able to estimate the radial position of the
5067 electron. This position degeneracy may lead to magnetic field uniformity requirements
5068 that are too challenging to meet due to mechanical uncertainties in cavity and magnet
5069 construction, as well as uncertainties caused by nuisance external magnetic fields such
5070 as the Earth's field and magnetic fields from building materials. A multi-mode cavity
5071 experiment may provide a way to extract more precise information on the position of
5072 the electron by analyzing the coupling of the electron to several modes that overlap in
5073 different ways.

5074 **6.4 Single-mode Resonant Cavity Design and Simulations**

5075 The single-mode cylindrical cavities envisioned for the Phase III and IV experiments must
5076 be carefully engineered in order to measure the neutrino mass with the desired sensitivity.
5077 In this section I summarize some simulation studies performed to analyze early design
5078 concepts for a single-mode cavity. The primary tool for these investigations was Ansys
5079 HFSS, which was also used for the development of the SYNCA antenna described in
5080 Section 5.3.

5081 **6.4.1 Open Cylindrical Cavities with Coaxial Terminations**

5082 **Design Concept**

5083 A basic cavity design question relevant to Project 8's ultimate goal of an atomic tritium
5084 CRES experiment is how to build a cavity that can be efficiently filled with atomic
5085 tritium. To keep the rate of atom loss from recombination on surfaces it is ideal if the
5086 ends of the cylindrical cavity are as open as possible so that tritium atoms can flow
5087 inside unimpeded. Additionally, one of the primary calibration techniques planned for
5088 future CRES experiments involves CRES measurements using electrons injected from
5089 an electron gun source, which also requires an opening at the cavity end. Cylindrical
5090 cavities with open ends can be manufactured, however, the intrinsic Q-factors of these
5091 cavities are orders of magnitude less than their sealed counterparts, which reduces the
5092 signal-to-noise ratio when that cavity is used for CRES measurement.

5093 Cylindrical cavities with mostly open ends that also exhibit Q values for the $TE_{01\ell}$
5094 modes similar to sealed cavities can be built by using coaxial endcaps to terminate the
5095 cavity. Cavities of this type have been manufactured for specialized applications related
5096 to the measurements of the dielectric constants of liquefied gasses (see Figure 6.9) [2, 3].
5097 This cavity design leaves the ends of the cavity wide open, but retains high Q-values for
5098 the $TE_{01\ell}$ modes due to the coaxial endcap, which are designed to perfectly reflect the
5099 electric fields of $TE_{01\ell}$ modes. Coupling to the $TE_{01\ell}$ mode is achieved via an aperture
5100 located at the center of the cavity wall.

5101 A cavity similar to Figure 6.9 is a candidate design for the future CRES experiments
5102 by Project 8, since it appears to elegantly solve many practical issues that arise when
5103 combining cavity CRES and atomic tritium. The coaxial endcaps leave significant regions
5104 of the cavity ends completely open, which allows for the entrance of atomic tritium as
5105 well as the pumping away of molecular tritium that has recombined on the cavity walls.

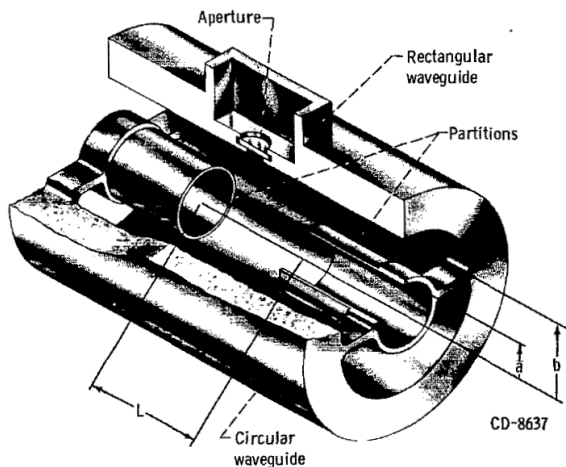


Figure 6.9. An image of an open cavity with coaxial terminations used for dielectric constant measurements. Figure from [2].

These open ends are achieved while preserving the high Q-values of the $\text{TE}_{01\ell}$ modes, which is important for extracting as much signal power from the electron as possible. In subsequent sections we shall analyze this cavity design in more detail, primarily by using HFSS simulations to analyze the resonant mode structure of this cavity geometry.

Coaxial Terminator Constraints

The reason that coaxial endcaps can be used to achieve high Q-values for the $\text{TE}_{01\ell}$ modes is that the electric fields for these modes are purely azimuthally polarized (see Equations 6.12 and 6.13). Therefore, the boundary conditions that require the electric field to go to zero at the cavity ends can be supplied using a coaxial partition of the correct radius (see Figure 6.10). Because the cylindrical shape enforced by the partition does not match the boundary conditions of other cavity modes, these terminations also significantly suppress the Q-factors of non- $\text{TE}_{01\ell}$ modes, which is potentially beneficial for a single-mode cavity CRES experiment.

The correct radius of the cylindrical partition is derived by setting up the boundary value problem in Figure 6.10, and analyzing the reflection and transmission coefficients for waves incident on the coaxial terminators. The basic problem is to identify the radius a where the reflection coefficient for the $\text{TE}_{01\ell}$ modes becomes equal to 1. One can show that if the coaxial partitions are made sufficiently long relative to the wavelength of the TE_{01} modes than perfect reflection can be achieved. This derivation is quite lengthy and complex and is presented in full in [3]. Here, we shall simply explain the resulting

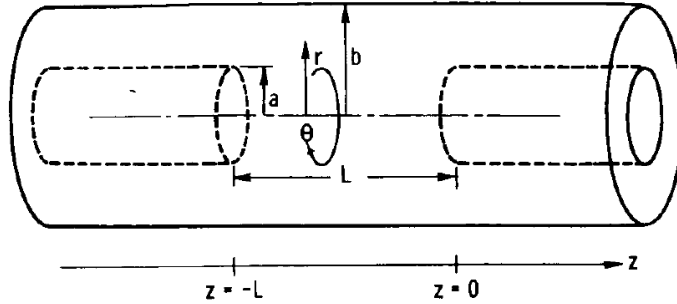


Figure 6.10. The simplified geometry of an open cavity with coaxial terminations. Figure from [3].

5126 conditions on the partition radius for perfect reflection.

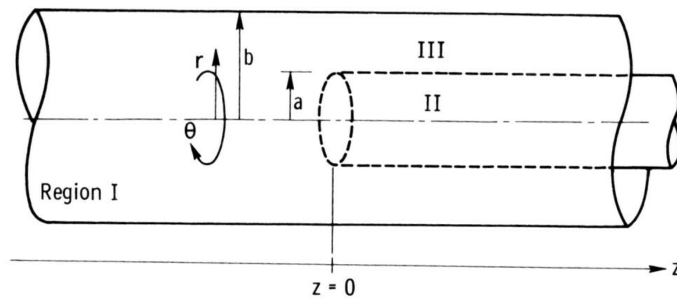


Figure 6.11. Electric field regions for the open cavity boundary value problem. Figure from [3].

5127 The open cavity boundary value problem is solved by expressing the forms of the
 5128 electric fields in the different regions of the cavity and requiring that the electric fields are
 5129 continuous. There are effectively three distinct regions in the open cavity corresponding
 5130 to the central cavity volume, the inner coaxial volume, and the outer coaxial volume (see
 5131 Figure 6.11).

5132 In Region I, the boundary conditions are those of a cylindrical waveguide, and we
 5133 require that E_ϕ for the TE_{0m} modes go to zero at the cavity wall ($r = b$). This requires
 5134 that $J'_{0m}(k_{c0m} b) = 0$. We aim to solve for the radius a in the specific situation where the
 5135 TE_{01} mode can propagate but all other TE_{0m} modes are below the cutoff frequency for
 5136 the circular waveguide. This is equivalent to requiring

$$3.832 < k_{c0m} b < 7.016, \quad (6.41)$$

5137 where the numbers 3.832 and 7.016 correspond to the first and second zeros of the Bessel
 5138 function (see Table 6.1).

5139 In Region II the boundary conditions are those of a cylindrical waveguide, but with
 5140 a smaller radius. The condition that $E_\phi = 0$ at the cylindrical partition radius is that
 5141 $J'_{0m}(k_{c0m}a) = 0$. To ensure perfect reflection, we want all modes in Region 1 of the cavity
 5142 to be below the cutoff frequency of the circular waveguide formed by the inner volume of
 5143 the coaxial terminator. Therefore, we consider the solutions where

$$k_{c0m}a < 3.832. \quad (6.42)$$

5144 Finally, in Region III the boundary condition are those of a coaxial waveguide. We
 5145 need to guarantee that $E_\phi = 0$ at both $r = b$ and $r = a$, which involves finding the
 5146 eigenvalues of the following equation

$$J'_0(k_{c0m}a)Y'_0(k_{c0m}b) - J'_0(k_{c0m}b)Y'_0(k_{c0m}a) = 0, \quad (6.43)$$

5147 where Y'_0 the zeroth-order derivatives of the Bessel function of the second kind. The
 5148 solutions to this equation depend on the value of the ratio b/a . The approximate solution
 5149 is given by

$$\delta_n a \simeq \frac{n\pi}{b/a - 1}, \quad (6.44)$$

5150 where δ_n are eigenvalues of Equation 6.43. Similar to Region II, we are interested in
 5151 solutions for which the TE₀₁ modes of Region I are below the cutoff of Region III.
 5152 Therefore, we require that

$$k_{c0m} < \delta_1. \quad (6.45)$$

5153 In general, one has some freedom in specifying the value of b/a . A value typically used
 5154 in practice is $b/a = 2.082$, which corresponds to positioning the radius of the cylindrical
 5155 partition at the maxima of the TE₀₁ electrical fields.

5156 Using the constraints from the three field regions one can develop a coaxial terminator
 5157 that acts as a virtual perfectly conducting surface for the TE₀₁ modes. The only required
 5158 inputs are the desired frequency of the TE₀₁₁ mode and a choice for the value of b/a .

5159 **6.4.2 Mode Filtering**

5160 The general case of an electron coupling to a resonant cavity is complicated. This is
 5161 because cavities contain an infinite number of resonant modes, which for higher order
 5162 modes, have couplings to the electron with a complex spatial dependence. The danger is
 5163 that improper modeling of the electron's coupling to the cavity can lead to systematic

5164 errors in the CRES measurements that prevent a high-resolution measurement of the
5165 electron's kinetic energy. This in part drives the preference for a single-mode cavity
5166 experiment that uses only the electron's coupling to the TE₀₁₁ mode to perform CRES,
5167 assuming that sufficient information on the electron's position can be obtained with a
5168 single mode.

5169 The TE₀₁₁ mode is in a region where there are relatively few other modes to which
5170 the electron could couple(see Figure 6.8). However, one can see that the frequency of
5171 the TE₀₁₁ is perfectly degenerate with the TM₁₁₁ mode, which means that electrons will
5172 inevitably couple to both modes if they have the correct cyclotron frequency.

5173 The magnitude of the impact of the electron coupling to both TE₀₁₁ and TM₁₁₁ is
5174 currently unknown. To first order an electron coupling to more both modes will lose more
5175 energy overtime, which can be measured by observing the frequency chirp rate of the
5176 signal. This effect may be small enough to be negligible or simple enough to model that
5177 the cavity can be treated as an effective single-mode cavity. Alternatively, the one could
5178 consider devising a coupling scheme that is sensitive to both the TE₀₁₁ and the TM₁₁₁
5179 modes. By measuring the coupling of the electron to both modes more information on
5180 the position of the electron could be obtained, which could improve the position and
5181 energy resolution of the CRES measurements.

5182 A different approach is the mode filtering approach, which seeks to obtain a single
5183 TE₀₁₁ mode cavity using perturbations to the cavity walls that selectively impede the
5184 TM modes, while leaving the TE modes mostly unperturbed. The type of perturbations
5185 required can be determined by visualizing the surface currents induced in the cavity
5186 walls by each type of mode (see Figure 6.12). By definition, all TM have electric fields
5187 directed along the vertical axis of the cylindrical cavity, which means that perturbations
5188 that impede currents in this direction will modify TM resonances. On the other hand,
5189 the TE₀₁ modes induce azimuthal currents in the cavity walls, therefore, it is possible to
5190 break the degeneracy between TE₀₁ and TM₁₁ using a cavity perturbation that impedes
5191 axial currents, but does not affect the flow of azimuthal currents.

5192 Figure 6.12 shows two cavity design concepts that achieve this selective current
5193 perturbation. The resistive approach inserts a series of thin dielectric rings into the walls
5194 of the cavity that introduces a resistive and capacitive impedance to the longitudinal
5195 currents, while leaving azimuthal current paths intact. Cavities of this type with high
5196 TE₀₁ Q's have also been constructed by tightly wrapping a thin, dielectric coated wire
5197 around a mold to form the cavity wall. An alternative method is to introduce an inductive
5198 impedance by cutting grooves or a thread pattern on the inside wall of the cavity. For

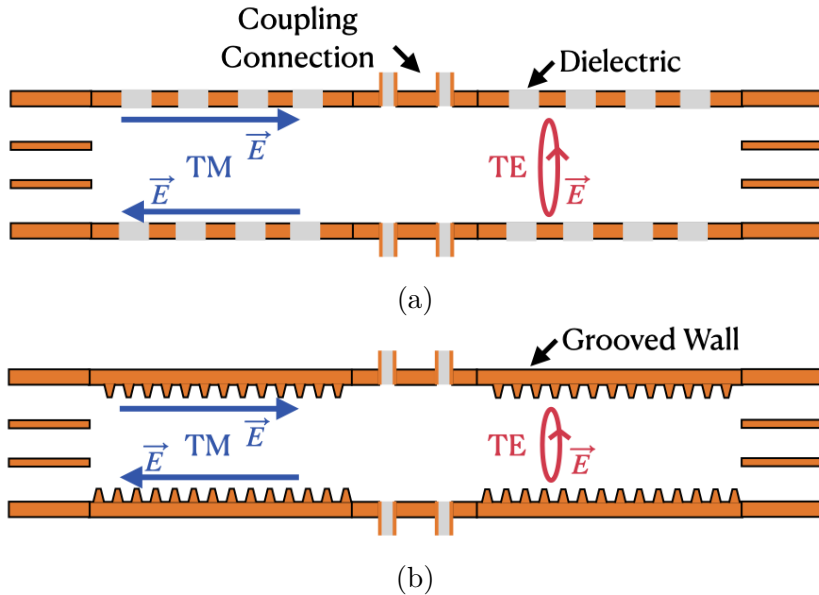


Figure 6.12. Two mode filtering concepts to break the degeneracy of TE_{01} and TM_{11} modes. The resistive approach uses dielectric materials to impede currents that travel vertically along the cavity while leaving azimuthal currents unperturbed. An alternative approach is to impede the currents using grooves cut into the cavity wall, which achieve the same effect with an inductive impedance.

5199 reasons of manufacturability and compatibility with tritium the grooved cavity approach
 5200 is the preferred method for mode-filtered cavity construction by Project 8.

5201 **6.4.3 Simulations of Open, Mode-filtered Cavities**

5202 A candidate design for a single TE_{011} mode CRES experiment is a cavity that utilizes
 5203 the coaxial terminations combined with a mode-filtering wall. The first step towards
 5204 validating that a cavity that combines these two design features will operate as expected
 5205 is a thorough simulation effort for which finite element method (FEM) simulation software
 5206 is invaluable. The primary tool for electromagnetic FEM calculations inside Project 8 is
 5207 Ansys HFSS, which has a robust and well-established eigenmode solver that can identify
 5208 the resonant frequencies and associated Q-factors for given structure.

5209 Four variations of a cavity design with a ~ 1 GHz TE_{011} resonance were implemented
 5210 in HFSS (see Figure 6.13). The four designs include a standard cylindrical cavity, an
 5211 open cavity with smooth walls, an open cavity with resistive walls, and an open cavity
 5212 with grooved walls. The relevant design parameters are summarized in Table 6.3. All
 5213 cavities were simulated using copper walls and filled with a vacuum dielectric. The
 5214 identities of the resonant modes found by HFSS were validated by visual inspection of

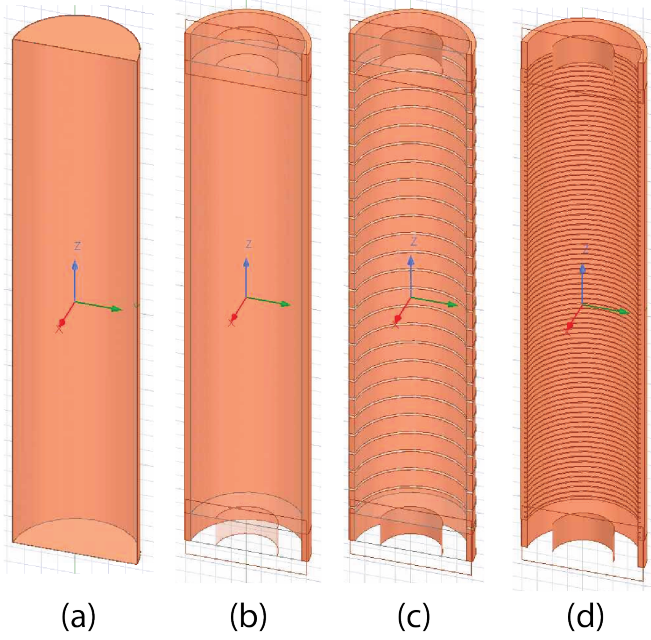


Figure 6.13. Four cavity design variations. (a) is a standard sealed cylindrical cavity, (b) is an open cavity with smooth walls, (c) is an open cavity with resistive walls, and (d) is an open cavity with grooved walls. The main cavity and coaxial terminator parameter are identical for all four cavities.

5215 the electric and magnetic field patterns and by comparison to analytical calculations of
 5216 the mode frequencies.

Table 6.3. A table of cavity design parameters used for HFSS simulations.

Name	Qty.	Unit	Description
D_{cav}	326.4	mm	Cavity diameter
L_{cav}	1668.0	mm	Cavity length
D_{term}	200.2	mm	Inner diameter of coaxial terminator
L_{term}	100.0	mm	Terminator length
l_{die}	8.3	mm	Dielectric spacer thickness
Δl_{die}	66.7	mm	Distance between dielectric spacers
l_{groove}	3.0	mm	Groove height
d_{groove}	9.0	mm	Groove depth
Δl_{groove}	18.3	mm	Distance between grooves

5217 The results of the HFSS simulations validate our predictions of the resonant behavior
 5218 of an open, mode-filtered cavity developed in the preceding sections (see Figure 6.14) One
 5219 can see that for a standard cavity the TE_{01} and the TM_{11} are degenerate in frequency
 5220 with relatively high Q-factors. The open-ended cavity preserves the high Q-factors of
 5221 the TE_{01} modes, while the other modes, since their boundary conditions do not match

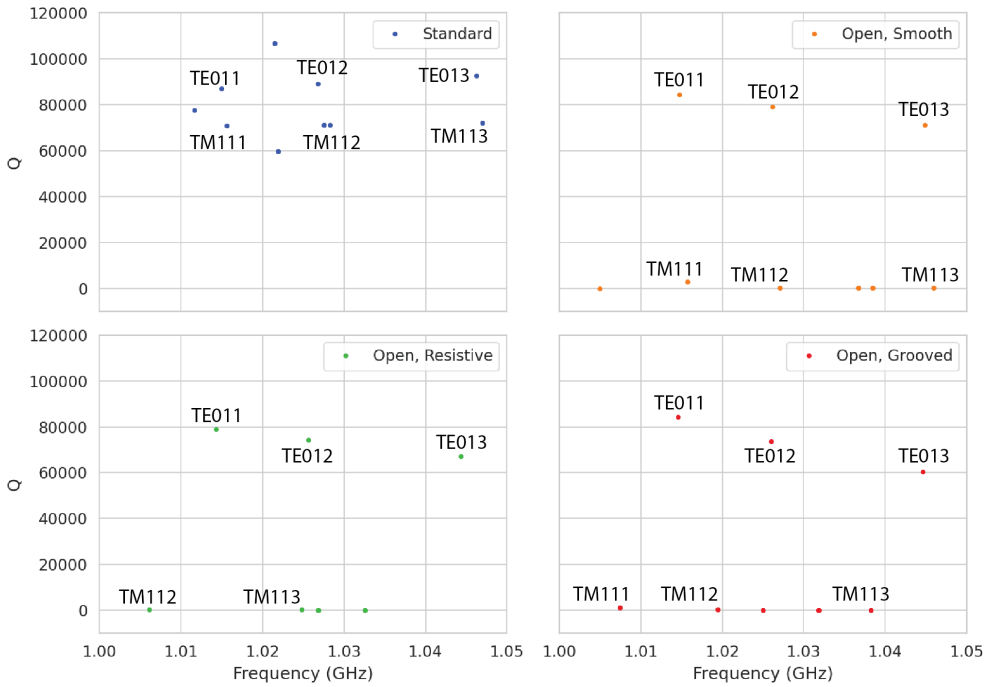


Figure 6.14. The frequencies and Q-factors of the resonant modes identified by HFSS for the cavity variations shown in Figure 6.13. The fully-sealed cavity with smooth walls has several high-Q modes near the TE_{011} resonance. Introducing the open-termination preserves the Q-factors of the $TE_{01\ell}$ modes and suppresses the Q-factors of the modes whose boundary conditions do not match the cylindrical partition. Both the resistive and grooved wall perturbations shift the resonant frequencies of the TM modes away from the TE_{011} mode. By properly tuning the geometry of the grooves or the resistive spacers several MHz of frequency separation can be achieved.

the coaxial geometry, have their Q-factors suppressed. One can see that the effect of the resistive and inductive mode-filtering schemes is to effectively shift the resonant frequencies of the TM_{11} modes below those of the associated TE_{01} modes, which breaks the degeneracy. Optimization of the dielectric spacer or groove parameters can ensure that the TE_{011} mode is isolated from other modes by $O(10)$ MHz, which provides sufficient bandwidth for a measurement of the tritium spectrum endpoint.

Further optimization of the cavity design requires a more detailed cavity simulation that includes the cavity coupling mechanism as well as other geometry modifications required for integration into the magnetic and tritium gas subsystems. Perhaps more important is the development of the capability to simulate the interaction of electrons with the cavity so that simulated CRES signals can be generated using cavities designed for CRES measurements. Simulated CRES signals can then be used to estimate the neutrino mass sensitivity of the experiment, which allows for the optimization of the cavity

5235 design towards the configuration that provides the best measurement of the neutrino
5236 mass.

5237 **6.5 Single-mode Resonant Cavity Measurements**

5238 Measurement test stands play an important role in the research and development process
5239 that cannot be replaced by simulations. For example, constructing a prototype CRES
5240 cavity forces one to consider important practical issues such as manufacturability and
5241 machine tolerances that may require modifications to the design. Furthermore, by
5242 comparing laboratory measurements of a real cavity to simulations, one can quantify
5243 the impact of imperfections and real-life measurement systematics, which allows for
5244 more accurate sensitivity estimates of the experiment. Lastly, the development of these
5245 prototypes helps to build the necessary experience and expertise within the collaboration
5246 required for more complicated experiments to succeed.

5247 In this spirit a prototype cavity was constructed to demonstrate the open, mode-
5248 filtered cavity concept explored in the previous sections. The primary goal of the
5249 measurements was to validate that an open, mode-filtered cavity suppressed the TM_{11}
5250 modes as predicted by HFSS simulations.

5251 **6.5.1 Cavities and Setup**

5252 Two rudimentary, cavities were constructed using segments of copper pipe available from
5253 McMaster-Carr (see Figure 6.15). The design consists of copper pipes of two diameters.
5254 The larger diameter pipe forms the main cavity wall and the smaller diameter pipe is
5255 used to create a coaxial termination. The diameter of the outer pipe was chosen to
5256 produce a TE_{011} resonance of approximately 6 GHz, while the diameter of the smaller
5257 pipe was selected based on the open termination criteria introduced in Section 6.4.1. The
5258 approximate diameters and lengths of the copper pipe are summarized in Table 6.4.

5259 Coupling to the cavity was achieved using a hand-formable segment of coaxial cable
5260 stripped at one end to form a loop antenna. This was inserted into a small hole located
5261 at the center of the main cavity wall. The coaxial terminators were supported inside the
5262 main cavity by carving a spacer from polystyrene foam (styrofoam) so that they could
5263 be easily inserted into the cavity and repositioned. The dielectric constant of styrofoam
5264 is quite close to air at microwave frequencies so this is expected to have minimal impact
5265 on the resonant properties of the cavity.

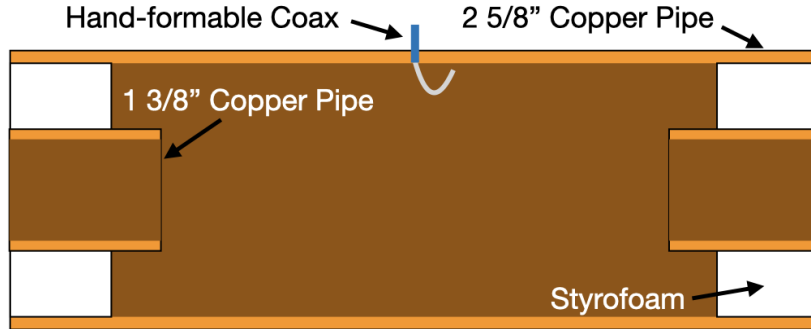


Figure 6.15. A cartoon depicting the design of the open-ended cavity prototype designed to operate at approximately 6 GHz. The main cavity wall was composed of a single copper pipe. A mode-filtered version of this cavity was constructed by

Table 6.4. A table of parameters describing the cavity prototypes. Certain values such as the cavity length and the distance between dielectric spacers are approximate due to variation in the machining of the copper. In particular, the filtered cavity was constructed from conducting copper segments that varied in size from 1.50" to 1.85".

Name	Qty.	Unit	Description
D_{cav}	2.625	in	Cavity diameter
L_{cav}	≈ 13	in	Cavity length
D_{term}	1.375	in	Inner diameter of coaxial terminator
L_{term}	1.575	in	Terminator length
l_{die}	0.75	in	Dielectric spacer thickness
Δl_{die}	≈ 1.50 to 1.85	in	Distance between dielectric spacers

5266 The actual length of the cavity is given by the distance between the inner edges of the
 5267 coaxial terminations. The length of the outer section of pipe that forms the main wall of
 5268 the cavity is approximately 16" in length which leads to a cavity length of $\approx 13"$ when
 5269 both terminators are inserted in the cavity. Because the terminators were not rigidly
 5270 mounted this distance is only approximate, however, the uncertain length of the cavity
 5271 will not prevent us from validating the open cavity design.

5272 Along with the smooth-walled open cavity a resistively mode-filtered cavity was
 5273 constructed by creating dielectric spacers out of segments of clear PVC pipe (see Figure
 5274 6.16). The spacers were machined such that the conductive segments of the cavity would
 5275 be separated by 0.75" when the cavity was fully assembled. Due to variations in the
 5276 lengths of the copper segments that make up the cavity wall the distance between spacers
 5277 has significant variation with average value of about 1.7". Eight total spacers were used
 5278 to build the cavity, which when assembled was approximately 16" in total length similar
 5279 to the non-filtered cavity.

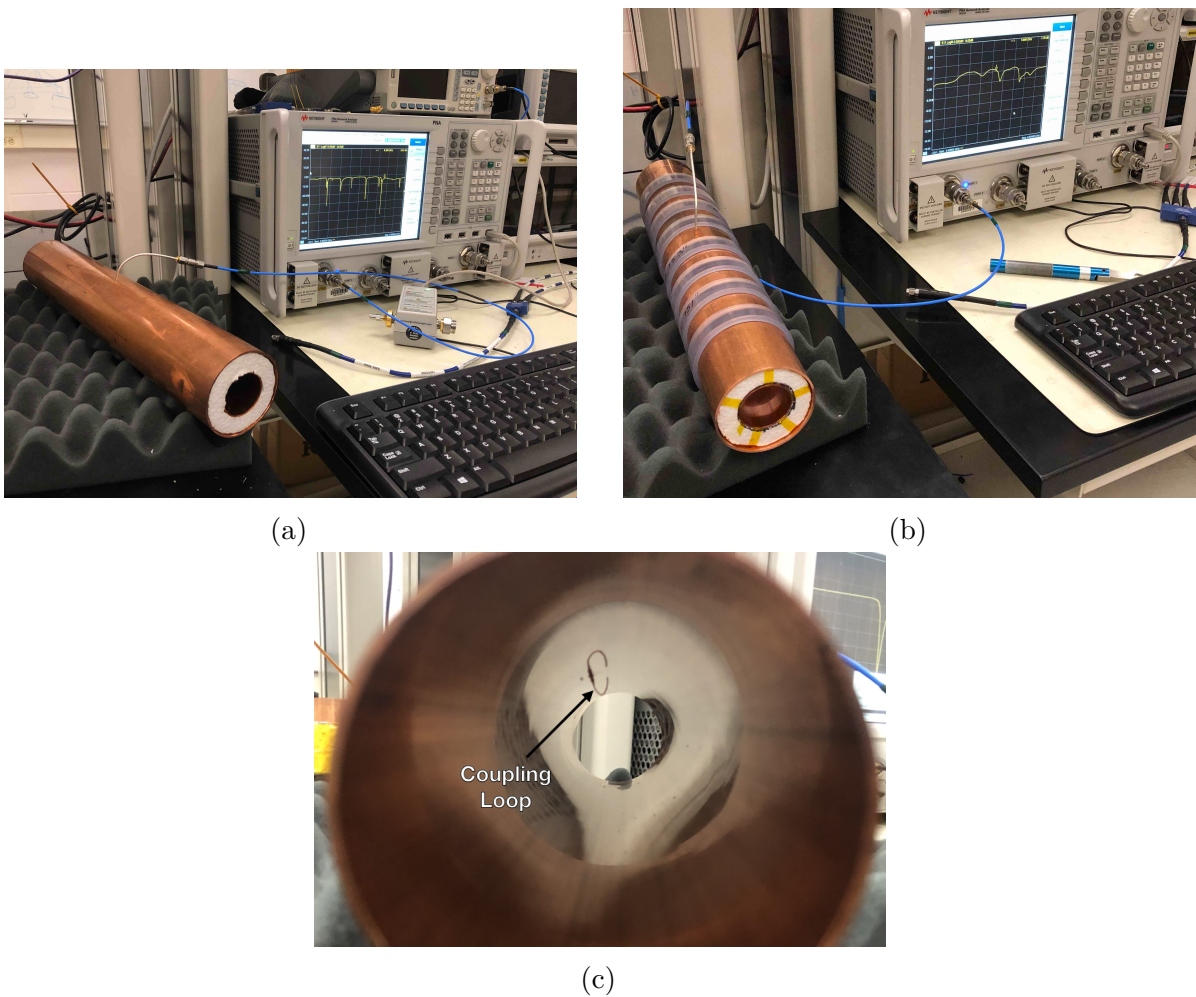


Figure 6.16. Images depicting the measurement of the filtered and non-filtered open cavities using the VNA. The coupling loop in the figure is shown in the TE orientation.

5280 Measurements of both cavities were performed using a VNA connected to the cavity
 5281 coupling probe (see Figure 6.16). By measuring the return loss over a range of frequencies
 5282 one can measure the frequencies and relative Q-factors of the resonant modes in the
 5283 cavity. Due to the opposite polarity of the electric fields for the TE and TM modes,
 5284 the loop coupling probe must be rotated 90° to change the polarity of the loop antenna.
 5285 When the antenna is oriented such that the loop opening faces the ends of the cavity, it
 5286 couples primarily to the TE modes which have magnetic fields directed along the long
 5287 axis of the cavity (see Figure 6.16). If the coupling loop is turned by 90° from where
 5288 it is shown in the image then it will couple to the TM modes which have azimuthally
 5289 directed magnetic fields. In this way both the TE and TM resonances can be measured
 5290 independently.

5291 6.5.2 Results and Discussion

5292 The primary analysis for the prototype cavities involved a simple visualization of the
5293 return loss as measured by the VNA and a comparison between the filtered and non-
5294 filtered variations. Since the resonances measured by the VNA are not labeled, there is
5295 an uncertainty about the true identities of the modes measured by the VNA. To resolve
5296 this I performed a simulation of the simplest possible cavity that could be created from
5297 the prototype components, which is a fully open cavity created by removing the coaxial
5298 inserts. The fully-open cavity with the as-built dimensions was simulated in HFSS to get
5299 estimates on the positions of the TE₀₁₁ and TM₁₁₁ modes (see Figure 6.17).

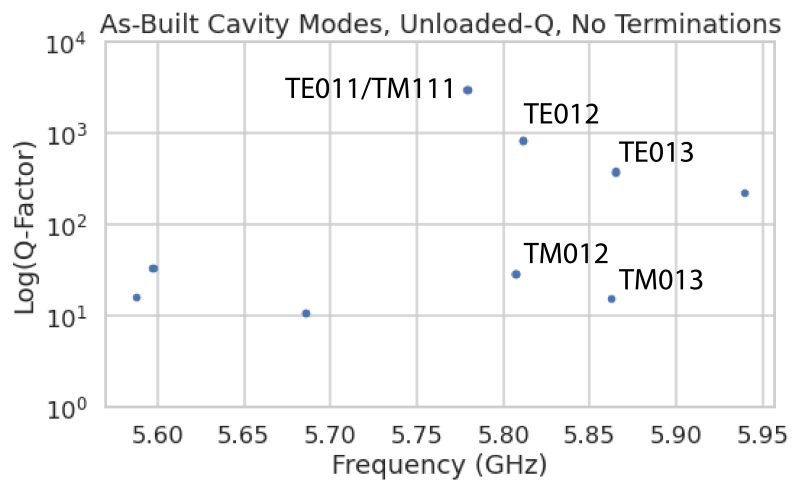


Figure 6.17. HFSS simulation results for a the as-built cavity with the coaxial terminators removed. The TE₀₁₁/TM₁₁₁ frequency is approximately 5.78 GHz.

5300 Simulation of the fully open cavity shows that the TE₀₁₁/TM₁₁₁ modes have a
5301 frequency of approximately 5.78 GHz in the fully open cavity. If the frequency of this
5302 mode is compared to the measurements of the filtered and non-filtered cavities with the
5303 terminators removed one can easily identify the TE₀₁₁ mode at approximately 5.75 GHz
5304 (see Figure 6.18).

5305 Both variations of the non-filtered cavities one sees that the TE₀₁₁ mode is degenerate
5306 in frequency with what appears to be a doublet of TM modes located at the TM₁₁₁
5307 frequency position. This doublet is actually the TM₁₁₁ mode, which has two polarizations
5308 with opposite polarizations. Because the pipe used to construct the cavity is not perfectly
5309 round, the frequency degeneracy between the two polarizations is broken resulting in the
5310 doublet peaks.

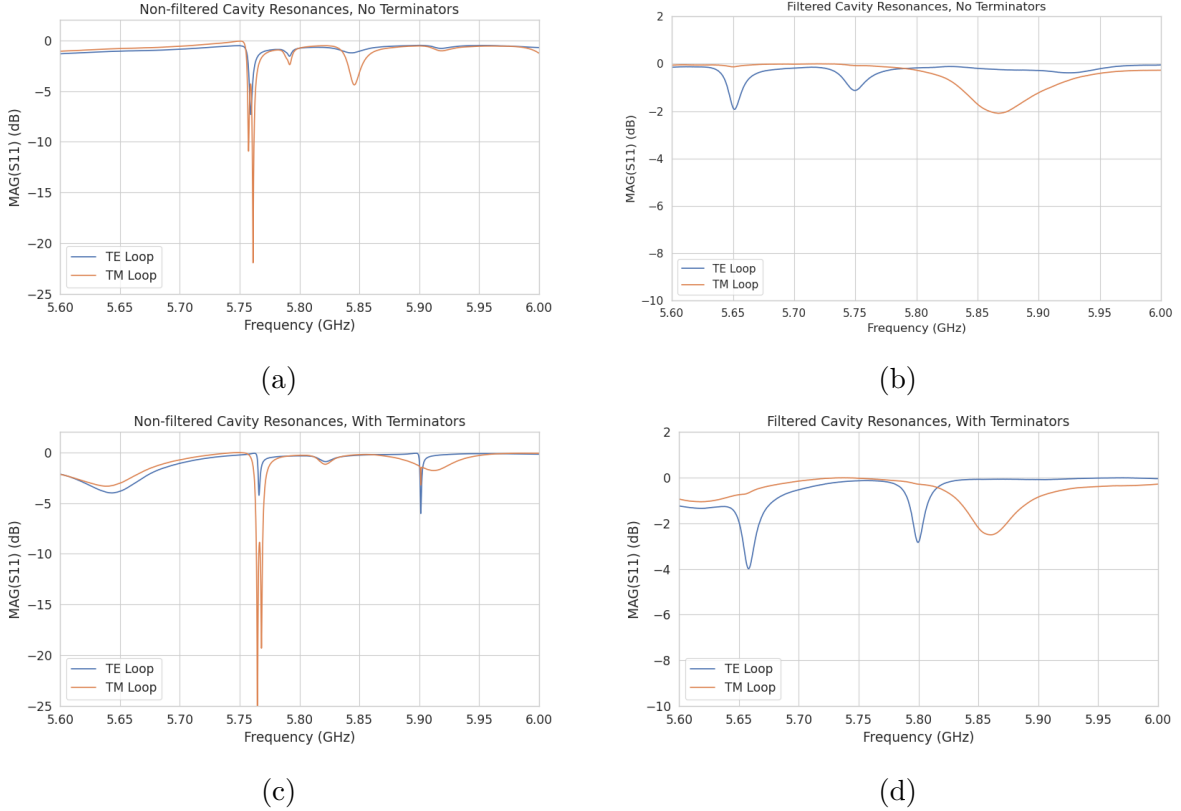


Figure 6.18. Measurements of the filtered and non-filtered prototype cavities acquired with the VNA.

The S-parameter plot for the filtered cavity without terminators has an isolated TE resonance at 5.65 GHz, associated with the TE_{011} mode. The frequency of this mode is lower than the non-filtered cavity due to a difference in the overall lengths of the cavities. An obvious difference between the filtered and non-filtered cavities is that there is no TM_{111} doublet at the TE_{011} frequency. This is what one would expect if the mode-filtering was suppressing the TM modes. There appears to be a noticeable difference in the Q of the TE_{011} resonance between non-filtered and filtered variations as indicated by the increased resonance depth for the filtered cavity. Overall, the Q-factors of the filtered cavity appear significantly smaller than the non-filtered cavity due to the increase in resonance width. This is likely caused by the relatively large widths of the dielectric spacers, which are partially impeding the TE modes.

In conclusion, one can see from these cavity measurements that, in principle, mode-filtering can be used to separate the TE_{011} resonance from the degenerate TM_{111} mode in combination with the an open cavity design. The next step would be to construct a prototype cavity that could be used to perform CRES measurements and measure its

5326 mode-structure using a technique such as a bead-puller [101] to study the coupling of an
5327 electron to a more realistic cavity mode structure.

5328 **Chapter 7 |**

5329 **Conclusion and Future Prospects**

5330 In this dissertation we have discussed research and development efforts towards the
5331 development of a scalable CRES measurement technology that can be used to build a
5332 CRES experiment at cubic-meter scales with sensitivity to neutrino masses of 40 meV.
5333 The primary contributions of my dissertation are the development and analysis of signal
5334 reconstruction algorithms for an antenna array based CRES experiment [102], which leads
5335 to estimates of the neutrino mass sensitivity; the development of a synthetic cyclotron
5336 radiation antenna (SYNCA) [81], which allowed for laboratory validation of antenna
5337 array CRES simulation models [44]; and the development of an open-ended cavity design
5338 compatible with atomic tritium for a cavity based CRES experiment. A measurable
5339 impact of this work is the transition of the Project 8 collaboration’s experimental plan
5340 from an antenna array based approach to a cavity based approach, where my work played
5341 a key role in demonstrating the significantly higher cost and complexity of the antenna
5342 array experiment.

5343 The transition from antenna arrays to cavities requires a new set of demonstrator
5344 experiments to make incremental progress towards a 40 meV measurement of the neutrino
5345 mass. At the time of writing, the near-term plan of Project 8 is to design and construct a
5346 small-scale cavity CRES experiment utilizing the 1 T magnet installed in the UW-Seattle.
5347 This cavity is designed to have a TE011 resonance with a frequency of about 26 GHz with
5348 a length-to-diameter ratio that mimics the larger cavities intended for the pilot-scale and
5349 Phase IV experiments. The goal of this experiment is to demonstrate cavity CRES as
5350 well as validate models of CRES systematics using electrons from ^{83m}Kr and an electron
5351 gun. Though the primary goal is demonstration, near-term physics measurements are
5352 available in the form of high-resolution measurements of the ^{83m}Kr conversion spectrum
5353 of interest to the KATRIN collaboration.

5354 Furthermore, Project 8 is currently constructing a low-frequency CRES setup located
5355 at Yale University to better understand the principles of cavity based CRES at lower

5356 magnetic fields. The Low, UHF Cavity Krypton Experiment at Yale (LUCKEY) is
5357 a 1.5 GHz cavity CRES experiment the will use conversion electrons from ^{83m}Kr to
5358 perform CRES measurements at the lowest frequencies ever attempted with the technique.
5359 LUCKEY will validate frequency scaling models developed by Project 8 and will pave
5360 the way for the future Low-Frequency Apparatus (LFA), which will be a larger, 1 GHz
5361 cavity CRES experiment that includes a molecular tritium source. The target for the
5362 LFA is a measurement of the neutrino mass with a sensitivity of approximately 0.2 eV,
5363 which will build towards the atomic pilot-scale CRES experiment.

5364 In parallel to the development of cavity CRES is the development of the atomic
5365 tritium source. Recent demonstrations of the production of atomic hydrogen are excellent
5366 steps towards the atomic tritium production needed for the pilot-scale experiment. One
5367 area of future study includes the development of a more detailed understanding of the
5368 efficiency of atomic hydrogen production. Near-term plans include the development of a
5369 magnetic, evaporatively cooled beamline, as well as the prototyping of a Halbach array
5370 atoms trap. Nearly all of the components of the atomic tritium system will require
5371 demonstration before the complete system can be built. The long-term goal of the
5372 atomic tritium work is to construct a full atomic tritium prototype that demonstrates
5373 the production, cooling, trapping, and recycling of tritium at the rates needed for the
5374 pilot-scale experiment.

5375 More broadly, the long-term goal of the Project 8 collaboration is to fully develop
5376 both the atomic tritium and cavity CRES technologies so that both can be combined in
5377 a pilot-scale CRES experiment. It is envisioned that this process will take approximately
5378 10 years for both atomic tritium and cavity CRES. After these developments comes
5379 the pilot-scale experiment which will be the first CRES experiment that simultaneously
5380 demonstrates all the required technologies for Phase IV. Scaling to Phase IV with cavity
5381 CRES will require the construction of multiple copies (approximately 10) of the pilot-scale
5382 experiment to obtain sufficient statistics for 40 meV sensitivity.

5383 Development of the CRES experimental technique by Project 8 has led to new
5384 experiments utilizing the CRES technique for basic physics research, such as the ^6He -
5385 CRES collaboration [103], and has also found applications as a new approach to x-ray
5386 spectroscopy [104]. Recently, a new experimental effort called CRESDA has begun in
5387 the UK to develop new quantum technologies applied to CRES measurements for the
5388 neutrino mass [105]. This flourishing of new experimental efforts based on the CRES
5389 technique is likely to continue as Project 8 continues to develop the technique towards
5390 its neutrino mass measurement goal.

5391

Bibliography

- 5392 [1] AGOSTINI, M., G. BENATO, and J. DETWILER (2017) “Discovery probability of
5393 next-generation neutrinoless double- β decay experiments,” *Phys. Rev. D*, **96**(5), p.
5394 053001, 1705.02996.
- 5395 [2] WENGER, N. C. and J. SMETANA (1972) “Hydrogen Density Measurements Using
5396 an Open-Ended Microwave Cavity,” *IEEE Transactions on Instrumentation and
5397 Measurement*, **21**(2), pp. 105–114.
- 5398 [3] WENGER, N. (1967) “Resonant Frequency of Open-Ended Cylindrical Cavity,”
5399 *IEEE Transactions on Microwave Theory and Techniques*, **15**(6), pp. 334–340.
- 5400 [4] DAS, A. and T. FERBEL (2003) *Introduction to Nuclear and Particle Physics*,
5401 World Scientific.
- 5402 [5] CURIE, P. (1898) “Sur une nouvelle substance fortement radioactive, contenue
5403 dans la pechblende,” *Comptes rendus de l’Academie des Sciences, Paris*, **127**, pp.
5404 1215–1217.
- 5405 [6] RUTHERFORD, E. (1899) “Uranium radiation and the electrical conduction pro-
5406 duced by it,” *Philos. Mag.*, **47**, p. 109.
5407 URL <https://cds.cern.ch/record/261896>
- 5408 [7] GERWARD, L. (1999) “Paul Villard and his Discovery of Gamma Rays,” *Physics
5409 in Perspective*, **1**, pp. 367–383.
- 5410 [8] BECQUEREL, H. (1900) “Deviation du rayonnement du radium dans un champ
5411 électrique,” *C.R.*, **130**, pp. 809–815.
- 5412 [9] D.Sc., E. R. M. and F. S. B.A. (1902) “XLI. The cause and nature of ra-
5413 dioactivity.—Part I,” *The London, Edinburgh, and Dublin Philosophical Mag-
5414 azine and Journal of Science*, **4**(21), pp. 370–396, [https://doi.org/10.1080/
5415 14786440209462856](https://doi.org/10.1080/14786440209462856).
5416 URL <https://doi.org/10.1080/14786440209462856>
- 5417 [10] CHADWICK, J. (1914) *Intensitätsverteilung im magnetischen Spektrum der β -
5418 Strahlen von Radium B+C*, Druck von Friedr. Vieweg und Sohn.
5419 URL <https://books.google.com/books?id=8s8UmQEACAAJ>

- 5420 [11] BROWN, L. M. (1978) “The idea of the neutrino,” *Physics Today*, **31**(9).
- 5421 [12] PAULI, W. (1978) “Dear radioactive ladies and gentlemen,” *Phys. Today*, **31N9**,
5422 p. 27.
- 5423 [13] AMALDI, E. (1984) “From the discovery of the neutron to the discovery of nuclear
5424 fission,” *Physics Reports*, **111**(1), pp. 1–331.
5425 URL <https://www.sciencedirect.com/science/article/pii/037015738490214X>
- 5427 [14] CHADWICK, J. (1932) “The existence of a neutron,” *Proceedings of the Royal
5428 Society of London. Series A, Containing Papers of a Mathematical and Physical
5429 Character*, **136**(830), pp. 692–708, <https://royalsocietypublishing.org/doi/pdf/10.1098/rspa.1932.0112>.
5430 URL <https://royalsocietypublishing.org/doi/abs/10.1098/rspa.1932.0112>.
- 5432 [15] WILSON, F. L. (1968) “Fermi’s Theory of Beta Decay,” *American Journal of
5434 Physics*, **36**(12), pp. 1150–1160, https://pubs.aip.org/aapt/ajp/article-pdf/36/12/1150/11891052/1150_1_online.pdf.
5436 URL <https://doi.org/10.1119/1.1974382>
- 5437 [16] CRANE, H. R. and J. HALPERN (1938) “New Experimental Evidence for the
5438 Existence of a Neutrino,” *Phys. Rev.*, **53**, pp. 789–794.
5439 URL <https://link.aps.org/doi/10.1103/PhysRev.53.789>
- 5440 [17] COWAN, C. L., F. REINES, F. B. HARRISON, H. W. KRUSE, and A. D.
5441 MC GUIRE (1956) “Detection of the Free Neutrino: a Confirmation,” *Science*,
5442 **124**(3212), pp. 103–104, <https://www.science.org/doi/pdf/10.1126/science.124.3212.103>.
5444 URL <https://www.science.org/doi/abs/10.1126/science.124.3212.103>
- 5445 [18] ANICIN, I. V. (2005) “The Neutrino - Its Past, Present and Future,” *arXiv e-prints*,
5446 physics/0503172, [physics/0503172](https://arxiv.org/abs/physics/0503172).
- 5447 [19] DAVIS, R. (2003) “Nobel Lecture: A half-century with solar neutrinos,” *Rev. Mod.*
5448 *Phys.*, **75**, pp. 985–994.
- 5449 [20] McDONALD, A. B. ET AL. (2002) “Direct evidence for neutrino flavor transfor-
5450 mation from neutral-current interactions in SNO,” *AIP Conf. Proc.*, **646**(1), pp.
5451 43–58.
- 5452 [21] FUKUDA, Y. ET AL. (1998) “Evidence for oscillation of atmospheric neutrinos,”
5453 *Phys. Rev. Lett.*, **81**, pp. 1562–1567, [hep-ex/9807003](https://arxiv.org/abs/hep-ex/9807003).
- 5454 [22] GIGANTI, C., S. LAVIGNAC, and M. ZITO (2018) “Neutrino oscillations: The rise
5455 of the PMNS paradigm,” *Prog. Part. Nucl. Phys.*, **98**, pp. 1–54, [1710.00715](https://arxiv.org/abs/1710.00715).

- 5456 [23] AN, F. ET AL. (2016) “Neutrino Physics with JUNO,” *J. Phys. G*, **43**(3), p. 030401,
5457 1507.05613.
- 5458 [24] BIAN, J. ET AL. (2022) “Hyper-Kamiokande Experiment: A Snowmass White
5459 Paper,” in *Snowmass 2021*, 2203.02029.
- 5460 [25] ABI, B. ET AL. (2020) “Long-baseline neutrino oscillation physics potential of the
5461 DUNE experiment,” *Eur. Phys. J. C*, **80**(10), p. 978, 2006.16043.
- 5462 [26] WORKMAN, R. L. ET AL. (2022) “Review of Particle Physics,” *PTEP*, **2022**, p.
5463 083C01.
- 5464 [27] ZUBER, K. (2020) *Neutrino Physics*, CRC Press.
- 5465 [28] XING, Z. Z. and S. ZHOU (2011) *Neutrinos in Particle Physics, Astronomy and*
5466 *Cosmology*, Springer.
- 5467 [29] MOHAPATRA, R. N. ET AL. (2007) “Theory of neutrinos: A White paper,” *Rept.*
5468 *Prog. Phys.*, **70**, pp. 1757–1867, hep-ph/0510213.
- 5469 [30] DE GOUVÊA, A. (2016) “Neutrino Mass Models,” *Ann. Rev. Nucl. Part. Sci.*, **66**,
5470 pp. 197–217.
- 5471 [31] WORKMAN, R. L. and OTHERS (2022) “Review of Particle Physics,” *PTEP*, **2022**,
5472 p. 083C01.
- 5473 [32] WONG, Y. Y. Y. (2011) “Neutrino mass in cosmology: status and prospects,”
5474 *Ann. Rev. Nucl. Part. Sci.*, **61**, pp. 69–98, 1111.1436.
- 5475 [33] ADE, P. A. R. ET AL. (2016) “Planck 2015 results. XIII. Cosmological parameters,”
5476 *Astron. Astrophys.*, **594**, p. A13, 1502.01589.
- 5477 [34] CARLSTROM, J., K. ABAZAJIAN, G. ADDISON, P. ADSHEAD, Z. AHMED,
5478 S. W. ALLEN, D. ALONSO, M. ALVAREZ, A. ANDERSON, K. S. ARNOLD,
5479 C. BACCIGALUPI, K. BAILEY, D. BARKATS, D. BARRON, P. S. BARRY, J. G.
5480 BARTLETT, R. BASU THAKUR, N. BATTAGLIA, E. BAXTER, R. BEAN, C. BE-
5481 BEK, A. N. BENDER, B. A. BENSON, E. BERGER, S. BHIMANI, C. A. BISCHOFF,
5482 L. BLEEM, S. BOQUET, K. BODDY, M. BONATO, J. R. BOND, J. BOR-
5483 RILL, F. R. BOUCHET, M. L. BROWN, S. BRYAN, B. BURKHART, V. BUZA,
5484 K. BYRUM, E. CALABRESE, V. CALAFUT, R. CALDWELL, J. E. CARLSTROM,
5485 J. CARRON, T. CECIL, A. CHALLINOR, C. L. CHANG, Y. CHINONE, H.-
5486 M. S. CHO, A. COORAY, T. M. CRAWFORD, A. CRITES, A. CUKIERMAN,
5487 F.-Y. CYR-RACINE, T. DE HAAN, G. DE ZOTTI, J. DELABROUILLE, M. DE-
5488 MARTEAU, M. DEVLIN, E. DI VALENTINO, M. DOBBS, S. DUFF, A. DUIVEN-
5489 VOORDEN, C. DVORKIN, W. EDWARDS, J. EIMER, J. ERRARD, T. ESSINGER-
5490 HILEMAN, G. FABBIAN, C. FENG, S. FERRARO, J. P. FILIPPINI, R. FLAUGER,
5491 B. FLAUGHER, A. A. FRAISSE, A. FROLOV, N. GALITZKI, S. GALLI, K. GANGA,

M. GERBINO, M. GILCHRIESE, V. GLUSCEVIC, D. GREEN, D. GRIN, E. GROHS,
 R. GUALTIERI, V. GUARINO, J. E. GUDMUNDSSON, S. HABIB, G. HALLER,
 M. HALPERN, N. W. HALVERSON, S. HANANY, K. HARRINGTON, M. HASEGAWA,
 M. HASSELFIELD, M. HAZUMI, K. HEITMANN, S. HENDERSON, J. W. HEN-
 NING, J. C. HILL, R. HLOŽEK, G. HOLDER, W. HOLZAPFEL, J. HUBMAYR,
 K. M. HUFFENBERGER, M. HUFFER, H. HUI, K. IRWIN, B. R. JOHNSON,
 D. JOHNSTONE, W. C. JONES, K. KARKARE, N. KATAYAMA, J. KERBY,
 S. KERNOVSKY, R. KESKITALO, T. KISNER, L. KNOX, A. KOSOWSKY, J. KO-
 VAC, E. D. KOVETZ, S. KUHLMANN, C.-L. KUO, N. KURITA, A. KUSAKA,
 A. LAHTEENMAKI, C. R. LAWRENCE, A. T. LEE, A. LEWIS, D. LI, E. LINDER,
 M. LOVERDE, A. LOWITZ, M. S. MADHAVACHERIL, A. MANTZ, F. MATSUDA,
 P. MAUSKOPF, J. McMAHON, P. D. MEERBURG, J. MELIN, J. MEYERS,
 M. MILLEA, J. MOHR, L. MONCELSI, T. MROCZKOWSKI, S. MUKHERJEE,
 M. MUNCHMEYER, D. NAGAI, J. NAGY, T. NAMIKAWA, F. NATI, T. NATOLI,
 M. NEGRELLO, L. NEWBURGH, M. D. NIEMACK, H. NISHINO, M. NORDBY,
 V. NOVOSAD, P. O'CONNOR, G. OBIED, S. PADIN, S. PANDEY, B. PARTRIDGE,
 E. PIERPAOLI, L. POGOSIAN, C. PRYKE, G. PUGLISI, B. RACINE, S. RAGHU-
 NATHAN, A. RAHLIN, S. RAJAGOPALAN, M. RAVERI, M. REICHANADTER, C. L.
 REICHARDT, M. REMAZEILLES, G. ROCHA, N. A. ROE, A. ROY, J. RUHL,
 M. SALATINO, B. SALIWANCHIK, E. SCHAAN, A. SCHILLACI, M. M. SCHMITT-
 FULL, D. SCOTT, N. SEHGAL, S. SHANDERA, C. SHEEHY, B. D. SHERWIN, E. SHI-
 ROKOFF, S. M. SIMON, A. SLOSAR, R. SOMERVILLE, S. T. STAGGS, A. STARK,
 R. STOMPOR, K. T. STORY, C. STOUGHTON, A. SUZUKI, O. TAJIMA, G. P.
 TEPLY, K. THOMPSON, P. TIMBIE, M. TOMASI, J. I. TREU, M. TRISTRAM,
 G. TUCKER, C. UMLTA, A. VAN ENGELEN, J. D. VIEIRA, A. G. VIEREGG,
 M. VOGELSBERGER, G. WANG, S. WATSON, M. WHITE, N. WHITEHORN, E. J.
 WOLLACK, W. L. K. WU, Z. XU, S. YASINI, J. YECK, K. W. YOON, E. YOUNG,
 and A. ZONCA (2019) "CMB-S4," in *Bulletin of the American Astronomical Society*,
 vol. 51, p. 209, 1908.01062.

- [35] ELLIOTT, S. R. and P. VOGEL (2002) "Double beta decay," *Ann. Rev. Nucl. Part. Sci.*, **52**, pp. 115–151, [hep-ph/0202264](#).
- [36] DOLINSKI, M. J., A. W. P. POON, and W. RODEJOHANN (2019) "Neutrinoless Double-Beta Decay: Status and Prospects," *Ann. Rev. Nucl. Part. Sci.*, **69**, pp. 219–251, [1902.04097](#).
- [37] FORMAGGIO, J. A., A. L. C. DE GOUVÉA, and R. G. H. ROBERTSON (2021) "Direct measurements of neutrino mass," *Physics Reports*, **914**, pp. 1–54, direct measurements of neutrino mass.
 URL <https://www.sciencedirect.com/science/article/pii/S0370157321000636>

- 5531 [38] AKER, M. ET AL. (2022) “New Constraint on the Local Relic Neutrino Background
 5532 Overdensity with the First KATRIN Data Runs,” *Phys. Rev. Lett.*, **129**(1), p.
 5533 011806, 2202.04587.
- 5534 [39] FORMAGGIO, J. A., A. L. C. DE GOUVÊA, and R. G. H. ROBERTSON (2021)
 5535 “Direct Measurements of Neutrino Mass,” *Phys. Rept.*, **914**, pp. 1–54, 2102.00594.
- 5536 [40] MONREAL, B. and J. A. FORMAGGIO (2009) “Relativistic cyclotron radiation
 5537 detection of tritium decay electrons as a new technique for measuring the neutrino
 5538 mass,” *Phys. Rev. D*, **80**, p. 051301.
 5539 URL <https://link.aps.org/doi/10.1103/PhysRevD.80.051301>
- 5540 [41] ESFAHANI, A. A., S. BÖSER, N. BUZINSKY, M. C. CARMONA-BENITEZ,
 5541 C. CLAESSENS, L. DE VIVEIROS, P. J. DOE, S. ENOMOTO, M. FERTL, J. A.
 5542 FORMAGGIO, J. K. GAISON, M. GRANDO, K. M. HEEGER, X. HUYAN, A. M.
 5543 JONES, K. KAZKAZ, M. LI, A. LINDMAN, C. MATTHÉ, R. MOHIUDDIN, B. MON-
 5544 REAL, R. MUELLER, J. A. NIKKEL, E. NOVITSKI, N. S. OBLATH, J. I. PEÑA,
 5545 W. PETTUS, R. REIMANN, R. G. H. ROBERTSON, G. RYBKA, L. SALDAÑA,
 5546 M. SCHRAM, P. L. SLOCUM, J. STACHURSKA, Y. H. SUN, P. T. SURUKUCHI,
 5547 J. R. TEDESCHI, A. B. TELLES, F. THOMAS, M. THOMAS, L. A. THORNE,
 5548 T. THÜMMLER, W. V. D. PONTSEELE, B. A. VANDEVENDER, T. E. WEISS,
 5549 T. WENDLER, and A. ZIEGLER (2022) “The Project 8 Neutrino Mass Experiment,”
 5550 2203.07349.
- 5551 [42] ESFAHANI, A. A., S. BÖSER, N. BUZINSKY, M. C. CARMONA-BENITEZ,
 5552 C. CLAESSENS, L. DE VIVEIROS, P. J. DOE, M. FERTL, J. A. FORMAG-
 5553 GIO, J. K. GAISON, L. GLADSTONE, M. GUIQUE, J. HARTSE, K. M. HEEGER,
 5554 X. HUYAN, A. M. JONES, K. KAZKAZ, B. H. LAROQUE, M. LI, A. LIND-
 5555 MAN, E. MACHADO, A. MARSTELLER, C. MATTHÉ, R. MOHIUDDIN, B. MON-
 5556 REAL, R. MUELLER, J. A. NIKKEL, E. NOVITSKI, N. S. OBLATH, J. I. PEÑA,
 5557 W. PETTUS, R. REIMANN, R. G. H. ROBERTSON, D. R. D. JESÚS, G. RYBKA,
 5558 L. SALDAÑA, M. SCHRAM, P. L. SLOCUM, J. STACHURSKA, Y. H. SUN, P. T.
 5559 SURUKUCHI, J. R. TEDESCHI, A. B. TELLES, F. THOMAS, M. THOMAS, L. A.
 5560 THORNE, T. THÜMMLER, L. TVRZNIKOVA, W. V. D. PONTSEELE, B. A. VAN-
 5561 DEVENDER, J. WEINTROUB, T. E. WEISS, T. WENDLER, A. YOUNG, E. ZAYAS,
 5562 and A. ZIEGLER (2023) “Cyclotron Radiation Emission Spectroscopy of Electrons
 5563 from Tritium Beta Decay and ^{83m}Kr Internal Conversion,” 2303.12055.
- 5564 [43] ESFAHANI, A. A., S. BÖSER, N. BUZINSKY, M. C. CARMONA-BENITEZ,
 5565 C. CLAESSENS, L. DE VIVEIROS, P. J. DOE, M. FERTL, J. A. FORMAG-
 5566 GIO, J. K. GAISON, L. GLADSTONE, M. GRANDO, M. GUIQUE, J. HARTSE,
 5567 K. M. HEEGER, X. HUYAN, J. JOHNSTON, A. M. JONES, K. KAZKAZ, B. H.
 5568 LAROQUE, M. LI, A. LINDMAN, E. MACHADO, A. MARSTELLER, C. MATTHÉ,
 5569 R. MOHIUDDIN, B. MONREAL, R. MUELLER, J. A. NIKKEL, E. NOVITSKI,
 5570 N. S. OBLATH, J. I. PEÑA, W. PETTUS, R. REIMANN, R. G. H. ROBERT-
 5571 SON, D. R. D. JESÚS, G. RYBKA, L. SALDAÑA, M. SCHRAM, P. L. SLOCUM,

- 5572 J. STACHURSKA, Y. H. SUN, P. T. SURUKUCHI, J. R. TEDESCHI, A. B. TELLES,
 5573 F. THOMAS, M. THOMAS, L. A. THORNE, T. THÜMMLER, L. TVRZNIKOVA,
 5574 W. V. D. PONTSEELE, B. A. VANDEVENDER, J. WEINTROUB, T. E. WEISS,
 5575 T. WENDLER, A. YOUNG, E. ZAYAS, and A. ZIEGLER (2023) “Tritium Beta Spec-
 5576 trum and Neutrino Mass Limit from Cyclotron Radiation Emission Spectroscopy,”
 5577 2212.05048.
- 5578 [44] “Antenna Arrays for Physics Measurements with Large-scale CRES Detectors,” *In
 5579 preparation*.
- 5580 [45] NICHOLSON, T. ET AL. (2015) “Systematic evaluation of an atomic clock at 2 x
 5581 10-18 total uncertainty,” *Nature Communications*, **6**(6896).
- 5582 [46] HÄNSCH, T. W. (2006) “Nobel Lecture: Passion for precision,” *Rev. Mod. Phys.*,
 5583 **78**, pp. 1297–1309.
 5584 URL <https://link.aps.org/doi/10.1103/RevModPhys.78.1297>
- 5585 [47] GABOR, D. (1946) “Theory of communication. Part 1: The analysis of information,”
 5586 *Journal of the Institution of Electrical Engineers-part III: radio and communication
 5587 engineering*, **93**(26), pp. 429–441.
- 5588 [48] ESFAHANI ASHTARI, A. ET AL. (2022) “Viterbi decoding of CRES signals in
 5589 Project 8,” *New J. Phys.*, **24**(5), p. 053013, 2112.05265.
- 5590 [49] JACKSON, J. D. (1999) *Classical electrodynamics*, 3rd ed., Wiley, New York, NY.
 5591 URL <http://cdsweb.cern.ch/record/490457>
- 5592 [50] F.R.S., J. L. D. (1897) “LXIII. On the theory of the magnetic influence on
 5593 spectra; and on the radiation from moving ions,” *The London, Edinburgh, and
 5594 Dublin Philosophical Magazine and Journal of Science*, **44**(271), pp. 503–512,
 5595 <https://doi.org/10.1080/14786449708621095>.
 5596 URL <https://doi.org/10.1080/14786449708621095>
- 5597 [51] ESFAHANI, A. A. ET AL. (2022) “The Project 8 Neutrino Mass Experiment,” in
 5598 *2022 Snowmass Summer Study*, 2203.07349.
- 5599 [52] KRAUS, C. ET AL. (2005) “Final results from phase II of the Mainz neutrino mass
 5600 search in tritium beta decay,” *Eur. Phys. J. C*, **40**, pp. 447–468, [hep-ex/0412056](https://arxiv.org/abs/hep-ex/0412056).
- 5601 [53] ASEEV, V. N. ET AL. (2011) “An upper limit on electron antineutrino mass from
 5602 Troitsk experiment,” *Phys. Rev. D*, **84**, p. 112003, 1108.5034.
- 5603 [54] SAENZ, A., S. JONSELL, and P. FROELICH (2000) “Improved Molecular Final-
 5604 State Distribution of HeT+ for the β -Decay Process of T2,” *Phys. Rev. Lett.*, **84**(2),
 5605 p. 242.

- 5606 [55] BODINE, L. I., D. S. PARNO, and R. G. H. ROBERTSON (2015) “Assessment
 5607 of molecular effects on neutrino mass measurements from tritium β decay,” *Phys.
 5608 Rev. C*, **91**(3), p. 035505, 1502.03497.
- 5609 [56] ASNER, D. M. ET AL. (2015) “Single electron detection and spectroscopy via
 5610 relativistic cyclotron radiation,” *Phys. Rev. Lett.*, **114**(16), p. 162501, 1408.5362.
- 5611 [57] VÉNOS, D., J. SENTKERESTIOVÁ, O. DRAGOUN, M. SLEZÁK, M. RYŠAVÝ, and
 5612 A. ŠPALEK (2018) “Properties of 83mKr conversion electrons and their use in the
 5613 KATRIN experiment,” *JINST*, **13**(02), p. T02012.
- 5614 [58] LAGENDIJK, A., I. F. SILVERA, and B. J. VERHAAR (1986) “Spin exchange and
 5615 dipolar relaxation rates in atomic hydrogen: Lifetimes in magnetic traps,” *Phys.
 5616 Rev. B*, **33**, pp. 626–628.
 5617 URL <https://link.aps.org/doi/10.1103/PhysRevB.33.626>
- 5618 [59] SILVERA, I. and J. WALRAVEN (1986) “Spin-polarized atomic hydrogen,” *Prog.
 5619 Low Temp. Phys.*, **X**, pp. 139–370.
- 5620 [60] FURSE, D. ET AL. (2017) “Kassiopeia: a modern, extensible C++ particle tracking
 5621 package,” *New Journal of Physics*, **19**(5), p. 053012.
 5622 URL <https://doi.org/10.1088/1367-2630/aa6950>
- 5623 [61] ESFAHANI, A. A., V. BANSAL, S. BÖSER, N. BUZINSKY, R. CERVANTES,
 5624 C. CLAESSENS, L. DE VIVEIROS, P. J. DOE, M. FERTL, J. A. FORMAGGIO,
 5625 L. GLADSTONE, M. GUIGUE, K. M. HEEGER, J. JOHNSTON, A. M. JONES,
 5626 K. KAZKAZ, B. H. LAROQUE, M. LEBER, A. LINDMAN, E. MACHADO, B. MON-
 5627 REAL, E. C. MORRISON, J. A. NIKKEL, E. NOVITSKI, N. S. OBLATH, W. PET-
 5628 TUS, R. G. H. ROBERTSON, G. RYBKA, L. SALDAÑA, V. SIBILLE, M. SCHRAM,
 5629 P. L. SLOCUM, Y.-H. SUN, J. R. TEDESCHI, T. THÜMMLER, B. A. VAN-
 5630 DEVENDER, M. WACHTENDONK, M. WALTER, T. E. WEISS, T. WENDLER,
 5631 and E. ZAYAS (2019) “Electron radiated power in cyclotron radiation emission
 5632 spectroscopy experiments,” *Phys. Rev. C*, **99**, p. 055501.
 5633 URL <https://link.aps.org/doi/10.1103/PhysRevC.99.055501>
- 5634 [62] ASHTARI ESFAHANI, A. ET AL. (2019) “Locust: C++ software for simulation of
 5635 RF detection,” *New J. Phys.*, **21**, p. 113051, 1907.11124.
- 5636 [63] WIECHERT, E. (1901) “Elektrodynamische Elementargesetze,” .
 5637 URL <https://doi.org/10.1002/andp.19013090403>
- 5638 [64] LIÉARD, A. (1898) “Champ électrique et Magnétique,” *Léclairage électrique*, **16**(27-
 5639 29).
- 5640 [65] BALANIS, C. (2015) *Antenna Theory: Analysis and Design*, Wiley.
 5641 URL <https://books.google.com/books?id=PTFcCwAAQBAJ>

- 5642 [66] <https://www.ansys.com/products/electronics/ansys-hfss>.
- 5643 [67] https://en.wikipedia.org/wiki/Linear_time-invariant_system.
- 5644 [68] NYQUIST, H. (1928) “Certain Topics in Telegraph Transmission Theory,” *Transactions of the American Institute of Electrical Engineers*, **47**(2), pp. 617–644.
- 5645
- 5646 [69] BRUN, R. and F. RADEMAKERS (1997) “ROOT: An object oriented data analysis framework,” *Nucl. Instrum. Meth. A*, **389**, pp. 81–86.
- 5647
- 5648 [70] ASHTARI ESFAHANI, A. ET AL. (2021) “Bayesian analysis of a future β decay experiment’s sensitivity to neutrino mass scale and ordering,” *Phys. Rev. C*, **103**, p. 065501.
- 5649
- 5650 URL <https://link.aps.org/doi/10.1103/PhysRevC.103.065501>
- 5651
- 5652 [71] KAY, S. (1998) *Fundamentals of Statistical Signal Processing: Detection Theory, Volume II*, Pearson.
- 5653
- 5654 [72] NEYMAN, J. and E. PEARSON (1933) “On the problem of the the most efficient
- 5655 tests of statistical hypotheses,” *Phil. Trans. R. Soc. Lond. A*, **231**.
- 5656 [73] STUMPF, M. (2018) *Electromagnetic Reciprocity in Antenna Theory*, Wiley.
- 5657 [74] BISHOP, C. (2016) *Pattern Recognition and Machine Learning*, Springer.
- 5658 [75] PLEHN, T., A. BUTTER, B. DILLON, and C. KRAUSE (2022) “Modern Machine
- 5659 Learning for LHC Physicists,” [2211.01421](https://arxiv.org/abs/2211.01421).
- 5660 [76] GEORGE, D. and E. A. HUERTA (2018) “Deep Learning for Real-time Gravitational
- 5661 Wave Detection and Parameter Estimation: Results with Advanced LIGO Data,”
- 5662 *Phys. Lett. B*, **778**, pp. 64–70, [1711.03121](https://arxiv.org/abs/1711.03121).
- 5663 [77] GABBARD, H., C. MESSENGER, I. S. HENG, F. TONOLINI, and R. MURRAY-
- 5664 SMITH (2022) “Bayesian parameter estimation using conditional variational au-
- 5665 toencoders for gravitational-wave astronomy,” *Nature Phys.*, **18**(1), pp. 112–117,
- 5666 [1909.06296](https://arxiv.org/abs/1909.06296).
- 5667 [78] REIMANN, R. (2022) “Project 8: R&D for a next-generation neutrino mass experi-
- 5668 ment,” *PoS, PANIC2021*, p. 283.
- 5669 [79] LAROQUE, B. (2020) “Zero-deadtime processing in beta spectroscopy for measure-
- 5670 ment of the non-zero neutrino mass,” *EPJ Web Conf.*, **245**, p. 01014.
- 5671 [80] BUZINSKY, N. (2021) *Statistical Signal Processing and Detector Optimization in*
- 5672 *Project 8*, Ph.D. thesis, Massachusetts Institute of Technology.

- 5673 [81] ESFAHANI, A. A., S. BÖSER, N. BUZINSKY, M. CARMONA-BENITEZ,
 5674 C. CLAESSENS, L. DE VIVEIROS, M. FERTL, J. FORMAGGIO, L. GLADSTONE,
 5675 M. GRANDO, J. HARTSE, K. HEEGER, X. HUYAN, A. JONES, K. KAZKAZ,
 5676 M. LI, A. LINDMAN, C. MATTHÉ, R. MOHIUDDIN, B. MONREAL, R. MUELLER,
 5677 J. NIKKEL, E. NOVITSKI, N. OBLATH, J. PEÑA, W. PETTUS, R. REIMANN,
 5678 R. ROBERTSON, L. SALDAÑA, P. SLOCUM, J. STACHURSKA, Y.-H. SUN, P. SU-
 5679 RUKUCHI, A. TELLES, F. THOMAS, M. THOMAS, L. THORNE, T. THÜMM-
 5680 LER, L. TVRZNIKOVA, W. V. D. PONTSEELE, B. VANDEVENDER, T. WEISS,
 5681 T. WENDLER, E. ZAYAS, A. ZIEGLER, and P. . COLLABORATION (2023) “SYNCA:
 5682 A Synthetic Cyclotron Antenna for the Project 8 Collaboration,” *Journal of In-*
 5683 *strumentation*, **18**(01), p. P01034.
 5684 URL <https://dx.doi.org/10.1088/1748-0221/18/01/P01034>
- 5685 [82] <https://www.nvidia.com/en-us/data-center/v100/>.
- 5686 [83] <https://www.nvidia.com/en-us/data-center/h100/>.
- 5687 [84] HE, K., X. ZHANG, S. REN, and J. SUN (2016) “Deep Residual Learning for
 5688 Image Recognition,” in *2016 IEEE Conference on Computer Vision and Pattern
 5689 Recognition (CVPR)*, pp. 770–778.
- 5690 [85] SIMONYAN, K. and A. ZISSERMAN (2015) “Very Deep Convolutional Networks
 5691 for Large-Scale Image Recognition,” in *3rd International Conference on Learning
 5692 Representations, ICLR 2015, San Diego, CA, USA, May 7-9, 2015, Conference
 5693 Track Proceedings* (Y. Bengio and Y. LeCun, eds.).
 5694 URL <http://arxiv.org/abs/1409.1556>
- 5695 [86] FRIIS, H. (1946) “A Note on a Simple Transmission Formula,” *Proceedings of the
 5696 IRE*, **34**(5), pp. 254–256.
- 5697 [87] POZAR, D. M. (2005) *Microwave engineering*; 3rd ed., Wiley, Hoboken, NJ.
 5698 URL <https://cds.cern.ch/record/882338>
- 5699 [88] AKER, M. ET AL. (2022) “Direct neutrino-mass measurement with sub-electronvolt
 5700 sensitivity,” *Nature Physics*, **18**(2), pp. 160–166.
 5701 URL <https://doi.org/10.1038/s41567-021-01463-1>
- 5702 [89] MONREAL, B. and J. A. FORMAGGIO (2009) “Relativistic Cyclotron Radiation
 5703 Detection of Tritium Decay Electrons as a New Technique for Measuring the
 5704 Neutrino Mass,” *Phys. Rev. D*, **80**, p. 051301, 0904.2860.
- 5705 [90] ASHTARI ESFAHANI, A. ET AL. (2017) “Determining the neutrino mass with
 5706 cyclotron radiation emission spectroscopy—Project 8,” *J. Phys. G*, **44**(5), p. 054004,
 5707 1703.02037.
- 5708 [91] ESFAHANI, A. A. ET AL. (2022) “The Project 8 Neutrino Mass Experiment,” in
 5709 *2022 Snowmass Summer Study*, 2203.07349.

- 5710 [92] ASHTARI ESFAHANI, A. ET AL. (2019) “Locust: C++ software for simulation of
 5711 RF detection,” *New Journal of Physics*, **21**(11), p. 113051.
 5712 URL <https://doi.org/10.1088/1367-2630/ab550d>
- 5713 [93] FURSE, D. ET AL. (2017) “Kassiopeia: a modern, extensible C++ particle tracking
 5714 package,” *New Journal of Physics*, **19**(5), p. 053012.
 5715 URL <https://doi.org/10.1088/1367-2630/aa6950>
- 5716 [94] BALANIS, C. (2011) *Modern Antenna Handbook*, Wiley.
 5717 URL <https://books.google.com/books?id=UYpV8L8GNCwC>
- 5718 [95] WIRTH, W. (2001) *Radar Techniques Using Array Antennas*, Institution of Engi-
 5719 neering and Technology.
 5720 URL <https://books.google.com/books?id=ALht42gkzLsC>
- 5721 [96] BROWN, L. S., G. GABRIELSE, K. HELMERSON, and J. TAN (1985) “Cyclotron
 5722 motion in a microwave cavity: Lifetime and frequency shifts,” *Phys. Rev. A*, **32**,
 5723 pp. 3204–3218.
 5724 URL <https://link.aps.org/doi/10.1103/PhysRevA.32.3204>
- 5725 [97] HANNEKE, D., S. FOGWELL HOOGERHEIDE, and G. GABRIELSE (2011) “Cavity
 5726 control of a single-electron quantum cyclotron: Measuring the electron magnetic
 5727 moment,” *Phys. Rev. A*, **83**, p. 052122.
 5728 URL <https://link.aps.org/doi/10.1103/PhysRevA.83.052122>
- 5729 [98] HANNEKE, D. A. (2007) *Cavity control in a single-electron quantum cyclotron: an
 5730 improved measurement of the electron magnetic moment*, Ph.D. thesis, Harvard U.
- 5731 [99] PURCELL, E. (1946) “Spontaneous Emission Probabilities at Radio Frequencies,”
 5732 *Phys. Rev.*, **69**, pp. 674–674.
 5733 URL <https://link.aps.org/doi/10.1103/PhysRev.69.674>
- 5734 [100] MOSKOWITZ, B. E. and J. ROGERS (1988) “ANALYSIS OF A MICROWAVE
 5735 CAVITY DETECTOR COUPLED TO A NOISY AMPLIFIER,” *Nucl. Instrum.
 5736 Meth. A*, **264**, pp. 445–452.
- 5737 [101] RAPIDIS, N. M. (2018) “Application of the Bead Perturbation Technique to a
 5738 Study of a Tunable 5 GHz Annular Cavity,” *Springer Proc. Phys.*, **211**, pp. 45–51,
 5739 1708.04276.
- 5740 [102] “Real-time Signal Detection for Cyclotron Radiation Emission Spectroscopy Mea-
 5741 surements using Antenna Arrays,” *In preparation*.
- 5742 [103] BYRON, W. ET AL. (2022) “First observation of cyclotron radiation from MeV-scale
 5743 e^{pm} following nuclear beta decay,” 2209.02870.

⁵⁷⁴⁴ [104] KAZKAZ, K. and N. WOOLLETT (2021) “Using Cyclotron Radiation Emission
⁵⁷⁴⁵ for Ultra-high Resolution X-Ray Spectroscopy,” *New J. Phys.*, **23**(3), p. 033043,
⁵⁷⁴⁶ 1911.05869.

⁵⁷⁴⁷ [105] CANNING, J. A. L., F. F. DEPPISCH, and W. PEI (2023) “Sensitivity of future
⁵⁷⁴⁸ tritium decay experiments to New Physics,” *JHEP*, **03**, p. 144, 2212.06106.

5749

Vita

5750

Andrew Douglas Ziegler

5751

Education

5752

- Doctor of Philosophy, Physics, The Pennsylvania State University, 2023
- Bachelor of Science, Physics, The University of Minnesota, 2017

5753

Selected Publications

5754

Selected Presentations

5755